Fakultät für Physik der Technischen Universität München

Max-Planck-Institut für Physik
(Werner-Heisenberg-Institut)

Measurement of Higgs Boson Production via Vector Boson Fusion in Decays into W Bosons with the ATLAS Detector

Johanna Bronner

Für meine Großmütter
Ingeborg Schoppel
und
Elisabeth Bronner

Abstract

The vector boson fusion production rate of the Standard Model Higgs boson has been measured in decays into two W bosons, each subsequently decaying into an electron or muon and a neutrino, with the ATLAS detector at the Large Hadron Collider (LHC). The vector boson fusion production cross section in the Standard Model is about an order of magnitude smaller than the dominant Higgs boson production cross section from gluon fusion. Proton-proton collision data at a center-of-mass energy of 8 TeV delivered by the LHC recorded with the ATLAS detector corresponding to an integrated luminosity of $21 \, \mathrm{fb}^{-1}$ have been analyzed. Motivated by the recent discovery of a Higgs-like boson with a mass of $(125.5 \pm 0.6) \, \mathrm{GeV}$ and $(125.7 \pm 0.4) \, \mathrm{GeV}$ by the ATLAS and CMS collaborations at the LHC, the analysis is optimized for this mass. An excess of events, compatible with the Standard Model expectation for a Higgs boson with $m_H = 125 \, \mathrm{GeV}$, is observed with a significance of 2.8 standard deviations when compared to the background-only expectation. The corresponding signal strength, the observed event rate relative to the Standard Model prediction of $m_H = 125 \, \mathrm{GeV}$ is $2.1^{+1.0}_{-0.8}$. A Higgs boson produced via vector boson fusion is excluded with 95% confidence level in the mass range between $152 \, \mathrm{GeV}$ and $185 \, \mathrm{GeV}$.

When combined with measurements of other Higgs boson production and decay channels by ATLAS, evidence for vector boson fusion production with a significance of 3.3 standard deviations is observed. All measurements of Higgs boson couplings to Standard Model particles are in agreement with the predictions of the Standard Model.

Acknowledgments

I would like to thank Sandra Kortner and Hubert Kroha for accepting me as a PhD student and guiding me through the past years. I am in particular thankful for the long term stay at CERN. It has been a unique chance I deeply appreciate. Also I am very thankful for all the time they devoted in the thesis corrections. In addition I would like to thank Robert Richter, Rikard Sandström, Max Goblirsch-Kolb and Hans Lehmann for their help. Many thanks also to Olivier Arneaz, who helped me a lot with all the physics related questions, that came up while writing up the thesis.

I am very thankful for the social and professional environment I worked within. Thanks to all those at CERN and at the MPP for many fruitful physics discussions and pleasant social activities. I would like to thank Evelyn Schmidt for opening me the doors to the HSG3 group and Joana Machado Miguéns for our very good cooperation. Thanks to Sebastian Stern for his enchanting travel company and for losing all those bets. Lastly, special Thanks to Philipp Schwegler for being the best possible office mate.

I am very grateful for the support of my family in particular of Anne, Nina and Dorothea Bronner. Thanks to all my friends bearing with the little time I invested in our friendships the past years. I am in particular thankful to the Family Becerici-Schmidt, whose house has become a shelter where all the PhD problems seemed largely irrelevant.

Through all the ups and downs of the past years I have been a generally cheerful person with a strong believe that everything will be alright, thanks to Jonathan Burdalo Gil, who pushed me when I needed a push, who made me relax when I needed to relax and who made me laugh, when life didn't give me much reason to. Thank you for making me the happy person I am.

Contents

Chapter 1

Introduction

The Standard Model, developed in the second half of the 20th century, successfully describes the interactions between the elementary particles via the principle of local gauge symmetry. Its predictions have been precisely confirmed by experiments. No contradictions to the Standard Model have yet been observed. In particular, the Standard Model explains the masses of the gauge bosons mediating the weak interaction and the origin of fermion masses by the Higgs mechanism developed by Englert, Brout [1] and Higgs [2,3] as well as Hagen, Guralnik and Kibbel [4]. The mechanism predicts a massive scalar particle, the Higgs boson, which couples to all massive Standard Model particles. A description of the Standard Model and the Higgs mechanism as well as a summary of the predictions of the Higgs boson properties is given in Chapter 2.

The discovery of the Higgs boson is an essential step in verifying the Higgs mechanism. The Large Hadron Collider (LHC) at CERN, designed for colliding proton beams with a center-of-mass energy of 14 TeV, has been constructed in order to finally discover the Higgs boson. It is in operation since autumn 2009 with an interruption for repairs in 2013 and 2014. The beam energies reached 4 TeV in 2012. Data corresponding to an integrated luminosity of 21 fb^{-1} were collected at this energy. Another 5 fb^{-1} of data were collected at a center-of-mass energy of 7 TeV in 2011. The design energy is expected to be reached with the restart of the LHC in 2015.

The data used in this thesis have been recorded with the ATLAS* detector at the LHC. The detector is described together with the LHC accelerator system in Chapter 3. The reconstruction of particles and jets, physics objects needed for the analysis, is described in Chapter 4.

---

*ATLAS: A Toroidal LHC AparatuS

In July 2012 the ATLAS [5] and CMS* [6] experiments discovered a Higgs boson candidate. Employing the full available dataset a mass of 125.5 GeV [7] and 125.7 GeV [8] was measured by the ATLAS and CMS experiments, respectively. The properties of the boson have been tested in detail for their compatibility with the Standard Model predictions. One necessary test is the verification of the different production and decay processes predicted by the Standard Model.

The thesis focusses on the measurement of the production of the Higgs boson through Vector Boson Fusion (VBF) in the decay channel into two W bosons, each subsequently decaying into an electron or muon accompanied by a neutrino, i.e. $H \to WW^{(*)} \to \ell\nu\ell\nu$. This final state is one of the most important Higgs boson search channels due to the large branching fraction and clear signature. The VBF production mode is identified by its characteristic signature with two energetic jets in the final state produced dominantly in forward direction and well separated in rapidity.

Different processes contribute to the background of this channel. The largest ones are W boson and top-quark-pair production as well as Drell-Yan processes. The gluon fusion production of the Higgs boson with an order of magnitude larger cross section than the VBF production counts as a background contribution. The background expectation from Monte-Carlo simulations are, wherever possible, corrected for using control measurements. The event selection, background determinations and results for this analysis are presented in Chapter 5.

Finally, the combination of the above result with other Higgs boson decay channels in VBF and gluon fusion preselection measurements by the ATLAS experiment are presented in Chapter 6. The result of a combined VBF production rate measurement as well as the measurement of the Higgs boson couplings to Standard Model particles are discussed.

---

*CMS: Compact Muon Solenoid

Chapter 2

The Higgs Boson
in the Standard Model

This chapter introduces the theoretical framework for this thesis. It begins with an introduction to the *Standard Model* of particle physics in Section 2.1 (see also [9]). In Section 2.2 the theoretical predictions for Higgs boson production cross sections at hadron colliders and the Higgs boson decay branching ratios are discussed. The discovery of the Higgs boson candidate and the results of its property measurements with the ATLAS and CMS experiments at the LHC are outlined in Section 2.3.

Throughout this thesis natural units are used, with $\hbar = c = 1$, such that momentum and mass have units of energy.

2.1   The Standard Model of Elementary Particles

The Standard Model is a quantum field theory based on local gauge symmetries with the symmetry group

$$SU(3) \otimes SU(2) \otimes U(1) \quad , \tag{2.1}$$

comprising the color symmetry $SU(3)$ of the strong interaction and the symmetry $SU(2) \otimes U(1)$ of the electroweak interaction*. The latter is spontaneously broken by the *Higgs-mechanims*. The properties of the interactions are determined by the group structure of the gauge symmetry. Since the gauge theories are renormalizable precise predictions in higher-order perturbation theory are possible (see Section 2.2). The Standard Model has been verified in many experimental tests. Up to now no significant

---

*The gravitational force is not included in the Standard Model.

deviations from the Standard Model have been found.

All particles described by the Standard Model have been observed, including a Higgs boson candidate. The elementary particles of the Standard Model (see Table 2.1) are classified in the following way:

Fermions: Two types of fermions, both with spin-1/2, are the building blocks of matter: *quarks* and *leptons*. There are charged leptons and neutral leptons, the neutrinos. While quarks participate in all known interactions, leptons do not interact strongly and neutrinos in addition do not interact electromagnetically. Three generations of quarks and leptons have been observed. The masses of the fermions spread over a large range. For each fermion f an anti-fermion $\bar{f}$ with the same mass and opposite electric charge and parity quantum number exists.

Vector Bosons carrying spin-one are the mediators of the fundamental interactions: Eight gluons for the strong, $W^\pm$ and Z^0 bosons for the weak and the photon for the electromagnetic interaction. The $W^\pm$ and Z^0 bosons are massive while the gluons and the photon are massless.

Higgs Boson: The only elementary spin-zero particle described by the Standard Model is the scalar (CP even) Higgs boson. It is predicted to be massive.

The fundamental interactions of the particles in the Standard Model are described by local quantum gauge field theories with the simplest unitary symmetry groups $U(1)$, $SU(2)$ and $SU(3)$:

- **Quantum electrodynamics (QED)** [12–17] describes the electromagnetic interaction between electrically charged particles which is mediated by the massless photon and defined by the Abelian $U(1)$ gauge symmetry.

- The **weak interaction** is described together with the electromagentic interaction by the Glashow-Salam-Weinberg theory [18–21], a non-Abelian $SU(2){\otimes}U(1)$ gauge theory. It is mediated by the massive W^+, W^- and Z^0 bosons.

- **Quantum chromodynamics (QCD)** [22] describes the strong interaction between particles carrying color charge and is defined by the non-Abelian $SU(3)$ gauge symmetry. Eight massless gluons carrying different combinations of color and anti-color are the mediators of the strong interaction. A characteristic of QCD

Table 2.1: Overview of the particles in the Standard Model. J denotes the spin and P the parity of the particle. The masses are taken from [7, 10, 11]. The uncertainties for the lepton masses are below 0.01%.

			Name	Symbol	Charge[e]	Mass
Fermions	**Leptons**	$J^P = 1/2^+$	Electron neutrino	ν_e	0	$< 2\,\mathrm{eV}$
			Electron	e	-1	$0.511\,\mathrm{MeV}$
			Myon neutrino	ν_μ	0	$< 0.12\,\mathrm{MeV}$
			Myon	μ	-1	$105.7\,\mathrm{MeV}$
			Tau neutrino	ν_τ	0	$< 18.2\,\mathrm{MeV}$
			Tau	τ	-1	$1.777\,\mathrm{GeV}$
	Quarks	$J^P = 1/2^+$	Up	u	$+2/3$	$2.3^{+0.7}_{-0.5}\,\mathrm{MeV}$
			Down	d	$-1/3$	$4.8^{+0.5}_{-0.3}\,\mathrm{MeV}$
			Strange	s	$+2/3$	$95 \pm 5\,\mathrm{MeV}$
			Charm	c	$-1/3$	$1.275 \pm 0.025\,\mathrm{GeV}$
			Bottom	b	$+2/3$	$4.18 \pm 0.03\,\mathrm{GeV}$
			Top	t	$-1/3$	$173.29 \pm 0.95\,\mathrm{GeV}$
Bosons	**Vector**	$J^P = 1^-$	Gluon	g	0	0
			Photon	γ	0	0
			W boson	$W^\pm$	± 1	$80.385 \pm 0.015\,\mathrm{GeV}$
			Z boson	Z^0	0	$91.1876 \pm 0.0021\,\mathrm{GeV}$
	Scalar	$J^P = 0^+$	Higgs boson	H	0	$125.6^{+0.5}_{-0.6}\,\mathrm{GeV}$

is that the strong coupling constant α_s increases with distance. Particles carrying color charges, gluons and quarks, are *confined* in color-singlet bound states of either quark-antiquark pairs (*mesons*) or triplets of quarks (*baryons*). At short distances, the strong coupling strength decreases and quarks and gluons behave like free particles inside the bound states (*asymptotic freedom*).

Non-Abelian gauge symmetries, as for QCD and the weak interaction, lead to self interaction of the mediating vector bosons which is not present for the photon. Local gauge theories predict massless gauge bosons mediating the interactions, like the photon and the gluons. This is in contradiction with the observed large masses of the weak gauge bosons $W^\pm$ and Z^0. The theory of the electroweak interaction unifying the electromagnetic and weak forces provides a mechanism to overcome this problem.

Electroweak Unification   The electroweak interaction is a unification of the electromagnetic and weak forces with the gauge symmetry $SU(2) \otimes U(1)$ introduced by Glashow [18], Salam [20, 21] and Weinberg [19]. The $SU(2)$ and $U(1)$ gauge symmetries require four massless vector fields. The vector fields corresponding to the $SU(2)$ group are denoted by W_μ^a ($a = 1,\ 2,\ 3$) and the vector field of the $U(1)$ group by B_μ. The observed $W_\mu^\pm$ and Z_μ boson fields and the photon field A_μ are related to the four vector fields W_μ^a and B_μ by the transformation

$$
\begin{aligned}
W_\mu^\pm &= \quad \frac{1}{\sqrt{2}}(W_\mu^1 \mp i W_\mu^2) \quad , \\
Z_\mu &= \quad W_\mu^3 \cdot \cos\theta_\mathrm{W} - B_\mu \cdot \sin\theta_\mathrm{W} \quad , \\
A_\mu &= \quad W_\mu^3 \cdot \sin\theta_\mathrm{W} + B_\mu \cdot \cos\theta_\mathrm{W}
\end{aligned}
\tag{2.2}
$$

where the rotation angle θ_W is the *weak mixing angle*. It relates the elementary charge e and the gauge coupling strengths g and g' corresponding to the $SU(2)$ and $U(1)$ groups, respectively, by

$$
e = g \cdot \sin\theta_\mathrm{W} = g' \cdot \cos\theta_\mathrm{W} \quad .
\tag{2.3}
$$

The Higgs-Mechanism   The electroweak gauge symmetry $SU(2) \otimes U(1)$ is spontaneously broken to the $U(1)$ symmetry of the electromagnetic interaction,

$$
SU(2) \otimes U(1) \xrightarrow[\text{symmetry breaking}]{\text{spontaneous}} U(1) \quad ,
\tag{2.4}
$$
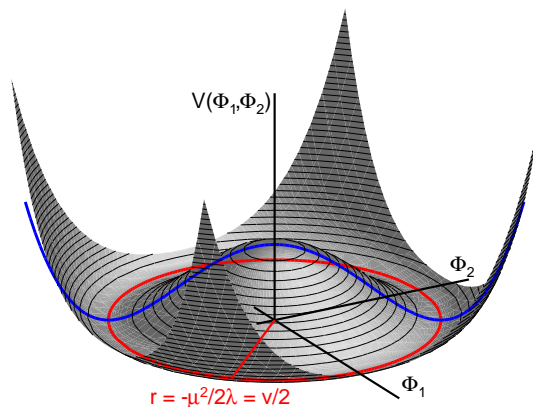
Figure 2.1: Illustration of the shape of the Higgs potential V depending on the real and imaginary parts Φ_1 and Φ_2 of a complex scalar field breaking local $U(1)$ symmetry. The minima of the potential lie on a circle with radius $r = \sqrt{\Phi_1^2 + \Phi_2^2} = v/2$ around the origin.

giving masses to the weak gauge bosons $W^\pm$ and Z^0 while the photon corresponding to the remaining unbroken $U(1)$ symmetry of QED stays massless. This mechanism, the *Higgs-mechanism*, was independently proposed by Higgs [2,3], Englert and Brout [1] as well as Guralnik, Hagen and Kibble [4].

In its minimal version, the Higgs-mechanism of the Standard Model introduces a $SU(2)$ doublet of complex scalar fields

$$\Phi = \begin{pmatrix} \phi^+ \\ \phi^0 \end{pmatrix} \quad . \tag{2.5}$$

The self-interaction potential of this scaler Higgs doublet field,

$$V(\Phi) = \mu^2 \Phi^\dagger \Phi + \lambda (\Phi^\dagger \Phi)^2 \quad , \tag{2.6}$$

has, for $\lambda > 0$ and $\mu^2 < 0$, a shape as illustrated in Fig. 2.1 in the example of $U(1)$ symmetry breaking. The potential has a minimum fulfilling the criterion

$$\Phi^\dagger \Phi = -\frac{\mu^2}{2\lambda} \equiv \frac{v}{2} \quad , \tag{2.7}$$

where v is called the vacuum expectation value of the scalar field. While the full set

of ground states is $SU(2) \times U(1)$ symmetric, choosing one specific ground state or vacuum spontaneously breaks the symmetry leaving only a $U(1)$ symmetry for the electromagnetic interaction. A possible choice of ground state is

$$\Phi_0 = \frac{1}{\sqrt{2}} \begin{pmatrix} 0 \\ v \end{pmatrix} \quad . \tag{2.8}$$

Excitations from the ground state can be parameterized by:

$$\Phi(x) = \frac{\exp[iT_a\theta^a(x)]}{\sqrt{2}} \begin{pmatrix} 0 \\ v + H(x) \end{pmatrix} \tag{2.9}$$

where θ^a are three scalar fields corresponding to massless Goldstone bosons which accompany the symmetry breaking [23, 24]. The Goldstone bosons correspond to excitations within the set of symmetric ground states, i.e. tangential to the circle of minima in the example in Fig. 2.1. The Goldstone fields can be eliminated by a local gauge transformation (unitary gauge)

$$\Phi(x) \to \Phi'(x)\exp[-iT_a\theta^a(x)] \quad . \tag{2.10}$$

The additional scalar field $H(x)$, a massive excitation, i.e. orthogonal to the set of ground states, cannot be transformed away. $H(x)$ is called the *Higgs boson* field.

The $W^{\pm}_{\mu}$ and Z_{μ} boson acquire masses by absorbing the degrees of freedom of the three Goldstone bosons after the gauge transformation, while the photon field A_{μ} remains massless. The masses of the weak gauge bosons are given by

$$m_W = \frac{vg}{2} = m_Z \cos\theta_{\mathrm{W}} \quad , \tag{2.11}$$

in lowest order of perturbation theory. The Higgs boson mechanism also leads to couplings between the Higgs boson H and the weak vector bosons $V = W, Z$ with a strength given by

$$g_{HVV} = -2i\frac{m_V^2}{v} \qquad \text{and} \qquad g_{HHVV} = -2i\frac{m_V^2}{v^2} \quad . \tag{2.12}$$

Since the masses of the $W^{\pm}$ and Z^0 bosons are related via the weak mixing angle θ_{W} (Eq. (2.11)), the strengths of the Higgs boson coupling to the $W^{\pm}$ and Z^0 are related as well which is referred to as *custodial symmetry*.

Fermions acquire their masses by *Yukawa couplings* to the scalar field with a strength of g_f proportional to the fermion masses m_f not predicted by the Standard Model:

$$g_f = im_f \cdot \frac{\sqrt{2}}{v} \quad .$$

(2.13)

The mass $m_H = \sqrt{2\lambda v^2}$ of the Higgs boson, is also not predicted by the Standard Model like the Higgs self interaction strength λ. However, since $\lambda > 0$ is required for spontaneous symmetry breaking, the Higgs boson cannot be massless. The existence of a massive scalar particle, like the Higgs boson is needed to preserve, for instance, unitarity in WW scattering.

2.2   Higgs Boson Production in Proton-Proton Collisions

In this section the theoretical predictions for Higgs boson production and decays at proton colliders are outlined (see [25]). The calculation of production cross sections at proton colliders has to take into account that protons are composite particles. The processes of interest take place between proton constituents and are accompanied by interactions of the residual constituents. These calculations are explained in Section 2.2.1. A more detailed summary can be found in [26].

The main mechanisms of Higgs boson productions are discussed in Section 2.2.2. The most important Higgs boson decays are discussed in Section 2.2.3. The predicted differential cross sections and decay rates for signal and background processes are used in Monte-Carlo generators to simulate events that can be compared to real collision data. The event generators used are described in Section 2.2.4.

2.2.1   Phenomenology of Proton-Proton Scattering

Protons are composite particles, consisting of three valence quarks, gluons and sea quarks, together called partons. A parton-parton collisions is classified as either hard or soft depending on the momentum transfer in the collision. QCD calculations are much more precise for hard than for soft processes, since for large momentum transfer perturbation theory is applicable. The soft processes however, are by far dominating at hadron colliders. A hard scattering process is, therefore, usually accompanied by soft reactions taking place between the partons not participating in the hard scatter process.
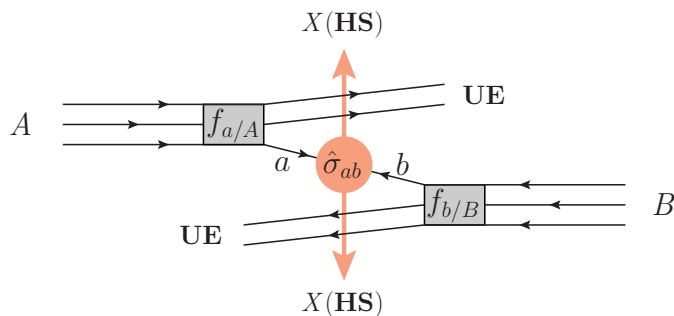
Figure 2.2: Factorization of proton-proton scattering into the hard scattering (HS) process $ab \to X$ with cross section $\hat{\sigma}_{ab \to X}$ and the remaining soft scattering processes leading to the underlying event (UE). The functions $f_{a/A}$ and $f_{b/B}$ are the experimentally determined Parton Distribution Functions (PDF) describing the momentum distribution of quarks and gluons in the proton.

The soft part of a proton-proton collision is referred to as the *underlying event.*

To describe the proton-proton interaction of two protons A and B, the process is *factorized* into its hard and its soft part (see Fig. 2.2). For the hard reaction $ab \to X$ of two partons a and b in the two protons into a final state X pertubation theory can be used to calculate the cross section $\hat{\sigma}_{ab \to X}$. The total proton scattering cross section σ_{AB} can then be determined as:

$$\sigma_{AB} = \int dx_a \, dx_b \, f_{a/A}(x_a, \mu_F^2) \, f_{b/B}(x_b, \mu_F^2) \, \hat{\sigma}_{ab \to X} \quad . \tag{2.14}$$

The function $f_{a/A}(x_a)$ is the *Parton Distribution Function* (PDF), which depends on the parton momentum fraction $x_a = p_a/E_{\text{beam}}$.

Perturbative QCD corrections, in particular from collinear gluon radiation from the incoming quarks, leads to large logarithmic terms. Factorization theorems [27] tell that the logarithmic terms for the hard scattering processes can be absorbed in the PDF introducing a dependence on the *factorization scale* μ_F which can be understood as the energy scale separating hard and soft physics.

The perturbative calculation of the hard scattering processes leads to expressions in powers of the strong coupling constant α_s depending on the renormalization scale μ_R relevant for the process:

$$\hat{\sigma}_{ab \to X} = \hat{\sigma}_0 + \alpha_s(\mu_R^2)\hat{\sigma}_1 + \dots \quad . \tag{2.15}$$
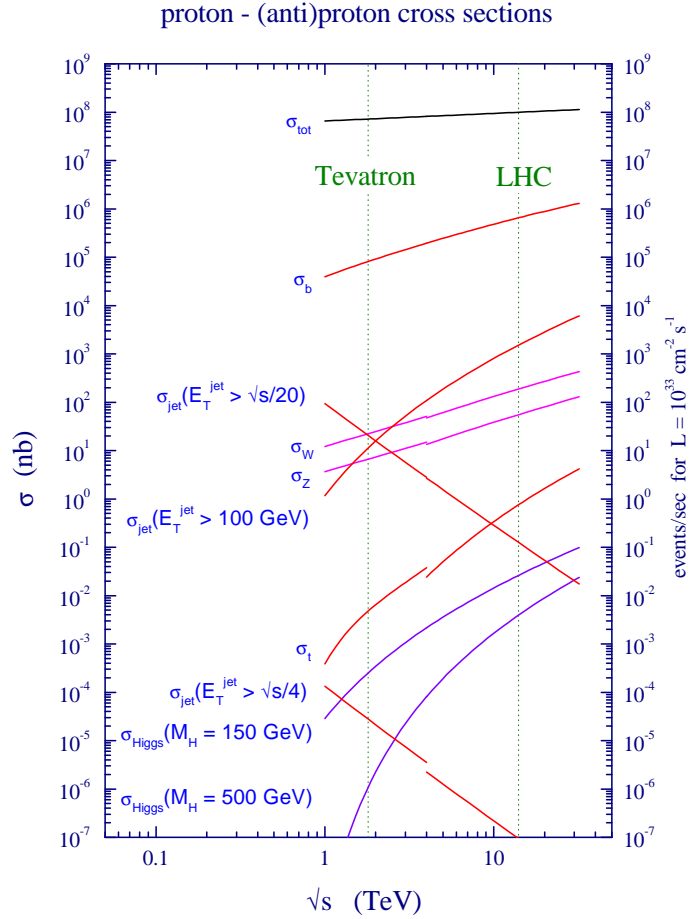
Figure 2.3: Next-to-leading-order cross sections σ as well as the expected number of events for an integrated lumniosity of $L = 10^{33}\,\mathrm{s}^{-1}\mathrm{cm}^{-2}$ of Standard Model processes in pp (LHC) and $p\bar{p}$ (Tevatron) collisions as a function of the center-of-mass energy $\sqrt{s}$ (from [26]).
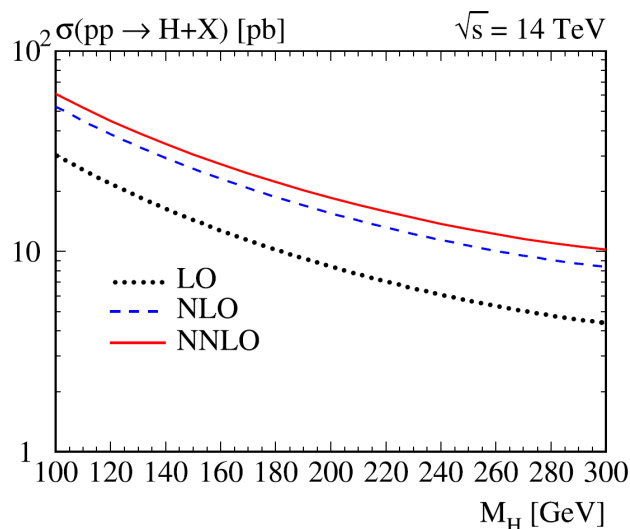
Figure 2.4: Inclusive Higgs boson cross section in proton-proton collisions as a function of the Higgs boson mass (from [26]).

Cross sections at hadron colliders calculated up to next-to-leading order in perturbation theory as a function of the center-of-mass energy are shown in Fig. 2.3. Figure 2.4 shows the inclusive Higgs boson cross section as a function of the Higgs boson mass calculated at leading-order (LO), next-to-leading-order (NLO) and next-to-next-to-leading-order (NNLO) in perturbation theory. The higher-order corrections are significant.

The calculated cross sections do not depend on the choice of the two scales μ_F and μ_R if all terms of the perturbation series are included. However, at finite order, a proper choice for the scales has to be made. A very common choice is $\mu_F = \mu_R = Q$, with the momentum transfer Q of the hard scattering process. The more higher-order terms there are calculated, the smaller the dependence on the scales is expected to be. To account for the residual scale dependence from unknown higher-order terms, a theoretical uncertainty is assigned to the predicted cross sections estimated from variations of μ_F and μ_R.

While the dependence of the PDFs on μ_F can be determined theoretically [28], the dependence on the parton momentum $x_{a/b}$ is obtained from fitting deep inelastic scattering data. Two PDF determinations, CT10 [29] and CTEQ6L1 [30] , are used for this thesis. As an example, the CT10 parton distribution functions for different quark flavors and gluons are shown in Fig. 2.5. On average gluons carry much smaller
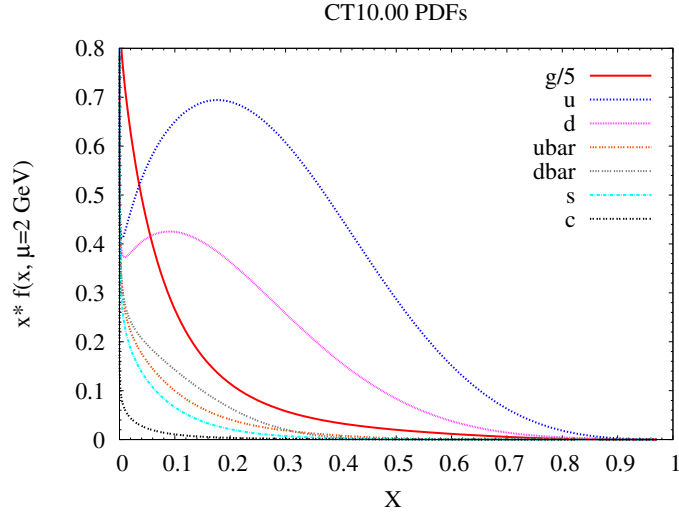
Figure 2.5: Parton distribution functions determined from CT10 [29] for a factorization scale $\mu = 2\,\text{GeV}$.

momentum fractions than the valence quarks. Uncertainties in the PDFs propagate to the predicted cross sections [31].

2.2.2 Higgs Boson Production at the LHC

The Standard Model Higgs boson is produced via several production mechanisms (see Fig. 2.6). An overview of the most important production mechanism is given in Table 2.2 together with the predicted cross sections at a center-of-mass energy of $\sqrt{s} = 8\,\text{TeV}$ and for a Higgs boson mass of $m_H = 125\,\text{GeV}$.

The by far dominant production process is via gluon fusion (ggF) occurring through quark loops dominated by heavy quarks, followed by the vector boson fusion (VBF) with by an order of magnitude smaller cross section. The cross sections for associated productions (VH) with vector bosons, $V = W$ and Z, are yet further factors of two (WH) and four (ZH) smaller than the VBF production. Production in association with a top-quark-pair occurs even less frequently. The cross sections as a function of the Higgs boson mass are shown in Fig. 2.7a. The cross section falls rapidly with increasing Higgs boson mass for all production modes. The calculations of the cross sections are described in [32]. A summary of the calculations relevant for this thesis is given below.

The ggF cross section has been computed up to NNLO in QCD [34–39] including

Table 2.2: The dominant Higgs boson production processes at the LHC and their cross section at a center-of-mass energy of $\sqrt{s} = 8 \, \text{TeV}$ for a Higgs boson mass of $m_H = 125 \, \text{GeV}$ [33].

Production mode	Symbol	Cross section [pb] $(m_H = 125 \, \text{GeV})$	Diagram (Figure)
$gg \to H$	ggF	$19.52 \, ^{+14.7\,\%}_{-14.7\,\%}$	2.6a
$qq \to qqH$	VBF	$1.58 \, ^{+2.8\,\%}_{-3.0\,\%}$	2.6b
$qq \to WH$	WH	$0.70 \, ^{+3.7\,\%}_{-4.1\,\%}$	2.6c
$qq \to ZH$	ZH	$0.39 \, ^{+5.1\,\%}_{-5.0\,\%}$	2.6c
$gg \to ttH$	ttH	$0.13 \, ^{+11.6\,\%}_{-17.0\,\%}$	2.6d
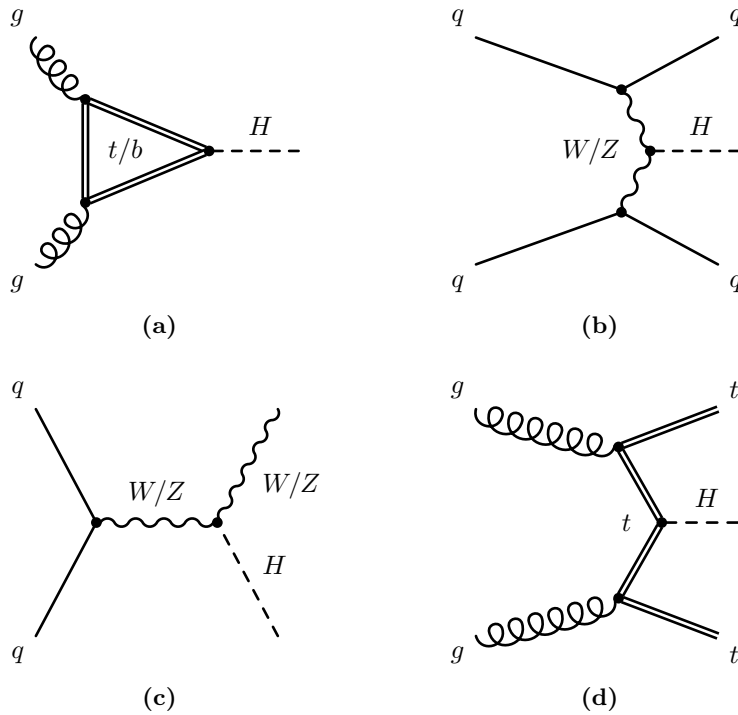
Figure 2.6: Leading-order Feynman diagrams for the dominant Higgs boson production mechanisms (a) gluon fusion (ggF), (b) weak vector boson fusion (VBF), (c) associated production with W or Z bosons (VH) and (d) associated production with a top-quark-pair (ttH).
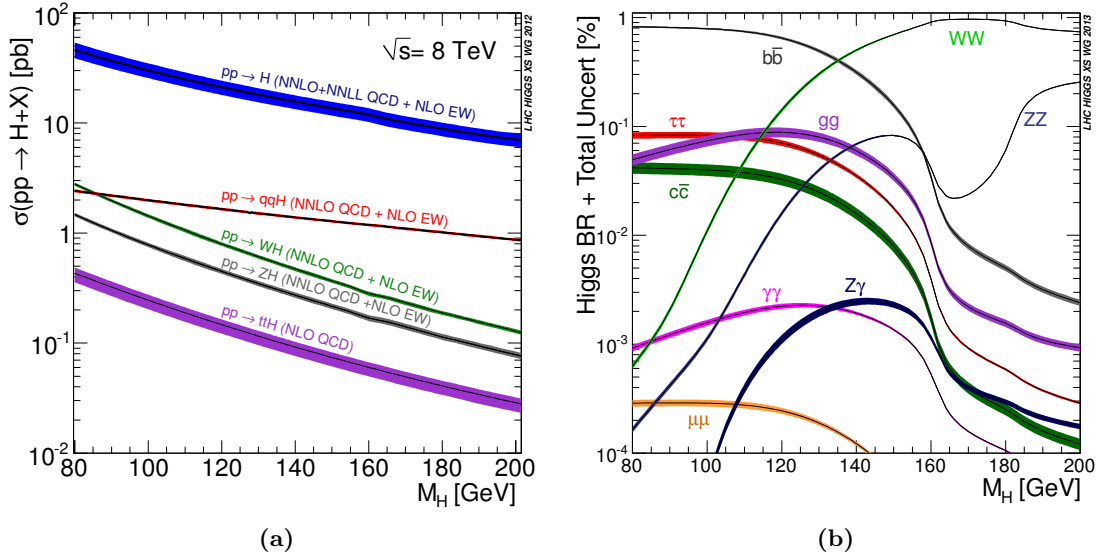
Figure 2.7: Predictions for (a) Higgs boson production cross section for proton-proton collisions at $\sqrt{s} = 8$ TeV and (b) branching ratios for the most important Higgs boson decay channels as a function of the Higgs boson mass m_H (from [33]). The uncertainties are indicated as bands.

NLO electroweak (EW) corrections [40, 41] and QCD soft-gluon resummation up to next-to-next-to-leading logarithmic (NNLL) terms [42]. These calculations are detailed in [43–45] and assume factorization of QCD and EW corrections.

The VBF cross section has been computed with full NLO QCD and EW corrections [46–48] and approximate NNLO QCD corrections [49] and full NLO QCD and EW corrections [46–48]. The cross section for the associated VH production has been calculated using NLO QCD and approximate NNLO corrections [50, 51] and NLO EW corrections [52]. The ttH production, not relevant here due to the small cross section, has been calculated only in NLO QCD.

The uncertainties, given in Table 2.2 and indicated by the bands in Fig. 2.7a, arise from uncertainties in the PDFs as well as from uncertainties from the choice of the factorization and normalization scales [32, 53].

The production mode through vector boson fusion is the focus of this thesis. Even though the cross section is smaller than for the dominant ggF production, it has the advantage of a characteristic signature with additional forward jets in the final state which can be exploited to separate the VBF production process from the background.

The ggF process contributing due to its much larger cross section is considered as additional background.

The two quarks in the final state of the VBF production, remnants of the incoming protons, are produced in forward direction while the Higgs boson decay products are expected in the central region of the detector. Since quarks from the incoming protons carry larger momenta than gluons (see Fig. 2.5) the invariant mass of the two additional quarks in the VBF process is expected to be larger than for QCD background processes where predominantly gluons are emitted from the incoming quarks. Since there is no color exchange between the initial and final state particles in the lowest-order weak VBF production, hadron activity in the central region, between the two quarks is suppressed [54–57]. In contrast, most backgrounds as well as the ggF production are QCD processes with hadronic activity expected in the central region. The exploitation of these characteristic properties for the selection of VBF events is explained in Chapter 5.

2.2.3 Higgs Boson Decays

The Higgs boson, as predicted by the Standard Model, decays through many different decay modes. The Standard Model Higgs boson favors decays to heavy vector bosons and fermions. Table 2.3 lists the dominant decay modes, ordered according to their branching fractions exemplary for $m_H = 125\,\mathrm{GeV}$. A Higgs boson with $m_H = 125\,\mathrm{GeV}$ dominantly decays into a b-quark-pair, followed by the decay into two W bosons. The decay to photons occurs predominantly via W boson and top quark loops. The $H \to gg$ decay process occurs in a similar manner via heavy quark loops like in ggF production (see Fig. 2.6a).

The sensitivity of the Higgs boson search depends not only on the branching fraction but also the final state signature and the amount of background for a particular final state. Strongly interacting decay products, such as b and c quarks, gluons or hadronic decays of W and Z bosons therefore are less sensitive final states in a hadron collider environment than final states with leptons.

When estimating the sensitivity for different Higgs boson decay channels, the subsequent decays of unstable daughter particles, such as the massive vector bosons, have to be considered as well. The analysis in this thesis uses $H \to WW^{(*)} \to \ell\nu\ell\nu$ decays where both W bosons decay leptonically. A theoretical study of this final state in combination with VBF production can be found in [59].

Table 2.3: Overview of the dominant Higgs boson decay modes for a Higgs boson mass $m_H = 125\,\text{GeV}$ [58]. Details on the branching fraction calculations can be found in [53].

Decay mode	Branching fraction $(m_H = 125\,\text{GeV})$	Diagram (Figure)
$H \to b\bar{b}$	$5.77\,^{+3.2}_{-3.3} \cdot 10^{-1}$	2.8c
$H \to WW^{(*)}$	$2.15\,^{+4.3}_{-4.2} \cdot 10^{-1}$	2.8b
$H \to gg$	$8.57\,^{+10.2}_{-10.0} \cdot 10^{-2}$	2.6a
$H \to c\bar{c}$	$2.91\,^{+12.2}_{-12.2} \cdot 10^{-2}$	2.8c
$H \to \tau\bar{\tau}$	$6.32\,^{+5.7}_{-5.7} \cdot 10^{-2}$	2.8c
$H \to ZZ^{(*)}$	$2.64\,^{+4.3}_{-4.2} \cdot 10^{-2}$	2.8b
$H \to \gamma\gamma$	$2.28\,^{+5.0}_{-4.9} \cdot 10^{-3}$	2.8a
$H \to \mu\bar{\mu}$	$2.20\,^{+6.0}_{-5.9} \cdot 10^{-4}$	2.8c
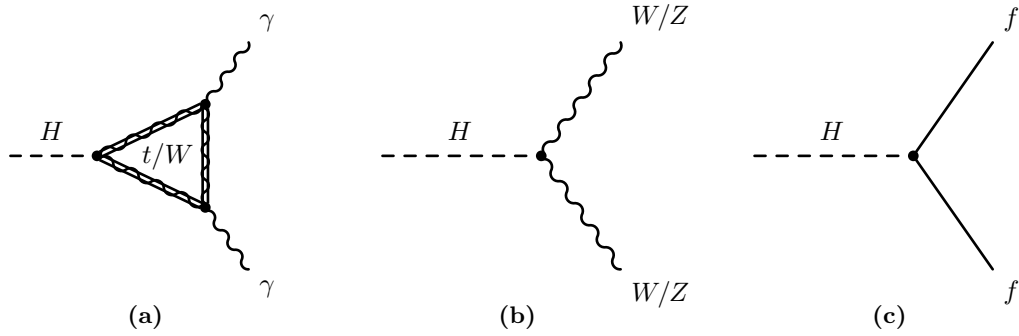
Figure 2.8: Leading-order Feynman diagrams for the main decay modes of the Standard Model Higgs boson.

The HDECAY [60] program computes Higgs boson decay widths and branching ratios for all channels. All available higher-order QCD corrections are taken into account. The Monte-Carlo generator PROPHECY4F [61, 62] simulates Higgs boson decays into four-leptons and is used for the branching fraction calculation. It takes into account all NLO QCD and electroweak corrections as well as interference terms from higher-order processes at LO and NLO, contributing to both the $H \to VV$ and the subsequent $V \to ff$ decays.

The determination of the uncertainties in the branching fraction calculations is detailed in [53]. Uncertainties in the input parameters α_s and m_c, m_b and m_t and uncertainties due to missing higher-order corrections are taken into account. Both contribute at the same level to the uncertainty in the branching ratio of dibosonic decays.

2.2.4 Event Generation and Simulation

In order to compare proton-proton collision data with theoretical predictions, large samples of simulated events are needed. The simulation proceeds in several steps, starting from the hard scattering process at the parton-level using the highest-order *matrix element* (ME) calculation available. In a second step, *parton shower* (PS) algorithms are used to simulate higher-order processes like gluon radiation by initial or final state particles, not taken into account in the matrix element calculation. The Monte-Carlo event generation is described in [63].

The hadronization of the final state partons is simulated using Monte-Carlo methods like the *Lund String model* [64]. The model parameters are tuned to electron-positron annihilation data where the hadronization process can be investigated in a clean environment.

In the last step, the underlying event is simulated. Like for the hadronization, the underlying event descriptions are tuned to data. Besides the underlying event, additional soft proton-proton interactions not involved in the hard scatter process, so called *pile-up* events, discussed in Section 3.1, have to be taken into account. The simulation of the pile-up contributions is performed in the same way as it is done for the underlying event.

The presented analysis uses several Monte-Carlo generators for the simulation of the signal and background processes. An overview is given in Table 2.4. The generators are specialized either for the simulation of the hard or the soft part of the process

Table 2.4: Overview of the Monte-Carlo event generators used in the presented analysis. The part of the event simulation the program is used for is indicated by HS for hard scattering process; had. for hadronization; PS for parton showering; UE+PU for underlying event and pile-up modelling. "All" indicates the case where the generator is used for the full event description.

	Name	Application	Remarks
NLO	Powheg [66]	HS	
	MC@NLO [67]	HS	
LO	Alpgen [68]	HS	Combined with Herwig and Jimmy using MLM [65] matching scheme
	AcerMC [69]	HS	
	MadGraph [70–72]	HS	
	GG2WW 3.2.1 [73,74]	HS	Dedicated to $gg \to WW$
	Sherpa [75]	All	Includes higher-order electroweak corrections
	Pythia6/8 [76,77]	had., PS, UE+PU	Also for $qq \to VH$ HS
	Herwig [78]	had., PS	
	Jimmy [79]	UE+PU	Combined with Herwig

and, therefore, are combined for the full event simulation. Most generators only include leading-order calculations. The Powheg generator used for the signal simulation takes next-to-leading order corrections into account. The Alpgen generator is based only on leading-order ME calculations but employs the MLM scheme [65] to match parton shower contributions generated by the Herwig program to the matrix-element calculations in an optimal way.

The generators used for simulation of the hard scattering process need Parton Distribution Functions (PDF) as input. The Powheg and MC@NLO generators use the PDF set of CT10 [29] while the Alpgen, Madgraph and Pythia6/8 generators use the PDF set of CTEQ6L1 [30].

2.3 Higgs Boson Properties

The Standard Model Higgs boson is a scalar CP-even particle, i.e. $J^P = 0^+$ where J denotes the spin and P the parity. Furthermore, all couplings of the Higgs boson to Standard Model particles are determined, and can be tested experimentally. The mass of the Higgs boson is not predicted by the Standard Model. However, upper limits on the Higgs boson mass arise from the requirement of unitarity in WW scattering amplitudes ($m_H \lesssim 870$ [80]), from the requirement of perturbativity of the branching fraction calculation of $H \to VV^{(*)}$ decays ($m_H \lesssim 700\,\mathrm{GeV}$ [81]) as well as from constraints due to quadratic Higgs boson self coupling terms leading to a divergence (*Landau pole*) at a scale depending on the Higgs boson mass ($m_H \lesssim 170$ [82]). A lower bound on the Higgs boson mass arises from the claim for a stable vacuum ($m_H > (129.4\pm1.8)\,\mathrm{GeV}^*$ [83]). The constraints arising from Higgs boson self coupling terms and from the vacuum stability claim assume no new physics up to the Planck scale ($M_p \sim 2 \times 10^{18}\,\mathrm{GeV}$). In addition electroweak precision measurements, sensitive to the Higgs boson mass through higher-order corrections, are best compatible with a Higgs boson with $m_H = 94^{+29}_{-24}\,\mathrm{GeV}$ [84].

Since the startup of the LHC the Higgs boson has been searched for extensively by the LHC experiments ATLAS and CMS. In the higher mass range ($m_H \gtrsim 2 \times m_W$) the decays into W and Z boson pairs are most sensitive for Higgs boson searches due to the large branching fractions (see Fig. 2.7b) while in the lower mass range ($m_H \lesssim 2 \times m_W$) despite the small branching fraction decays into two photons provide the highest sensitivity due to the very clean signature and high Higgs boson mass resolution.

Already in July 2012 the ATLAS [5] and CMS [6] experiments observed a significant excess of events, well compatible with the expectations for a Standard Model Higgs boson with a mass around $125\,\mathrm{GeV}$, with a fraction of the full dataset ($5\,\mathrm{fb}^{-1}$ at $\sqrt{s} = 7\,\mathrm{TeV}$ and $5.8\,\mathrm{fb}^{-1}$ at $\sqrt{s} = 8\,\mathrm{TeV}$). Except for a small mass region around $125\,\mathrm{GeV}$ a Standard Model Higgs boson is excluded (see Fig. 2.9) in the mass region favored by theoretical and electroweak precision measurement constraints. Once the full dataset was analyzed the excluded mass region was extended to 110–$123\,\mathrm{GeV}$ and 127–$710\,\mathrm{GeV}$ [5, 85–88].

Employing the full available dataset measurements in the most sensitive decays to

---

*The measured Higgs boson mass ($m_H = (125.5 \pm 0.6)\,\mathrm{GeV}$ [7] and $m_H = (125.7 \pm 0.4)\,\mathrm{GeV}$ [8]) is in contradiction to this constraint with a significance of two standard deviations. In case of confirmation with higher precision this leads to the conclusion that either there has to be new physics before the Planck scale or the vacuum is meta-stable. The lifetime of the meta-stable vacuum could, however, be longer than the age of the universe [82].
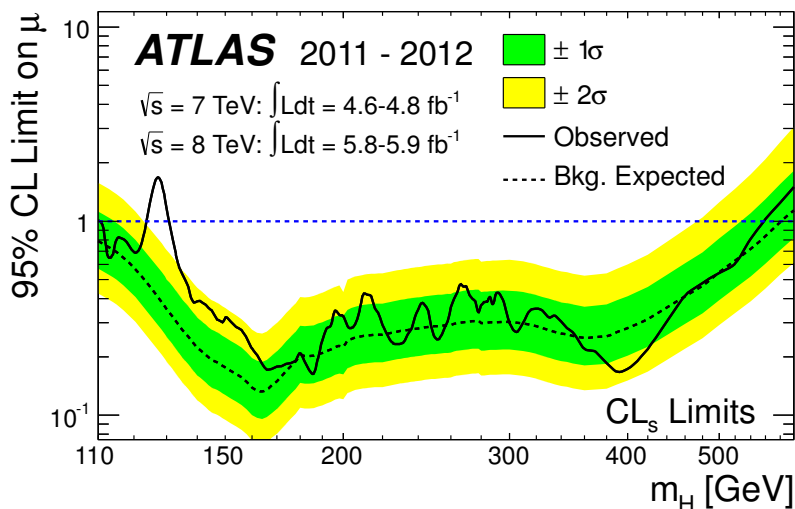
Figure 2.9: Exclusion limit at 95% confidence level as a function of the Higgs boson mass, m_H. The observed limit (solid line) is compared to the limit expected from the background-only hypothesis (dashed line) including the $\pm 1\sigma$ (green) and $\pm 2\sigma$ (yellow) uncertainty bands in the expectation (from [5]).

two photons by the ATLAS [89] experiment, and two Z bosons by the ATLAS [86] and CMS [90] experiments show discovery-level signal significances with over six standard deviations, while the diphoton channel measurement by the CMS [87] experiment shows a significance of 3.2 standard deviations. These two channels additionally provide a precise measurement of the Higgs boson mass by means of the invariant mass computed from the final state particle four-momenta. Combining the two mass measurements a value of $m_H = (125.5 \pm 0.6)\,\text{GeV}$ [7] and $m_H = (125.7 \pm 0.4)\,\text{GeV}$ [8] is found by the ATLAS and CMS experiments, respectively.

Evidence, with roughly four standard deviation significance is found for the decays into two W bosons [91,92] and two τ leptons [93,94]. The former will be discussed in detail in Chapters 5 and 6. The latter is of particular interest since the coupling of the Higgs boson to leptons is directly confirmed. Indirect confirmation of the Yukawa coupling of the quark sector is given by the production via gluon fusion. No significant signal, i.e. with above three standard deviations, is yet observed in the decay modes to b quarks [95,96] and muons [97,98].

An important test to identify the new boson as the Standard Model Higgs boson is

the measurement of spin and parity which are investigated in angular distributions of final state particles. The most sensitive Higgs boson decay channel is $H \to ZZ^{(*)} \to 4\ell$ where the final state can be fully described by six angles defined between the final state leptons as well as between the leptons and the beam axis. Those angles are sensitive to spin and parity of the Higgs boson. For the measurement of the spin also the $H \to \gamma\gamma$ and $H \to WW^{(*)}$ channels can be used. The spin-1 hypothesis is excluded already by the observation of the decays to two photons with spin-1 and zero mass because of the Landau-Yang theorem [99,100]. Evidence against eigenstates $J^P = 1^-$, 1^+, 2^{+*} is found at a significance level of three standard deviations and the odd-parity eigenstate 0^- is disfavored at a level of two standard deviations [90, 102].

The Higgs boson mass, spin, parity and decay rates have been measured as well as the couplings of the Higgs boson to Standard Model particles and the different production mechanisms. The latter two are described in Chapter 6. All measurements show good agreement with the Standard Model predictions and the results of the ATLAS and CMS experiments are well compatible with each other.

---

*A large number of spin-2 models are possible. A specific one, corresponding to a graviton-inspired tensor with minimal couplings to Standard Model particles is investigated by ATLAS and CMS as described in [101].

Chapter 3

The ATLAS Detector at the Large Hadron Collider

The Large Hadron Collider (LHC) is a proton storage ring with $27\,\mathrm{km}$ circumference located at the European Organization for Nuclear Research CERN which collides proton beams circulating in opposite directions. It was designed to provide collision energies and beam intensities sufficient for either the discovery or the exclusion of the Standard Model Higgs boson. The technologies needed to reach this goal, are summarized in Section 3.1 following the detailed description in [103–106].

The LHC provides proton-proton collisions for several experiments. The main ones are ATLAS [107], CMS [108], LHCb* [109] and ALICE† [110]. LHCb is dedicated to heavy flavor physics while ALICE studies the quark-gluon-plasma using special fills of the LHC with lead ions. ATLAS and CMS are multi-purpose experiments, dedicated to the search for the Higgs boson and for new physics beyond the Standard Model. The ATLAS detector, which delivered the data for the presented analysis, will be described in Section 3.2.

3.1 The Large Hadron Collider

The LHC physics goals require large collision energy since the cross sections of processes of interest, such as Higgs boson productions, raise faster with increasing collision energy compared to the cross sections of most background processes (see Fig. 2.3). Since the processes of interests are rare, many collision events are needed to gain statistical

---

*LHCb: Large Hadron Collider Beauty
†ALICE: A Large Ion Collider Experiment

significance. This requires high beam intensity. The LHC collides proton beams in the tunnel of the former LEP electron-positron collider [111, 112] using superconducting dipole magnets to keep the protons on their orbits.

The protons are pre-accelerated before injected into the LHC as illustrated in Fig. 3.1. *Linac 2* accelerates the protons to 50 MeV before they are injected into the *booster* which accelerates them further to 1.4 GeV. The *Proton Synchrothron* (PS) increases the energy to 25 GeV and the *Super Proton Synchrotron* (SPS) to 450 GeV. The protons are then injected into the LHC in two opposite directions where they are accelerated to their final energies. The maximum design energy is 7 TeV per beam.

The pre-acceleration stages provide protons in bunches. The LHC is designed to accelerate up to $n_b = 2835$ bunches per beam with $N_b \approx 10^{11}$ protons per bunch and collisions every 25 ns. The event rate, $dN/dt = L\,\sigma$, for a given process with cross section σ is determined by the instantaneous luminosity L, which depends on the beam parameters:

$$L = \frac{N_b^2 n_b f_{\text{rev}} \gamma_r}{4\pi \epsilon_n \beta^*} \cdot F \quad , \tag{3.1}$$

where f_{rev} is the revolution frequency of the protons, γ_r their relativistic gamma-factor, ϵ_n the beam emittance, β^* the transverse beam amplitude at the interaction point and F a geometric reduction factor taking into account that the beams cross under an angle.

The design peak luminosity of the LHC is $10^{34}\,\text{s}^{-1}\text{cm}^{-2}$. However, not all beam parameters have reached their design values in the past years. In the year 2011, the LHC was running with a beam energy of 3.5 TeV which was increased to 4 TeV in 2012. The number of bunches per beam was increased from 200 to 1380 during 2011 and kept at 1380 in 2012. Peak luminosities of about $4 \times 10^{33}\,\text{s}^{-1}\text{cm}^{-2}$ and $8 \times 10^{33}\,\text{s}^{-1}\text{cm}^{-2}$ have been reached in 2011 and 2012, respectively.

The physics program relies on the *integrated* luminosity $\mathscr{L} = \int L\,dt$ collected over time. The integrated luminosities delivered by the LHC and recorded by the ATLAS detector are shown in Fig. 3.2a. An integrated luminosity of $5.46\,\text{fb}^{-1}$ was delivered by the LHC at a collision energy of 7 TeV in the year 2011 of which $4.57\,\text{fb}^{-1}$ were recorded by ATLAS and classified as good quality data. In the year 2012 an integrated luminosity of $22.8\,\text{fb}^{-1}$ was delivered by the LHC at a collision energy of 8 TeV of which $20.3\,\text{fb}^{-1}$ were recorded under good conditions by the ATLAS detector.

For a given peak luminosity, the expected number of inelastic proton-proton interactions per bunch crossing can be calculated from the total inelastic cross section σ_{tot}

24
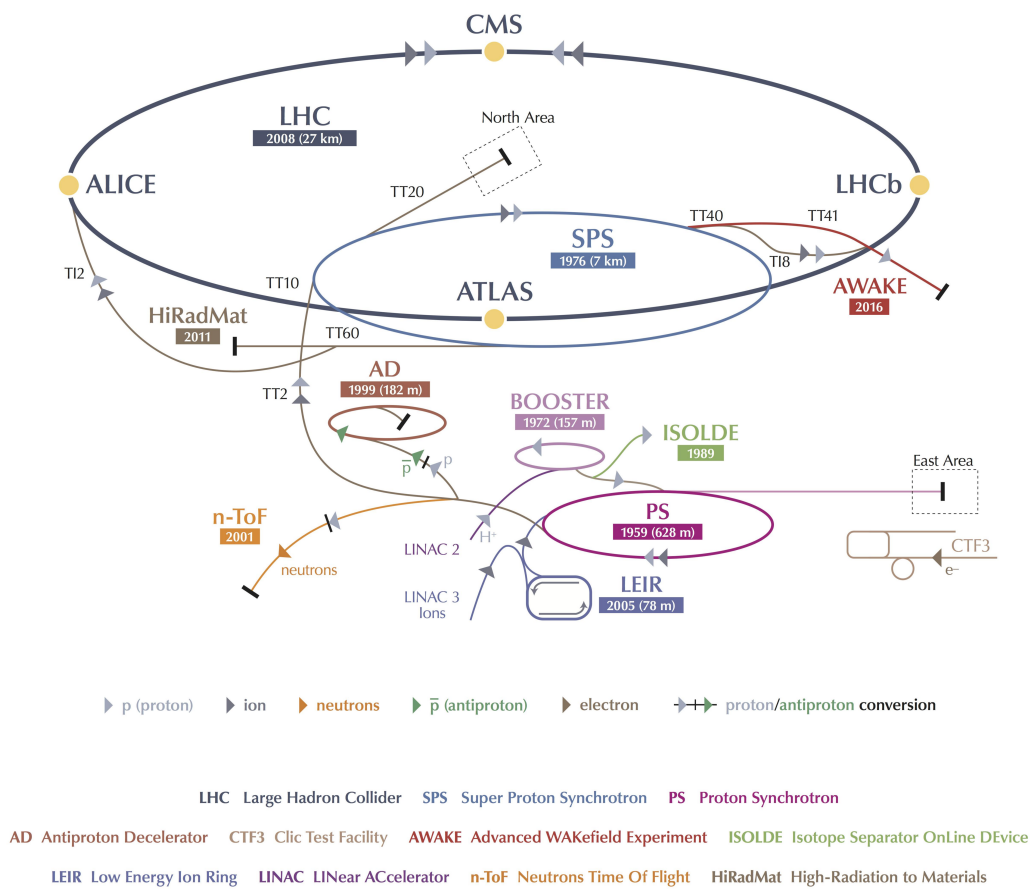
Figure 3.1: Illustration (from [113]) of the CERN accelerator system. The acceleration chain starts with *Linac 2* and is followed by the acceleration in the *booster*. The protons are then accelerated further by the *Proton Synchrothron* (PS) and the *Super Proton Synchrotron* (SPS) before they are injected into the LHC.

shown in Fig. 2.3. For the design parameters of the LHC and the ones used in the years 2011 and 2012, the expected numbers of inelastic proton-proton interactions per bunch crossing are 23, 9 and 20, respectively. The distributions of the mean numbers of interactions per bunch crossing measured by the ATLAS detector in 2011 and 2012 are shown in Fig. 3.2b.

The rates of most processes of interest, such as Higgs boson production, are small (see Fig. 2.3). The processes of interest are therefore accompanied by additional inelastic proton-proton interactions in the same event due to the large inelastic cross section. These contributions to the event are referred to as *in-time pile-up*, if the additional inelastic proton-proton interaction occurred in the same bunch crossing. In particular for 25 ns bunch spacing, also proton-proton interactions from previous bunch crossings contribute which is referred to as *out-of-time pile-up*. In addition neutrons and γ-rays from interactions of protons produced in collisions with the detector material, referred to as *cavern background*, and cosmic-ray particles maybe overlaid to the event of interest. In-time pile-up has by far the largest impact on the physics analyses.
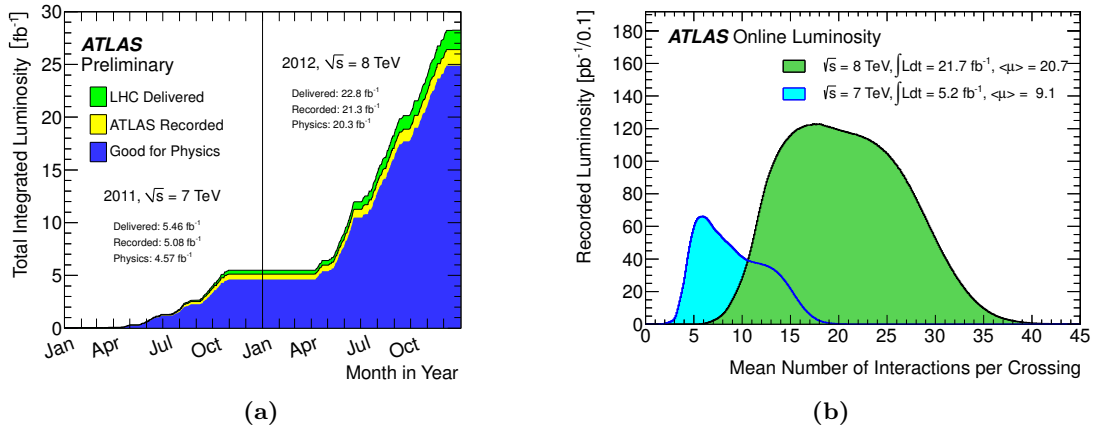
Figure 3.2: (a) Total integrated luminosity delivered by the LHC (green), recorded by ATLAS (yellow) and classified as good quality data (blue) at $\sqrt{s} = 7$ TeV and $\sqrt{s} = 8$ TeV in 2011 and 2012, respectively. (b) Luminosity weighted distributions of the mean number of interactions per bunch crossing for 2011 and 2012. The figures are from [114].

3.2   The ATLAS Detector

The ATLAS detector is designed both for precision measurements of Standard Model processes as well as for discovery of new physics processes with small cross sections including Higgs boson production. Very good spacial and time resolution is needed to reconstruct proton-proton interactions at the large instantaneous luminosity and the high collision rate at the LHC. An overview of the ATLAS detector is given below following [107].

The physics goals of the ATLAS experiment lead to the following requirements on the detector design [107]:

- High granularity of the detector elements to cope with the large particle densities.

- Large solid angle coverage.

- High momentum resolution for charged particle tracks.

- High energy and angular resolution for electrons and photons in the electromagnetic calorimeters.

- Accurate jet and missing transverse energy measurements in the electromagnetic and hadronic calorimeters.

- High muon reconstruction efficiency and momentum resolution up to very high muon momenta.

- Highly selective triggering with high efficiency for the processes of interest.

- Fast, radiation hard detectors and readout electronics to cope with the high particle rates.

A schematic view of the ATLAS detector is shown in Fig. 3.3. The detector is 44 m long and 25 m high. It consists of cylindrical layers around the beam pipe in the *barrel* part of the detector complimented by dishes in the forward regions, the *endcaps*. The ATLAS detector can be subdivided in three main parts which are from the inside out:

The Inner Detector performs track and momentum measurement of charged particles in a 2 T magnetic field generated by a super-conducting solenoid. It has a length of 5.3 m and a diameter of 2.5 m.

27

The Calorimeter System is subdivided into electromagnetic and hadron calorimeters performing energy measurement of electrons and photons and of hadrons and jets, respectively.

The Muon Spectrometer performs identification and precise momentum measurement of muons in a toroidal magnetic field of 0.2–2.5 T in the barrel and of up to 3.5 T in the endcaps. To minimize the material in the path of the muons and thus the multiple scattering, three large super-conducting air-core toroid magnets, one for the barrel and one for each endcap, are used.

The three sub-detector systems are described in Sections 3.2.2, 3.2.3 and 3.2.4, respectively. An overview of the trigger system is given in Section 3.2.5. Beforehand, the ATLAS coordinate system is outlined in Section 3.2.1.

The luminosity measurement described in Section 3.2.6 employs, in addition to the Inner Detector, two dedicated detectors: the Beam Condition Monitor (BCM) and the LUCID detector which is a Cherenkov detector consisting of sixteen aluminum tubes filled with C_4F_{10} and surrounding the beam pipe at a distance of 17 m from the interaction point. LUCID measures photons created by charged particles in the gas. The BCM detects charged particles from the interaction region with four diamond sensors of about $1\,cm^2$ arranged around the beam pipe at a distance of 184 cm from the interaction point.

The ATLAS detector simulation needed to compare the Standard Model predictions to data is described in Section 3.2.7.

3.2.1   The ATLAS Coordinate System

The interaction region is located at the origin of the coordinate system. The z-axis points along the beam direction, the y-axis upwards and the x-axis towards the center of the LHC ring. The azimuthal angle ϕ is defined around the beam axis starting from the positive x-axis. Related to the polar angle θ measured from the z-axis, is the pseudorapidity variable

$$\eta = 1/2 \cdot \ln \tan \theta/2 \tag{3.2}$$

in which the cross sections at colliders are more uniform. For massive particles the rapidity

$$y = 1/2 \cdot \ln \frac{E + p_z}{E - p_z} \tag{3.3}$$
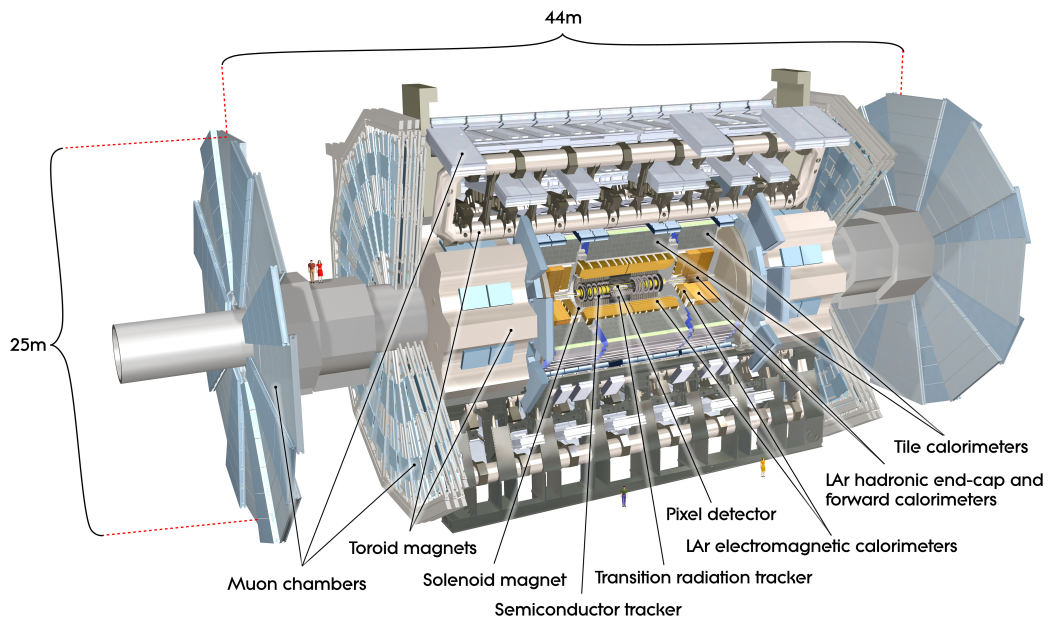
Figure 3.3: Cut-away view of the ATLAS detector showing its main components (from [107]): The Inner Detector consisting of the Pixel detector, the Semi-Conductor Tracker (SCT) and the Transition Radiation Tracker (TRT), the calorimeter system with the Liquid Argon (LAr) electromagnetic calorimeters, the hadronic endcaps and the hadron Tile Calorimeters and the Muon Spectrometer with its large superconducting toroid magnets.
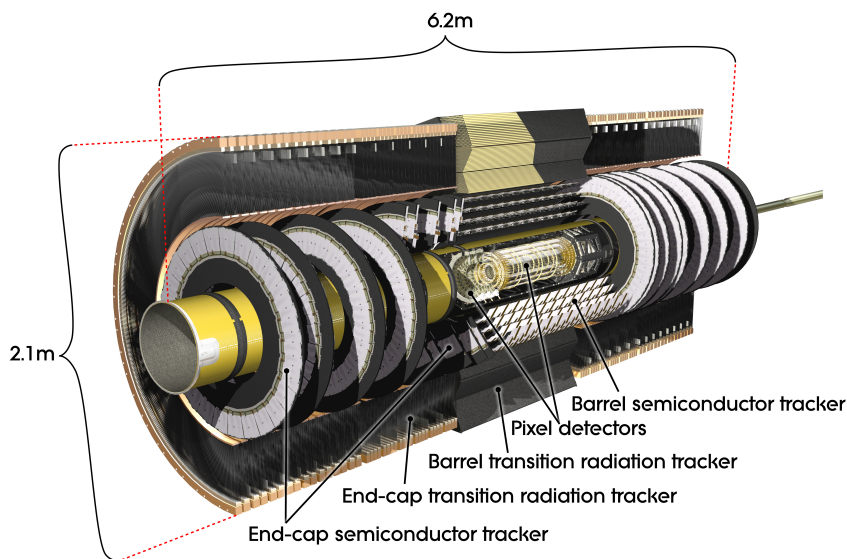
Figure 3.4: Cut-away view of the ATLAS Inner Detector (from [107]).

is used, which is equal to the pseudorapidity in the limit of large E/m. Angular separation between two particles is measured by the distance parameter $\Delta R = \sqrt{\Delta\eta^2 + \Delta\phi^2}$.

While the center-of-mass energy of two colliding partons is not known since they carry only a fraction of the proton momentum, their momentum in transverse direction to the beam is small enough to be neglected. The transverse momenta p_T of the particles produced in the collision must therefore be balanced. Particles not identified in the detector, like neutrinos, contribute to the missing transverse energy E_T^{miss} which due to transverse momentum conservation is given by the vectorial sum of the visible transverse momenta.

3.2.2 The Inner Detector

On average 1000 tracks per bunch-crossing are produced at the LHC design luminosity leading to a very high track density in the inner tracking detectors. Therefore, highly granular detectors are used to provide sufficient spatial resolution to reconstruct all the tracks. The Inner Detector consists of three independent detector systems, sketched in Fig. 3.4.

The Pixel Detector is the innermost detector consisting of silicon pixel sensors in

three cylindrical layers in the barrel and in disks in each endcap. The cylindrical layer closest to the beam pipe is referred to as the *B-Layer* because it is most important for b quark identification. The pixel detectors are arranged in such a way that each particle originating from the interaction region traverses a minimum of three layers.

The Semi-Conductor Tracker (SCT), surrounds the Pixel Detector with four cylindrical layers of silicon strip sensors in the barrel and nine disks in each endcap. The SCT sensor modules in the barrel consist of two layers, with strips oriented along the beam axis under a small angle of ± 20 mrad allowing for a measurement of the z-coordinate. The orientation of the strips in the modules on the endcap disks is alternating between radial and azimuthal orientation.

The spatial resolution of the pixel sensors is $10\,\mu$m in the transverse and $115\,\mu$m in the longitudinal direction with respect to the beam. The SCT achieves a transverse resolution of $17\,\mu$m and a longitudinal resolution of $590\,\mu$m. The two silicon detector tracking systems cover a pseudorapidity region of $|\eta| < 2.5$.

The outermost layer of the Inner Detector is the Transition Radiation Tracker (TRT) composed of 4 mm diameter Kapton straw tubes with $30\,\mu$m diameter tungsten-rhenium anode wires in their center. The tubes are filled with a gas mixture (70% Xe, 27% CO_2 and 3% O_2) allowing for the detection of transition radiation photons. The TRT extends up to $|\eta| = 2.0$. Traversing charged particles hit on average 36 straw tubes each providing a spatial resolution of $130\,\mu$m in the transverse plane.

3.2.3   The Calorimeter System

The ATLAS calorimeter system consists of the electromagnetic and the hadron calorimeter as shown in Fig. 3.5. The electromagnetic calorimeter surrounds the Inner Detector and the solenoid coil and is dedicated to identify electrons and photons and measure their energy and direction, whereas the subsequent hadronic calorimeter measures the energy of hadrons and jets. Both calorimeters are sampling calorimeters consisting of alternating layers of passive absorber material and of active material where the energy deposition in form of secondary particles is measured.

The electromagnetic calorimeter extends up to $|\eta| = 1.5$ in the barrel while the endcaps cover the region $1.4 < |\eta| < 3.2$. The active material of the electromagnetic calorimeters is liquid argon while lead is used as absorber material. To achieve homogeneous ϕ-coverage, the lead absorber plates have an accordion-like shape in particle
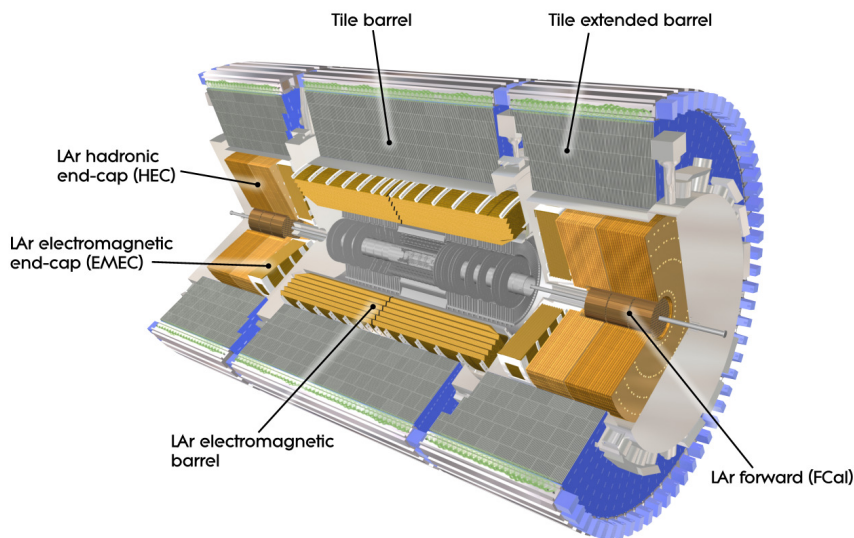
Figure 3.5: Cut-away view of the ATLAS calorimeter system (from [107]).

direction.

The hadron calorimeter consists of three parts. The *Tile Calorimeter* covers the region $|\eta| < 1.0$ with an *extension* to $0.8 < |\eta| < 1.7$ as shown in Fig. 3.5. Scintillating tiles are used as active material and steel as absorber. The Tile Calorimeter is segmented in three radial layers.

The hadronic endcap calorimeter uses liquid argon as active and copper as absorber material. It covers the region $1.5 < |\eta| < 3.2$ overlapping with the Tile Calorimeter to guarantee sufficient material thickness also in the transition region between the calorimeters, which nevertheless has less energy resolution. Electron candidates traversing the pseudorapidity region $1.37 < |\eta| < 1.52$, referred to as the *crack region*, are, therefore, excluded from the analysis to prevent from hadrons misidentified as electrons.

The Liquid Argon *Forward CALorimeter* (FCAL) consists of three consecutive modules in z-direction in each endcap. The module closest to the interaction region uses copper as absorber material, whereas the other two modules use tungsten. The FCAL covers a region $3.1 < |\eta| < 4.9$.

Thin-gap chambers (TGC)

Cathode strip chambers (CSC)

Barrel toroid

Resistive-plate
chambers (RPC)

End-cap toroid

Monitored drift tubes (MDT)
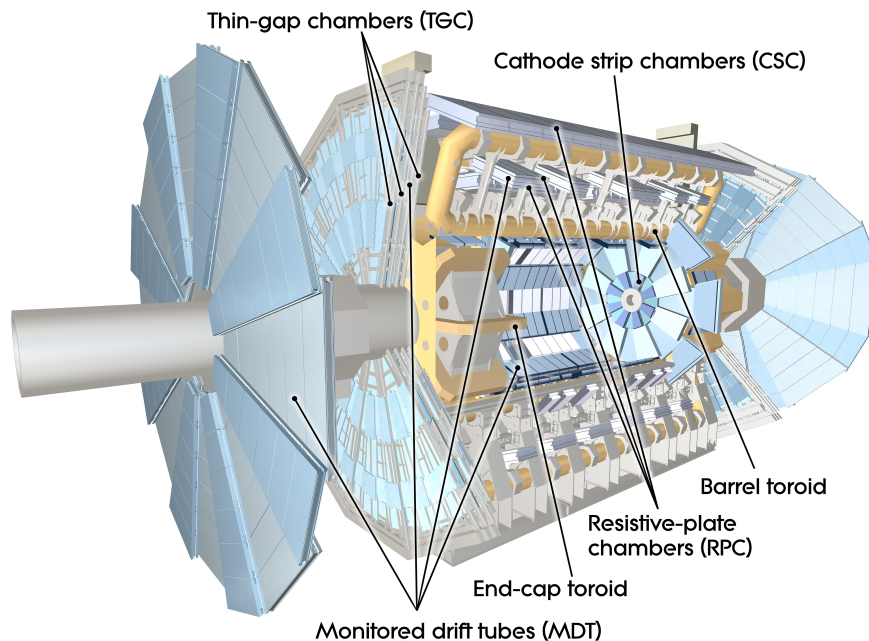
Figure 3.6: Cut-away view of the Muon Spectrometer (from [107]).

3.2.4   The Muon Spectrometer

The Muon Spectrometer forms the outermost layer of the ATLAS detector and is used for muon identification and precise momentum measurement in the magnetic field of superconducting air-core toroid magnets up to $|\eta| = 2.7$ where $|\eta| < 1.4$ is the barrel and $1.6 < |\eta| \leq 2.7$ the endcap region. The region $1.4 < |\eta| < 1.6$ is referred to as the *transition region* of the Muon Spectrometer, where the fields of the barrel and endcap toroids overlap resulting in a relatively inhomogeneous magnetic field. Muons above $3\,\text{GeV}$ reach the Muon Spectrometer. Precise momentum measurement is possible up to momenta of $1\,\text{TeV}$. Best momentum resolution of 3–4% is reached for muons with $p_\text{T} \sim 100\,\text{GeV}$. Resolutions of 10% are reached for muons with momenta up to $1\,\text{TeV}$. An overview of the Muon Spectrometer is shown in Fig. 3.6.

In the barrel region, three cylindrical layers of muon chambers are installed between and on the magnet coils. In the transition and endcap regions the chambers are installed on wheels perpendicular to the beam.

For precise momentum measurement Monitored Drift Tube (MDT) chambers are

used which, combined with Cathode Strip Chambers (CSC) in the innermost endcap layer, cover $2.0 < |\eta| < 2.7$. CSCs are multi-wire proportional chambers with cathodes segmented into strips.

The relative alignment of the different chambers traversed by a muon has crucial impact on the muon momentum resolution. High alignment precision, on the order of $50\,\mu$m is achieved by means of an optical alignment monitoring system and by measurements of muon tracks from cosmic rays and from proton-proton collisions.

For the fast muon trigger decision, Resistive Plate Chambers (RPC) and Thin Gap Chambers (TGC) are used in the barrel and endcaps, respectively, covering a region up to $|\eta| = 2.4$.

3.2.5   The Trigger and Data Acquisition System

The high instantaneous luminosity and the high bunch crossing frequency demand a fast and highly selective trigger system to reduce the event rate to an acceptable level while keeping the rare interesting events with high efficiency. Three consecutive trigger levels are used referred to as *Level-1*, *Level-2* and *Event Filter*, each refining the trigger decision of the previous one. The event rate is reduced in this way from $40\,$MHz to 75–$100\,$kHz after the Level-1 trigger stage to $3.5\,$kHz after the Level-2 trigger and to the final rate of $200\,$Hz after the Event Filter.

The Level-1 trigger defines the Regions of Interest (RoI) in η and ϕ for the higher-level trigger decisions and detector readout. The region to be investigated by the detailed and time consuming reconstruction at the Level-2 and Event Filter stages is reduced in this way to 2–6% of the full detector coverage. The Level-1 trigger exploits the fast muon trigger chambers (RPC and TGC) and the calorimeter information. The decision is taken in less than $2.5\,\mu$s and the event rate reduced from $40\,$MHz to 75–$100\,$kHz.

The event rate after the Level-1 stage is further reduced to $3.5\,$kHz by the Level-2 triggers using the full detector granularity in the RoIs defined by the Level-1 trigger. A fast event reconstruction is performed including identification of muons, electrons, photons and jets and determination of their four-momenta. The Event Filter finally employs the full ATLAS reconstruction algorithms reducing the event rate to the required $200\,$Hz. A detailed description of the reconstruction algorithms is given in Chapter 4.

3.2.6   Luminosity Measurements

The luminosity delivered by the LHC varies over time and is monitored by measurements of the Inner Detector, the BCM and the LUCID detector. Several independent measurements are performed to control the systematic uncertainty in the measurement of the luminosity which is needed for the determination of cross sections of the physics processes studied. A detailed description of the luminosity measurements can be found in [115]. A luminosity measurement is recorded about once per minute corresponding to a *luminosity block* of data. The integrated luminosity is calculated by summing over all luminosity blocks of a given data taking run.

The ATLAS detector monitors the interaction rate per bunch crossing from which the luminosity can be calculated. The measurement is calibrated using dedicated beam-separation scans [116, 117].

The Inner Detector measures the luminosity by counting the number of reconstructed proton-proton interaction vertices from the intersections of charged particle tracks (see Section 4.1). The distribution of the vertex multiplicity is proportional to the luminosity delivered by the LHC.

LUCID measures the luminosity per-bunch by the number of Cherenkov photons, which is proportional to the number of charged particles produced. The BCM equipped with a very fast readout counts the number of collisions per bunch crossing and hence provides an independent luminosity estimate.

3.2.7   Detector Simulation

To compare the Standard Model predictions to real collision data, events simulated by the event generators (see Section 2.2.4) are passed through a detailed detector simulation with particle interactions in the detector material described by the GEANT4 program [118]. The detector geometry, material distribution and the magnetic fields are described in detail, as well as the trigger and detector response and the readout electronics. Details on the full ATLAS detector simulation can be found in [119]. The output of the detector simulation is reconstructed in the same way as is the collision data (see Chapter 4).

The full detector simulation is time consuming due to the detailed detector description. In particular, the complex shower processes in the calorimeters require significant simulation time. An alternative to the full simulation has been developed using a fast calorimeter simulation [120], employing shower parameterizations.

Chapter 4

Reconstruction of Physics Objects

The presented analysis depends on the objects present in the signal final state, electrons, muons, neutrinos and quarks. Their reconstruction, employing the ATLAS event reconstruction software framework ATHENA [121], is described in this section. Electrons and muons are stable* charged particles and can be reconstructed in the tracking detectors and calorimeters as discussed in Sections 4.4 and 4.5. Neutrinos and quarks, on the other hand, are not directly observable.

Quarks do not exist as free particles and immediately hadronize after being produced in a proton-proton collision forming jets consisting of a large number of hadrons in a narrow cone around the quark direction. Jets are detected in the calorimeters but the reconstruction also exploits information from the tracking system. The jet reconstruction is outlined in Section 4.2.

Gluons, produced mainly via initial or final state radiation, form hadron jets as well. No attempt is made to distinguish between quark- and gluon-jets. The discrimination between jets from different quark-flavors is impossible, with the exception of jets originating from b quarks (and to some extend also from c quarks) as discussed in Section 4.3.

Neutrinos are stable particles interacting only weakly and are, therefore, not directly detectable. However, neutrinos escaping the detector carry away part of the total energy and momentum. In proton-proton collisions, energy and momentum is lost in the z-direction, where there are no detectors. Therefore, energy-momentum conservation can

---

*For muons with kinetic energy above a few MeV, the decay length is larger than the radius of the detector.

only be exploited in the plane orthogonal to the direction of the incoming protons. Neutrinos are, for instance, identified by missing transverse energy in the event. The reconstruction of the missing transverse energy is discussed in Section 4.6.

Charged particle tracks are reconstructed in the Inner Detector. About 1000 tracks per bunch crossing are observed at the maximum luminosity recorded in 2012, which have to be simultaneously reconstructed. Tracks of charged particles are essential for the object reconstruction of electrons, muons, jets and missing transverse energy and are needed to identify the proton collision and particle decay vertices. The reconstruction of charged particles is discussed in Section 4.1.

The last section is dedicated to describe the trigger definitions used for the presented analysis.

4.1 Inner Detector Track and Vertex Reconstruction

Charged particles follow a circular trajectory in the transverse plane in the magnetic field of the Inner Detector. A circular track is described by a set of five parameters with respect to a reference point. The following parameter set is chosen:

- The inverse transverse momentum q/p_{T}, where q is the particle charge,

- the azimuthal angle ϕ,

- the polar angle θ,

- the transverse impact parameter d_0 and

- the longitudinal impact parameter z_0.

The impact parameters d_0 and z_0 are the distances of the points of closest approach to the reference point in the transverse and longitudinal plane, respectively.

The reference point used is the reconstructed proton-proton interaction point of interest, the so called the *hard scatter primary vertex*. The reconstruction of the primary vertices from the intersection of tracks extrapolated to the proton-proton interaction region in an event and the selection of the hard scatter vertex are described in Section 4.1.2. When the primary vertex is not yet known, the center of the beam spot is used as a preliminary reference point for track finding and fitting procedures. The beam

spot is the proton-proton interaction region and depends on the beam conditions. It is monitored during each LHC run (see Section 4.1.2).

The track reconstruction relies on Pixel Detector and SCT information and is, therefore, limited to the region $|\eta| < 2.5$.

4.1.1 Track Reconstruction

Track reconstruction is described in [122, 123]. The standard track finding algorithm uses an inside-out approach where track candidates are build from silicon detector hits ($r \approx 5 - 56\,\mathrm{cm}$) which are, in a later step, extrapolated to the TRT region ($r \approx 55- - 108\,\mathrm{cm}$). An outside-in track finding algorithm, seeded from TRT hits, complements the standard algorithm in order to recover tracks from decays of long lived particles, like kaons, where less hits may be present in the inner-most detector layers.

For the standard inside-out approach, track seeds are built from three-dimensional space-points of pixel hits and SCT cluster pairs*. The directional information of a track seed is sufficient to build *roads* where further hits from the same track are expected. The track fit is performed using a *Kalman filter* algorithm [124]. Hits on the road of the track candidate are added iteratively, and the track is refitted every time a new hit is added. A newly added hit is identified as an "outlier", if its contribution to the χ^2 of the fit is larger than a predefined value. The performance of the silicon detector track reconstruction has been tested with data at $\sqrt{s} = 7\,\mathrm{TeV}$ and a good description by the Monte-Carlo simulation was found [125].

Before the track is extended towards the TRT, ambiguities in the cluster-to-track association are resolved while fake tracks are rejected by applying track quality criteria. The surviving track candidates are extrapolated searching for additional hits in the TRT. A combined fit of the silicon track and matching TRT hits is performed providing the final track parameters. Tracks with $p_\mathrm{T} > 100\,\mathrm{MeV}$ are written to the database for further usage by the object reconstruction.

4.1.2 Primary Vertex Reconstruction

The primary vertex finding and fitting algorithm is adapted to the pile-up conditions at the LHC. On average 21 proton-proton collisions occurred per bunch crossing in the year

---

*The information of two SCT modules glued back-to-back under a stereo angle are combined to provide a three-dimensional space-point.

2012 (see Fig. 3.2b). The algorithm therefore needs to reconstruct multiple interactions simultaneously taking into account sharing of tracks by close-by vertices. The vertex reconstruction method and performance is described in [126, 127].

The vertex finding algorithm starts from all well reconstructed tracks. A first vertex is found at the maximum of the distribution of track z-coordinates, computed at the point of closest approach to the beam spot center. The position of the vertex is then determined using the *adaptive vertex fitter* [128] taking as input the seed z-position. Tracks incompatible with the fitted vertex by more than seven standard deviations are used as input to the fit of the next vertex. The procedure is repeated until no tracks are left. A refit of all tracks is performed, constraining the tracks to intersect at the position of the vertex they are associated with.

The vertex as well as the track fitting rely on the beam spot position which is determined every few minutes during collisions. It is derived from the distribution of vertices reconstructed without the beam spot constraint.

The vertex with the largest sum of squared transverse momenta of tracks associated to this vertex is identified as the hard scatter primary vertex and used as reference point for all track parameters used in the further analysis. All other vertices are assumed to result from minimum bias interactions also referred to as pile-up interactions.

The analysis presented uses the selected hard scatter vertex position to identify objects originating from the collision of interest. It requires that the selected hard scatter vertex is reconstructed from at least three tracks. In addition, the primary vertex multiplicity per event is used to estimate the pile-up level, for example for correcting the pile-up model used in the simulation to realistically describe pile-up conditions in the data.

4.2   Jet Reconstruction and Energy Calibration

The jet reconstruction and identification is described in [129, 130] and a description of the jet energy calibration can be found in [131]. The procedures are outlined below.

4.2.1   Jet Reconstruction

As a first step, energy depositions in the approximately 200,000 calorimeter cells are associated to "objects" with η and ϕ coordinates and transverse momentum p_T values

by a *topological* cluster algorithm as described in [129]. The algorithm starts from a seed cell with a signal-to-noise ratio larger than a given threshold. All neighboring cells are added to the cluster while neighbors of neighbors are added only if their signal-to-noise ratio passes a second, lower threshold. A cluster is finally surrounded by "guard cells", passing a very low signal-to-noise ratio. Clusters can be split if several maxima are found within one cluster.

Topological clusters are the starting point for the jet algorithm. For the presented analysis a *sequential jet finder* using an anti-k_t algorithm [130] in the FASTJET program [132,133] is used. Sequential jet finders search for the smallest distance d_{ij} or d_{iB} between two clusters i and j or between any cluster i and the beam axis, respectively. If the smallest distance is a d_{iB}, the cluster i is labeled as an individual jet and removed from the list. If the smallest distance is a d_{ij}, cluster i and j are combined and the combined cluster is added to the list. The procedure is repeated until no more clusters are found in the list. The main difference between different sequential jet finders is the definition of the distance, which can be written in a generalized form as:

$$d_{ij} = \min(k_{t,i}^{2p}, k_{t,j}^{2p}) \cdot \frac{\Delta R_{ij}^2}{R^2} \tag{4.1}$$

$$d_{iB} = k_{t,i}^{2p} \tag{4.2}$$

where $k_{t,i}$ is the transverse momentum of the i-th cluster and $\Delta R_{ij} = \sqrt{\Delta \Phi_{ij}^2 + \Delta y_{ij}^2}$ is the angular distance in y-ϕ space. R is a fixed distance parameter with $R = 0.4$ chosen for this analysis. The exponent p is chosen to be $p = -1$ for the anti-k_t algorithm*. The anti-k_t algorithm prefers clustering of soft activity to large energy deposits over combining two close-by soft energy deposits. Hence, a high-p_T jet will accumulate the soft activity surrounding it leading to conical jet shapes, which are insensitive to fluctuations in the soft activity, which is difficult to simulate.

It is expected that a large fraction of jets does not originate from the hard scatter process, but from pile-up proton-proton interactions. It is important to distinguish jets from the hard scatter process, referred to as *hard scatter jets*, from jets produced in pile-up interactions, referred to as *pile-up jets*. The jet direction measurement in the calorimeters is not precise enough to allow for the association of a jet to a vertex. Instead Inner Detector track information is exploited by defining the so called *jet vertex fraction*:

---

*The k_t-algorithm corresponds to $p = 1$.
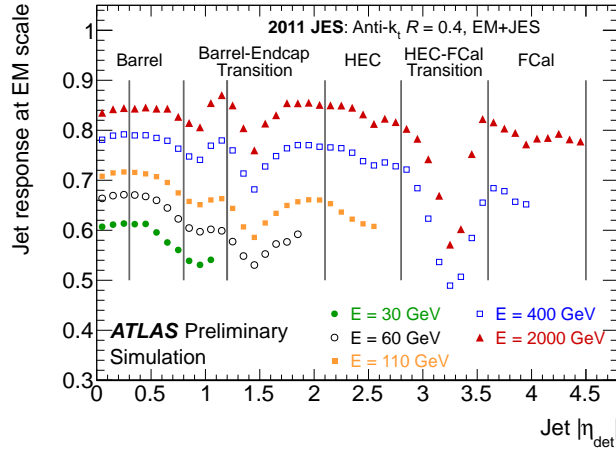
Figure 4.1: Jet energy response $\mathcal{R} = E_{\text{jet}}^{\text{EM}}/E_{\text{jet}}^{\text{truth}}$ at the EM scale for different detector regions and jet energies [131]

$$\text{JVF} = \sum_{\text{track,PV}} p_{\text{T}} / \sum_{\text{track}} p_{\text{T}} \quad , \tag{4.3}$$

where the sums are over all tracks associated to the jet and the tracks of the jet associated to the hard scatter primary vertex (PV), respectively. If many tracks in the jet originate from the hard scatter primary vertex, the JVF is close to one. For pile-up jets, where many tracks originate from a pile-up vertex, the JVF will be small. Since it relies on track reconstruction, the JVF is only properly defined within the Inner Detector coverage ($|\eta| < 2.5$), while jet reconstruction in the calorimeters with good efficiency is possible up to $|\eta| < 4.5$.

4.2.2 Jet Energy Calibration

The calorimeters have initially been calibrated using test beam measurements with electrons (see [134]) to provide a correct response for electromagnetic showers. Hence, at first the jet energy is measured at the electromagnetic (EM) scale which correctly measures the energy of particles produced in electromagnetic showers. The jet energy scale (JES) is further calibrated for clusters identified as originating from hadronic deposits employing single pion Monte-Carlo simulation.

Further, two corrections are applied to account for an energy offset introduced by
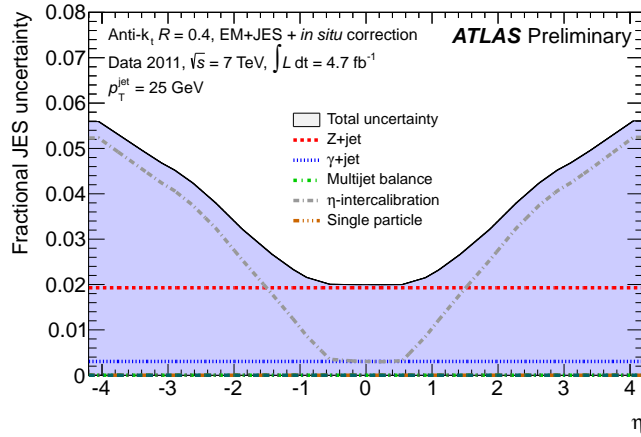
Figure 4.2: Breakdown of contributions to the jet energy scale uncertainty for jets with $p_\mathrm{T} = 25\,\mathrm{GeV}$ as a function of the jet pseudorapidity η [131]

pile-up. The first is based on the event transverse momentum and jet area which is a measure of the jets susceptibility to diffuse noise as described in [135]. The second is based on Monte-Carlo simulation and depends on the primary vertex multiplicity, the jet pseudorapidity and transverse momentum. The direction of the jet is further corrected to point to the hard scatter primary vertex. The jet energy is then corrected to the true jet energy using simulation including pile-up. The corrections range from 15% to 100% depending on the detector region and jet energy, as can be seen in Fig. 4.1, where the average energy response $\mathcal{R} = E_\mathrm{jet}^\mathrm{EM}/E_\mathrm{jet}^\mathrm{truth}$, the inverse of the calibration correction factor, is shown.

Several off-line jet energy scale corrections are applied for better agreement between data and simulation. From those the systematic uncertainties in the JES description in the simulation are derived. The total systematic uncertainty in the jet energy scale simulation and its main contributions are shown in Fig. 4.2 as a function of the jet pseudorapidity, for jets with $p_\mathrm{T} = 25\,\mathrm{GeV}$ as an example. A correction based on well balanced Z+jets or γ+jets events is applied. The uncertainties arise mainly from Monte-Carlo modelling, detector inefficiencies and the photon purity of the γ+jets data sample. For jets with large transverse momenta ($p_\mathrm{T} > 1\,\mathrm{TeV}$) a system with many soft jets recoiling against a hard jet are used for further JES correction (denoted with *multijet balance* in Fig. 4.2). Forward jets are further corrected, employing calibration coefficients derived from jets in the central region. An uncertainty arising from this extrapolation is

assigned, which is estimated from generator comparisons (denoted with η-*intercalibration* in Fig. 4.2). Central high-p_{T} jets are further corrected from measurements of single hadron responses (denoted with *single particle* in Fig. 4.2 but not visible for $p_{\mathrm{T}} = 25\,\mathrm{GeV}$ since it is only relevant for very high-p_{T} jets).

In addition to the jet energy scale also the jet energy resolution (JER) is corrected for better agreement between data and simulation. The procedure exploits the momentum balance between two leading jets in dijet events. Uncertainties in the jet energy resolution are 10-20% depending on the jet pseudorapidity and transverse momentum [136].

4.3   *b*-jet Identification

Jets originating from b quarks, b-jets, can be identified based on the relatively long life time of B mesons. B meson decays result in secondary decay vertices displaced from the hard scatter primary vertex. The identification of b-jets, called *b-tagging*, relies mainly on the reconstruction of tracks and vertices in the Inner Detector. The jet momentum and direction measured in the calorimeters, however, is needed for the association of tracks to the jet.

All tracks associated to a jet and to the hard scatter primary vertex are input to the b-tagging algorithms. Different methods, exploiting different properties of B meson decays, are used [137]. The *MV1* tagging algorithm, used in the presented analysis, combines three different methods using an artificial neural network. One is based on the track impact parameters, one on a secondary vertex finding algorithm and one on the reconstruction of the full B meson decay chain including subsequent D meson decays.

The performance of a b-tagging algorithm is given by the b-tagging efficiency $\epsilon_{b\text{-tag}}$, the fraction of correctly tagged b-jets, as a function of the *mistag rate*, defined as the fraction of falsely tagged non-b-jets. For the presented analysis a working point of $\epsilon_{b\text{-tag}} = 85\%$ is used.

The b-tagging efficiency and the mistag rate have been measured in data and compared to simulation results in [138–140]. Good agreement has been found. A correction for residual efficiency differences between data and simulation due to the slightly better impact parameter resolution in the simulation, is applied in the presented analysis.

4.4 Electron Reconstruction

Electrons are reconstructed combining calorimeter and Inner Detector information. In order to reduce the probability of jets faking electrons a sophisticated electron identification procedure is employed [141] which is outlined below.

Electrons are reconstructed from clusters in the electromagnetic calorimeters which are matched to Inner Detector tracks. A sliding window algorithm finds cluster seeds with energy deposits larger then $2.5\,\mathrm{GeV}$ in a region of 3×5 middle layer cells, corresponding to an angular range of $\Delta\eta\times\Delta\phi = 0.025\times0.025$. Within the tracking acceptance ($|\eta| < 2.5$), energy clusters are matched to Inner Detector tracks by extrapolating from the outermost measurement in the Inner Detector to the second layer in the electromagnetic calorimeter. If successful an electron candidate is found.

The cluster energy is now recomputed and corrections are applied accounting for the electron energy loss in the material in front of the calorimeters, the lateral energy leakage and the energy loss when the electron shower is not fully contained in the electromagnetic calorimeter. While the energy of electrons is taken from the calorimeter measurement, the direction in η and ϕ and the impact parameters are taken from the assigned track measurements in the Inner Detector.

Electrons have a significant radiation probability when traversing detector material due to their low mass. This is taken into account by refitting the tracks using a *Gaussian Sum Filter (GSF)* [142]. The use of the GSF significantly improves the track parameter and, hence, the electron four-momentum measurement and the track-to-cluster matching.

Reconstructed electrons without further selection are contaminated by backgrounds of jets and converted photons. *Loose*, *medium* and *tight* electron quality requirements are therefore applied, where the loose and the medium category is contained in the medium and the tight category, respectively. The identification criteria are:

Loose: Only shower shape and hadronic leakage variables are used.

Medium: Information from the strip layer of the electromagnetic calorimeter is used and stricter track quality and track-to-cluster matching requirements are applied.

Tight: Even tighter track-to-cluster matching and track quality requirements are used. Converted photons are rejected by requiring a hit in the B-layer, if it is expected from the direction, and the TRT electron identification capability is employed.
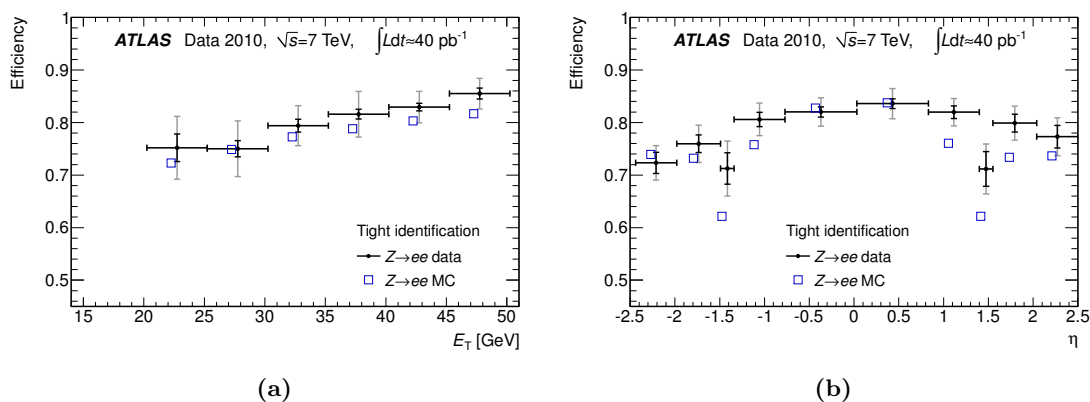
Figure 4.3: Identification efficiency of tight electron candidates measured as a function of (a) the electron transverse energy E_T and of (b) the electron pseudorapidity η using $Z \to ee$ events in data and simulation [143].

Tight electron candidates are used in the presented analysis. The quality criteria are slightly modified compared to [141] to adapt to the larger pile-up in 2012.

The electron identification efficiency is measured using a *tag-and-probe* method in $Z \to ee$, $W \to e\nu$ and $J/\Psi \to ee$ events. This method requires a high quality electron (or missing transverse energy in case of $W \to e\nu$), called the *tag* object, and a *probe* electron which may fulfill much looser requirements. The tag-probe pair has to be compatible with a Z, W or J/Ψ decay. The fraction of correctly identified probes is the identification efficiency. In Fig. 4.3 the efficiency measured in data is compared to the one determined from simulation using $Z \to ee$ decays, where the tight selection criteria are used (see [143]). An η- and p_T-dependent efficiency correction is applied to simulated electron candidates to weight them to the data.

Additional corrections are applied to the energy scale and resolution of simulated electrons [143]. The energy scale is determined, both in data and in simulation, from the di-electron mass in $Z \to ee$ and $J/\Psi \to ee$ decays as well as from the E/p measurement in $W \to e\nu$ events. The energy resolution is determined from the width of the Z boson resonance in $Z \to ee$ decays. The resolution found in simulation is slightly better than the one in data. The simulated electron transverse momentum hence is smeared in order to correctly describe the observed Z mass resolution.

Another important lepton property for the presented analysis is the isolation from neighboring particles and jets. The isolation is measured by summing up the activity in

a cone around the electron of a given radius, $\Delta R = 0.3$ in this analysis. Two types of isolation criteria are used:

Track isolation measured by the scalar sum $p_{\mathrm{T}}^{\mathrm{cone30}}$ of the track transverse momenta within a cone of radius $\Delta R = 0.3$ around the electron direction. The electron transverse momentum itself is left out of the summation.

Calorimeter isolation measured by the scalar sum $E_{\mathrm{T}}^{\mathrm{topo,cone30}}$ of topological energy clusters within in a cone of radius $\Delta R = 0.3$ around the electron direction. Clusters associated to the electron are left out of the summation.

The calorimeter isolation is corrected for pile-up contributions estimated from the vertex multiplicity.

4.5   Muon Reconstruction

Muons traversing the ATLAS detector leave a trace in all detector parts. The outermost layer, the Muon Spectrometer, is the main detector to identify muons, since all other detectable particles are essentially stopped in the calorimeters. Besides muon identification, the precise measurement of the muon momentum is the task of the Muon Spectrometer. Both identification and momentum measurement can be significantly improved by exploiting information provided by the Inner Detector and the calorimeters. Two muon reconstruction chains are in use (see [129]). The discussion below focusses on the muon reconstruction algorithm used in this analysis, referred to as *chain 1* muon reconstruction [144].

For muons reconstructed by stand-alone measurements in the Muon Spectrometer, referred to as *stand-alone muons*, straight track segments are reconstructed from hits in each of the three muon detector layers and then combined to form a track. This track is extrapolated to the hard scatter primary vertex taking into account multiple scattering and energy loss in the calorimeters. The algorithm used to perform this task is called *Muonboy* [144].

The advantage of the stand-alone measurement is the large Muon Spectrometer coverage up to $|\eta| = 2.7$. Only small gaps exist at $|\eta| < 0.1$ for Inner Detector services and at $|\eta| \approx 1.2$ where muon chambers were not yet installed in 2012. However, stand-alone muons are prone to background from weak pion and kaon decays into muons in the calorimeters or the Inner Detector.

The background can be efficiently reduced by exploiting the independent momentum measurement of the muon track in the Inner Detector. Each stand-alone muon track detected in the Muon Spectrometer is matched to an Inner Detector track taking into account the covariance matrices of both track measurements. Successful matches are referred to as *combined muons*. The combination of the two measurements considerably improves the momentum resolution over a wide momentum range. The Inner Detector dominates the momentum resolution of low-p_T, the Muon Spectrometer the one of high-p_T muons. The reconstruction of combined muons is limited to the Inner Detector coverage $|\eta| < 2.5$.

A looser muon reconstruction category, called *MuTag* [144], starts the reconstruction in the Inner Detector rather than in the Muon Spectrometer. It recovers partially instrumented detector regions and very low-p_T muons which do not reach the outer Muon Spectrometer layers. Taking into account so called *CaloMuons* reconstructed from energy deposits in the calorimeters compatible with the ones expected from minimum ionizing particles, increase the muon reconstruction efficiency even more. As the presented analysis is very sensitive to background, however, only high-purity combined muons are used in the reduced η coverage of the Inner Detector.

Muon reconstruction efficiency, momentum resolution and energy scale are compared between data and simulation [145]. The comparison for chain 1 muons is shown in Fig. 4.4a. Correction factors have been determined to correct for detector inefficiencies over time which are not accounted for in the simulation.

The reconstruction efficiency correction is measured in $Z \rightarrow \mu\mu$ events using a tag-and-probe method, as described in Section 4.4. The probe-muon can either be a CaloMuon, if the efficiency of stand-alone or combined muons is to be measured, or a stand-alone muon, if the efficiency of the Inner Detector reconstruction is to be determined.

The purity of $Z \rightarrow \mu\mu$ events is higher than 99.9% in the dataset used for efficiency measurements. Uncertainties in the efficiency measurement arise from residual background and from the probe selection. The systematic uncertainties due to the residual background and from comparing the correction factors determined using as probes Inner Detector tracks and CaloMuons, respectively, add up to 0.2%. The efficiency measurement can be performed only in the muon transverse momentum range covered by the $Z \rightarrow \mu\mu$ selection. Within this range no p_T-dependence of the efficiency is observed (see
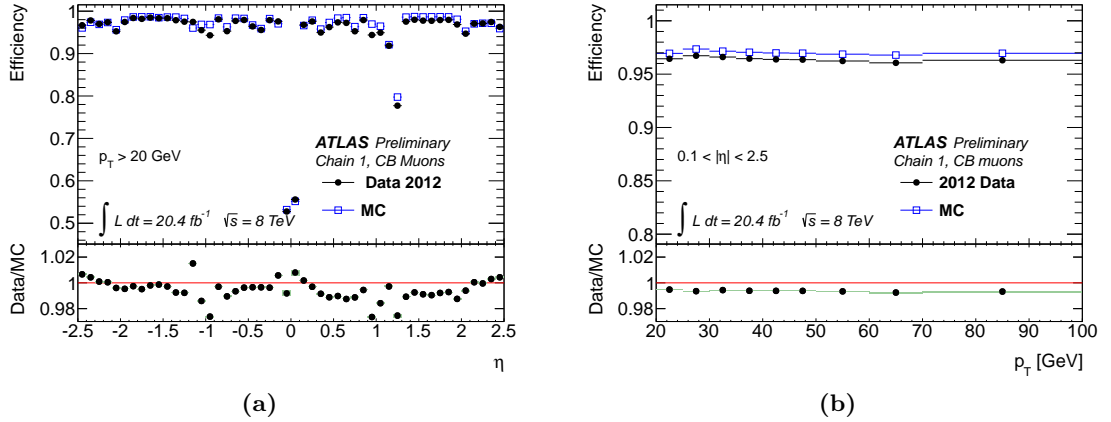
Figure 4.4: Muon Spectrometer reconstruction efficiency for chain 1 combined muons as a function of (a) the pseudorapididty η and (b) the transverse momentum p_T in $Z \rightarrow \mu\mu$ data and Monte-Carlo simulation and their ratio in the lower panel which is the efficiency correction factor applied to the simulation [145].

Fig. 4.4b). The correction factors derived in this p_T-range are also applied to muons with higher and lower transverse momenta with increased systematic uncertainties. In the low momentum regime, a comparison with muons from $J/\Psi \rightarrow \mu\mu$ decays is performed leading to uncertainties of 2 %, 1 % and 0.5 % in the p_T intervals $p_T < 7\,\mathrm{GeV}$, $7\,\mathrm{GeV} < p_T < 10\,\mathrm{GeV}$ and $10\,\mathrm{GeV} < p_T < 20\,\mathrm{GeV}$, respectively. In the high momentum regime, Monte-Carlo simulations with variations of the muon energy loss in the detector by 10% resulting in an uncertainty of 10% in the muon momentum for $p_T > 100\,\mathrm{GeV}$ are used.

In addition to the reconstruction efficiency, the muon momentum scale and resolution are measured and corrected using di-muon decays of Z, Υ and J/Ψ [145]. The simulation predicts a slightly larger momentum scale and better resolution than observed in the data. Figure 4.5a compares the uncorrected simulated and observed di-muon mass spectrum from $Z \rightarrow \mu\mu$ events. A template fit to the mass spectrum is applied to determine muon momentum resolution and scale and to correct the simulation as a function of the pseudorapidity and transverse momentum (see Fig. 4.5b). A systematic uncertainty in the resolution correction arises from the di-muon event selection including the choice of the di-muon mass window. Systematic uncertainties of 1% in the central region and of 2% in the forward regions are assigned to the momentum scale correction to take into
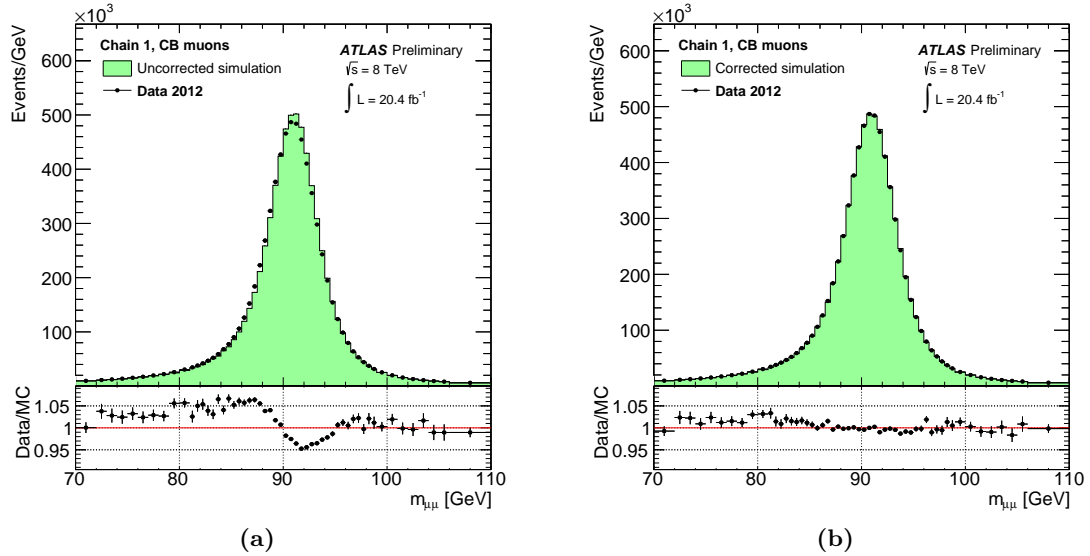
Figure 4.5: Simulated and measured dimuon invariant mass distribution for chain 1, combined muons with $p_T > 25\,\text{GeV}$ from $Z \to \mu\mu$ events. The distribution is shown (a) without any corrections and (b) with momentum smearing and scale corrections [145].

account a possible p_T dependence which is validated using J/Ψ and Υ decays.

As in the case of electrons, isolation criteria are used also for muons summing transverse momenta of Inner Detector tracks and energy deposits in the calorimeters within a cone of radius $\Delta R = 0.3$ around the muon direction. While the track isolation is defined in the same way as for electrons, the calorimeter isolation criteria use calorimeter cell deposits rather than topological clusters. The track and energy deposits of the muon itself are left out of the sum as for electrons. The calorimeter isolation variable is corrected for pile-up effects.

4.6 Missing Transverse Energy Reconstruction

The missing transverse energy is the absolute value of the vectorial sum of the transverse momenta in the event. For a complete reconstruction of the event it is expected to be zero. Undetected particles, such as neutrinos or other only weakly interacting particles, lead to non-zero values of missing transverse energy which is the essential signal for such particles. The reconstruction of the missing transverse energy relies on the reconstruction

of all physics objects in the event (see [146, 147]).

The missing transverse energy reconstruction includes energy deposits in the calorimeters and muon tracks. Inner Detector tracks are included to take into account low-p_{T} particles not well reconstructed in the calorimeters. The calorimeter cells are associated to reconstructed objects in a specific order, first electrons, then photons, hadronically decaying τ-leptons, jets and muons. The cells are then calibrated depending on the object they are associated with. Cells not associated to any object are included as the so called *CellOut* term of the missing transverse energy.

The x- and y-components of the missing transverse energy vector $\boldsymbol{E}_{\mathrm{T}}^{\mathrm{miss}} = -\sum \boldsymbol{p}_{\mathrm{T}}$ consists of the following contributions:

$$
\begin{aligned}
E_{x(y)}^{\mathrm{miss}} = {} & E_{x(y)}^{\mathrm{miss},e} + E_{x(y)}^{\mathrm{miss},\gamma} + E_{x(y)}^{\mathrm{miss},\tau} + E_{x(y)}^{\mathrm{miss,jets}} \\
& + E_{x(y)}^{\mathrm{miss,softjets}} + E_{x(y)}^{\mathrm{miss,calo},\mu} + E_{x(y)}^{\mathrm{miss,CellOut}} + E_{x(y)}^{\mathrm{miss},\mu} \quad .
\end{aligned}
\tag{4.4}
$$

Each associated term, except $E_{x(y)}^{\mathrm{miss},\mu}$, is the negative sum of calibrated cell energies associated to the respective objects projected onto the x- and y-axes. To suppress noise contributions, only cells belonging to topological clusters are included. $E_{x(y)}^{\mathrm{miss},\mu}$ is determined from the momenta of muon tracks. The energy loss of muons in the calorimeters, is included in the term $E_{x(y)}^{\mathrm{miss,calo},\mu}$. Low-$p_{\mathrm{T}}$ ($10\,\mathrm{GeV} < p_{\mathrm{T}} < 20\,\mathrm{GeV}$) and high-$p_{\mathrm{T}}$ ($p_{\mathrm{T}} > 20\,\mathrm{GeV}$) jets are treated separately in the terms $E_{x(y)}^{\mathrm{miss,softjets}}$ and $E_{x(y)}^{\mathrm{miss,jets}}$, respectively, (see [146]). The magnitude $E_{\mathrm{T}}^{\mathrm{miss}}$ and the azimuthal coordinate ϕ^{miss} of the missing energy vector are given by:

$$
\begin{aligned}
E_{\mathrm{T}}^{\mathrm{miss}} &= \sqrt{(E_x^{\mathrm{miss}})^2 + (E_y^{\mathrm{miss}})^2} \quad , \\
\phi^{\mathrm{miss}} &= \arctan(E_y^{\mathrm{miss}}/E_x^{\mathrm{miss}}) \quad .
\end{aligned}
\tag{4.5}
$$

The performance of the missing transverse energy reconstruction has been studied in leptonic Z and W boson decays [147]. To measure the missing transverse energy scale $W \to \ell\nu$ decays are used, where $E_{\mathrm{T}}^{\mathrm{miss}} > 0$ is expected because of the neutrino in the final state. For events with $E_{\mathrm{T}}^{\mathrm{miss}} > 40\,\mathrm{GeV}$, 5% and 3% difference between the data and simulation is found in the $E_{\mathrm{T}}^{\mathrm{miss}}$ scale in $W \to e\nu$ and $W \to \mu\nu$ events, respectively.

No genuine $E_{\mathrm{T}}^{\mathrm{miss}}$ is expected in $Z \to ee/\mu\mu$ events. The widths of the E_x^{miss}- and E_y^{miss}-distributions for $Z \to ee/\mu\mu$ events are therefore used to estimate the $E_{\mathrm{T}}^{\mathrm{miss}}$ resolution, limited by the imperfections of the calorimeter response and energy reconstruction.
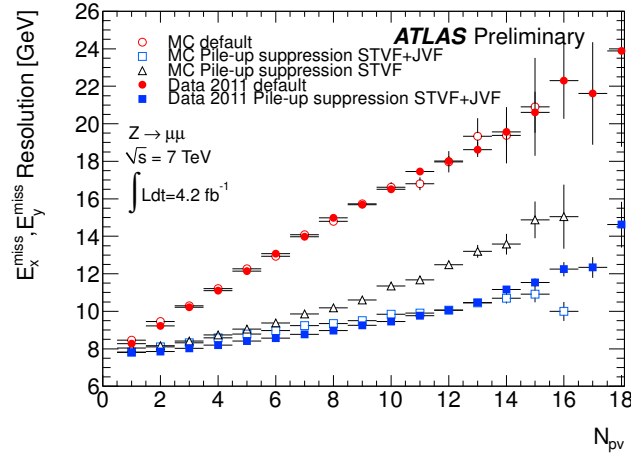
Figure 4.6: $E_{x,y}^{\mathrm{miss}}$ resolution in measured (full symbols) and simulated (empty symbols) $Z \rightarrow \mu\mu$ events as a function of the primary vertex multiplicity N_{PV} for the standard and the pile-up suppressed definition of the missing transverse energy [147]. The red dots correspond to the standard $E_{\mathrm{T}}^{\mathrm{miss}}$ definition and the black triangles and blue squares to the version with pile-up suppression by STVF and by STVF and JVF, respectively (see text).

A comparison between the resolution measured in data and simulation of $Z \rightarrow \mu\mu$ events is shown in Fig. 4.6 as a function of the primary vertex multiplicity N_{PV} which is a measure of pile-up. The $E_{\mathrm{T}}^{\mathrm{miss}}$ resolution degrades with increasing pile-up. The simulation provides a good description of the data.

The terms in the missing transverse energy measurement most affected by pile-up are the CellOut and soft-jet terms which are combined in the so called *soft term*

$$E_{x(y)}^{\mathrm{miss,SoftTerm}} = E_{x(y)}^{\mathrm{miss,softjets}} + E_{x(y)}^{\mathrm{miss,CellOut}} \quad . \tag{4.6}$$

A modified definition of the missing transverse energy denoted by $E_{\mathrm{T,STVF}}^{\mathrm{miss}}$ is used in the presented analysis in addition to suppress the impact of pile-up on the soft term, where the soft term is scaled with the *soft term vertex fraction*

$$\mathrm{STVF} = \sum_{\mathrm{track,PV}} p_{\mathrm{T}} / \sum_{\mathrm{track}} p_{\mathrm{T}} \tag{4.7}$$

with sums over all tracks not matched to physics objects and the subset associated to the hard scatter primary vertex (PV). The pile-up dependence of the $E_{\mathrm{T}}^{\mathrm{miss}}$-resolution
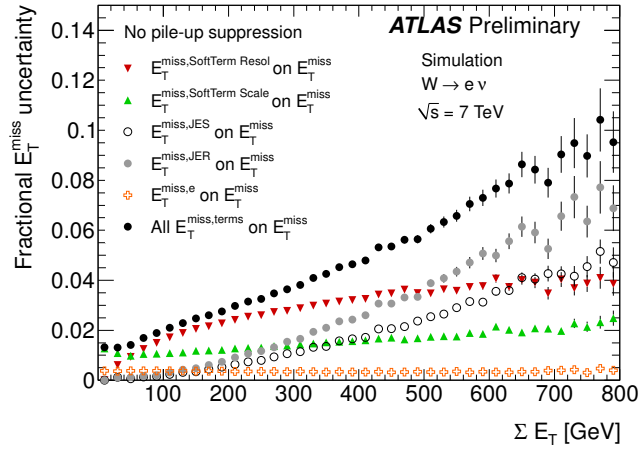
Figure 4.7: Relative systematic uncertainty of E_T^{miss} and its different contributions as a function of the total transverse energy $\sum E_T$ [147].

is considerably reduced by this scaling (see Fig. 4.6). The residual pile-up dependence resulting from the jet term is reduced by scaling each jet with the jet vertex fraction (JVF) explained in Section 4.2.

Systematic uncertainties in the E_T^{miss} reconstruction arise from the reconstruction of different objects with the largest contribution from electron, jet and soft term reconstruction. The relative uncertainty of E_T^{miss} estimated in simulated $W \to e\nu$ events is shown in Fig. 4.7 as a function of the total transverse energy measured in the calorimeters,

$$\sum E_T = \sum E_T^e + \sum E_T^\gamma + \sum E_T^\tau + \sum E_T^{\text{jets}} \\ + \sum E_T^{\text{calo},\mu} + \sum E_T^{\text{softjets}} + \sum E_T^{\text{CellOut}} \quad , \tag{4.8}$$

the scalar sum of the transverse energies of cells associated to different objects and calibrated accordingly. The uncertainty due to the soft term, for example is determined from differences between $Z \to \mu\mu$ data and simulation, where no electrons and jets are present in the final state and differences mainly result from the soft term itself.

4.7   Trigger Requirements

An overview of the ATLAS trigger system and its performance is given in [148]. Here only the muon and electron triggers used in the presented analysis are discussed. A

detailed description of the muon and electron triggers can be found in [149,150].

The ATLAS trigger system consists of three stages. The *Level-1 (L1)* trigger is a hardware trigger which reduces the event rate to ∼100 kHz and selects the *Regions of Interest (RoI)* to be further investigated by the *High Level Trigger (HLT)*. The HLT comprises the *Level-2 (L2)* trigger employing fast reconstruction algorithms and the *Event Filter* exploiting the full ATLAS event reconstruction.

The muon and electron trigger efficiencies are determined using a tag-and-probe method (see Section 4.4) [149,150]. For the 2012 data, the efficiencies were found to be 90% for electrons and 90% and 65% for muons in the barrel and endcaps, respectively. To correct for efficiency differences between data and simulation, the analysis applies a per-event weighting factor to the simulation.

4.7.1 Muon Trigger

The L1 muon trigger exploits information from the fast muon trigger chambers, RPCs covering 80% of the barrel part of the Muon Spectrometer and TGCs covering 99% of the endcaps, requiring coincidences between different chamber layers along the track. An estimate of the transverse momentum and the information about the RoI is passed on to the L2 trigger. The RoI information reduce the area of the detector that needs to be checked by the L2 trigger algorithms to 2–6% of the total detector coverage.

The L2 trigger uses also the information of the MDT and CSC precision chambers. A fast track finding algorithm reconstructs stand-alone muons. A refined estimate of the muon transverse momentum is made using look-up tables storing information for a fast p_T assignment. The stand-alone muons are combined with Inner Detector tracks reconstructed in the RoIs. The muon is classified as isolated, if no other tracks in the Inner Detector and no energy deposits in the calorimeters are found around the muon trajectory. About one out of 30 events passes the L2 muon trigger.

The Event Filter has access to the complete event data such that the full muon reconstruction described in Section 4.5 can be used. The position of the hard scatter primary vertex is exploited such that muons from the hard scatter event can be distinguished from pile-up interactions. Except for muon reconstruction efficiency, momentum scale and momentum resolution corrections not applied in the Event Filter, the transverse momentum reconstruction employed by the Event Filter, corresponds to the one used in the off-line analysis.

Several trigger criteria exploiting muon reconstruction quality, transverse momentum and isolation in different combinations have been used for the 2012 data taking period with the aim to reject as few interesting events as possible while keeping the trigger rate low. The presented analysis uses events selected by at least one of the two single-muon trigger requirements:

- A combined, isolated muon with $p_T > 24\,\mathrm{GeV}$ or

- a combined muon with $p_T > 36\,\mathrm{GeV}$,

where the p_T measurement is at the Event Filter level.

4.7.2 Electron Trigger

At the L1 trigger stage, calorimeter measurements with reduced granularity are used in trigger towers of $\Delta\eta \times \Delta\phi \approx 0.1 \times 0.1$ to define the RoIs. The calorimeter cells in each trigger tower, including the hadronic calorimeters with the exception of their outer-most layers, are summed in order to obtain a measure of the energy. Electromagnetic clusters are found by a sliding window algorithm based on a group of 4×4 η-ϕ trigger towers. The energy in the central region of the window is required to exceed a given energy threshold.

At the L2 trigger stage, electron and photon reconstruction algorithms building cell clusters in the RoIs provided by the L1 trigger are used. Due to limitations in the trigger latency, only the second layer of the electromagnetic calorimeter is used to identify the so called *pre-seeds*, the cells with the largest transverse energy deposit within a RoI. The cluster position is determined as the energy-weighted center-of-gravity in a 3×7 cell grid around the pre-seed. Simplified track reconstruction in the Inner Detector and cluster-to-track matching algorithms are used in the RoIs to refine the position and transverse energy measurements. A first electron identification is performed, using the energy deposition shower shapes in the electromagnetic calorimeter.

At the Event Filter level, the full reconstruction algorithms, as described in Section 4.4 are used. Only reconstruction and identification efficiency, energy scale and energy resolution corrections are not applied.

Electron trigger requirements based on different combinations of transverse momentum thresholds, isolation and electron reconstruction quality are used. The presented analysis uses events selected by at least one of two electron trigger requirements:

- One isolated electron with $p_\mathrm{T} > 24\,\mathrm{GeV}$ measured at the Event Filter level fulfilling the tight quality criteria together with a veto against events with significant hadronic leakage at the L1 stage or

- one medium-quality electron with $p_\mathrm{T} > 60\,\mathrm{GeV}$ at the Event Filter level.

The requirement on the hadronic leakage in the first set of requirements had to be applied due to the large L1 trigger rates in 2012. The second set of requirements recovers for electrons, which have failed the tight quality and isolation requirements in the first set of trigger definitions.

Chapter 5

Measurement of the VBF $H \to \ell\nu\ell\nu$ Production Rate

5.1 Analysis Strategy

The analysis is aimed at the investigation of the properties of the newly discovered Higgs boson with a mass of $(125.5 \pm 0.6)\,\mathrm{GeV}$ [7], to test the compatibility with the Standard Model predictions. The Standard Model Higgs boson production via Vector Boson Fusion (VBF) is studied in events where the Higgs boson decays into two oppositely charged W bosons, which subsequently decay into a charged lepton (electron or muon, denoted by ℓ) and a neutrino, i.e. in the process $qq \to qqH \to qqWW^* \to qq\ell\nu\ell\nu$. Both the Higgs boson production process and the decay have several characteristic properties that can be exploited to separate the Higgs-signal from background processes. Based on these properties, event selection criteria are defined that reduce the contamination by different processes while preserving as much as possible the signal contribution.

Due to the two neutrinos in the final state, the mass of the Higgs boson cannot be fully reconstructed from its decay products. Instead, the so called transverse mass is used as a discriminant between the signal and background processes with a relatively poor resolution. The similar shapes of the transverse mass distributions for signal and background processes call for precise understanding of all background contributions.

There is a large variety of background processes passing the analysis selection criteria. The contribution of each background process can be predicted from Monte-Carlo simulated events. Event generators take into account the currently best theoretical knowledge of the generated processes as discussed in Section 2.2.4. Generated events are fed into a detector simulation (see Section 3.2.7) with detailed description of the material and

response of the detector. The predictions from simulation are nevertheless subject to uncertainties in the theoretical description of the process or from time dependent detector conditions that cannot be taken into account by the simulation. To reduce the impact of such uncertainties on the analysis results, the background predictions from simulation are corrected, wherever possible, or even replaced by control measurements.

The final results are expressed in terms of observed and expected exclusion limits or significance in the signal strength with respect to the Standard Model predictions. They are obtained by comparing the transverse mass distribution of observed events that have passed the full selection to the corresponding predictions from simulation or data-based control measurements. A statistical hypothesis test using a frequentist approach [151] is carried out to evaluate the agreement of the background-only and signal-plus-background hypotheses with the observation.

Motivated by the recent discovery, the event selection criteria are optimized assuming a signal with a Higgs boson mass of 125 GeV. The same selection criteria are applied in the search for a Higgs boson signal with different mass, scanning the mass range from 110 GeV to 200 GeV. The analysis is performed on a dataset of proton-proton collisions recorded in the year 2012 with the ATLAS detector corresponding to an integrated luminosity of $\int L\,dt = 20.7\,\text{fb}^{-1*}$.

This chapter is structured in the following way: The properties of the signal and background processes are discussed in Section 5.2. The event selection criteria are described in Section 5.3. The measurement of the background contributions is presented in Section 5.4. Systematic uncertainties and their impact on the analysis are discussed in Section 5.5. In Section 5.6, the final results are shown, obtained with a statistical method described in Section 5.6.2. Finally, possibilities to improve the analysis are discussed in Section 5.7.

5.2 Signal and Background Processes

The analysis aims not only at measuring the rate of VBF Higgs boson productions but also, in a further step, at measuring the couplings of the Higgs boson to vector bosons. Therefore, the production of a Higgs boson in association with a vector boson (VH)

---

*An additional $\int L\,dt = 4.6\,\text{fb}^{-1}$ of collision data is available from the data taking in the year 2011. Due to different pile-up conditions this dataset has been analyzed separately and only the final results of both analyses are combined, as shown in Section 5.6.3.

is also considered as part of the signal. In practice, this process is not relevant for the final event selection due to the small cross section (Fig. 2.7a). In the following the VH production process will not be explicitly mentioned, but is considered as part of the signal and not of the background.

The cross section of gluon fusion production (ggF), on the contrary, is an order of magnitude larger compared to the VBF production cross section. Gluon fusion production depends on the coupling strength of the Higgs boson to fermions and is therefore considered as a background contribution in the analysis.

This section introduces the main signal and background properties. The key features of the VBF Higgs boson signal are given in Section 5.2.1 followed by a description of the most important backgrounds and their properties in Section 5.2.2.

5.2.1 The Signal Signature

The lowest-order Feynman diagram of the Higgs boson production via vector boson fusion with subsequent Higgs boson decay into two W bosons is shown in Fig. 5.1. Initial state quarks from the two colliding protons radiate vector bosons (W or Z), which fuse to produce the Higgs boson. The energy transfer of the incoming quarks to the vector bosons is relatively small compared to their initial energy. Therefore, the two final state quarks are only slightly diffracted and tend to follow the original proton trajectory. The quarks hadronize and can be reconstructed in the detector as jets (see Section 4.2). Hence, the VBF Higgs boson production leads to two highly energetic, forward jets in the final state that are well separated in rapidity. In addition, the Higgs boson decay products are expected to be observed in between the two jets.

The Higgs boson decay investigated is the decay into two oppositely charged W bosons, each subsequently decaying into a charged lepton and a neutrino. Due to their short lifetime, τ leptons decay before entering the detector and, hence, are more difficult to reconstruct and identify than electrons and muons. For the analysis presented here only final states with electrons and muons are considered*.

---

*An electron or muon ($\ell = e, \mu$) is produced in a W boson decay either directly ($W \to \ell\nu$) or indirectly in a secondary τ lepton decay ($W \to \tau\bar{\nu}_\tau \to \ell\bar{\nu}_\ell\nu_\tau\bar{\nu}_\tau$). The contribution of the processes with leptonically decaying τ leptons is small due to the small branching fractions of the leptonic W boson and τ lepton decays ($\mathcal{B}(W \to \tau\nu) \approx 11\%$ and $\mathcal{B}(\tau \to \ell\nu\nu) \approx 17\%$ [10]) and due to the lower energies of electrons and muons from the secondary τ lepton decays.
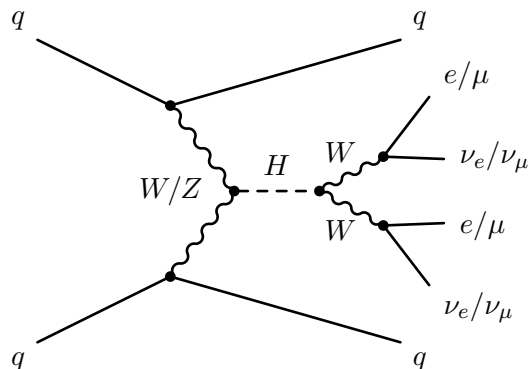
Figure 5.1: Tree-level Feynman diagram for VBF Higgs boson production and the subsequent Higgs boson decay into a pair of W bosons, each decaying leptonically.

Two final states are distinguished because of different background compositions:

- *Same-flavor* final states: $H \to W^{\pm}W^{\mp(*)} \to e^{+}\nu_{e}e^{-}\bar{\nu}_{e}/\mu^{+}\nu_{\mu}\mu^{-}\bar{\nu}_{\mu}$.

- *Different-flavor* final states: $H \to W^{\pm}W^{\mp(*)} \to e^{+}\nu_{e}\mu^{-}\bar{\nu}_{\mu}/\mu^{+}\nu_{\mu}e^{-}\bar{\nu}_{e}$.

In the Standard Model the Higgs boson is a scalar particle with spin quantum number $s_H = 0$. This leads to an angular correlation between the two charged leptons, as illustrated in Fig. 5.2. In the rest frame of the Higgs boson and for Higgs boson masses of up to about twice the W boson mass the two W bosons are produced at rest. Hence, the two W boson decay products, the lepton and the neutrino, are emitted back-to-back. For $s_H = 0$, the spin directions of the W bosons are anti-parallel and the spin directions of lepton and neutrino from the W boson decays are parallel to each other. Since the neutrinos are left-handed, the neutrino originating from the W^+ boson is emitted in anti-parallel direction to its spin, while the momentum of the anti-neutrino from the W^- boson decay points in the direction of its spin. Since the spin directions of the two neutrinos are anti-parallel, the two neutrinos tend to be emitted in the same direction. As the charged lepton is produced back-to-back with its neutrino-partner, the two leptons will also be emitted in the same direction resulting in a small opening angle $\Delta\phi(\ell\ell)$ between them and a small dilepton invariant mass $m_{\ell\ell}$. This spin correlation is used to separate signal from background.

Due to the presence of two neutrinos with unknown four-momenta in the final state it is not possible to fully reconstruct the mass of the Higgs boson. Instead, the
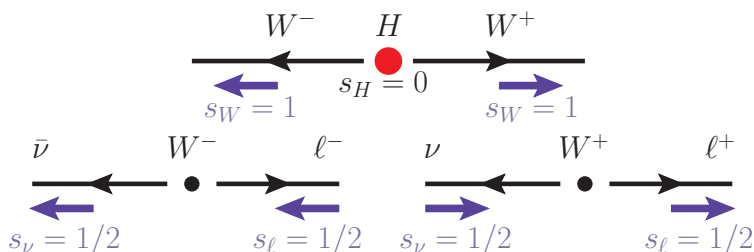
Figure 5.2: Illustration of the angular correlation of the final state leptons in the example of the spin-0 Higgs boson decay into two W bosons with positive helicity. In this case the directions of the charged leptons are parallel to the W^+ momentum whereas the directions of the neutrinos are parallel to the W^- momentum.

transverse mass m_{T} is reconstructed from the measured lepton four-momenta and the missing transverse energy vector $\boldsymbol{E}_{\text{T}}^{\text{miss}}$, which corresponds to the sum of the transverse components of the neutrino four-momenta:

$$m_{\text{T}} = \sqrt{(E_{\text{T}}^{\ell\ell} + E_{\text{T}}^{\text{miss}})^2 - |\boldsymbol{p}_T^{\ell\ell} + \boldsymbol{E}_{\text{T}}^{\text{miss}}|^2} \text{ with } E_{\text{T}}^{\ell\ell} = \sqrt{|\boldsymbol{p}_{\text{T}}^{\ell\ell}|^2 + m_{\ell\ell}^2}, \qquad (5.1)$$

where $\boldsymbol{p}_{\text{T}}^{\ell\ell}$ and $m_{\ell\ell}$ are the transverse momentum and invariant mass of the dilepton system, respectively.

Figure 5.3 shows the transverse mass distribution for the VBF $H \to WW^{(*)} \to \ell\nu\ell\nu$ signal for different Higgs boson mass values. The mass resolution is rather poor, on the order of 50–100 GeV depending on the Higgs boson mass. Nevertheless, the m_{T}-variable is powerful in rejecting background contributions as will be shown in Section 5.3.

The cross sections of the signal processes are shown in Table 5.1 for a Higgs boson mass of 125 GeV together with the Monte-Carlo generators used for the signal modelling. The cross sections for other mass values are given in Appendix A . The calculation of the cross sections and decay branching fractions is discussed in Section 2.2.

5.2.2   The Background Processes

The contribution of different backgrounds to the analysis depends on their cross sections and on their resemblance to the signal topology. The most important backgrounds to the presented analysis arise from diboson production processes, in particular of W-boson-pairs, as well as from top quark production where the largest contribution is expected from processes with top-quark-pairs in the final state. Drell-Yan processes

Table 5.1: List of signal ($m_H = 125\,\mathrm{GeV}$) and background processes together with the event generators used for the simulation (compare also Table 2.4). The corresponding cross sections (σ) times the branching fractions ($\mathcal{B}$) are given for $\sqrt{s} = 8\,\mathrm{TeV}$ (in case of unspecified initial and final state particles all possible production and decay mechanisms are taken into account). Here, ℓ denotes all lepton flavors ($\ell = e/\mu/\tau$). Corresponding figures with lowest-order Feynman diagrams are also indicated.

		Process	Monte-Carlo generator	$\sigma \times \mathcal{B}$ (pb)	Diagrams (Figure)
Signal		$qq \to qqH \to qq\ell\nu\ell\nu$	POWHEG +PYTHIA8	0.035	5.1,2.6b
		$qq \to VH \to V\ell\nu(\ell\nu$ or $qq)$	PYTHIA8	0.13	2.6c
ggF		$gg \to H \to \ell\nu\ell\nu$	POWHEG+PYTHIA8	0.44	2.6a
Diboson	QCD	$q\bar{q}, gg \to WW \to \ell\nu\ell\nu$	POWHEG+PYTHIA6	5.7	5.4a–c
		$gg \to WW \to \ell\nu\ell\nu$	GG2WW 3.1.2+HERWIG	0.20	5.4c
		$WZ/\gamma^* \to \ell\nu\ell\ell,\ (m_{\gamma^*} > 7\,\mathrm{GeV})$	POWHEG+PYTHIA8	0.83	
		$W\gamma^* \to \ell\nu\ell\ell\ (m_{\gamma^*} \leq 7\,\mathrm{GeV})$	MadGraph +PYTHIA6	11	5.4a,b
		$W\gamma \to \ell\nu\gamma\ (p_\mathrm{T}^\gamma > 8\,\mathrm{GeV})$	ALPGEN+HERWIG	116	
		$Z^*Z^* \to \ell\ell\ell\ell$	POWHEG+PYTHIA8	0.73	5.4a
	EW	$WW \to \ell\nu\ell\nu + 2j$	SHERPA with no $\mathcal{O}(\alpha_s)$	0.039	
		$WZ \to \ell\ell\ell\nu + 2j$	SHERPA with no $\mathcal{O}(\alpha_s)$	0.013	5.4d
		$ZZ \to \ell\ell\nu\nu + 2j$	SHERPA with no $\mathcal{O}(\alpha_s)$	0.0012	
		$ZZ \to \ell\ell\ell\ell + 2j$	SHERPA with no $\mathcal{O}(\alpha_s)$	0.00074	
Top quark		$t\bar{t} \to q\bar{q}WW \to q\bar{q}\ell\nu\ell\nu$	MC@NLO+HERWIG	26	5.5a–c
		$W(\to \ell\nu)t$	MC@NLO+HERWIG	22	5.5d,e
		$t(\to qW \to q\ell\nu)qb$ (t-channel)	AcerMC+PYTHIA6	30	5.5g,h
		$t(\to qW \to q\ell\nu)b$ (s-channel)	MC@NLO+HERWIG	1.8	5.5f
Z/γ^*	QCD	$Z/\gamma^* \to \ell\ell\ (m_{\ell\ell} > 10\,\mathrm{GeV})$	ALPGEN+HERWIG	16000	5.6b
	EW	$qq \to qqZ^* \to qq\ell\ell$	SHERPA up to $\mathcal{O}(\alpha_s)$	1.2	5.6c
W+jets		$W \to \ell\nu$	ALPGEN+HERWIG	37000	5.6b
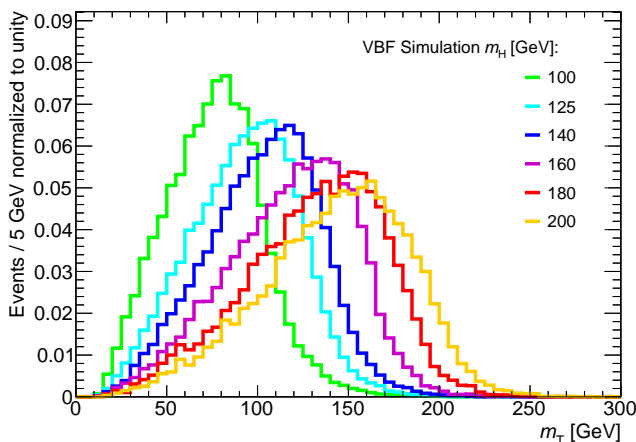
Figure 5.3: Distribution of the transverse mass m_T, calculated from the reconstructed leptons and missing transverse energy, for simulated VBF $H \to WW^{(*)}$ events in the $\ell\nu\ell\nu$ final state requiring two oppositely charged leptons and two jets for different Higgs boson masses m_H.

play a significant role in same-flavor final states. Only minor contributions are expected from single W boson production with accompanying jets (W+jets). Finally, gluon fusion Higgs boson production is considered as additional background.

An overview of the different background processes together with the corresponding event generators is given in Table 5.1. A detailed list of Monte-Carlo samples generated for background modelling is given in Appendix A. For the background cross sections the highest-order calculations available are used. In particular, diboson production cross sections are calculated up to next-to-leading order using the MCFM program [152]. The top-quark-pair production cross section is calculated at approximate next-to-next-to-leading-order [153].

Background from Gluon Fusion Higgs Boson Production

The Higgs boson production via gluon fusion (ggF) contaminates the analysis due to the larger cross section compared to the VBF signal process (see Table 5.1). While the lepton and missing transverse momentum kinematics from Higgs boson decays are almost identical for signal and ggF background, the jet kinematics, are very distinct between the VBF and ggF production process.
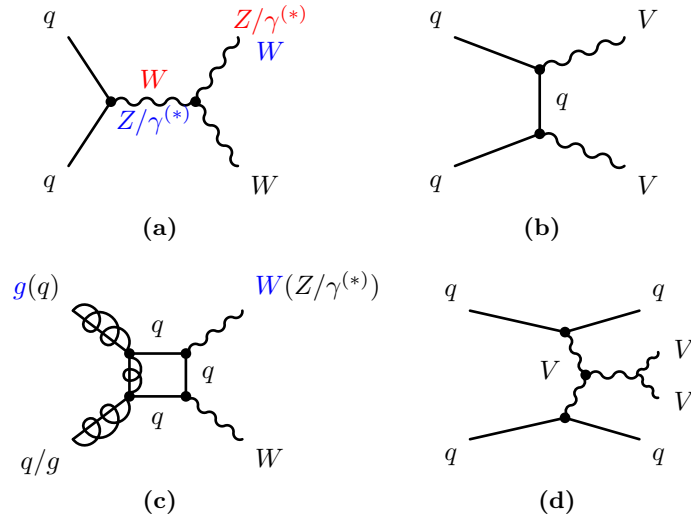
Figure 5.4: Tree-level Feynman diagrams of the most important diboson background processes. Vector boson production via quark-antiquark annihilation and quark-quark scattering is shown in (a) and (b). Diboson production via gluon-gluon or quark-gluon scattering in higher-orders is shown in (c). Electroweak diboson production is shown in (d).

Diboson Background

At the LHC, gauge boson pairs $(VV \equiv WW, WZ/\gamma^{(*)}, ZZ)^*$ are produced via several mechanisms. Examples of Feynman diagrams are shown in Fig. 5.4. The processes are classified in two groups:

- Non-VBF-like VV production, referred to as $QCD\ VV$ processes, where the jets in the final state are produced via initial or final state radiation, i.e. via higher-order QCD processes (Figs. 5.4a–c).

- VBF-like VV production, referred to as *electroweak (EW) VV* processes, where production of jets does not require higher-order QCD processes (Fig. 5.4d).

QCD VV production predominantly proceeds through interaction of two quarks (see Figs. 5.4a and b). The production via gluon-quark or gluon-gluon scattering is possible

---

*Here, $W\gamma$ and $W\gamma^*$ are distinguished since their modelling is performed by different event generators (compare Table 5.1). Generally, the production of virtual photons is denoted by the symbol "$*$". While for the heavy gauge bosons the main background contribution is expected from on-shell production, the contribution of virtual photon production is significant and therefore emphasized by the label "$(*)$", indicating that both real and virtual photon production contributes.

in higher-order perturbation theory (Fig. 5.4c). The EW VV process (Fig. 5.4d) involves fusion of two vector bosons irradiated from the two incoming quarks.

The most important diboson background is W^+W^- (or simply WW) production, with very a signal-like topology. While the QCD WW background can be rejected by requiring two forward jets with signal-like kinematic properties, the EW WW background is almost irreducible. A separation from the signal is still possible to some extent using the spin correlation in Higgs boson decays.

Other diboson backgrounds such as WZ, $W\gamma^{(*)}$ and ZZ are less important. These processes have a lower probability to pass the event selection due to different lepton multiplicities compared to the signal. They only contribute because of lepton misidentification or inefficiencies. Exceptions are the $ZZ \to \ell\ell\nu\nu$ and $WZ \to qq\ell\ell$ processes which contribute only to same-flavor final states and either miss two jets or genuine missing transverse energy.

Backgrounds with Top Quarks

Top quarks are expected to decay with a branching ratio of essentially 100% into a W boson and a b quark ($t \to Wb$). Since the signal is accompanied by jets originating mostly from u and d quarks, so called *light-jets*, the absence of b-jets (originating from b quarks) can be used to separate the signal from top quark processes.

Two background processes with top quarks are distinguished, the dominant top-quark-pair production ($t\bar{t}$) shown in Figs. 5.5a–c and the less important *single top quark* production (see Figs. 5.5d–h). The latter is further categorized into top quark production in association with a W boson (Wt) as shown in Fig. 5.5d and e and the *s*- and *t-channel* production shown in Fig. 5.5f and Figs. 5.5g and h, respectively.

Processes including top quarks, in particular the $t\bar{t}$ process, are important backgrounds due to their large cross section (see Table 5.1). However, the presence of b-jets in the final state and the different origin of the jets allows for rejection of a large fraction of the top quark background.

Z/γ^* Background

Z/γ^* bosons are produced predominantly via the Drell-Yan process $qq \to Z/\gamma^*$ shown in Fig. 5.6a. Additional jets in the final state occur only via initial state radiation. Smaller contributions from gluon-gluon and gluon-quark interactions involve higher-
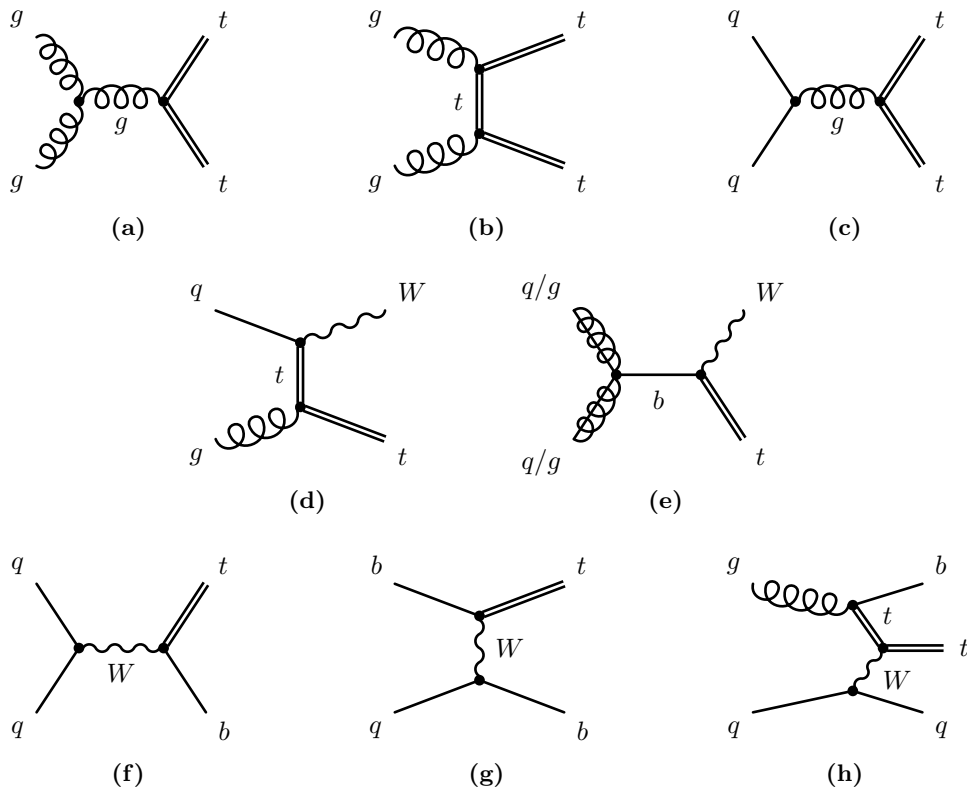
Figure 5.5: Tree-level Feynman diagrams for top quark production. $t\bar{t}$ production is shown in (a) to (c), top quark production in association with a W boson (Wt) in (d) and (e) and single top quark production in the s-channel and t-channel in (f) and in (g) and (h), respectively.
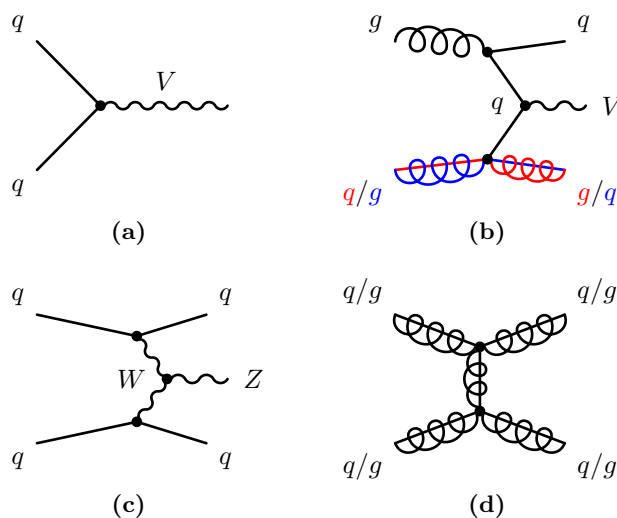
Figure 5.6: Tree-level Feynman diagrams for vector boson and multijet production. The Drell-Yan process is shown in (a), vector boson production in gluon-quark and gluon-gluon interactions in (b) and electroweak Z boson production in (c). Dijet production, the dominant QCD multijet process at the LHC, is shown in (d).

order diagrams (see Fig. 5.6b). Jets, required by the analysis selection, originate from higher-order QCD production in the above processes which are therefore referred to as the *QCD Z/γ^** background.

In addition to the QCD processes, there is *electroweak Z* boson production (see Fig. 5.6c) which has a VBF-like topology. This is only a small background despite of the signal-like production mechanism, due to the much smaller cross section compared to the QCD Z/γ^* process.

Two decay modes of the Z/γ^* bosons are distinguished:

- $Z/\gamma^* \to \ell\ell$ decays, which contribute only to same-flavor final states, differ from the signal since no neutrinos are produced.

- $Z/\gamma^* \to \tau\tau \to \ell\nu\nu\ell\nu\nu$ decays contribute to both same-flavor and different-flavor final states. This background is more difficult to reject due to neutrinos produced in leptonic τ lepton decays. However, the contribution of this background is suppressed by the small branching ratio for τ lepton decays into electrons and muons.

67

W+jets and Multijet Background

Single W bosons are produced via the same processes as Z bosons shown in Figs. 5.6a and b. Despite the large cross section, this is a minor background since it involves only one prompt lepton from the W boson decay. The second lepton can originate in this case from a jet either misidentified as a lepton or containing a lepton which is in both cases rare and well rejectable. Such leptons are in the following referred to as *fake* leptons. In addition, as the analysis requires two jets in the final state, the fake lepton needs to originate from a third jet significantly reducing the W+jets contribution.

Similarly, the multijet QCD background (see Fig. 5.6d) contributes only if two fake leptons occur in the final state. In addition, no highly energetic neutrinos are present such that the missing transverse energy is expected to be small.

5.3   The Event Selection

In this section a detailed description of the event selection shall be given based on the signal and background topologies described. The selection is performed in several stages correlated with the selection of control data for the measurement of various background contributions which will be addressed in Section 5.4.

Preselection   The preselection applies data quality criteria and requires the presence of a primary interaction vertex reconstructed from at least three charged particle tracks. Furthermore, exactly two oppositely charged leptons with $p_\mathrm{T} > 15\,\mathrm{GeV}$ and at least two jets are required in each event passing the single electron or single muon triggers. At least one of the two selected leptons is required to have $p_\mathrm{T} > 25\,\mathrm{GeV}$ to ensure p_T-independent trigger efficiencies. The invariant mass $m_{\ell\ell}$ of the two leptons is required to be greater than $10\,\mathrm{GeV}$ and $12\,\mathrm{GeV}$ for different-flavor and same-flavor final states, respectively. This criterion rejects events from low mass Drell-Yan processes and from J/ψ or Υ decays.

The leptons are required to originate from the primary interaction vertex by means of cuts on the transverse and longitudinal impact parameters and to be isolated by employing both track and calorimeter isolation criteria. The thresholds of isolation requirements depend on the lepton transverse momentum p_T.

Jets are required to have a transverse momentum greater than $25\,\mathrm{GeV}$ in the central

Table 5.2: Requirements on the physics objects used in the analysis. The calorimeter isolation variables are corrected for effects of pile-up (PU). The reconstruction of the different objects is described in Chapter 4.

Trigger	
Electron	Medium isolated electron with $p_\mathrm{T} > 24\,\mathrm{GeV}$
	OR medium electron with $p_\mathrm{T} > 60\,\mathrm{GeV}$
Muon	Combined isolated muon with $p_\mathrm{T} > 24\,\mathrm{GeV}$
	OR combined muon with $p_\mathrm{T} > 36\,\mathrm{GeV}$
Muons	
Reconstruction algorithm	Combined muon
Identification quality	
Pseudorapidity range	$|\eta| < 2.5$
Transverse momentum range	$p_\mathrm{T} > 15\,\mathrm{GeV}$
Isolation	$E_\mathrm{T,PU\,corr}^\mathrm{cone30}/p_\mathrm{T} < \min[0.014\,p_\mathrm{T} - 0.15, 0.20]$
	$p_\mathrm{T}^\mathrm{cone30}/p_\mathrm{T} < \min[0.01\,p_\mathrm{T} - 0.105, 0.15]$
Transverse impact parameter	$d_0/\sigma(d_0) < 3.0$
Longitudinal impact parameter	$z_0 \cdot \sin\theta < 1.0\,\mathrm{mm}$
Electrons	
Identification quality	Tight
Pseudorapidity range	$|\eta| < 2.47$, $1.37 < |\eta| < 1.52$ excluded
Transverse momentum range	$p_\mathrm{T} > 15\,\mathrm{GeV}$
Isolation	$E_\mathrm{T,PU\,corr}^\mathrm{topo,cone30}/p_\mathrm{T} < 0.16$
	$p_\mathrm{T}^\mathrm{cone30}/p_\mathrm{T} < 0.12(0.16)$ for $p_\mathrm{T} = 15 - 25(> 25)\,\mathrm{GeV}$
Transverse impact parameter	$d_0/\sigma(d_0) < 3.0$
Longitudinal impact parameter	$|z_0|\sin\theta < 0.4\,\mathrm{mm}$
Jets	
Reconstruction algorithm	AntiKt (distance parameter $R = 0.4$)
Pseudorapidity range	$|\eta| < 4.5$
Transverse momentum range	$p_\mathrm{T} > 25(30)\,\mathrm{GeV}$ for $|\eta| < (>)2.4$
Pile-up suppression	$|\mathrm{JVF}| > 0.5$ for $p_\mathrm{T} < 50\,\mathrm{GeV}$ and $|\eta| < 2.4$
b-jets	
b-tagging	MV1 < 0.148 ($\epsilon_{b\text{-tag}} = 85\%$)
likelihood discriminant	
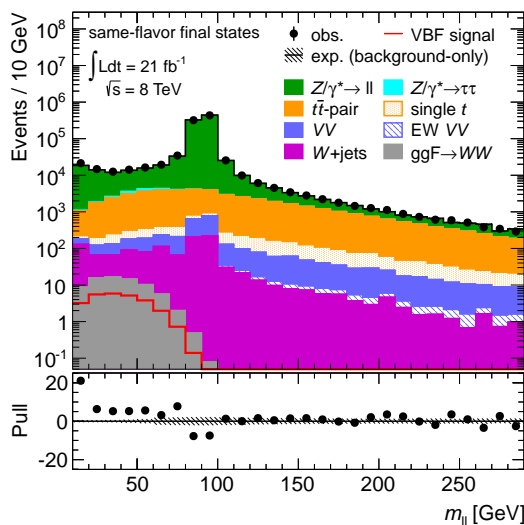
Figure 5.7: Monte-Carlo predicted and observed distributions of the dilepton invariant mass $m_{\ell\ell}$ for same-flavor final states after the preselection without the requirement $m_{\ell\ell} > 12\,\text{GeV}$. In the bottom part the pull $= \frac{N^{\text{obs}} - N^{\text{exp}}}{\sigma(N^{\text{exp}})}$ distribution is shown with N^{obs} and N^{exp} being the numbers of observed and expected events, respectively, and $\sigma(N^{\text{exp}})$ the Poisson error. The background contributions are stacked on top of each other. The expected signal is overlaid in red. The black hatched area represents the statistical uncertainty in the background prediction. The statistical errors of the data are smaller than the data points.

$(|\eta| < 2.4)$ and greater than $30\,\text{GeV}$ in the forward region $(|\eta| \geq 2.4)$ of the detector. To remove jets from pile-up interactions, the absolute value of the jet vertex fraction (JVF) is required to be greater then 0.5 for jets with $p_{\text{T}} < 50\,\text{GeV}$ and $|\eta| < 2.4$. Furthermore, the rapidity regions of the leptons and jets are constrained to the detector coverage needed for lepton and jet reconstruction. The preselection requirements for all reconstructed physics objects used in the analysis are summarized in Table 5.2.

Z Background Rejection After the preselection the following requirements are applied mainly to remove $Z/\gamma^* \to \ell\ell$ background:

- The $Z \to \ell\ell$-veto requiring $|m_{\ell\ell} - m_Z| > 15\,\text{GeV}$, where m_Z is the mass of the Z boson, is applied for same-flavor final states and rejects the bulk of the $Z \to \ell\ell$ background. The dilepton invariant mass distribution after the preselection is shown in Fig. 5.7 for the signal and background processes.
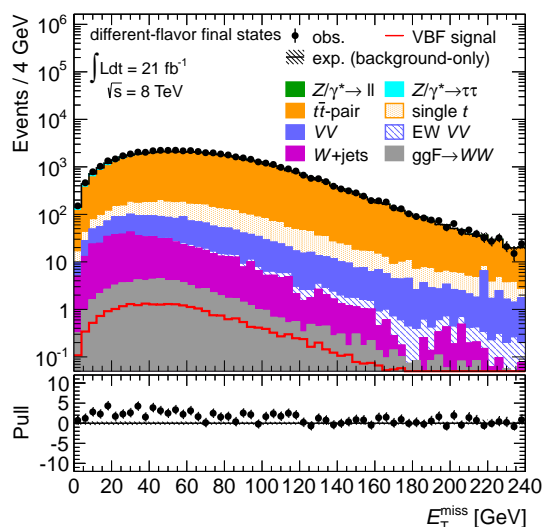
Figure 5.8: Monte-Carlo predicted and observed distributions of the missing transverse energy E_T^{miss} for different-flavor final states after the preselection. The background contributions are stacked on top of each other. The expected signal is overlaid in red. The statistical uncertainty in the background prediction (black hatched area) is invisible on this scale. The vertical error bars indicate the statistical uncertainty of the data.

- In addition, the presence of the two neutrinos in the final state is exploited by requiring high missing transverse energy. For different-flavor final states $E_T^{miss} > 20\,\text{GeV}$ is required to reject multijet processes. The E_T^{miss}-distribution for these final states is shown in Fig. 5.8. For same-flavor final states $E_T^{miss} > 45\,\text{GeV}$, and subsequently with STVF pile-up corrections $E_{T,STVF}^{miss} > 35\,\text{GeV}$, are required rejecting mainly the $Z/\gamma^* \to \ell\ell$ background. The E_T^{miss}-distribution and the $E_{T,STVF}^{miss}$-distribution after requiring $E_T^{miss} > 45\,\text{GeV}$ are shown for same-flavor final states in Figs. 5.9a and b, respectively. Even though the two missing transverse energy variables are highly correlated, $E_{T,STVF}^{miss}$ gives additional rejection of $Z/\gamma^* \to \ell\ell$ background since it is less sensitive to pile-up.

The $Z/\gamma^* \to \ell\ell$ background rejection criteria are followed by additional requirements for suppressing other background processes.

b-Jet Veto   It is required that no reconstructed jet in the event is identified as a b-jet. This reduces the contribution of the top quark background by one order of magnitude.
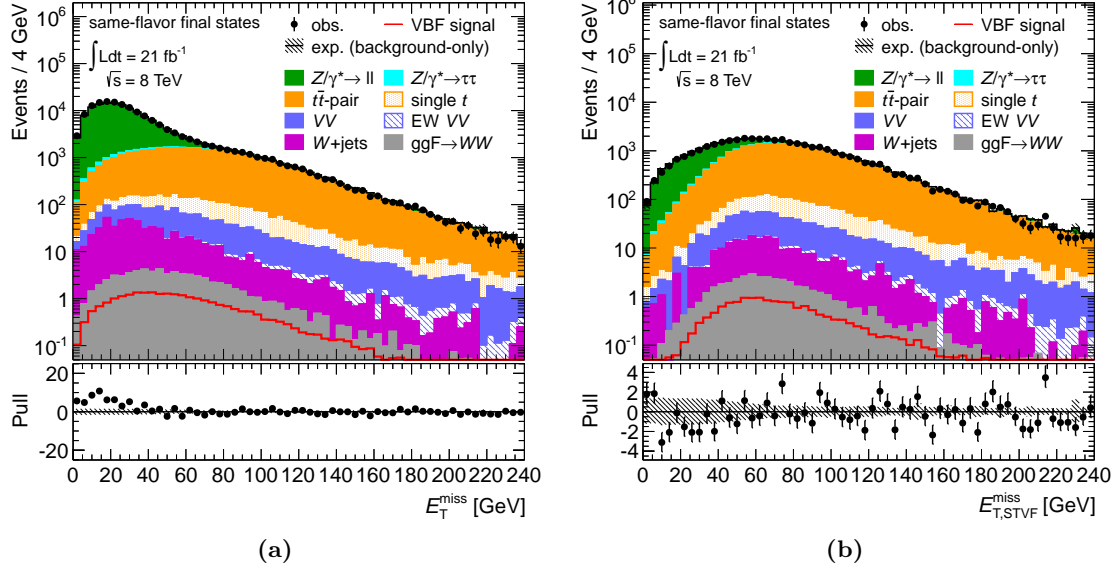
**Figure 5.9:** Monte-Carlo predicted and observed distributions of the missing transverse energy for same-flavor final states: (a) E_T^{miss} after the $Z \to \ell\ell$-veto and (b) $E_{T,STVF}^{miss}$ after requiring $E_T^{miss} > 45\,\text{GeV}$. The background contributions are stacked on top of each other. The expected signal is overlaid in red. The black hatched area represents the statistical uncertainty in the background prediction. The vertical error bars indicate the statistical uncertainty of the data.

Total Transverse Momentum p_T^{tot} The absolute value of the vectorial sum of the transverse momenta of all selected leptons, jets and the missing transverse energy in the event, the total transverse momentum $p_T^{tot} = \sum p_{T,lep} + \sum p_{T,jet} + E_T^{miss}$, is expected to be small because of transverse momentum conservation. The requirement of small total transverse momentum suppresses the contamination by mis-reconstructed events such as $Z/\gamma^* \to \ell\ell$ production with large missing transverse energy due to mis-measurements. A rather loose requirement of $p_T^{tot} < 45\,\text{GeV}$ is chosen, since the separation between signal and background is small as shown in Fig. 5.10a.

$Z \to \tau\tau$ Veto To reject the $Z/\gamma^* \to \tau\tau \to \ell\nu\nu\ell\nu\nu$ contribution, the di-tau invariant mass $m_{\tau\tau}$ is required to obey $|m_{\tau\tau} - m_Z| > 25\,\text{GeV}$. It is determined in the *collinear approximation*, i.e. assuming that the leptons (e/μ) and neutrinos from the τ lepton decay are emitted collinearly to the τ lepton due to their strong boost. This assumption makes it possible to determine separately the contributions of each τ lepton decay
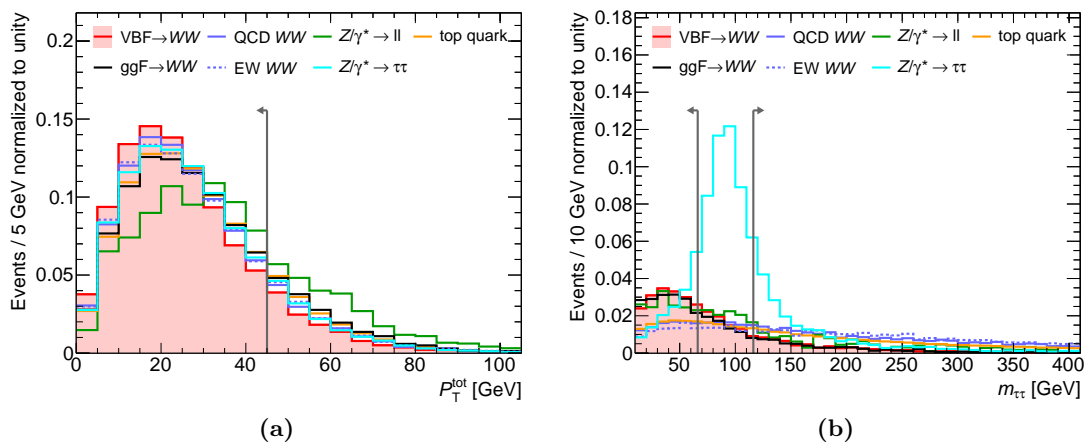
Figure 5.10: Expected distributions for signal and background processes of (a) the total transverse momentum p_T^{tot} and (b) the di-tau mass $m_{\tau\tau}$ after the preselection and the Z rejection criteria combining different-flavor and same-flavor events. The $Z/\gamma^* \to \tau\tau$ contribution in (b) appears enhanced compared to the other background, since events with unphysical solutions of the $m_{\tau\tau}$ calculation are not included. The vertical lines indicate the selection criteria.

to the total missing transverse energy and thus to reconstruct the four-momenta of the τ leptons and hence their invariant mass $m_{\tau\tau}$. The $m_{\tau\tau}$-distribution is shown in Fig. 5.10b. Since the $m_{\tau\tau}$ requirement introduces an additional implicit dependence on the missing transverse energy and associated systematic uncertainties, the criterion is not applied to same-flavor final states, where there is no net gain in sensitivity.

VBF selection The VBF selection criteria exploit the topology of the VBF Higgs boson production.

- First, the two highest momentum jets in the event are assumed to be the jets originating from the VBF Higgs boson production, *tagging* this production process. A large rapidity gap ΔY_{jj} between the two tagging jets and a high dijet invariant mass m_{jj} are required: $\Delta Y_{jj} > 2.8$ and $m_{jj} > 500\,\text{GeV}$. The distributions of these discriminating variables are shown in Figs. 5.11a and b, respectively.

- Properties of jets reconstructed in addition to the tagging jets are also exploited. For the signal, the probability for the emission of jets between the tagging jets is reduced compared to the ggF Higgs boson production and other backgrounds
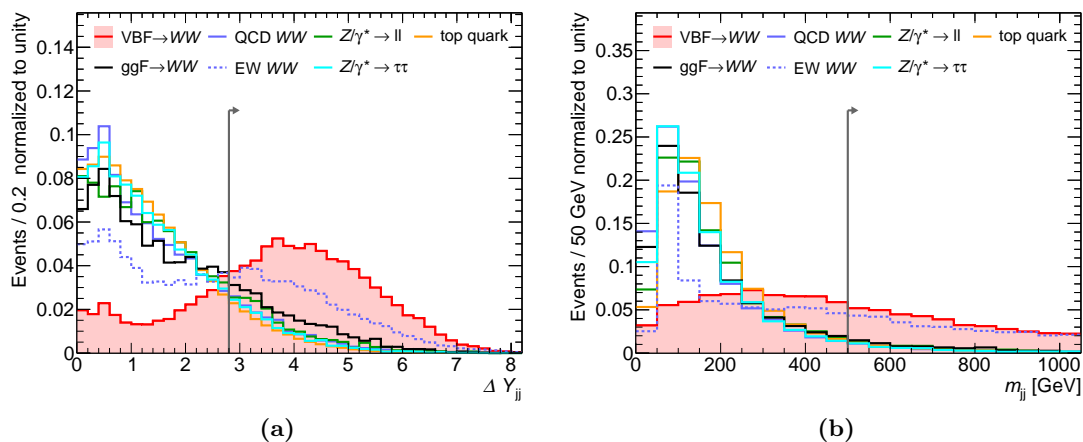
Figure 5.11: Expected distributions of (a) the rapidity gap ΔY_{jj} and (b) the invariant mass m_{jj} of the two tagging jets after the preselection and the Z rejection criteria combining different-flavor and same-flavor events. The vertical lines indicate the selection criteria.

[54] due to the color singlet exchange in VBF production [55, 57]. In the signal, additional jets can only arise from gluon radiation of the two initial or final state quarks. These jets are soft and collinear to the quarks. Hence no *central jets*, i.e. additional jets in between the two tagging jet rapidities, appear. In contrast, most background processes, including the ggF Higgs boson production, have high-p_T QCD jet activity in the central rapidity region. The p_T-distribution of the highest momentum central jet is shown in Fig. 5.12. A *central jet veto (CJV)* is applied rejecting events containing central jets with $p_T > 20\,\text{GeV}$.

- Finally, it is expected that the two leptons produced in the Higgs boson decay are emitted in between the two tagging jets in the rz-plane. Therefore, the so called *outside lepton veto (OLV)* is applied rejecting events with at least one lepton in the rapidity range between the two tagging jets.

Higgs Boson Decay Topology   The final selection requirements are based on the Higgs boson decay topology.

- Motivated by the spin correlation small dilepton invariant masses, $m_{\ell\ell} < 60\,\text{GeV}$ are required as well as small dilepton opening angles, $\Delta\phi(\ell\ell) < 1.8$. The corresponding distributions are shown in Fig. 5.13a and b, respectively.

74
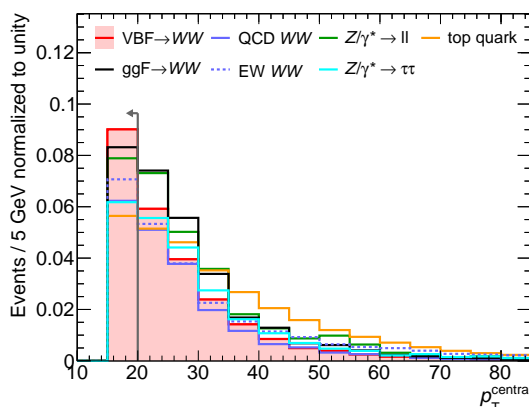
Figure 5.12: Expected distribution of the transverse momentum of the highest momentum central jet after the preselection and the Z rejection criteria combining different-flavor and same-flavor events. The vertical lines indicate the selection criteria.

- The statistical interpretation (see Section 5.6.2) of the data in comparison with the signal and background predictions is based on the shape and normalization of the transverse mass (m_T) distribution, shown in Fig. 5.13c. To estimate the analysis sensitivity, without employing the full formalism of the statistical interpretation, a requirement of $m_T < 1.2 \cdot m_H$ is applied for optimization purposes.

Figure 5.14 shows the signal and background contributions after each selection requirement, together with the corresponding signal-to-background ratio s/b and the signal significance $s/\sqrt{b}$. It can be seen that after the full selection, including the requirement $m_T < 1.2 \cdot m_H$, the signal-to-background ratio reaches 0.42 for different-flavor and 0.13 for same-flavor final states. Same-flavor final states have a lower signal fraction than different-flavor final states due to the additional $Z/\gamma^* \to \ell\ell$ background in the former.

For different-flavor final states, the main backgrounds are top quark and diboson processes as well as smaller contributions from $Z/\gamma^* \to \tau\tau$ processes and ggF Higgs boson production at comparable levels. In same-flavor final states, the $Z/\gamma^* \to \ell\ell$ background is by far the most important background. However, $Z/\gamma^* \to \tau\tau$, diboson and top quark processes also contribute.

For both final states, 30% of the total diboson background is from electroweak processes. Prior to the requirements based on the Higgs boson topology, this electroweak contribution is even about 50% of the total diboson background. Roughly 12% of the total top quark background comes from single top quark production. More details on

(a)

(b)

(c)
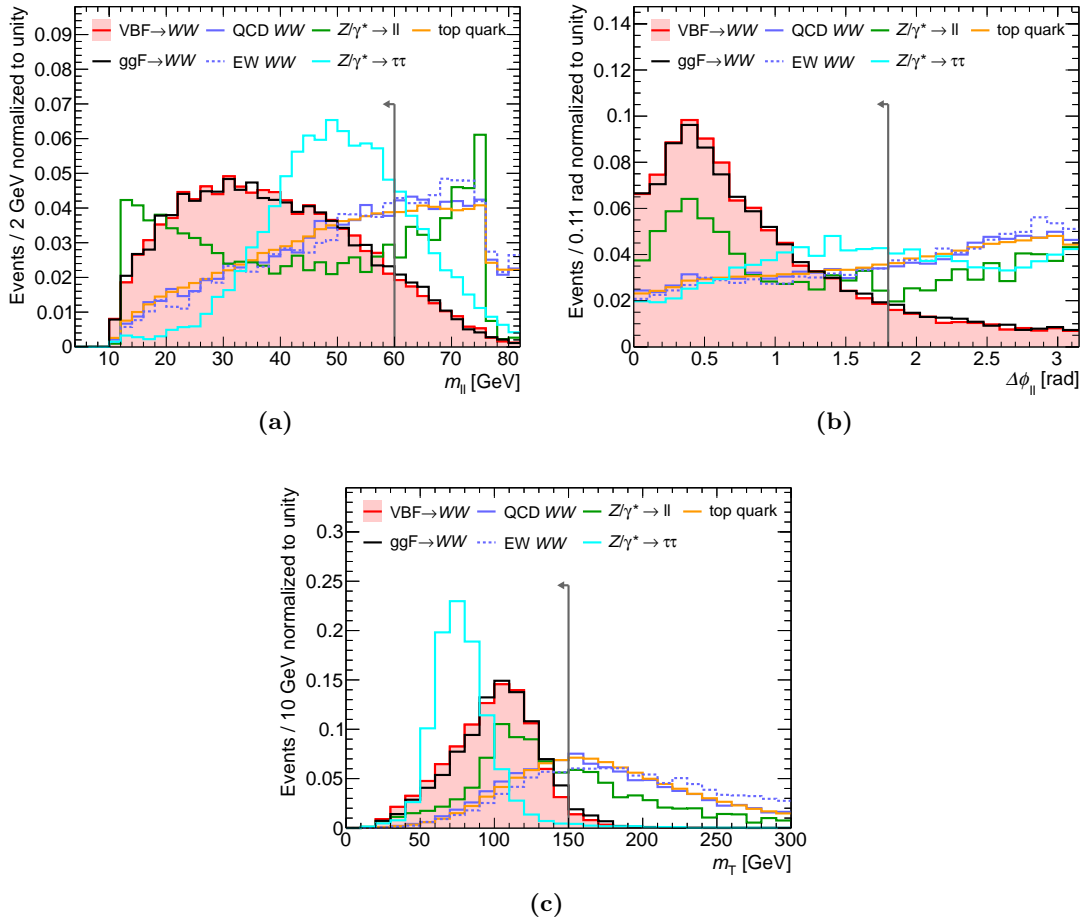
Figure 5.13: Expected distributions of (a) the dilepton invariant mass $m_{\ell\ell}$, (b) the dilepton opening angle $\Delta\phi(\ell\ell)$ and (c) the transverse mass m_T for signal and background processes after the preselection and the Z rejection criteria combining different-flavor and same-flavor events. The $m_{\ell\ell}$-distributions are sculpted by the requirements $m_{\ell\ell} > 12(10)\,\text{GeV}$ for same(different)-flavor events and $|m_{\ell\ell} - m_Z| < 15\,\text{GeV}$ for same-flavor events. The vertical lines indicate the selection criteria.
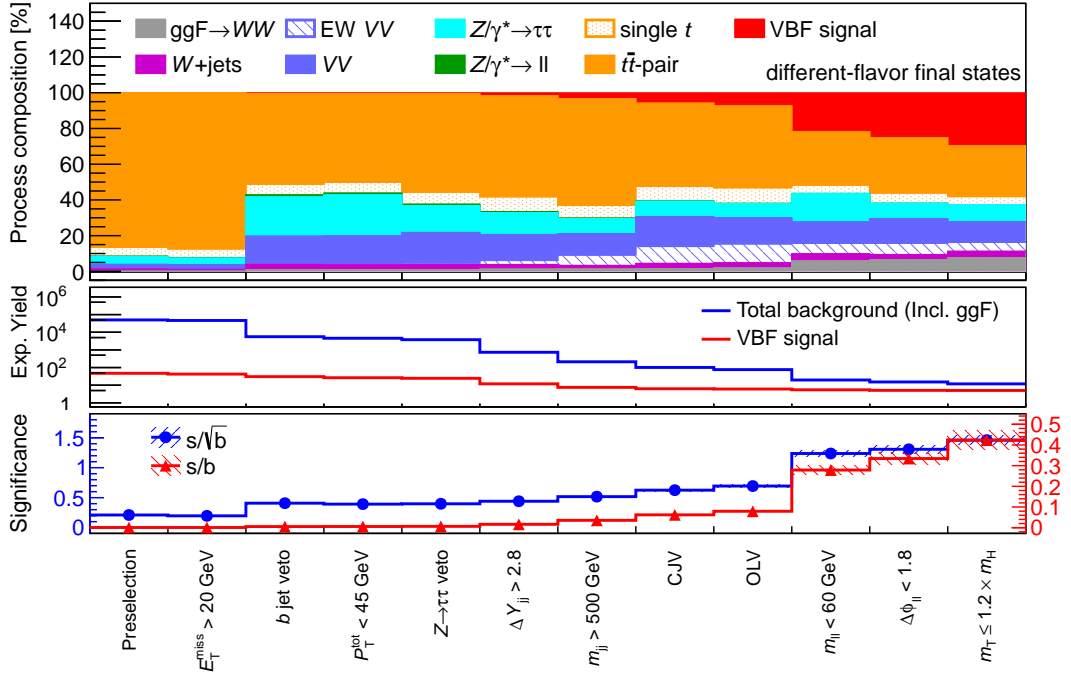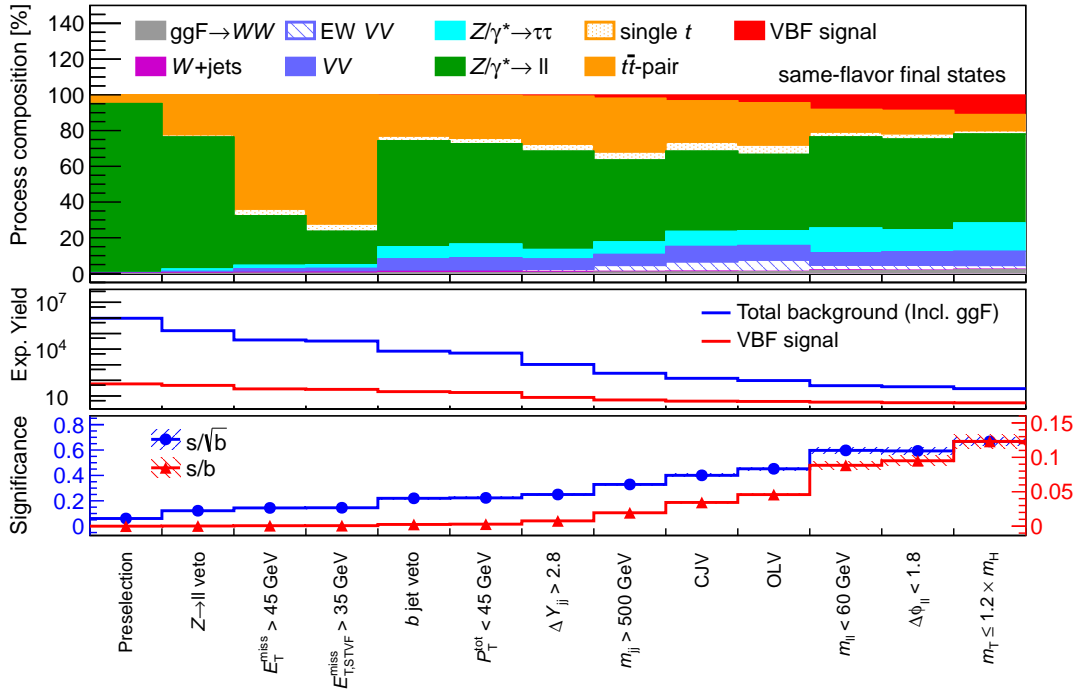
Figure 5.14: Expected signal and background yields and relative contribution for (a) different-flavor and (b) same-flavor final states for an integrated luminosity of 21 fb^{-1} after each selection requirement together with the expected signal-to-background ratio s/b and the signal significance $s/\sqrt{b}$, where s and b denote the expected signal and background yields, respectively. The shaded areas indicate the statistical uncertainty.

the background yields are given in Appendix B.

Where possible, the background contributions are estimated using control datasets for the final results rather than relying on the calculated cross sections and the Monte-Carlo simulation. The next section describes the selection criteria for determining the background contributions from data resulting in correction factors applied to the theoretically predicted cross sections.

5.4 Background Determination from Data

Due to the poor Higgs boson mass resolution in $H \to WW^{(*)} \to \ell\nu\ell\nu$ decays, the discrimination power between signal and background by means of the transverse mass distribution (see Fig. 5.13c) is limited. The shape of the total background distribution, essential for the statistical interpretation of the data, depends on the relative contributions of the individual background processes. Simulation-based predictions of the background normalizations have large theoretical and detector-based systematic uncertainties. These can be reduced by auxiliary measurements of the background yields using signal-depleted control datasets. For most background processes the measurement of the yield is extrapolated from the control (CR) to the signal region (SR) of the discriminating variable space based on the predictions from simulation. Uncertainties arising from this extrapolation are usually smaller than the uncertainties of the purely Monte-Carlo based predictions.

Selection criteria defining control regions are chosen to be orthogonal to the signal selection such that the signal and the control data sample are distinct. This is achieved by inverting one or more signal selection criteria. At the same time, event kinematics like the distributions of lepton and jet properties in the control region should be similar to those in the signal region, in order to minimize the uncertainty of the extrapolation of the measured yields to the signal region. The control regions are defined such that they contain only small contributions from signal and from other contaminating backgrounds. The number of selected events in the control region must be large enough to allow for a sufficiently low statistical uncertainty of the auxiliary measurement.

Comparison of data and predictions from simulation in a given control region is used

to derive a correction factor:

$$\alpha_i = \frac{\text{Number of observed events in } i\text{-CR}}{\text{Number of simulated events of process } i \text{ in } i\text{-CR}} \quad . \tag{5.2}$$

The normalization of the background i in the signal region is corrected by multiplying with α_i. The determination of the correction factors for the QCD $Z/\gamma^* \to \ell\ell$, top quark and QCD $Z/\gamma^* \to \tau\tau$ background is explained in Sections 5.4.2, 5.4.3 and 5.4.4, respectively. The control data sample is used to fully replace the simulation in the case of W+jets processes as described in Section 5.4.1.

Some of the control regions are contaminated by other background processes. The contamination is determined from simulation and, wherever possible, corrected using auxiliary measurements as for the signal region. The correction factors are denoted by $\beta_{\text{Bkg}}^{\text{CR}}$ where CR stands for the control region while Bkg denotes the contaminating background. Contributions from contaminating backgrounds are subtracted from the number of observed events in the control region, before α (Eq. (5.2)) is derived.

The diboson background estimate fully relies on simulation, due to the lack of a large enough control data sample free of top quark events. The EW Z/γ^* contribution is estimated by simulation as well. The Higgs boson production via gluon fusion is also considered as a background process and is within this section described by simulation assuming the Higgs boson mass of $125\,\text{GeV}$. For the final results, the number of events expected from the ggF processes is constrained using a dedicated dataset enhanced with ggF events as discussed in Section 5.6.3 (see also [91]). A schematic overview of the background estimation procedures used is given in Fig. 5.15. A summary of the background determinations is given in Section 5.4.5.

The correction factors for the top quark background are derived combining different-flavor and same-flavor events in the top quark control region to reduce the statistical uncertainty of the measurement. In case of the $Z/\gamma^* \to \tau\tau$ background, the correction factor is derived using only different-flavor events in the control region to reduce large contaminations from the $Z/\gamma^* \to \ell\ell$ process. The correction is applied to both different-flavor and same-flavor contributions in the signal region. The $Z/\gamma^* \to \ell\ell$ background correction is solely derived from and applied to same-flavor events since no $Z/\gamma^* \to \ell\ell$ events are expected to pass the selection criteria for different-flavor final states. The W+jets control datasets give independent estimates for different-flavor and same-flavor W+jets contributions in the signal region.

W + jets control sample

Process	DF[%]	SF[%]
W+jets(est)	70	50
VBF(mc)	-	-
Z/γ^*(mc)	10	26
Top quark(mc)	10	17
Diboson(mc)	10	7
ggF(mc)	-	-

predicts W+jets background in all CR's

$Z/\gamma^* \to \ell\ell$ CRs (SF only)

Process	B[%]	C[%]	D[%]
$Z/\gamma^* \to \ell\ell$(mc)	95	95	94
VBF(mc)	-	0.3	-
W+jets(est)	-	0.6	-
Top quark(mc)	2	0.5	-
$Z/\gamma^* \to \tau\tau$(mc)	-	0.9	-
Diboson(mc)	1	0.2	-
EW Z/γ^*(mc)	2	2.4	6
ggF(mc)	-	0.1	-

Top quark CR (DF+SF)

Process	[%]
Top quark(mc)	90.9
VBF(mc)	0.8
W+jets(est)	0.1
$Z/\gamma^* \to \ell\ell$(est)	2.9
$Z/\gamma^* \to \tau\tau$(est)	0.9
Diboson(mc)	3.5
EW Z/γ^*(mc)	0.7
ggF(mc)	0.2

$Z/\gamma^* \to \tau\tau$ CR (DF only)

Process	[%]
$Z/\gamma^* \to \tau\tau$(mc)	64
VBF(mc)	0.3
W+jets(est)	4.1
$Z/\gamma^* \to \ell\ell$(mc)	1.8
Top quark(est)	22
Diboson(mc)	7
EW Z/γ^*(mc)	0.3
ggF(mc)	0.5

Signal region

Process	DF[%]	SF[%]
VBF(mc)	29	10
W+jets(est)	3.4	0.2
$Z/\gamma^* \to \ell\ell$(est)	0.0	50
Top quark(est)	25.4	10.8
$Z/\gamma^* \to \tau\tau$(est)	8.3	11.7
Diboson(mc)	23.4	11.8
EW Z/γ^*(mc)	2.5	3.6
ggF(mc)	8	1.9

direct measurement

$\beta^{\text{top quark CR}}_{Z/\gamma^* \to \tau\tau}$ $\beta^{\text{top quark CR}}_{Z/\gamma^* \to \ell\ell}$ $\beta^{Z/\gamma^* \to \tau\tau \text{ CR}}_{\text{top quark}}$

$\alpha_{Z/\gamma^* \to \ell\ell}$ $\alpha_{\text{top quark}}$ $\alpha_{Z/\gamma^* \to \tau\tau}$

Figure 5.15: Overview of the procedures (see text) used for the estimation of background contributions in the signal region and in the control regions (CR). Purely Monte-Carlo-based predictions are indicated by "(mc)", predictions employing auxiliary control measurements by "(est)". SF and DF denote same-flavor and different-flavor final states. The B, C, and D regions are employed by the ABCD-method (see Section 5.4.2). The fractions of events from the signal and background processes in the different regions are given after correction factors have been applied. The fractions in the signal region are given without requirement on m_{T}. Contributions smaller than 0.05% are neglected ("-").

5.4.1 Measurement of the W+jets and Multijet Background

The production of W bosons in association with jets is a rather small background in the presented analysis. After the full signal selection (before the requirement on m_{T}) it contributes with 3% and 0.2% to the total background in different-flavor and same-flavor final states, respectively. Multijet processes are expected to contribute significantly less. The contribution of the two backgrounds has to be estimated from data, since it is not possible to simulate a sufficient number of events that pass the full signal selection. For both final states, signal-like events are caused by jets misidentified as electrons or jets containing a muon. Such leptons are in the following referred to as *fake leptons*. While any jet matching with an Inner Detector track is a possible fake electron, fake muons arise mainly from heavy flavor decays.

The contribution of backgrounds with fake leptons is estimated from a control data sample referred to as W+jets control sample. This sample contains events with one lepton passing the full lepton selection as summarized in Table 5.2 and a second lepton, called the *anti-identified* lepton, which fails at least one of those requirements and instead passes a looser set of selection criteria. The modified criteria defining anti-identified leptons are summarized in Table 5.3.

Table 5.3: Summary of selection criteria which differ for identified and anti-identified leptons

	Identified	**Anti-identified**
Electron selection	$E_{\mathrm{T,PU\ corr}}^{\mathrm{topo,cone30}}/p_{\mathrm{T}} < 0.16$ Passes tight quality criteria	$E_{\mathrm{T,PU\ corr}}^{\mathrm{topo,cone30}}/p_{\mathrm{T}} < 0.3$ Fails medium quality criteria
Muon selection	$E_{\mathrm{T,PU\ corr}}^{\mathrm{cone30}}/p_{\mathrm{T}} < \min[0.014\,p_{\mathrm{T}} - 0.15, 0.20]$ $d_0/\sigma(d_0) < 3.0$	$E_{\mathrm{T,PU\ corr}}^{\mathrm{cone30}}/p_{\mathrm{T}} < 0.3$ No requirement on $d_0/\sigma(d_0)$

For both muons and electrons the calorimeter isolation requirement is looser for the anti-identified lepton increasing the probability of accepting jets. The anti-identified electrons are required to fail the medium electron quality requirements. Fake muons predominantly arise from heavy flavor decays. Due to the long lifetimes of bottom and charm hadrons, large transverse impact parameters are expected for the final state muons. Thus the requirement on the transverse impact parameter is not applied for anti-identified muons.
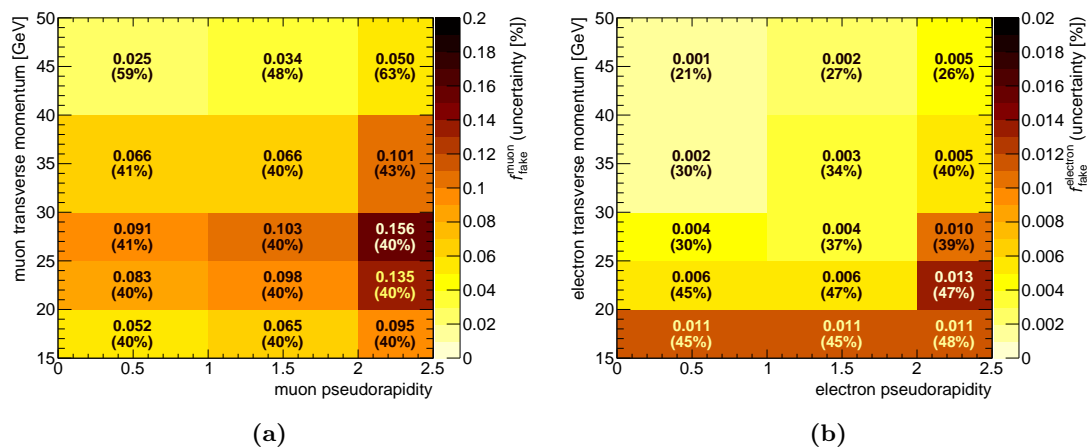
Figure 5.16: Fake factor f_{fake} for (a) muons and (b) electrons as a function of lepton transverse momentum and pseudorapidity. The numbers in brackets indicate the relative systematic uncertainty.

To correctly predict the normalization of the W+jets background in the signal region, each event is weighted depending on the lepton p_{T} and η by the *fake factor*

$$f_{\text{fake}}(\eta, p_{\text{T}}) = \frac{N_{\text{id}}(\eta, p_{\text{T}})}{N_{\text{anti-id}}(\eta, p_{\text{T}})} \quad , \tag{5.3}$$

where N_{id} is the number of reconstructed objects (predominantly jets) passing the full lepton selection and $N_{\text{anti-id}}$ the number of reconstructed objects passing the anti-identified lepton selection. The fake factors, measured separately for electrons and muons using a dedicated dijet data sample (see [91]) are shown in Fig. 5.16 as a function of the lepton transverse momentum and pseudorapidity.

The total systematic uncertainty in the fake factor ranges between 20–50% for electrons and between 40–60% for muons. This uncertainty arises mainly from differences in the jet kinematics and the flavor composition of the W+jets and dijet samples causing differences in the fake factor derived from the two. The differences are determined using Monte-Carlo simulation. The uncertainty in the muon fake factor is larger due to the greater impact of the flavor composition since fake muons predominantly originate from heavy flavor decays. Additional uncertainty arises from changing pile-up conditions during LHC operation and due to contamination of the dijet control sample with real leptons from W and Z boson decays.

The multijet background, predominantly dijet events, is estimated to contribute with less than 5% to the W+jets control sample. It contributes to the signal region if there are two fakes leptons rather than just one. The expected number of multijet events in the signal region is therefore

$$N_{\text{multijet}}^{\text{SR,exp}} = f_{\text{fake}}^2 \times N_{\text{multijet}}^{\text{anti-id+anti-id}} \quad , \tag{5.4}$$

where $N_{\text{multijet}}^{\text{anti-id+anti-id}}$ is the total number of multijet events in which two jets pass the criteria of the anti-identified lepton selection. The contribution of multijet events to the W+jets control region is however

$$N_{\text{multijet}}^{\text{CR,exp}} = 2 \times f_{\text{fake}} \times N_{\text{multijet}}^{\text{anti-id+anti-id}} \quad , \tag{5.5}$$

where the factor two arises from the fact that either of the two jets in a dijet event can be misidentified as a lepton. The extrapolation from the W+jets control to the signal region by multiplying with the fake factor then leads to an estimated number of multijet events in the signal region:

$$N_{\text{multijet}}^{\text{SR,est}} = N_{\text{multijet}}^{\text{CR,exp}} \times f_{\text{fake}} \tag{5.6}$$

$$= 2 \times f_{\text{fake}}^2 \times N_{\text{multijet}}^{\text{anti-id+anti-id}} \tag{5.7}$$

$$= 2 \times N_{\text{multijet}}^{\text{SR,exp}} \quad . \tag{5.8}$$

The multijet background, therefore, is double counted when extrapolated from the W+jets control region to the signal region. However, since the contribution of the multijet background is very small, this is acceptable within the uncertainty of the background estimate.

The observed number $N^{\text{CR,obs}}$ of different-flavor and same-flavor events in the W+jets data samples is shown in Table 5.4 together with the estimated number $N_{W+\text{jets}}^{\text{SR,est}}$ of W+jets events in the signal region at sequential stages of the signal selection. The estimate is derived by weighting each event in the W+jets control region by the corresponding fake factor and subtracting the contribution $N_{\text{non-}W+\text{jets}}^{\text{CR,est}}$ of non-W+jets backgrounds predicted from simulation (see Table 5.4). The contribution of non-W+jets processes to the total number of selected events ranges from 20–30% for different-flavor and from 30–50% for same-flavor final states. The W+jets data sample, hence, is highly

Table 5.4: Number $N^{\text{CR,obs}}$ of different-flavor and same-flavor events in the W+jets control data sample after the different selection requirements together with the estimated number $N^{\text{SR,est}}_{W+\text{jets}}$ of W+jets events in the signal region obtained by event-by-event weighting with the fake factor f_{fake}. The numbers $N^{\text{CR,exp}}_{\text{non-}W+\text{jets}}$ of non-W+jets background events in the W+jets control region, obtained from simulation, are subtracted. The errors are due to the control region data sample and Monte-Carlo statistics.

		$N^{\text{CR,obs}}$	$N^{\text{CR,exp}}_{\text{non-}W+\text{jets}}$	$N^{\text{SR,est}}_{W+\text{jets}}$
Different-flavor final states	Preselection	55364	17241 ± 230	537 ± 8
	$E_{\text{T}}^{\text{miss}} > 20\,\text{GeV}$	46985	14868 ± 192	444 ± 8
	b-jet veto	21044	4522 ± 160	171 ± 5
	$p_{\text{T}}^{\text{tot}} < 45\,\text{GeV}$	14406	3184 ± 131	126 ± 4
	$Z \to \tau\tau$ veto	12420	2657 ± 124	108 ± 4
	$\Delta Y_{\text{jj}} > 2.8$	2255	561 ± 67	19 ± 2
	$m_{\text{jj}} > 500\,\text{GeV}$	501	121 ± 6	4.4 ± 0.7
	Central jet veto	282	62 ± 4	3.1 ± 0.6
	Outside lepton veto	221	46 ± 4	2.4 ± 0.5
	$m_{\ell\ell} < 60\,\text{GeV}$	66	17 ± 3	1.0 ± 0.4
	$\Delta\phi(\ell\ell) < 1.8$	47	14 ± 2	0.6 ± 0.3
	$m_{\text{T}} \leq 1.2 \cdot m_H$	43	12 ± 2	0.6 ± 0.3
Same-flavor final states	Preselection	172070	105086 ± 1225	1032 ± 55
	$Z \to \ell\ell$ veto	67456	29521 ± 454	555 ± 22
	$E_{\text{T}}^{\text{miss}} > 45\,\text{GeV}$	23618	9117 ± 150	203 ± 9
	$E_{\text{T,STVF}}^{\text{miss}} > 35\,\text{GeV}$	21146	7964 ± 122	191 ± 7
	b-jet veto	8107	1998 ± 102	58 ± 4
	$p_{\text{T}}^{\text{tot}} < 45\,\text{GeV}$	5064	1385 ± 92	43 ± 3
	$\Delta Y_{\text{jj}} > 2.8$	876	300 ± 79	6 ± 1
	$m_{\text{jj}} > 500\,\text{GeV}$	222	80 ± 4.2	1.4 ± 0.6
	Central jet veto	118	39 ± 2.8	0.7 ± 0.4
	Outside lepton veto	82	31 ± 2.5	0.3 ± 0.3
	$m_{\ell\ell} < 60\,\text{GeV}$	37	18 ± 2.1	0.1 ± 0.2
	$\Delta\phi(\ell\ell) < 1.8$	29	14 ± 1.9	0.1 ± 0.2
	$m_{\text{T}} \leq 1.2 \cdot m_H$	26	12 ± 1.8	0.1 ± 0.2

contaminated by background mainly from top quark, diboson and Z/γ^* events. The latter background is particularly important for same-flavor final states (see Fig. 5.15).

The weighted W+jets control sample replaces the Monte-Carlo simulation as estimate of the W+jets and multijet background processes. This estimate is used for the signal region and for all control regions described below so that the analysis does not rely on W+jets and multijet simulation.

5.4.2 Measurement of the $Z/\gamma^* \to \ell\ell$ Background

Due to its large cross section, $Z/\gamma^* \to \ell\ell$ production is the dominant background for same-flavor final states even though it is suppressed by more than four orders of magnitude by the signal selection criteria. Since no neutrinos are present in $Z/\gamma^* \to \ell\ell$ decays, large missing transverse energy as required in the signal selection can only be caused by detector resolution or pile-up effects. Especially the latter are not well modelled by the Monte-Carlo simulation.

Also, the dilepton invariant mass distribution is not expected to be well described by the simulation, in particular for low mass values in the signal region. This is due to the $m_{\ell\ell}$-dependence of higher-order corrections to the Z/γ^* cross section [154] not taken into account in the scaling of the NLO predictions to the total NNLO cross sections.

In addition, the properties of the two tagging jets are difficult to model by Monte-Carlo simulation, since the jets are produced through higher-order QCD processes for the QCD Z/γ^* background, which is the bulk of the Z/γ^* background. In contrast, the EW Z/γ^* background contributes at leading-order making the predictions more reliable. The EW Z/γ^* background, therefore, is estimated by simulation.

A control data sample for same-flavor final states enriched with $Z/\gamma^* \to \ell\ell$ events can be selected by

- requiring $|m_{\ell\ell} - m_Z| < 15\,\mathrm{GeV}$ or

- by applying inverted signal selection cuts $E_\mathrm{T}^\mathrm{miss} < 45\,\mathrm{GeV}$ and $E_\mathrm{T,STVF}^\mathrm{miss} < 35\,\mathrm{GeV}$.

A discrepancy between data and simulation can be seen in both cases. Figure 5.17a and b show the distributions of $E_\mathrm{T}^\mathrm{miss}$ and $E_\mathrm{T,STVF}^\mathrm{miss}$, respectively, after the preselection and the requirement $|m_{\ell\ell} - m_Z| < 15\,\mathrm{GeV}$. The difference between data and simulation is larger for $E_\mathrm{T}^\mathrm{miss}$ than for $E_\mathrm{T,STVF}^\mathrm{miss}$, and originates mainly from deficiencies in the

(a)

(b)

(c)
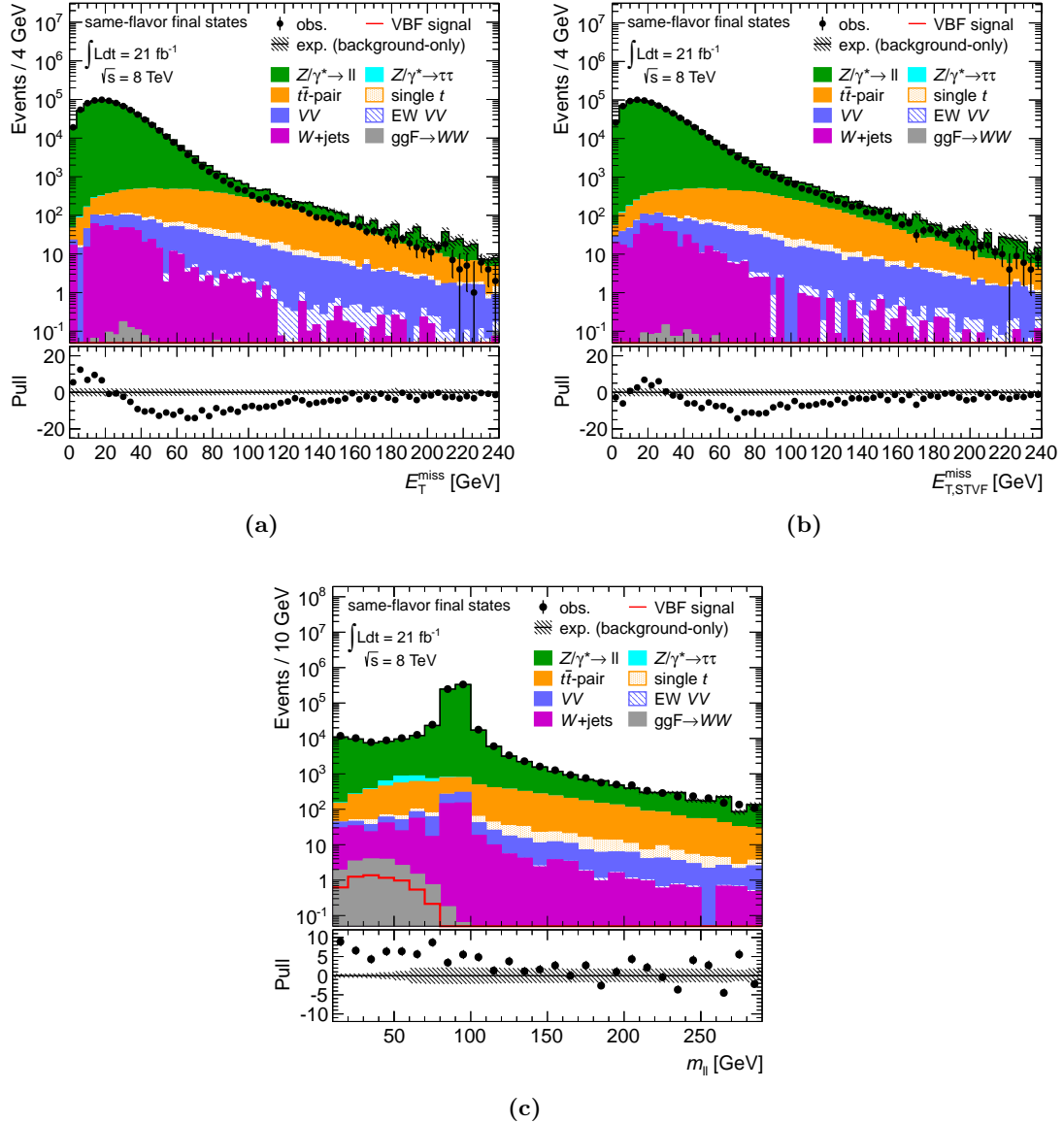
Figure 5.17: Expected and observed distributions of (a) E_T^{miss} and (b) $E_{T,STVF}^{miss}$ after the preselection and the requirement $|m_{\ell\ell} - m_Z| < 15$ GeV and of (c) $m_{\ell\ell}$ in the low-E_T^{miss} region for same-flavor events. The background contributions are stacked on top of each other. The expected signal is overlaid in red. The black hatched area represents the statistical uncertainty in the background prediction. The vertical error bars indicate the statistical uncertainty of the data.
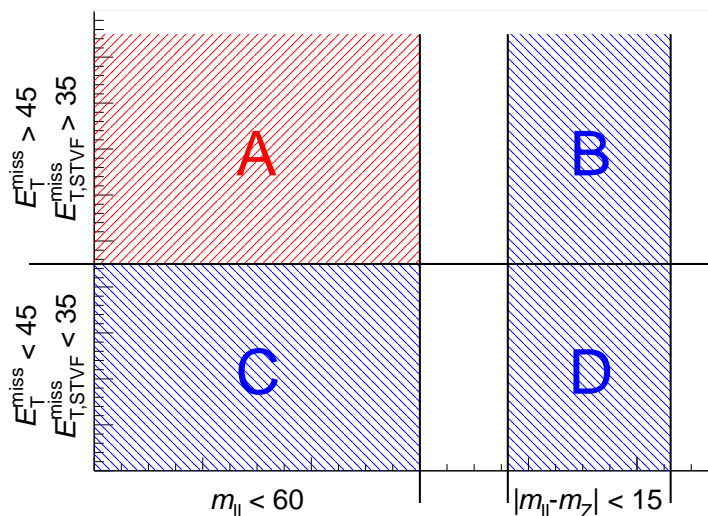
Figure 5.18: Definition of the signal-like region A and the background control regions B, C and D (cut values in GeV)

pile-up modelling. Fig. 5.17c shows the dilepton invariant mass distribution in the low-E_T^{miss} region, i.e. after the requirements $E_T^{\text{miss}} < 45\,\text{GeV}$ and $E_{T,\text{STVF}}^{\text{miss}} < 35\,\text{GeV}$. The disagreement between data and simulation is greatest for low dilepton invariant masses.

By combining the constraints on the dilepton invariant mass and the missing transverse energy, three control regions B, C and D illustrated in Fig. 5.18 are defined to predict the $Z/\gamma^* \to \ell\ell$ background contribution in the signal-like region A, using the so called *ABCD-method*. In the signal-like region A, the requirements in $m_{\ell\ell}$, E_T^{miss} and $E_{T,\text{STVF}}^{\text{miss}}$ are as in the signal-region, while in the B, C and D region at least one requirement is inverted. Events in each of the four regions are required to satisfy the preselection criteria as well as the b-jet veto, to reject top quark background, and the requirements on p_T^{tot} and m_{jj}, which are applied in order to obtain in region A events with kinematic properties as similar as possible to those in the real signal region.

Other signal selection criteria are not applied in the above control regions to minimize the statistical uncertainty in the ABCD estimate. The cuts in the discriminating variables m_{jj} and p_T^{tot} are applied because these variables show the largest correlation with the missing transverse energy as shown in Fig. 5.19a and b. The remaining discriminating variables used in the signal selection, such as ΔY_{jj} shown in Fig. 5.19c, show smaller correlations with the missing transverse energy and are corrected for in a separate step.
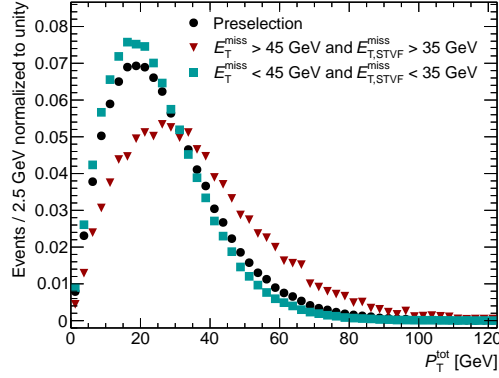
(a)
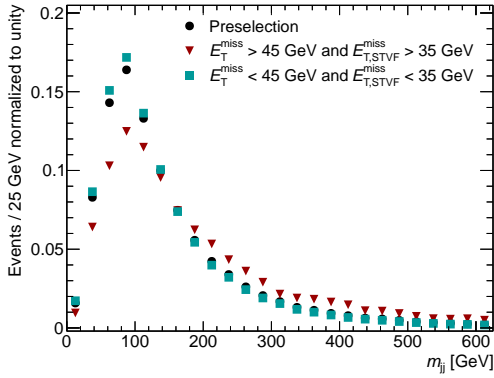
(b)
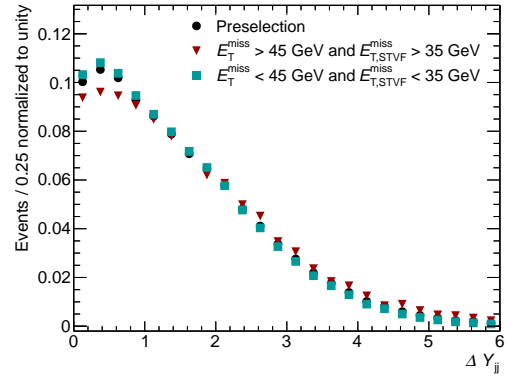
(c)

**Figure 5.19:** Simulated distributions of (a) the total transverse momentum p_T^{tot}, (b) the dijet invariant mass m_{jj} and (c) the dijet rapidity gap of same-flavor $Z/\gamma^* \to \ell\ell$ events for different requirements on the missing transverse energy applied in addition to the preselection.

The number $N^{A,est}_{Z/\gamma^* \to \ell\ell(QCD)}$ of QCD $Z/\gamma^* \to \ell\ell$ events in the signal-like region A is estimated from the numbers $N^{i,obs}_{Z/\gamma^* \to \ell\ell(QCD)}$ of observed QCD $Z/\gamma^* \to \ell\ell$ events in the regions $i = $ B, C, D

$$N^{A,est}_{Z/\gamma^* \to \ell\ell(QCD)} = N^{B,obs}_{Z/\gamma^* \to \ell\ell(QCD)} \cdot \frac{N^{C,obs}_{Z/\gamma^* \to \ell\ell(QCD)}}{N^{D,obs}_{Z/\gamma^* \to \ell\ell(QCD)}} \cdot f_{correlation} \quad , \tag{5.9}$$

where $N^{i,obs}_{Z/\gamma^* \to \ell\ell(QCD)}$ is obtained by subtracting the expected contaminations as given in Table 5.5 from the total number of observed events $N^{i,obs}$ in each region i. The factor $f_{correlation}$ accounts for correlation between the $m_{\ell\ell}$ and E^{miss}_T variables and is derived from the simulation:

$$f_{correlation} = \frac{N^{A,exp}_{Z/\gamma^* \to \ell\ell(QCD)} \cdot N^{D,exp}_{Z/\gamma^* \to \ell\ell(QCD)}}{N^{B,exp}_{Z/\gamma^* \to \ell\ell(QCD)} \cdot N^{C,exp}_{Z/\gamma^* \to \ell\ell(QCD)}} = 1.03 \pm 0.10 \text{ (stat.)} \quad . \tag{5.10}$$

According to the simulation, there are no significant correlations between E^{miss}_T and $m_{\ell\ell}$. Effects of possible correlations in data due to $m_{\ell\ell}$ and missing transverse energy mis-measurements are taken into account in the systematic errors (see Section 5.5).

Table 5.5 shows the expected and observed yields in the B, C and D control regions as well as in the signal-like region A. The largest contamination of 2–6% of the expected events arises from EW $Z/\gamma^* \to \ell\ell$ production ($N^{i,exp}_{Z/\gamma^* \to \ell\ell(EW)}$). Diboson, top quark, W+jets and $Z/\gamma^* \to \tau\tau$ processes ($N^{i,exp}_{non\text{-}Z/\gamma^* \to \ell\ell}$) also contribute. Nevertheless, the three control regions contain to about 95% events of QCD $Z/\gamma^* \to \ell\ell$ processes.

The contribution of the QCD $Z/\gamma^* \to \ell\ell$ background in the final signal region (SR) is obtained by multiplying the expected number of $Z/\gamma^* \to \ell\ell$ events in the signal region from simulation with the correction factor

$$\alpha^{ABCD}_{Z/\gamma^* \to \ell\ell} = \frac{N^{A,est}_{Z/\gamma^* \to \ell\ell(QCD)}}{N^{A,exp}_{Z/\gamma^* \to \ell\ell(QCD)}} = 0.81 \pm 0.06 \text{ (stat.)} \quad , \tag{5.11}$$

the ratio of the QCD $Z/\gamma^* \to \ell\ell$ yield $N^{A,est}_{Z/\gamma^* \to \ell\ell(QCD)}$ estimated by the ABCD-method and the expected yield $N^{A,exp}_{Z/\gamma^* \to \ell\ell(QCD)}$ in region A from simulation, which is about 20% higher compared to the estimate.

Table 5.5: Expected and observed same-flavor event yields $N^{i,\mathrm{exp}}$ and $N^{i,\mathrm{obs}}$ in the B, C and D control regions as well as in the signal-like region A as defined in Fig. 5.18. The errors are due to the control region data sample and Monte-Carlo statistics.

	B region	C region	D region	A region (signal-like)
$N^{i,\mathrm{obs}}$	1246	957	12786	168
$N^{i,\mathrm{exp}}_{Z/\gamma^* \to \ell\ell(\mathrm{EW})}$	34.7 ± 0.8	18.2 ± 0.6	689 ± 4	0.7 ± 0.1
$N^{i,\mathrm{exp}}_{\mathrm{non}\text{-}Z/\gamma^* \to \ell\ell}$	53 ± 3	18 ± 2	20 ± 5	61 ± 3
$N^{i,\mathrm{exp}}_{\mathrm{Higgs}}$	0.13 ± 0.08	2.6 ± 0.1	0.05 ± 0.01	7.2 ± 0.2
$N^{i,\mathrm{exp}}_{Z/\gamma^* \to \ell\ell(\mathrm{QCD})}$	1525 ± 74	740 ± 18	10347 ± 206	112 ± 9
$N^{i,\mathrm{obs}}_{Z/\gamma^* \to \ell\ell(\mathrm{QCD})}$	1158 ± 35	921 ± 31	12077 ± 113	107 ± 13

As mentioned before, several signal selection criteria are omitted for the selection of the regions A, B, C and D in order to determine $\alpha^{\mathrm{ABCD}}_{Z/\gamma^* \to \ell\ell}$ with sufficient statistical precision. However, some of the discriminating variables of omitted cuts are difficult to model in the simulation, in particular the variables used for the VBF selection: $\Delta Y_{\mathrm{jj}} > 2.8$, central jet veto (CJV) and the outside lepton veto (OLV). In Fig. 5.20, disagreement between the expected and observed dijet distributions can be seen. While disagreements due to the requirement on m_{jj} are already accounted for by the ABCD correction factor, an additional correction is necessary for mis-modelling of the other discriminating variables using a correction factor

$$\alpha^{\mathrm{VBF}}_{Z/\gamma^* \to \ell\ell} = \frac{\epsilon^{\mathrm{obs}}_{Z/\gamma^* \to \ell\ell(\mathrm{QCD})}}{\epsilon^{\mathrm{exp}}_{Z/\gamma^* \to \ell\ell(\mathrm{QCD})}} = 1.10 \pm 0.02 \; (\mathrm{stat.}) \tag{5.12}$$

for the expected and observed selection efficiencies

$$\epsilon^{\mathrm{obs/exp}}_{Z/\gamma^* \to \ell\ell(\mathrm{QCD})} = \frac{N^{\mathrm{obs/exp}}_{Z/\gamma^* \to \ell\ell(\mathrm{QCD})}(\text{before VBF requirements})}{N^{\mathrm{obs/exp}}_{Z/\gamma^* \to \ell\ell(\mathrm{QCD})}(\text{after VBF requirements})} \tag{5.13}$$

of the residual VBF requirements. $N^{\mathrm{obs/exp}}_{Z/\gamma^* \to \ell\ell(\mathrm{QCD})}$ are the numbers of events in the

Table 5.6: Expected and observed same-flavor event yields before and after applying the VBF selection criteria $\Delta Y_{\mathrm{jj}} > 2.8$, the central jet veto and the outside lepton veto in the low-$E_{\mathrm{T}}^{\mathrm{miss}}$ region, in addition to the ABCD selection described in the text. The errors are due to the control region data sample and Monte-Carlo statistics.

| | Low-$E_{\mathrm{T}}^{\mathrm{miss}}$ region + ABCD selection | |
	Before VBF requirements	After VBF requirements
N^{obs}	14778	5307
$N_{Z/\gamma^* \to \ell\ell(\mathrm{EW})}^{\mathrm{exp}}$	777 ± 4	497 ± 3
$N_{\mathrm{non}\text{-}Z/\gamma^* \to \ell\ell}^{\mathrm{exp}}$	63 ± 6	29 ± 3
$N_{\mathrm{Higgs}}^{\mathrm{exp}}$	3.0 ± 0.1	2.2 ± 0.1
$N_{Z/\gamma^* \to \ell\ell(\mathrm{QCD})}^{\mathrm{exp}}$	11865 ± 21	3709 ± 124
$N_{Z/\gamma^* \to \ell\ell(\mathrm{QCD})}^{\mathrm{obs}}$	13938 ± 122	4782 ± 73

low-$E_{\mathrm{T}}^{\mathrm{miss}}$ region ($E_{\mathrm{T,(STVF)}}^{\mathrm{miss}} < 45(35)\,\mathrm{GeV})^*$ including the ABCD selection (b-jet veto, $p_{\mathrm{T}}^{\mathrm{tot}} < 45\,\mathrm{GeV}$ and $m_{\mathrm{jj}} > 500\,\mathrm{GeV}$) shown in Table 5.6. To obtain the observed number $N_{Z/\gamma^* \to \ell\ell(\mathrm{QCD})}^{\mathrm{obs}}$ of QCD $Z/\gamma^* \to \ell\ell$ events the contributions from the EW $Z/\gamma^* \to \ell\ell$ background and other non-$Z/\gamma^* \to \ell\ell$ backgrounds are subtracted from the total number of observed events.

The correction factor $\alpha_{Z/\gamma^* \to \ell\ell}^{\mathrm{VBF}}$ together with $\alpha_{Z/\gamma^* \to \ell\ell}^{\mathrm{ABCD}}$ gives the final QCD $Z/\gamma^* \to \ell\ell$ correction factor of

$$\alpha_{Z/\gamma^* \to \ell\ell} = \alpha_{Z/\gamma^* \to \ell\ell}^{\mathrm{ABCD}} \cdot \alpha_{Z/\gamma^* \to \ell\ell}^{\mathrm{VBF}} = 0.89 \pm 0.07 \text{ (stat.)}. \tag{5.14}$$

Splitting the correction factor $\alpha_{Z/\gamma^* \to \ell\ell}$ into two separate factors $\alpha_{Z/\gamma^* \to \ell\ell}^{\mathrm{ABCD}}$ and $\alpha_{Z/\gamma^* \to \ell\ell}^{\mathrm{VBF}}$ is not optimal, but necessary to reduce the statistical error. Implications of the factorization have been investigated by replacing the requirements on m_{jj} and $p_{\mathrm{T}}^{\mathrm{tot}}$ in the ABCD-method one-by-one with the requirements on ΔY_{jj}, the central jet veto and the outside lepton veto and monitoring the change in the correction factor $\alpha_{Z/\gamma^* \to \ell\ell}$. No significant changes have been found.

---

*The region $|m_{\ell\ell} - m_Z| < 15\,\mathrm{GeV}$ is not used for the efficiency determination because the dijet kinematical properties in $Z/\gamma^* \to \ell\ell$ processes are correlated with the dilepton invariant mass.
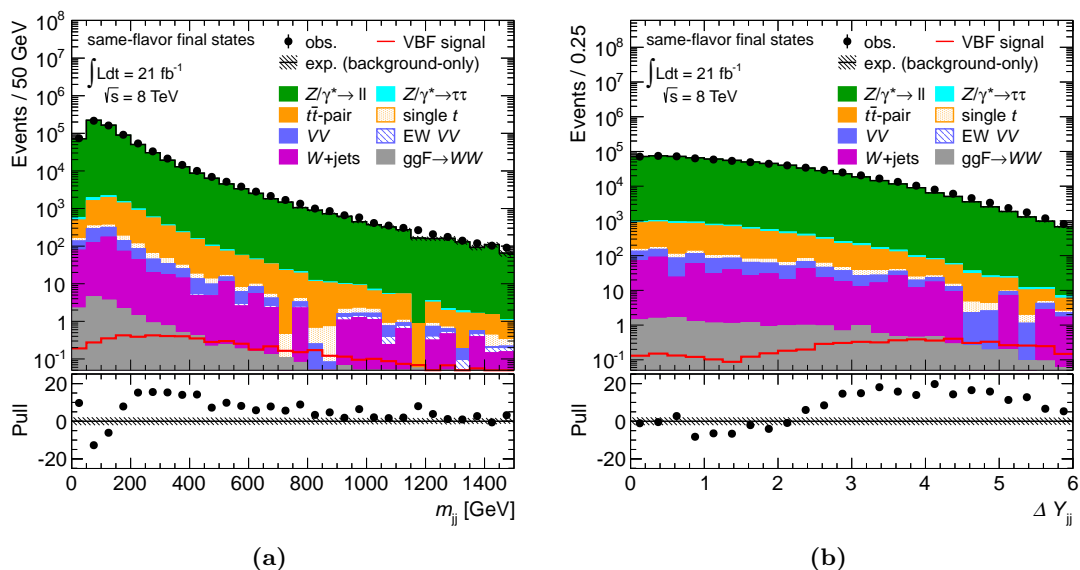
Figure 5.20: Expected and observed distributions of (a) m_{jj} and (b) ΔY_{jj} for same-flavor events in the low-E_T^{miss} region. The black hatched area represents the statistical uncertainty in the background prediction. The vertical error bars indicate the statistical uncertainty of the data.

The procedure described above does not take into account the signal selection criteria for the dilepton opening angle $\Delta\phi(\ell\ell)$ and the transverse mass m_T. The measurement relies on a good description of those variables by the simulation. Figure 5.21 shows the distributions of the two variables after the preselection, the Z rejection criteria and the b-jet veto. The expected signal contribution at this selection stage is still very small ($< 0.5\%$) and $Z/\gamma^* \to \ell\ell$ production is dominating the background. The correction factor $\alpha_{Z/\gamma^*\to\ell\ell}^{ABCD}$ is applied to the $Z/\gamma^* \to \ell\ell$ background normalization. Except for an insignificant disagreement in the low-m_T range, the agreement between the expected and observed distributions is good.

5.4.3 Measurement of the Top Quark Background

The signal selection reduces the top quark contribution ($t\bar{t}$ and single top quark processes) by four orders of magnitude. Nevertheless, top quark production, with 25% (11%) for different-flavor (same-flavor) final states, is one of the largest background contributions after the full signal selection. The kinematical properties of events passing the selection,
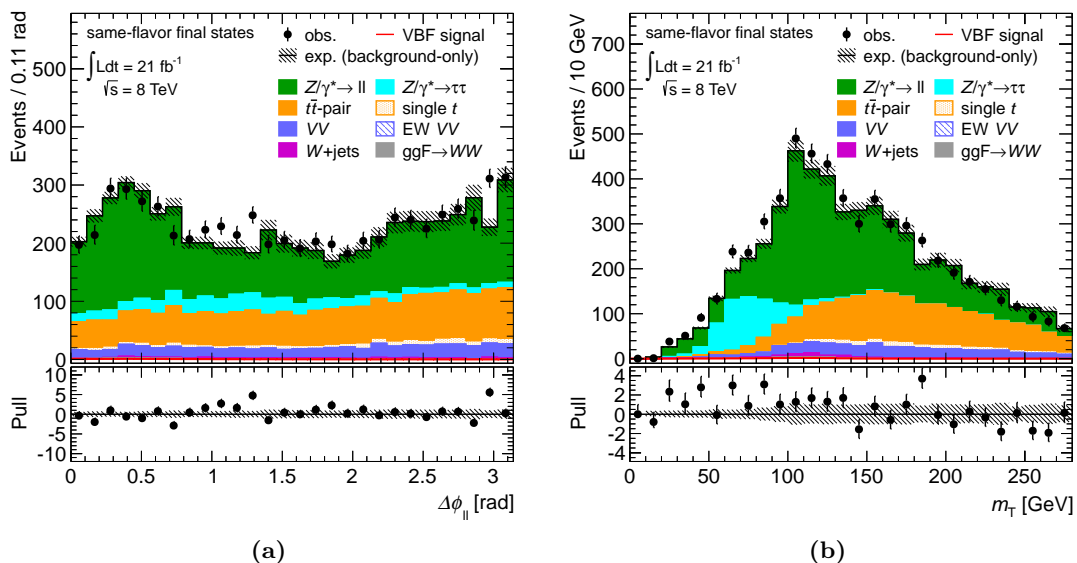
Figure 5.21: Expected and observed distributions of (a) $\Delta\phi(\ell\ell)$ and (b) m_T for same-flavor events after the preselection, the Z rejection criteria and the b-jet veto. The correction factors $\alpha^\text{ABCD}_{Z/\gamma^*\to\ell\ell}$ and $\alpha_\text{top quark}$ (see Section 5.4.3) are applied to the normalization of the $Z/\gamma^*\to\ell\ell$ and the top quark background, respectively. The black hatched area represents the statistical uncertainty in the background prediction. The vertical error bars indicate the statistical uncertainty of the data.

hence, are rather atypical for top quark production processes. The modelling of such events by the Monte-Carlo generators may therefore be unreliable.

A top quark control region is built by inverting the b-jet veto. To keep the kinematics closer to the signal region, *exactly* one identified b-jet is required ($N_{b\text{-jet}} = 1$) rather than requiring *at least* one b-jet ($N_{b\text{-jet}} \geq 1$), for the following reasons:

- Identification of b-jets is possible only in the pseudorapidity range covered by the Inner Detector ($|\eta| < 2.5$). The b-jet veto ($N_{b\text{-jet}} = 0$), therefore, mainly rejects events with jets in the central detector region introducing even a bump in the jet η distribution at about $|\eta| = 2.5$ as shown in Fig. 5.22. In contrast, the requirements of exactly one or at least one b-jet select events with jets in the central region. In this respect, requiring exactly one b-jet is closer to the signal region, since a larger fraction of events with forward jets, in particular subleading forward jets, is retained (see Fig. 5.22b).
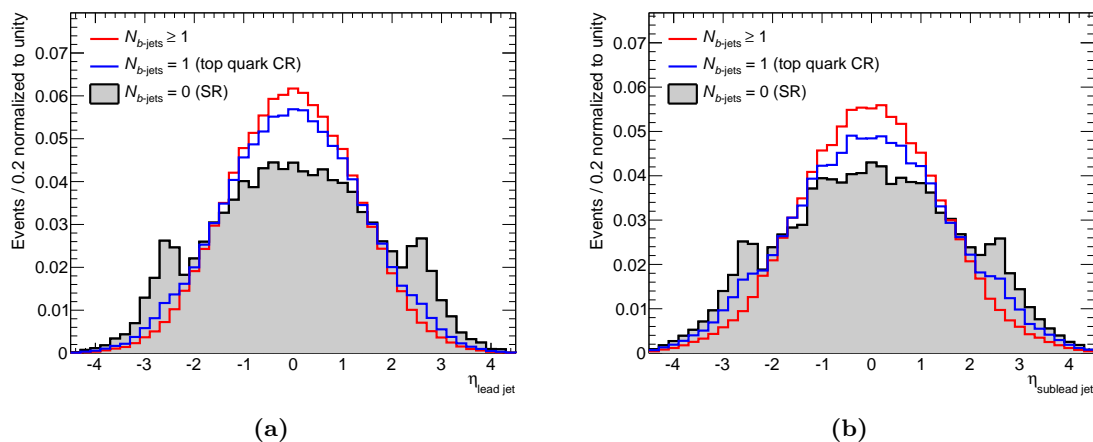
Figure 5.22: Pseudorapidity distribution of simulated top quark events for (a) leading and (b) subleading jets after the preselection and the Z rejection criteria. Different requirements on the b-jet multiplicity $N_{b\text{-jet}}$ are compared. $N_{b\text{-jet}} = 0$ corresponds to the b-jet veto applied in the signal region. Same-flavor and different-flavor events are combined.

- The generator-level flavor composition of the jets in the signal region is better reproduced by the requirement $N_{b\text{-jet}} = 1$ as illustrated in Table 5.7. Table 5.7a shows the fractions of simulated $t\bar{t}$ events with zero, one or two reconstructed jets associated with a generated b quark for different stages of the signal selection. The sample is dominated by events with one jet originating from a b quark while the second jet results from higher-order QCD processes (e.g. ISR/FSR). This is even more pronounced after the VBF selection. Table 5.7b shows the event fractions after the OLV for different requirements on the b-jet multiplicity. The ratio of the event fractions with two and one reconstructed jet originating from a b quark in the signal-like region is closer to the value for $N_{b\text{-jet}} = 1$ than for $N_{b\text{-jet}} \geq 1$.

As can be seen in Table 5.7b, a non-negligible fraction of the expected $t\bar{t}$ background surviving the signal selection are events where both jets originate from higher-order processes, such as ISR or FSR, and not from the leading-order process $tt \rightarrow WbWb \rightarrow \ell\nu b\ell\nu b$. While one extra jet is still described by the the next-to-leading order matrix element calculation of the generator MC@NLO, the properties of the second jet are determined by the parton shower model which is not reliable in particular for high-p_T jets. This has to be taken into account when comparing the top quark background measured in data with the predictions of the simulation.

Table 5.7: Fraction of simulated $t\bar{t}$ events with zero, one or two reconstructed jets associated to a generated b quark (a) for different stages of the signal selection and (b) for different requirements on $N_{b\text{-jet}}$ after all requirements up to the OLV. $N_{b\text{-jet}} = 0$ corresponds to the signal region (SR) and $N_{b\text{-jet}} = 1$ to the top quark control region. The errors are due to Monte-Carlo statistics.

$N_{\text{jets from } b \text{ quarks}}$	0 [%]	1 [%]	2 [%]
b-jet veto	19 ± 0	54 ± 0	27 ± 0
$p_{\text{T}}^{\text{tot}} < 45\,\text{GeV}$	17 ± 0	53 ± 0	30 ± 0
$Z \to \tau\tau$ veto	17 ± 0	53 ± 0	30 ± 0
$\Delta Y_{\text{jj}} > 2.8$	23 ± 1	60 ± 1	16 ± 1
$m_{\text{jj}} > 500\,\text{GeV}$	33 ± 2	62 ± 2	6 ± 1
Central jet veto	28 ± 2	66 ± 2	7 ± 1
Outside lepton veto	30 ± 2	63 ± 2	7 ± 1

(a)

$N_{\text{jets from } b \text{ quarks}}$	0 [%]	1 [%]	2 [%]	$\frac{2 \text{ jets}}{1 \text{ jets}}$
$N_{b\text{-jet}} = 0$ (SR)	30 ± 2	63 ± 2	7 ± 1	0.11
$N_{b\text{-jet}} = 1$ (top quark CR)	2 ± 1	84 ± 1	14 ± 1	0.16
$N_{b\text{-jet}} \geq 1$	2 ± 1	78 ± 1	20 ± 1	0.25

(b)

The criteria defining the top quark control region include the signal selection criteria up to and including the VBF selection, except for the b-jet veto which is replaced by the requirement $N_{b\text{-jet}} = 1$. The topological signal selection requirements ($m_{\ell\ell} < 60\,\text{GeV}$, $\Delta\phi(\ell\ell) < 1.8$, $m_{\text{T}} < 1.2 \cdot m_H$) are not applied to retain sufficient statistics. In top quark events no differences are expected between same-flavor and different-flavor final states. Therefore, the statistical uncertainty can be reduced by combining the two final states. This is possible also because the additional $Z/\gamma^* \to \ell\ell$ background contribution to same-flavor final states is small after requiring $N_{b\text{-jet}} = 1$.

The expected and observed event yields after the successive selection requirements are shown in Fig. 5.23. The top quark control sample is rather pure with over 90% top quark events. Single top quark and $t\bar{t}$ production cannot be distinguished in data and the ratio of the two is estimated using simulation. The fraction of single top quark events is, however, expected to be only 15% of all top quark events. The final top quark
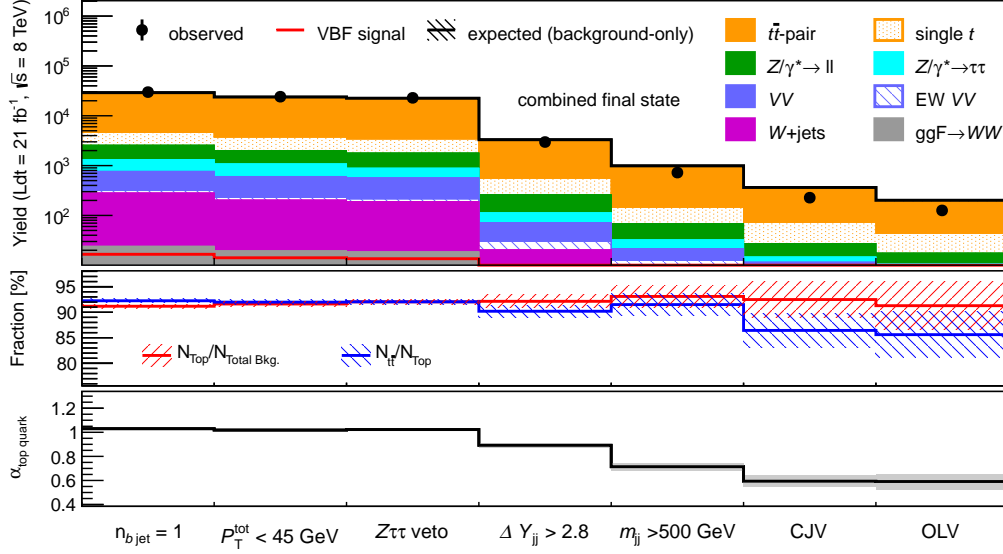
Figure 5.23: Expected and observed event yields for combined different-flavor and same-flavor final states depending on the stage of the top quark control region selection. The statistical uncertainty in the background prediction (black hatched area) is invisible on this scale. The statistical errors of the data are smaller than the data points. The middle panel shows the top quark event purity and the $t\bar{t}$ event fraction in the control region and the bottom panel the measured correction factor $\alpha_{\text{top quark}}$.

control region after the OLV is contaminated with 4% diboson, 3% $Z/\gamma^* \to \ell\ell$ and 1% $Z/\gamma^* \to \tau\tau$ background. While the first contribution is estimated from simulation, the other two are estimated from dedicated data, as described below.

The expectation for the QCD $Z/\gamma^* \to \ell\ell$ contribution in the top quark control region is corrected in a similar way as in the signal region. However, the ABCD-method described in the previous section cannot be used, since the requirement $m_{\ell\ell} < 60\,\text{GeV}$ is not applied for the top quark control region. Instead, the correction factor $\beta_{Z/\gamma^* \to \ell\ell}^{\text{top quark CR}}(E_{\text{T}}^{\text{miss}})$ for the normalization of the QCD $Z/\gamma^* \to \ell\ell$ background in the top quark control region is obtained from the data sample satisfying $|m_{\ell\ell} - m_Z| < 15\,\text{GeV}$:

$$\beta_{Z/\gamma^* \to \ell\ell}^{\text{top quark CR}}(E_{\text{T}}^{\text{miss}}) = \frac{r_{Z/\gamma^* \to \ell\ell(\text{QCD})}^{\text{obs}}(E_{\text{T}}^{\text{miss}})}{r_{Z/\gamma^* \to \ell\ell(\text{QCD})}^{\text{exp}}(E_{\text{T}}^{\text{miss}})} \tag{5.15}$$

$$= 0.77 \pm 0.01 \text{ (stat.)}, \tag{5.16}$$

Table 5.8: Expected and observed same-flavor event yields N^{exp} and N^{obs} after the additional requirement $|m_{\ell\ell} - m_Z| < 15\,\mathrm{GeV}$ for the signal-like and the inverted missing transverse energy cuts. The errors are due to the control region data sample and Monte-Carlo statistics.

	Preselection + $|m_{\ell\ell} - m_Z| < 15\,\mathrm{GeV}$	
	$E_{\mathrm{T(,STVF)}}^{\mathrm{miss}} > 45(35)\,\mathrm{GeV}$ (Signal-like)	$E_{\mathrm{T(,STVF)}}^{\mathrm{miss}} < 45(35)\,\mathrm{GeV}$ (Inverted)
N^{obs}	40988	607760
$N_{\text{non-}Z/\gamma^* \to \ell\ell}^{\mathrm{exp}}$	7639 ± 32	2156 ± 48
$N_{Z/\gamma^* \to \ell\ell(\mathrm{EW})}^{\mathrm{exp}}$	204 ± 2	2912 ± 8
$N_{\mathrm{Higgs}}^{\mathrm{exp}}$	5.0 ± 0.5	4.8 ± 0.5
$N_{Z/\gamma^* \to \ell\ell(\mathrm{QCD})}^{\mathrm{exp}}$	42845 ± 422	596518 ± 1670
$N_{Z/\gamma^* \to \ell\ell(\mathrm{QCD})}^{\mathrm{obs}}$	33145 ± 205	602692 ± 781

with

$$r^{\mathrm{obs/exp}}(E_{\mathrm{T}}^{\mathrm{miss}}) = \frac{N_{Z/\gamma^* \to \ell\ell(\mathrm{QCD})}^{\mathrm{obs/exp}}(E_{\mathrm{T(,STVF)}}^{\mathrm{miss}} > 45(35)\,\mathrm{GeV})}{N_{Z/\gamma^* \to \ell\ell(\mathrm{QCD})}^{\mathrm{obs/exp}}(E_{\mathrm{T(,STVF)}}^{\mathrm{miss}} < 45(35)\,\mathrm{GeV})} \tag{5.17}$$

where $r(E_{\mathrm{T}}^{\mathrm{miss}})$ is the ratio of the numbers $N_{Z/\gamma^* \to \ell\ell(\mathrm{QCD})}^{\mathrm{obs/exp}}$ of QCD $Z/\gamma^* \to \ell\ell$ events after applying signal-like ($E_{\mathrm{T(,STVF)}}^{\mathrm{miss}} > 45(35)\,\mathrm{GeV}$) and inverted ($E_{\mathrm{T(,STVF)}}^{\mathrm{miss}} < 45(35)\,\mathrm{GeV}$) missing transverse energy requirements. Again, non-$Z/\gamma^* \to \ell\ell$ contributions and the EW $Z/\gamma^* \to \ell\ell$ background expectation are subtracted from the observed numbers of events before $r_{Z/\gamma^* \to \ell\ell(\mathrm{QCD})}^{\mathrm{obs}}$ is calculated. The numbers of expected and observed events in the two missing transverse energy regions are shown in Table 5.8.

The above measurement still needs a correction for the impact of additional VBF selection criteria. A further efficiency correction factor $\beta_{Z/\gamma^* \to \ell\ell}^{\mathrm{top\ quark\ CR}}(\mathrm{VBF})$ is determined in the low-$E_{\mathrm{T}}^{\mathrm{miss}}$ region with $E_{\mathrm{T(,STVF)}}^{\mathrm{miss}} < 45(35)\,\mathrm{GeV}$, and for $N_{b\text{-jet}} = 1$

$$\beta_{Z/\gamma^* \to \ell\ell}^{\mathrm{top\ quark\ CR}}(\mathrm{VBF}) = \frac{\epsilon_{Z/\gamma^* \to \ell\ell(\mathrm{QCD})}^{\mathrm{obs}}}{\epsilon_{Z/\gamma^* \to \ell\ell(\mathrm{QCD})}^{\mathrm{exp}}} = 1.39 \pm 0.08\ (\mathrm{stat.}) \tag{5.18}$$

Table 5.9: Expected and observed same-flavor event yields in the low-$E_{\mathrm{T}}^{\mathrm{miss}}$ region with $N_{b\text{-jet}} = 1$ before and after the top quark control region requirements. The errors are due to the control region data sample and Monte-Carlo statistics.

| | Low-$E_{\mathrm{T}}^{\mathrm{miss}}$ region + $N_{b\text{-jet}} = 1$ | |
	Before top quark CR req.	After top quark CR req.
N^{obs}	168984	866
$N_{Z/\gamma^* \to \ell\ell(\mathrm{EW})}^{\mathrm{exp}}$	930 ± 5	133 ± 2
$N_{\text{non-}Z/\gamma^* \to \ell\ell}^{\mathrm{exp}}$	3147 ± 31	16 ± 4
$N_{\mathrm{Higgs}}^{\mathrm{exp}}$	8.7 ± 0.5	0.38 ± 0.04
$N_{Z/\gamma^* \to \ell\ell(\mathrm{QCD})}^{\mathrm{exp}}$	156523 ± 889	490 ± 48
$N_{Z/\gamma^* \to \ell\ell(\mathrm{QCD})}^{\mathrm{obs}}$	164908 ± 412	717 ± 30

with the top quark control region selection efficiency

$$
\epsilon_{Z/\gamma^* \to \ell\ell(\mathrm{QCD})}^{\mathrm{obs/exp}} = \frac{N_{Z/\gamma^* \to \ell\ell(\mathrm{QCD})}^{\mathrm{obs/exp}}(\text{after top quark CR requirements})}{N_{Z/\gamma^* \to \ell\ell(\mathrm{QCD})}^{\mathrm{obs/exp}}(\text{before top quark CR requirements})} \quad , \quad (5.19)
$$

where the top quark CR requirements are all signal selection requirements applied in the top quark control region*. The expected and observed event yields in the low-$E_{\mathrm{T}}^{\mathrm{miss}}$ region before and after the top quark control region requirements are shown in Table 5.9. The non-$Z/\gamma^* \to \ell\ell$ backgrounds and the significant contribution from the EW $Z/\gamma^* \to \ell\ell$ background are subtracted from the number of observed events before $\epsilon_{Z/\gamma^* \to \ell\ell(\mathrm{QCD})}^{\mathrm{obs}}$ is calculated. The final correction factor to the expected number of QCD $Z/\gamma^* \to \ell\ell$ same-flavor events in the top quark control region is

$$
\beta_{Z/\gamma^* \to \ell\ell}^{\text{top quark CR}} = \beta_{Z/\gamma^* \to \ell\ell}^{\text{top quark CR}}(E_{\mathrm{T}}^{\mathrm{miss}}) \cdot \beta_{Z/\gamma^* \to \ell\ell}^{\text{top quark CR}}(\text{VBF}) = 1.07 \pm 0.06 \text{ (stat.)} \quad (5.20)
$$

The small (1%) contribution of $Z/\gamma^* \to \tau\tau$ events in the top quark control region is corrected for mis-modelling of the dijet kinematics. The correction is derived in a similar

---

*The correction factor $\beta_{Z/\gamma^* \to \ell\ell}^{\text{top quark CR}}(\text{VBF})$ deviates more from unity than $\alpha_{Z/\gamma^* \to \ell\ell}^{\mathrm{VBF}}$ in Eq. (5.13) due to the m_{jj} requirement in the VBF selection criteria. In the case of the $\alpha_{Z/\gamma^* \to \ell\ell}^{\mathrm{VBF}}$ measurement, the m_{jj} requirement is applied in both the numerator and the denominator.

Table 5.10: Expected and observed event yields combined for different-flavor and same-flavor final states after the different stages of the top quark control region selection. The errors are due to the control region data sample and Monte-Carlo statistics.

	N^{obs}	$N^{\mathrm{exp}}_{\mathrm{Higgs}}$	$N^{\mathrm{exp}}_{\mathrm{non\text{-}top\ quark}}$	$N^{\mathrm{exp}}_{\mathrm{top\ quark}}$	$N^{\mathrm{obs}}_{\mathrm{top\ quark}}$
Exactly one b-jet	29837	40.6 ± 0.9	2540 ± 56	26478 ± 59	27297 ± 182
$p_{\mathrm{T}}^{\mathrm{tot}} < 45\,\mathrm{GeV}$	24124	33.6 ± 0.8	1970 ± 49	21732 ± 54	22154 ± 163
$Z \to \tau\tau$ veto	22880	32.1 ± 0.8	1767 ± 48	20628 ± 53	21113 ± 159
$\Delta Y_{\mathrm{jj}} > 2.8$	2973	8.5 ± 0.3	256 ± 19	3042 ± 20	2718 ± 58
$m_{\mathrm{jj}} > 500\,\mathrm{GeV}$	724	3.3 ± 0.1	67 ± 3	918 ± 11	657 ± 27
Central jet veto	227	2.2 ± 0.1	27 ± 2	336 ± 7	200 ± 15
Outside lepton veto	126	2.0 ± 0.1	17 ± 2	184 ± 5	109 ± 11

way as $\beta^{\mathrm{top\ quark\ CR}}_{Z/\gamma^* \to \ell\ell}(\mathrm{VBF})$ using same-flavor $Z/\gamma^* \to \ell\ell$ events. Since this correction is identical to the one applied to the QCD $Z/\gamma^* \to \tau\tau$ background contribution in the signal region, it is explained in detail in Section 5.4.4. The correction factor to the QCD $Z/\gamma^* \to \tau\tau$ event yield in the top quark control region is

$$\beta^{\mathrm{top\ quark\ CR}}_{Z/\gamma^* \to \tau\tau} = 1.20 \pm 0.02\ \mathrm{(stat.)} \quad . \tag{5.21}$$

The numbers of expected and observed events in the top quark control region after the individual selection requirements, including the above corrections on the Z/γ^* yields, are shown in Table 5.10.

The correction factor $\alpha_{\mathrm{top\ quark}}$ for the expected top quark background contribution in the signal region is determined from the numbers $N^{\mathrm{exp}}_{\mathrm{top\ quark}}$ and $N^{\mathrm{obs}}_{\mathrm{top\ quark}}$ of expected and observed events in the top quark control region, respectively, according to

$$\alpha_{\mathrm{top\ quark}} = \frac{N^{\mathrm{obs}}_{\mathrm{top\ quark}}}{N^{\mathrm{exp}}_{\mathrm{top\ quark}}} \tag{5.22}$$

with $N^{\mathrm{obs}}_{\mathrm{top\ quark}} = N^{\mathrm{obs}} - N^{\mathrm{exp}}_{\mathrm{non\text{-}top\ quark}}$. The result, after the outside lepton veto is

$$\alpha_{\mathrm{top\ quark}} = 0.59 \pm 0.06\ \mathrm{(stat.)} \quad . \tag{5.23}$$

As can be seen in Fig. 5.23, the correction factor deviates from unity after the VBF requirements. This is due to the rather poor modelling of the dijet kinematics by the MC@NLO generator as illustrated in Fig. 5.24. A systematic uncertainty of 15% in the
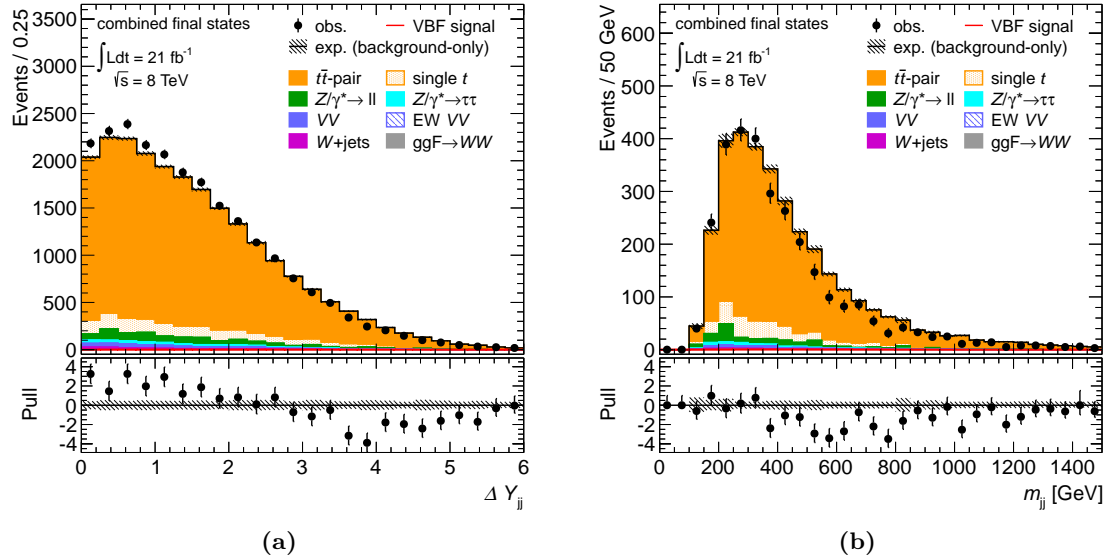
Figure 5.24: Expected and observed distributions of (a) ΔY_{jj} and (b) m_{jj} in the top quark control region combining both dilepton final states. The distributions are shown just before the corresponding cut on them is applied. The expected top quark yields are normalized to the observation to better show possible shape differences. The black hatched area represents the statistical uncertainty in the background prediction. The vertical error bars indicate the statistical uncertainty of the data.

extrapolation from the control to the signal region due to differences in the description of the dijet-system is derived by comparing different generators. The procedure is described in Appendix C.

The top quark background measurement relies on a good description of the topological variables $m_{\ell\ell}$, $\Delta\phi(\ell\ell)$ and m_{T} since they are not used in the selection of the top quark control region. Good agreement is found for the $m_{\ell\ell}$ and $\Delta\phi(\ell\ell)$ distributions (see Fig. 5.25) as well as for the m_{T}-distribution (see Fig. 5.26).

5.4.4 Measurement of the $Z/\gamma^* \to \tau\tau \to \ell\nu\ell\nu$ Background

In the same way as for the QCD $Z/\gamma^* \to \ell\ell$ background, two corrections have been derived for the QCD $Z/\gamma^* \to \tau\tau$ background. One accounts for the acceptance of $Z/\gamma^* \to \tau\tau$ events by a selection requiring at least two jets and the other one for dijet kinematics.
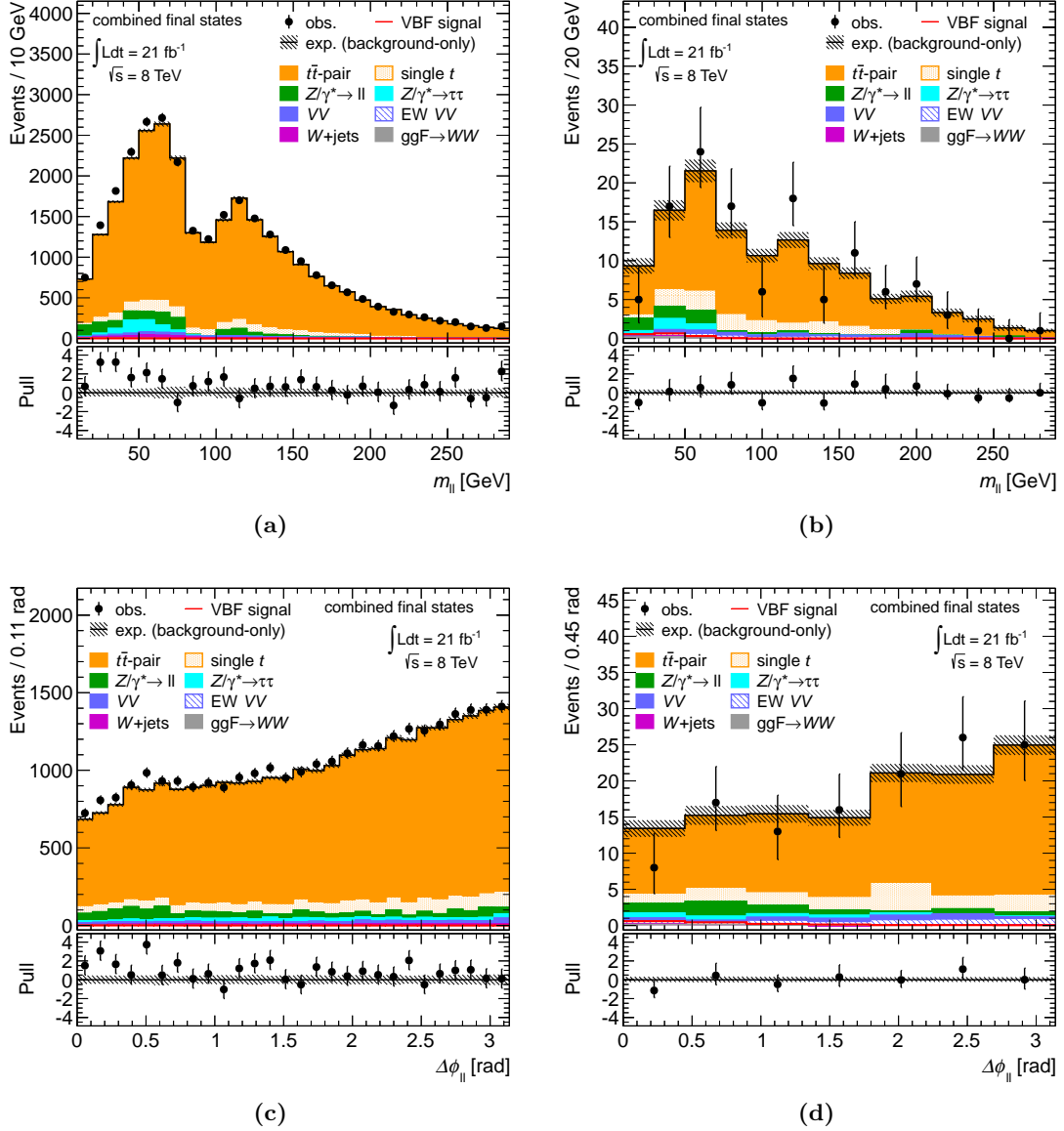
Figure 5.25: Expected and observed distributions of the dilepton invariant mass $m_{\ell\ell}$ and the dilepton opening angle $\Delta\phi(\ell\ell)$ at the beginning ((a) and (c)) and end ((b) and (d)) of the top quark control region requirements summed over all lepton final states. The expected top quark event yields are normalized to the data to better show possible shape differences. The black hatched area represents the statistical uncertainty in the background prediction. The vertical error bars indicate the statistical uncertainty of the data.
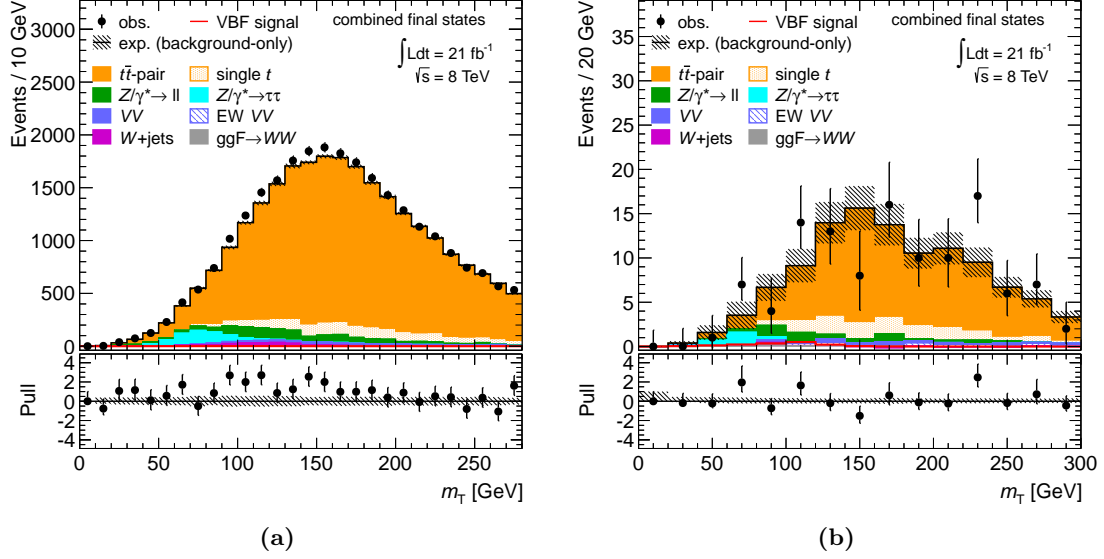
Figure 5.26: Expected and observed distributions of m_T at (a) the beginning and (b) the end of the top quark control region requirements summed over all lepton final states. The expected top quark event yields are normalized to the data to better show possible shape differences. The black hatched area represents the statistical uncertainty in the background prediction. The vertical error bars indicate the statistical uncertainty of the data.

For the first correction, a $Z/\gamma^* \to \tau\tau$ control region, enriched with $Z/\gamma^* \to \tau\tau \to \ell\nu\ell\nu$ events is defined by the following selection:

- Only different-flavor events are selected to avoid the contamination with $Z/\gamma^* \to \ell\ell$ events.

- The signal selection criteria up to the requirement $p_T^{tot} < 45 \, \text{GeV}$ are applied.

- The cut $m_{\ell\ell} < 80 \, \text{GeV}$ is chosen slightly looser than the one in the signal selection, to increase statistics.

- The requirement $\Delta\phi(\ell\ell) > 2.8$ on the dilepton opening angle is inverted, ensuring a control region selection orthogonal to the signal selection.

Remaining signal selection requirements are assumed to factorize similarly as for the measurement of the $Z/\gamma^* \to \ell\ell$ background.

The $m_{\ell\ell}$ and $\Delta\phi(\ell\ell)$ distributions after the p_T^{tot} cut in the signal selection are shown in Figs. 5.27a and b, respectively. The requirement of $m_{\ell\ell} < 80 \, \text{GeV}$ is used mainly to
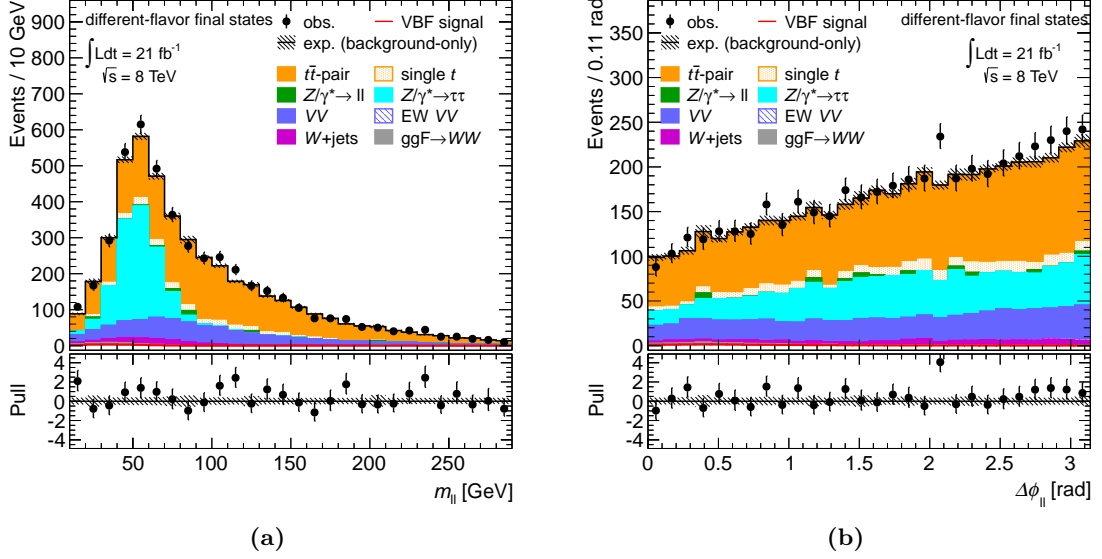
Figure 5.27: Expected and observed distributions of (a) the dilepton invariant mass $m_{\ell\ell}$ and (b) the dilepton opening angle $\Delta\phi(\ell\ell)$ in different-flavor events after the p_T^{tot} cut. The black hatched area represents the statistical uncertainty in the background prediction. The vertical error bars indicate the statistical uncertainty of the data.

suppress top quark background. After the full selection, the $Z/\gamma^* \to \tau\tau$ control region is contaminated with 22% top quark, 7% diboson, 4% W+jets and 2% $Z/\gamma^* \to \ell\ell$ background (see Fig. 5.15 and Table 5.11).

While the diboson and $Z/\gamma^* \to \ell\ell$ contributions are estimated from simulation, the W+jets background is estimated from data as described in Section 5.4.1. Also, the top quark contribution is corrected using a factor derived in the top quark control region where only the requirements up to the p_T^{tot} cut have been applied (see Fig. 5.23, second bin). This leads to a correction to the top quark contribution in the $Z/\gamma^* \to \tau\tau$ control region by the factor of

$$\beta_{\text{top quark}}^{Z/\gamma^* \to \tau\tau \text{ CR}} = 1.02 \pm 0.01 \text{ (stat.)} \quad . \tag{5.24}$$

Figure 5.28a shows the m_T-distribution in the $Z/\gamma^* \to \tau\tau$ control region. The total expected $Z/\gamma^* \to \tau\tau$ event yield and the shape of the m_T-distribution are well described. The correction factor to the expected $Z/\gamma^* \to \tau\tau$ background normalization

Table 5.11: Expected and observed different-flavor event yields in the $Z/\gamma^* \to \tau\tau$ control region. The errors are due to the control region data sample and Monte-Carlo statistics.

	$Z/\gamma^* \to \tau\tau$ control region
N^{obs}	212
$N^{\text{est}}_{\text{top quark}}$	49 ± 3
$N^{\text{exp}}_{\text{diboson}}$	16 ± 1
$N^{\text{est}}_{\text{W+jets}}$	9 ± 1
$N^{\text{exp}}_{Z/\gamma^* \to \ell\ell(\text{QCD})}$	4 ± 4
$N^{\text{exp}}_{Z/\gamma^*(\text{EW})}$	0.6 ± 0.1
$N^{\text{exp}}_{\text{Higgs}}$	1.7 ± 0.1
$N^{\text{exp}}_{Z/\gamma^* \to \tau\tau(\text{QCD})}$	143 ± 5
$N^{\text{obs}}_{Z/\gamma^* \to \tau\tau(\text{QCD})}$	133 ± 15

for same-flavor and different-flavor final states in the signal region is

$$\alpha^{\text{Acpt.}}_{Z/\gamma^* \to \tau\tau} = \frac{N^{\text{obs}}_{Z/\gamma^* \to \tau\tau(\text{QCD})}}{N^{\text{exp}}_{Z/\gamma^* \to \tau\tau(\text{QCD})}} = 0.93 \pm 0.11 \text{ (stat.)} \quad , \tag{5.25}$$

with $N^{\text{obs}}_{Z/\gamma^* \to \tau\tau(\text{QCD})} = N^{\text{obs}} - N^{\text{exp}}_{\text{non-}Z/\gamma^* \to \tau\tau \text{ (QCD)}}$.

The number of events and the purity in the $Z/\gamma^* \to \tau\tau$ control region, in particular in the far tails of the dijet kinematic distributions corresponding to the signal region selection (see Figs. 5.28b and c), is not sufficient to investigate also the impact of the residual signal selection requirements. To correct for mis-modelling of the remaining selection variables, same-flavor events passing the pre-selection and the requirement $|m_{\ell\ell} - m_Z| < 15 \, \text{GeV}$ are used. In addition the b-jet veto and the $p_{\text{T}}^{\text{tot}}$ cut are applied. This set of selection criteria is called $Z \to \ell\ell$ selection below. As for the $Z/\gamma^* \to \ell\ell$ background, the ratio of the observed and predicted VBF signal selection efficiencies

(a)

(b)

(c)
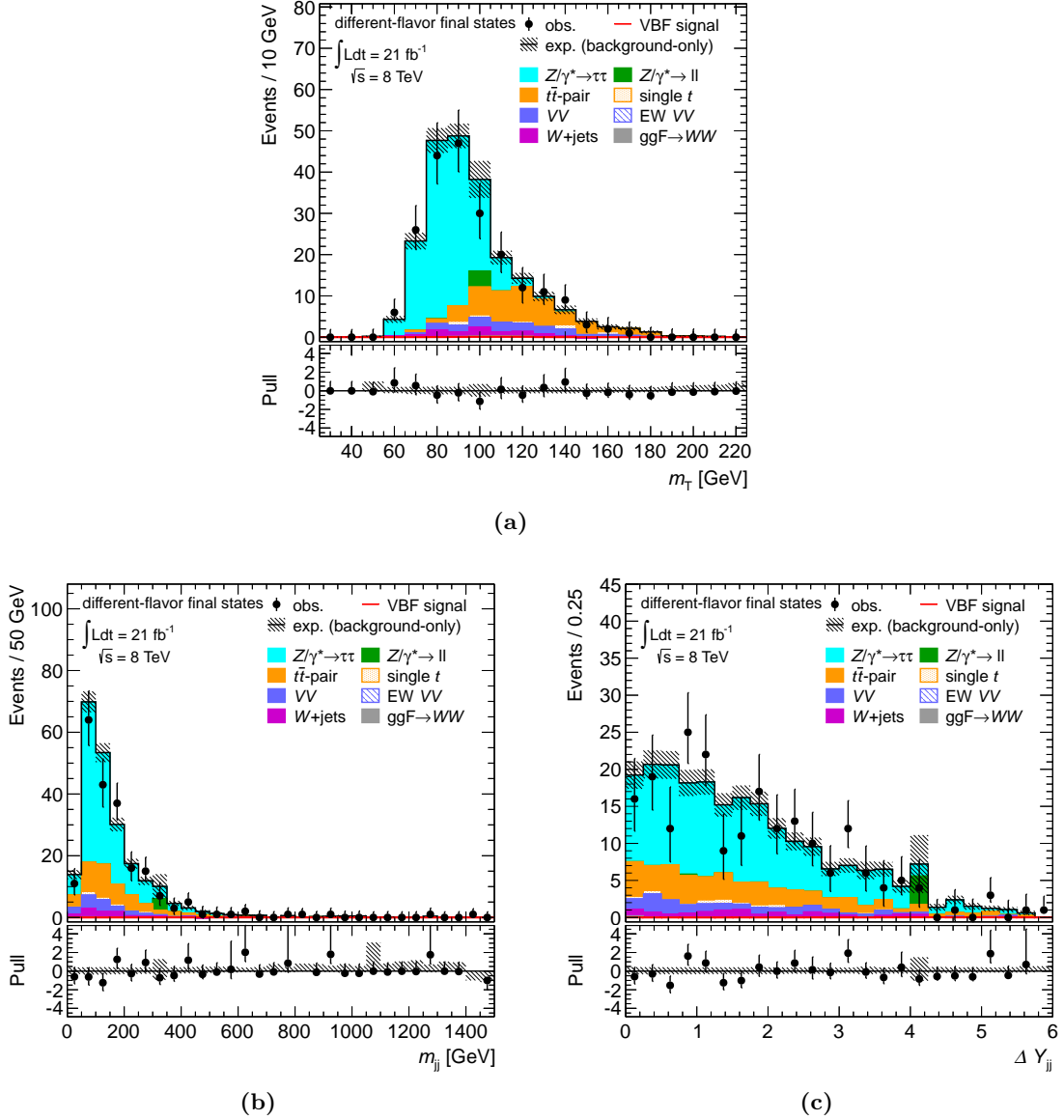
Figure 5.28: Expected and observed distributions of (a) the transverse mass m_T, (b) the dijet invariant mass m_{jj} and (c) the dijet rapidity gap ΔY_{jj} in the $Z/\gamma^* \to \tau\tau$ control region. The normalization of the top quark contribution is corrected. The black hatched area represents the statistical uncertainty in the background prediction. The vertical error bars indicate the statistical uncertainty of the data.

Table 5.12: Expected and observed same-flavor event yields before and after the VBF requirements in a region with $Z \to \ell\ell$ selection. The errors are due to the control region data sample and Monte-Carlo statistics.

| | $Z \to \ell\ell$ selection | |
	Before VBF requirements	After VBF requirements
N^{obs}	493230	6506
$N^{\mathrm{exp}}_{Z/\gamma^* \to \ell\ell(\mathrm{EW})}$	2199 ± 7	524 ± 3
$N^{\mathrm{exp}}_{\mathrm{non}\text{-}Z/\gamma^* \to \ell\ell}$	1599 ± 41	33 ± 5
$N^{\mathrm{exp}}_{\mathrm{Higgs}}$	6.4 ± 0.6	0.09 ± 0.01
$N^{\mathrm{exp}}_{Z/\gamma^* \to \ell\ell(\mathrm{QCD})}$	506378 ± 1497	5151 ± 148
$N^{\mathrm{obs}}_{Z/\gamma^* \to \ell\ell(\mathrm{QCD})}$	489432 ± 704	5949 ± 81

gives the correction factor

$$\alpha^{\mathrm{VBF}}_{Z/\gamma^* \to \tau\tau} = \frac{\epsilon^{\mathrm{obs}}_{Z/\gamma^* \to \ell\ell(\mathrm{QCD})}}{\epsilon^{\mathrm{exp}}_{Z/\gamma^* \to \ell\ell(\mathrm{QCD})}} = 1.20 \pm 0.02 \text{ (stat.) with} \tag{5.26}$$

$$\epsilon^{\mathrm{obs/exp}}_{Z/\gamma^* \to \ell\ell(\mathrm{QCD})} = \frac{N^{\mathrm{obs/exp}}_{Z/\gamma^* \to \ell\ell(\mathrm{QCD})}(\text{after VBF requirements})}{N^{\mathrm{obs/exp}}_{Z/\gamma^* \to \ell\ell(\mathrm{QCD})}(\text{before VBF requirements})} \quad . \tag{5.27}$$

As the jet production processes are identical for $Z/\gamma^* \to \tau\tau \to \ell\nu\ell\nu$ and $Z/\gamma^* \to \ell\ell$ events, it is justified to use same-flavor $Z/\gamma^* \to \ell\ell$ events, to determine the VBF selection efficiencies, rather than different-flavor $Z/\gamma^* \to \tau\tau$ events. In contrast to the $Z/\gamma^* \to \tau\tau$ control region, the $Z \to \ell\ell$ selection provides a pure and high-statistics control sample. The expected and observed event yields used to calculate the correction factor $\alpha^{\mathrm{VBF}}_{Z/\gamma^* \to \tau\tau}$ are shown in Table 5.12. As before, non-$Z/\gamma^* \to \ell\ell$ and EW $Z/\gamma^* \to \ell\ell$ backgrounds are subtracted from the number of observed events in the different regions to obtain $N^{\mathrm{obs}}_{Z/\gamma^* \to \ell\ell(\mathrm{QCD})}$. The correction factor $\alpha^{\mathrm{VBF}}_{Z/\gamma^* \to \tau\tau}$ is multiplied with the correction factor $\alpha^{\mathrm{Acpt.}}_{Z/\gamma^* \to \tau\tau}$ resulting in the final correction factor

$$\alpha_{Z/\gamma^* \to \tau\tau} = \alpha^{\mathrm{Acpt.}}_{Z/\gamma^* \to \tau\tau} \cdot \alpha^{\mathrm{VBF}}_{Z/\gamma^* \to \tau\tau} = 1.12 \pm 0.13 \text{ (stat.)} \tag{5.28}$$

Table 5.13: Summary of the correction factors for the background contributions in the signal region (SR) and in different control regions (CR). SF and DF denote same-flavor and different-flavor final states, which have been combined if they are not mentioned. The errors are due to the control region data sample and Monte-Carlo statistics.

Bkg	Derived in	Applied to	Symbol	Value
$Z/\gamma^* \to \ell\ell$	B,C,D region (SF)	SR (SF)	$\alpha_{Z/\gamma^* \to \ell\ell}$	0.89 ± 0.07
	B,C,D region (SF)	top quark CR (SF)	$\beta_{Z/\gamma^* \to \ell\ell}^{\text{top quark CR}}$	1.07 ± 0.06
t quark	top quark CR	SR	$\alpha_{\text{top quark}}$	0.59 ± 0.06
	top quark CR	$Z/\gamma^* \to \tau\tau$ CR	$\beta_{\text{top quark}}^{Z/\gamma^* \to \tau\tau \text{ CR}}$	1.02 ± 0.01
$Z/\gamma^* \to \tau\tau$	$Z/\gamma^* \to \tau\tau$ CR (DF) and B,C,D region (SF)	SR	$\alpha_{Z/\gamma^* \to \tau\tau}$	1.12 ± 0.13
	$Z \to \ell\ell$ CR (SF)	top quark CR	$\beta_{Z/\gamma^* \to \tau\tau}^{\text{top quark CR}}$	1.20 ± 0.02

for the different-flavor and same-flavor $Z/\gamma^* \to \tau\tau$ event yields in the signal region.

$\alpha_{Z/\gamma^* \to \tau\tau}^{\text{VBF}}$ is also used as correction factor $\beta_{Z/\gamma^* \to \tau\tau}^{\text{top quark CR}}$ applied to QCD $Z/\gamma^* \to \tau\tau$ events in the top quark control region:

$$\beta_{Z/\gamma^* \to \tau\tau}^{\text{top quark CR}} = \alpha_{Z/\gamma^* \to \tau\tau}^{\text{VBF}} = 1.20 \pm 0.02 \text{ (stat.)} \quad . \tag{5.29}$$

This is possible because the measurement of $\alpha_{Z/\gamma^* \to \tau\tau}^{\text{VBF}}$ is independent of the measurement in the top quark control region, which is not the case for $\alpha_{Z/\gamma^* \to \tau\tau}^{\text{Acpt.}}$ where the contamination of the $Z/\gamma^* \to \tau\tau$ control region with top quark events has to be taken into account.

5.4.5   Summary of the Background Measurements

Using the procedures described in this section, the simulated top quark and Z/γ^* background contributions in the signal region are corrected using the correction factors summarized in Table 5.13. For the final results a fit of the m_{T}-distribution to the data is performed where the α and β factors are free parameters and are allowed to vary around

the central values shown Table 5.13 within the uncertainties of the control measurements (see Section 5.6.2). The W+jets event yields are estimated by direct extrapolation from the W+jets control region using event-by-event weighting factors derived from a supplementary dijet control sample. The diboson background as well as the contribution of ggF Higgs boson production are estimated using the simulation. The expected yields of the different backgrounds after corrections are shown in Table 5.14 at different stages of the signal selection .

Table 5.14: Expected different-flavor and same-flavor event yields for $\int L\,dt = 21\,\mathrm{fb}^{-1}$ of data after each stage of the signal selection. The W+jets, Z/γ^* and top quark background yields have been corrected using auxiliary measurements as described in the text. The errors are due to Monte-Carlo statistics.

	$N^{\mathrm{exp}}_{\mathrm{ggF}}$	$N^{\mathrm{exp}}_{\mathrm{diboson}}$	$N^{\mathrm{est}}_{\mathrm{top\ quark}}$	$N^{\mathrm{est}}_{Z/\gamma^*}$	$N^{\mathrm{est}}_{W+\mathrm{jets}}$
Different-flavor final states					
Preselection	74.6 ± 1.0	1352 ± 17	45655 ± 76	2268 ± 31	537 ± 8
$E_{\mathrm{T}}^{\mathrm{miss}} > 20\,\mathrm{GeV}$	66.9 ± 0.9	1239 ± 16	42902 ± 74	1799 ± 28	444 ± 8
b-jet veto	49.1 ± 0.8	888 ± 9	3281 ± 22	1297 ± 22	171 ± 5
$p_{\mathrm{T}}^{\mathrm{tot}} < 45\,\mathrm{GeV}$	40.8 ± 0.7	746 ± 9	2604 ± 20	1100 ± 19	126 ± 4
$Z \to \tau\tau$ veto	38.0 ± 0.7	686 ± 9	2411 ± 19	602 ± 15	108 ± 4
$\Delta Y_{\mathrm{jj}} > 2.8$	9.5 ± 0.3	125 ± 4	431 ± 7	95 ± 5	19 ± 2
$m_{\mathrm{jj}} > 500\,\mathrm{GeV}$	2.9 ± 0.2	39 ± 1	105 ± 3	19 ± 2	4.4 ± 0.7
Central jet veto	1.7 ± 0.1	28 ± 1	35 ± 2	9 ± 1	3.1 ± 0.6
Outside lepton veto	1.6 ± 0.1	20.8 ± 0.9	27 ± 1	7 ± 1	2.4 ± 0.5
$m_{\ell\ell} < 60\,\mathrm{GeV}$	1.5 ± 0.1	4.5 ± 0.4	5.1 ± 0.8	4.4 ± 0.8	1.0 ± 0.4
$\Delta\phi(\ell\ell) < 1.8$	1.3 ± 0.1	4.1 ± 0.4	4.4 ± 0.7	1.9 ± 0.5	0.6 ± 0.3
$m_{\mathrm{T}} \leq 1.2 \cdot m_H$	1.3 ± 0.1	2.8 ± 0.4	3.3 ± 0.6	1.7 ± 0.5	0.6 ± 0.3
Same-flavor final states					
Preselection	74.0 ± 1.0	2333 ± 17	45716 ± 76	901948 ± 1967	1032 ± 55
$Z \to \ell\ell$ veto	72.9 ± 1.0	1200 ± 15	35838 ± 68	114542 ± 537	555 ± 22
$E_{\mathrm{T}}^{\mathrm{miss}} > 45\,\mathrm{GeV}$	43.0 ± 0.7	766 ± 11	26152 ± 58	11565 ± 159	203 ± 9
$E_{\mathrm{T,STVF}}^{\mathrm{miss}} > 35\,\mathrm{GeV}$	39.7 ± 0.7	720 ± 10	25169 ± 57	5417 ± 94	191 ± 7
b-jet veto	29.6 ± 0.6	521 ± 8	1947 ± 17	3809 ± 76	58 ± 4
$p_{\mathrm{T}}^{\mathrm{tot}} < 45\,\mathrm{GeV}$	24.4 ± 0.5	428 ± 7	1543 ± 15	2794 ± 66	43 ± 3
$\Delta Y_{\mathrm{jj}} > 2.8$	6.2 ± 0.3	73 ± 2	288 ± 6	560 ± 33	6 ± 1
$m_{\mathrm{jj}} > 500\,\mathrm{GeV}$	2.1 ± 0.2	28 ± 1	72 ± 3	142 ± 5	1.4 ± 0.6
Central jet veto	1.1 ± 0.1	19 ± 1	23 ± 1	74 ± 3	0.7 ± 0.4
Outside lepton veto	0.9 ± 0.1	15 ± 1	17 ± 1	51 ± 3	0.3 ± 0.3
$m_{\ell\ell} < 60\,\mathrm{GeV}$	0.81 ± 0.1	5 ± 1	4.5 ± 0.6	30 ± 2	0.1 ± 0.2
$\Delta\phi(\ell\ell) < 1.8$	0.72 ± 0.09	4 ± 1	4.0 ± 0.6	25 ± 2	0.1 ± 0.2
$m_{\mathrm{T}} \leq 1.2 \cdot m_H$	0.68 ± 0.09	3 ± 1	2.1 ± 0.5	20 ± 2	0.1 ± 0.2

5.5 Systematic Uncertainties

Systematic uncertainties are reduced if the background contributions can be measured from control data samples, as in the case of the top quark, Z/γ^* and $W+$jets backgrounds, rather than relying on the simulation. The contributions of VBF and ggF Higgs boson production and of diboson processes, on the contrary, can only be predicted from simulation and, hence, are more susceptible to systematic uncertainties.

Systematic errors in the modelling of the shape of the m_T-distribution have also been evaluated. The uncertainty in the shape is dominated by the uncertainties in the normalization of the different background processes.

The main classes of systematic uncertainties are uncertainties $\sigma^\mathrm{syst}_\mathrm{theoretical}$ in the theoretical calculations, uncertainties $\sigma^\mathrm{syst}_\mathrm{experimental}$ in detector response and efficiencies and the uncertainty $\sigma^\mathrm{syst}_\mathrm{luminosity}$ in the integrated luminosity of the analyzed dataset. The relative systematic uncertainty in the expected signal and background yields after the $\Delta\phi(\ell\ell)$ requirement are shown in Tables 5.15 and 5.16 for different-flavor and same-flavor final states, respectively. The different theoretical and experimental uncertainties are added in quadrature. Their components are discussed below.

5.5.1 Theoretical Uncertainties

The theoretical uncertainties are evaluated following the prescription in [32, 53] (see also Section 2.2) with the exception of the uncertainties in the top quark and WW normalization.

QCD cross section calculations (QCD scales)

Uncertainties in the inclusive cross sections for both VBF ($qq \rightarrow qqH$) and ggF ($gg \rightarrow H$) Higgs boson production due to the choice of renormalization and factorization scales are estimated, using the MCFM generator [155], by varying these scales independently by a factor of two. The uncertainties from this variation are on the order of 4%. In addition, an uncertainty on the order of 30% in the ggF production cross section with two or more jets in the final state arises from missing higher-order corrections.

Underlying event and parton shower processes (UE and PS)

Other sources of uncertainties arise from the Monte-Carlo description of the under-

Table 5.15: Relative systematic errors σ_i in the expected different-flavor event yields for the different signal and background processes i after the $\Delta\phi(\ell\ell)$ requirement. The symbol "-" indicates that the uncertainty is below 0.5%. The uncertainties arising from the control region dataset and Monte-Carlo statistics (σ^{stat}) are also shown.

	Uncertainty [%]	σ_{VBF}	σ_{ggF}	$\sigma_{\mathrm{diboson}}$	$\sigma_{\mathrm{top\ quark}}$	σ_{Z/γ^*}	$\sigma_{W+\mathrm{jets}}$
Theoretical	QCD scale	4	30	-	-	-	-
	UE and PS	3	17	-	-	-	-
	PDF modelling	3	8	4	-	4	-
	$\mathcal{B}(H \to WW^{(*)})$	4	4	-	-	-	-
	WW normalization	-	-	26	1	1	-
	Top quark normalization	-	-	-	15	-	-
	Fake factor	-	-	-	-	-	34
	$\sigma_{\mathrm{theoretical}}^{\mathrm{syst}}$	7	36	26	15	4	34
Experimental	JES/JER	5	3	12	12	52	-
	b-tagging efficiency	1	1	1	27	8	-
	Lepton reconstruction	2	2	2	4	2	-
	$E_{\mathrm{T}}^{\mathrm{miss}}$ reconstruction	1	1	2	1	9	-
	Pile-up modelling	3	2	1	5	8	-
	Trigger efficiency	1	1	1	-	1	-
	$\sigma_{\mathrm{experimental}}^{\mathrm{syst}}$	6	5	13	30	54	
	$\sigma_{\mathrm{luminosity}}^{\mathrm{syst}}$	4	4	4	-	-	-
$\sigma_{\mathrm{total}}^{\mathrm{syst}}$		10	37	29	34	54	34
σ^{stat}		2	8	8	19	29	50

Table 5.16: Relative systematic errors σ_i in the expected same-flavor event yields for the different signal and background processes i after the $\Delta\phi(\ell\ell)$ requirement. The symbol "-" indicates that the uncertainty is below 0.5%. The uncertainties arising from the control region dataset and Monte-Carlo statistics (σ^{stat}) are also shown.

	Uncertainty [%]	σ_{VBF}	σ_{ggF}	σ_{diboson}	$\sigma_{\text{top quark}}$	σ_{Z/γ^*}	$\sigma_{W+\text{jets}}$
Theoretical	QCD scale	4	30	-	-	-	-
	UE and PS	3	17	-	-	-	-
	PDF modelling	3	8	4	-	-	-
	$\mathcal{B}(H \to WW^{(*)})$	4	4	-	-	-	-
	WW normalization	-	-	20	1	-	-
	Top quark normalization	-	-	-	15	-	-
	Fake factor	-	-	-	-	-	37
	$\sigma^{\text{syst}}_{\text{theoretical}}$	7	36	20	15	-	37
Experimental	JES/JER	7	33	14	11	13	-
	b-tagging efficiency	1	1	1	19	2	-
	Lepton reconstruction	2	2	2	2	3	-
	$E_{\text{T}}^{\text{miss}}$ reconstruction	1	2	1	2	3	-
	Pile-up modelling	4	3	5	4	5	-
	Trigger efficiency	1	1	1	-	-	-
	$\sigma^{\text{syst}}_{\text{experimental}}$	8	33	15	22	14	
	$\sigma^{\text{syst}}_{\text{luminosity}}$	4	4	4	-	-	-
$\sigma^{\text{syst}}_{\text{total}}$		12	49	25	27	14	37
σ^{stat}		2	16	26	18	10	350

lying event (UE), i.e. of the contribution of spectator quarks to the final state, and from the parton shower model (PS) describing the hadronization process of quarks and gluons. The uncertainty in the underlying event description is estimated by comparing simulated event samples generated with and without the underlying event contribution. The uncertainty from the parton shower model is estimated by comparing the baseline signal generator POWHEG+PYTHIA6 to the generator MC@NLO+HERWIG, where PYTHIA and HERWIG use different models for the parton shower process.

Parton distribution functions (PDF modelling)

The effects of uncertainties in the parton distribution functions (PDF) are evaluated by comparing simulation with different PDF sets from CT10 [29], MSTW [156] and NNPDF [157] following the prescription in [31]. Variations are performed separately for quark-quark, quark-gluon and gluon-gluon initiated processes for both the signal and background processes.

$H \to WW^*$ branching ratio ($\mathcal{B}(H \to WW^*)$)

The uncertainty in the branching ratio for the Higgs boson decay into two W bosons, determined using the procedure described in [53], amounts to 4%. The uncertainty arises from missing higher-order calculations as well as from uncertainties in the input parameters, in particular in α_s and in the heavy quark masses.

WW background normalization

The theoretical uncertainty in the diboson production cross section is evaluated separately for the electroweak and the QCD diboson production. The uncertainties in the QCD diboson background are large compared to the ones for the electroweak production, because the jets in the former are produced via higher-order QCD corrections. An uncertainty of 40% is assigned to the QCD diboson production cross section, based on variations of the QCD scales and PDF sets, while the uncertainty in the electroweak diboson production cross section is only 10% based on the comparison of the SHERPA and MADGRAPH generators. The uncertainty in the electroweak contribution includes effects from QCD scale variations and from the interference of the electroweak diboson process with VBF Higgs boson production. The uncertainty from the interference between the electroweak and QCD diboson production is estimated by comparing the cross sections of the two

separate contributions to the cross section including interference of both processes using the MADGRAPH generator. The top quark and Z/γ^* background estimates are slightly affected by the WW background normalization uncertainty due to the contamination of the respective control regions with diboson processes.

Top quark background normalization

The uncertainty in the normalization of the top quark background arises from the extrapolation of the event yields from the control to the signal region. It is evaluated by comparing the predictions of the baseline generator MC@NLO+HERWIG with the ones of the ALPGEN+HERWIG and POWHEG+PYTHIA8 generators. The top quark event yields in the signal region after applying the normalization correction vary by about 15% for different generators. This variation is taken as the theoretical uncertainty in the top quark background estimate (see more details Appendix C).

W+jet background prediction (Fake factor)

An uncertainty in the W+jets background arises from the reweighting of the background events by means of fake factors. The uncertainty arises mainly from differences in the fake factors for the dijet and W+jets control samples (see Section 5.4.1).

5.5.2   Experimental Uncertainties

Below the sources of experimental systematic uncertainties are summarized (see also Chapter 4).

Jet energy scale and resolution (JES/JER)

The signal selection depends in many ways on the jet reconstruction, directly through the requirement of at least two jets and the selection cuts on m_{jj} and ΔY_{jj} and indirectly through, for example, the requirements on the missing transverse energy. Uncertainties in the jet energy scale and resolution, therefore, dominate the experimental uncertainties in the signal and background event yields except for the top quark background yield. The JES and JER uncertainty contribute at a similar level. The uncertainty is particularly large for the Z/γ^* background, since the definitions of the control regions depend on the missing transverse energy.

b-jet identification (b-tagging)

Due to the b-jet veto in the signal selection, systematic uncertainties arise from

the measurement of the b-jet identification efficiency and misidentification rate of light-jets as b-jets. Particularly sensitive to this uncertainty is the top quark background due to the different requirements on the b-jet multiplicity in the top quark control region and in the signal region.

Lepton reconstruction Uncertainties arising from the measurement of the lepton identification efficiencies, momentum and energy scales and resolutions have only a small impact on the signal and background event yields.

Missing transverse energy ($E_{\mathrm{T}}^{\mathrm{miss}}$) reconstruction

Since the missing transverse energy ($E_{\mathrm{T}}^{\mathrm{miss}}$ and $E_{\mathrm{T,STVF}}^{\mathrm{miss}}$) depends directly on the measurement of the jet and lepton energy, the related jet and lepton uncertainties are directly propagated to the uncertainty in the measurement of the missing transverse energy. An additional contribution arises from the soft term, i.e. the contributions to the missing transverse energy from soft jets and energy depositions in the calorimeters not associated with any high-p_{T} object.

Pile-up modelling

The simulation incorporates a detailed description of pile-up events. However, the expected amount of pile-up events accompanying the hard-scatter proton-proton collision, was not precisely known at the time the large-scale event simulation was launched. The simulated events are therefore reweighted to describe the observed amount of pile-up in the data, based on the distribution of the average number of proton-proton interactions per bunch crossing (see Fig. 3.2b). An uncertainty, evaluated by varying the event weights up and down by 10%, is assigned to this procedure.

Trigger efficiency

The trigger efficiencies provided by simulation have to be scaled by a small amount (the average trigger event weight is 0.98 ± 0.04 and 0.99 ± 0.07 for events with a leading electron and muon, respectively) to describe the efficiencies measured in data. An uncertainty in this weighting procedure is derived from varying the trigger scale factors within their statistical uncertainty.

5.6 Results

In this section the results of the VBF Higgs boson production measurement in $H \to WW^{(*)} \to \ell\nu\ell\nu$ decays are summarized. In Section 5.6.1 data is compared to the expectation in the signal region with the background contributions determined from data as described in Section 5.4. The statistical methods used for the final statistical interpretation are summarized in Section 5.6.2. The resulting exclusion limits and signal significance as well as the result of the production rate measurement are discussed in Section 5.6.3.

5.6.1 Comparison of Data and Predictions

To ensure that the total background yield after the final signal selection predicted by the simulation and corrected with the control measurement described in Section 5.4 is in agreement with the observation, good modelling of discriminating variables is essential. The modelling of the main discriminating variables is investigated by comparing the data with the predicted background distributions. Figure 5.29 shows the ΔY_{jj}- and m_{jj}-distributions after combining the same-flavor and different-flavor channel prior to applying the selection cut on the respective variable. No significant amount of signal is expected at this stage of the signal selection. The data are mainly well described by the total background expectation. Some smaller disagreement can be seen in the ΔY_{jj}-distribution for $\Delta Y_{\mathrm{jj}} \sim 0.5$. Taking into account a 20–40% systematic uncertainty on the total background, not shown in this comparison, the disagreement is well compatible with a statistical fluctuation. Since the signal selection requires $\Delta Y_{\mathrm{jj}} > 2.8$, the observed discrepancy is not expected to affect the final result.

The $m_{\ell\ell}$-, $\Delta\phi(\ell\ell)$- and m_{T}-distributions describing characteristic topological properties of the Higgs boson decay are shown separately for same-flavor and different-flavor final states in Figs. 5.30 and 5.31, again before applying the selection cuts on the respective variables. At this stage of the event selection, the VBF Higgs boson signal contribution is no longer negligible. Thus the signal distribution is stacked on top of the total background to better compare the signal-plus-background expectation to the data. The lower panel shows the distribution of the expected signal and the data after the subtraction of the total background. An excess of events is observed compared to the total background expectation which is in agreement with the signal expectation.

115
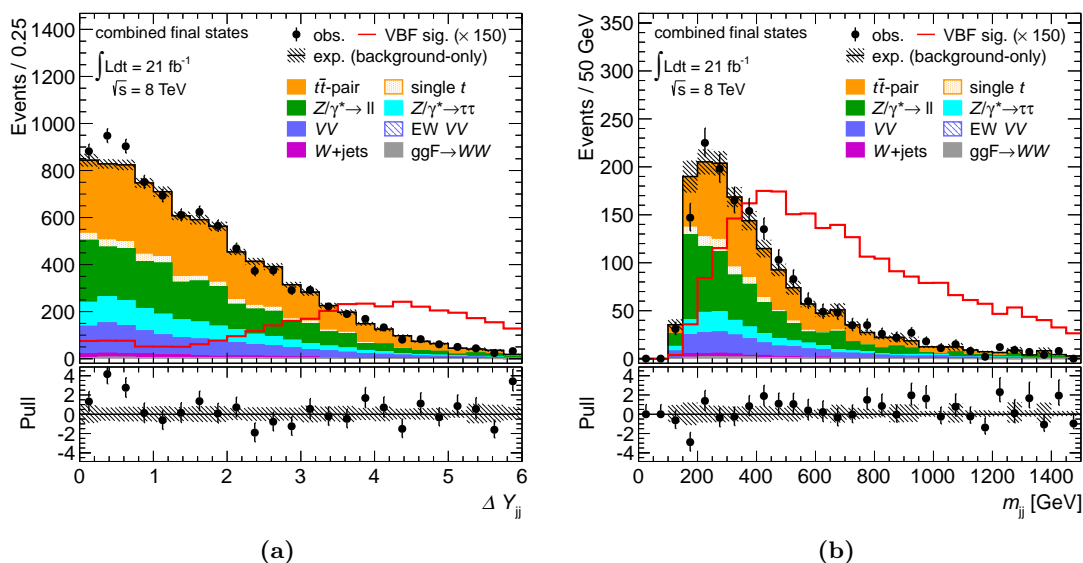
Figure 5.29: Expected and observed distributions of (a) the dijet rapidity gap ΔY_{jj} and (b) the invariant mass m_{jj} after combining same-flavor and different-flavor final states. The distributions are shown before the cut on the respective variable has been applied. The background contributions are stacked on top of each other. The expected signal multiplied by 150 is overlaid in red. The black hatched area represents the statistical uncertainty in the background prediction. The vertical error bars indicate the statistical uncertainty of the data.

One exception can be seen in the $\Delta\phi(\ell\ell)$-distribution of same-flavor final states shown in Fig. 5.30d where the data exceeds both the background-only as well as the signal-plus-background expectation in two bins ($\Delta\phi(\ell\ell) \sim 1.1$ and $\Delta\phi(\ell\ell) \sim 2$). In both cases the data is still compatible with the signal-plus-background and the background-only hypothesis within 2.5 standard deviations considering statistical uncertainties alone.

The expected and observed event yields after each stage of the event selection are shown separately for different-flavor and same-flavor final states in Table 5.18 and in Fig. 5.32. The expected event yields can only be compared to the observed event yields from the b-jet veto on, since before that the data driven corrections are not yet applied and processes, such as $b\bar{b}$ and semi-leptonic $t\bar{t}$ decays, are contributing, that are not included in the simulated processes. After all selection criteria are applied, including the cut on the transverse mass m_T, a ratio of $N^{\text{obs}}/N^{\text{exp}}_{\text{bkg-only}} = 2.1 \pm 0.5$ (statistical uncertainty) for different-flavor and 1.3 ± 0.25 (statistical uncertainty) for same-flavor final states is found for the background-only expectation (see Fig. 5.32). The observed yields are in

116

Table 5.17: Expected and observed event yields for $\int L\,dt = 21\,\text{fb}^{-1}$ of data after the selection requirement on $\Delta\phi(\ell\ell)$, shown separately for different-flavor and same-flavor final states. Uncertainties resulting from statistic (σ^{stat}) and from systematical (σ^{syst}) sources are shown. The former includes the uncertainty from the limited number of events in the control regions and in the simulated samples.

	Different-flavor			Same-flavor		
	Yield	$\sigma^{\text{stat}}[\%]$	$\sigma^{\text{syst}}[\%]$	Yield	$\sigma^{\text{stat}}[\%]$	$\sigma^{\text{syst}}[\%]$
$N_{\text{VBF}}^{\text{exp}}$	5.1	2	10	3.7	2	12
$N_{\text{ggF}}^{\text{exp}}$	1.3	8	37	0.7	16	49
$N_{\text{diboson}}^{\text{exp}}$	4.1	8	29	4.4	26	25
$N_{\text{top}}^{\text{est}}$	4.4	19	34	4.0	18	27
$N_{Z/\gamma^*}^{\text{est}}$	1.9	29	54	25	10	14
$N_{W+\text{jets}}^{\text{est}}$	0.6	50	34	0.06	350	37
$N_{\text{total Bkg}}$	12.3	17	36	34.2	14	18
$N^{\text{obs.}}$	23			42		

better agreement with the signal-plus-background expectation than with the background-only expectation. The significance of the observed excess over the background-only expectation is evaluated in Section 5.6.3.

The last selection criteria, $m_{\text{T}} \leq 1.2 \cdot m_H$, shown in Fig. 5.32 and Table 5.18 is not applied for the final result. Instead the full information stored in the m_{T}-distribution is exploited by means of a fit of both the background-only and the signal-plus-background prediction to data as will be detailed in Section 5.6.3. The input to the final statistical interpretation are hence the event yields expected after the selection criterion on the $\Delta\phi(\ell\ell)$ variable is applied. Table 5.17 summarizes the event yields and the uncertainties σ^{stat} from the limited number of events in the simulated samples and in the control data samples as well as from the systematic uncertainties σ^{syst} after this selection stage. The statistical uncertainty of the W+jets same-flavor event yield is large due to the small number of events both in the simulated samples used to subtract non-W+jets background in the control region as well as the small number of observed events in the W+jets control region itself (see Table 5.4).
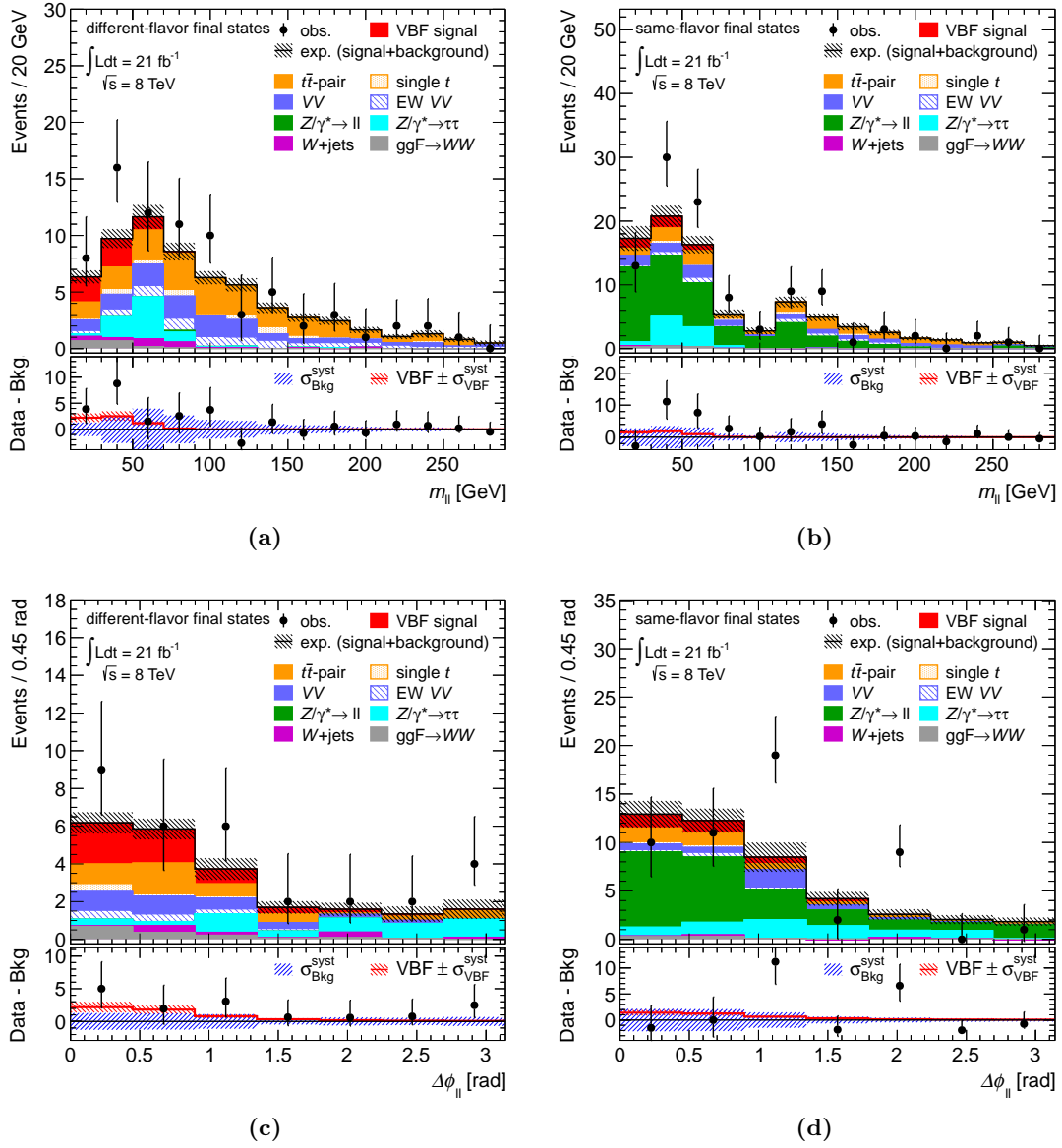
Figure 5.30: Expected and observed distributions of the dilepton invariant mass $m_{\ell\ell}$ in (a) and (b) and the dilepton opening angle in (c) and (d) for same-flavor and different-flavor events, respectively. The distributions are shown before the cut on the respective variable is applied. The predicted VBF Higgs signal is stacked on top of the total expected background. The black hatched area represents the statistical uncertainty in the signal-plus-background prediction. The vertical error bars indicate the statistical uncertainty of the data. The lower panel compares the residuals of the data with respect to the expected backgrounds to the distribution expected from a Standard Model VBF Higgs boson (red line). The red and blue hatched areas indicate the systematic uncertainties $\sigma_{\mathrm{VBF}}^{\mathrm{syst}}$ and $\sigma_{\mathrm{Bkg}}^{\mathrm{syst}}$ on signal and background, respectively.
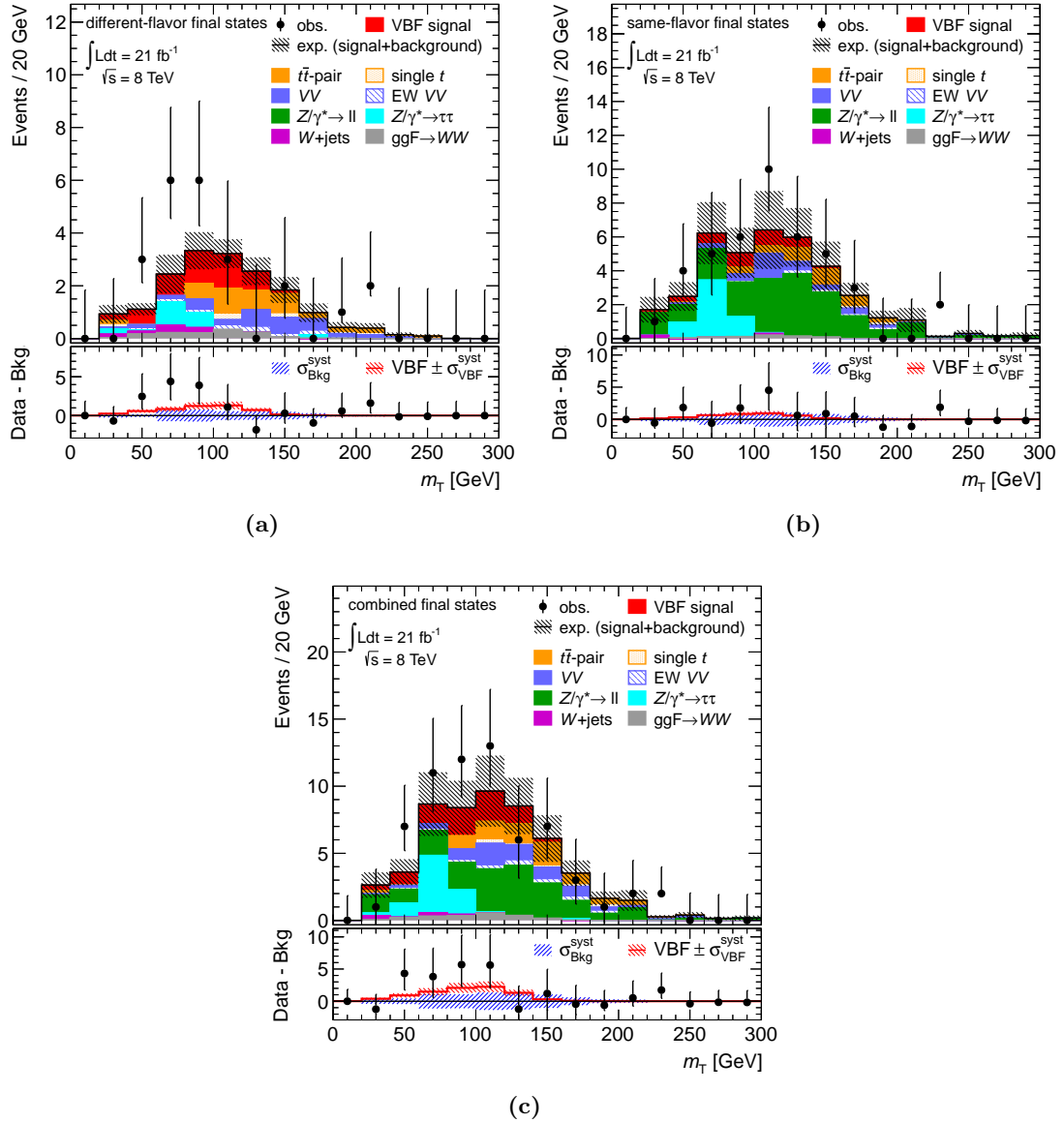
Figure 5.31: Expected and observed distributions of the transverse mass m_T for (a) the different-flavor, (b) the same-flavor and (c) the different-flavor and same-flavor combined channel. The distributions are shown after the $\Delta\phi(\ell\ell)$ criteria. The predicted VBF Higgs signal is stacked on top of the total expected background. The black hatched area represents the statistical uncertainty in the signal-plus-background prediction. The vertical error bars indicate the statistical uncertainty of the data. The bottom panel compares the residuals of the data with respect to the expected backgrounds to the m_T-distribution expected from a Standard Model VBF Higgs boson (red line). The red and blue hatched areas indicate the systematic uncertainties $\sigma_\text{VBF}^\text{syst}$ and $\sigma_\text{Bkg}^\text{syst}$ on the signal and total background, respectively.

119

Table 5.18: Expected and observed event yields for $\int L\,dt = 21\,\text{fb}^{-1}$ of data after the subsequent signal selection criteria in different-flavor and same-flavor final states. The W+jets, Z/γ^* and top quark yields are corrected from auxiliary measurements as described in the text. The errors are due to Monte-Carlo statistics.

		N^{obs}	$N^{\text{est}}_{\text{bkg}}$	$N^{\text{exp}}_{\text{VBF}}$
Different-flavor final states	Preselection	52488	49886 ± 85	47.3 ± 1.0
	$E_{\text{T}}^{\text{miss}} > 20\,\text{GeV}$	48723	46450 ± 81	42.6 ± 0.9
	b-jet veto	5852	5685 ± 33	30.6 ± 0.7
	$p_{\text{T}}^{\text{tot}} < 45\,\text{GeV}$	4790	4616 ± 29	26.6 ± 0.7
	$Z \to \tau\tau$ veto	4007	3844 ± 26	24.5 ± 0.6
	$\Delta Y_{\text{jj}} > 2.8$	696	681 ± 10	11.9 ± 0.2
	$m_{\text{jj}} > 500\,\text{GeV}$	198	170 ± 4	7.5 ± 0.1
	Central jet veto	92	77 ± 2	6.3 ± 0.1
	Outside lepton veto	78	59 ± 2	6.1 ± 0.1
	$m_{\ell\ell} < 60\,\text{GeV}$	31	17 ± 1	5.49 ± 0.1
	$\Delta\phi(\ell\ell) < 1.8$	23	12 ± 1	5.11 ± 0.09
	$m_{\text{T}} \leq 1.2 \cdot m_H$	20	9.7 ± 0.9	5.04 ± 0.09
Same-flavor final states	Preselection	947948	951102 ± 1969	59 ± 1
	$Z \to \ell\ell$ veto	157566	152207 ± 542	47.5 ± 1.0
	$E_{\text{T}}^{\text{miss}} > 45\,\text{GeV}$	38333	38728 ± 170	28.3 ± 0.7
	$E_{\text{T,STVF}}^{\text{miss}} > 35\,\text{GeV}$	32877	31537 ± 111	26.4 ± 0.7
	b-jet veto	6538	6366 ± 79	18.9 ± 0.6
	$p_{\text{T}}^{\text{tot}} < 45\,\text{GeV}$	4903	4832 ± 68	16.7 ± 0.5
	$\Delta Y_{\text{jj}} > 2.8$	958	934 ± 33	8.1 ± 0.2
	$m_{\text{jj}} > 500\,\text{GeV}$	298	245 ± 6	5.5 ± 0.1
	Central jet veto	147	119 ± 4	4.65 ± 0.1
	Outside lepton veto	108	85 ± 3	4.45 ± 0.09
	$m_{\ell\ell} < 60\,\text{GeV}$	52	40 ± 3	4.03 ± 0.09
	$\Delta\phi(\ell\ell) < 1.8$	42	34 ± 2	3.7 ± 0.09
	$m_{\text{T}} \leq 1.2 \cdot m_H$	35	27 ± 2	3.62 ± 0.09
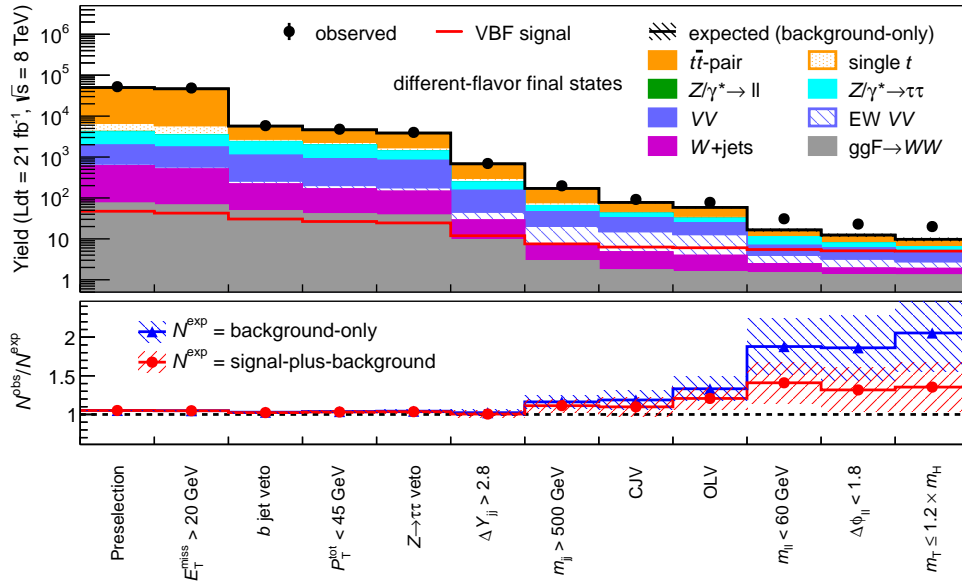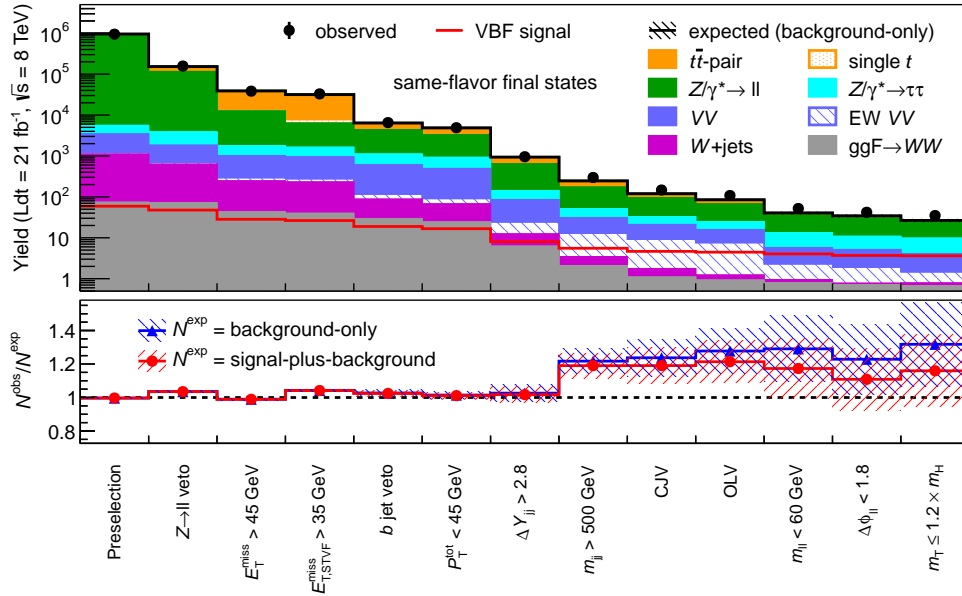
Figure 5.32: Expected and observed event yields after the subsequent selection criteria for (a) different-flavor and (b) same-flavor final states. The background contributions are stacked on top of each other. The expected signal is overlaid in red. The statistical uncertainty in the background prediction (black hatched area) is invisible on this scale. The statistical errors of the data are smaller than the data points. In the bottom part the ratio $N^{\mathrm{obs}}/N^{\mathrm{exp}}$ of observed and expected numbers of events is shown (for the background-only and signal-plus-background expectation). The statistical uncertainties of the data, the signal and total background expectation are shown as hatched bands.

5.6.2 Statistical Methods

After the candidate events have been selected and control regions have been defined for all background processes, the significance of a possible signal in the data is evaluated using the profile likelihood method [151, 158]. The analysis is performed for different-flavor and same-flavor final states separately and the m_{T}-distribution is divided in four m_{T}-bins as shown in Fig. 5.33a and b to exploit the variation in the signal-to-background ratio along m_{T}, leading to in total eight signal region categories.

The expected signal and background is fitted to the data simultaneously in the different lepton final states ($m = $ SF, DF) and m_{T}-categories ($n = 1, ..., N_{\mathrm{bin}}^{m_{\mathrm{T}}}$) using the likelihood function $\mathcal{L}$.

$$\mathcal{L}_{\mathrm{VBF}}(\mu, \boldsymbol{\alpha}, \boldsymbol{\beta}, \boldsymbol{\zeta}) = \tag{5.30}$$

$$\prod_{m=}^{\mathrm{SF,\ DF}} \prod_{n=1}^{N_{\mathrm{bin}}^{m_{\mathrm{T}}}} \left\{ P_{mn}\left(N_{mn}^{\mathrm{SR}} | \mu \cdot s^{\mathrm{SR}}(\boldsymbol{\zeta}) + \overbrace{\sum_{i} \alpha_i b_i^{\mathrm{SR}}(\boldsymbol{\zeta})}^{\text{total bkg } b \text{ in SR}} \right) \right\} \tag{5.31}$$

$$\times \prod_{i}^{\mathrm{CRs}} P_i\left(N^{i\text{-}\mathrm{CR}} | \mu \cdot s^{\mathrm{CR}}(\boldsymbol{\zeta}) + \alpha_i \cdot b_i^{i\text{-}\mathrm{CR}}(\boldsymbol{\zeta}) + \underbrace{\sum_{j \neq i} \beta_j b_j^{i\text{-}\mathrm{CR}}(\boldsymbol{\zeta})}_{\text{non-}i \text{ bkg. in } i\text{-CR}} \right) \tag{5.32}$$

$$\times \prod_{k=1}^{N^{\mathrm{syst}}} G(\zeta_k | 0, 1) \tag{5.33}$$

with the Poisson probability function P_{mn} (Eq. (5.31)) for observing N_{mn}^{SR} data events in the n-th bin of the m_{T}-distribution for the dilepton final state m given the number of signal events s expected from the Standard Model (for a given mass hypothesis) and background events b. b is the sum of all expected background contributions b_i multiplied by correction factors α_i. The signal strength parameter μ is a free parameter in the fit that scales the signal relative to the prediction of the Standard Model. The case $\mu = 0$ corresponds to the background-only and $\mu = 1$ to the signal-plus-background hypothesis.

For the top quark and the QCD Z/γ^* background the expected yields $\alpha_i b_i$ in the signal region (SR) are determined from auxiliary measurements $N^{i\text{-}\mathrm{CR}}$ in control regions (CR). For each control region a poisson term is added to the Likelihood function (see Eq. (5.32)). The measurement is extrapolated from the control to the signal region
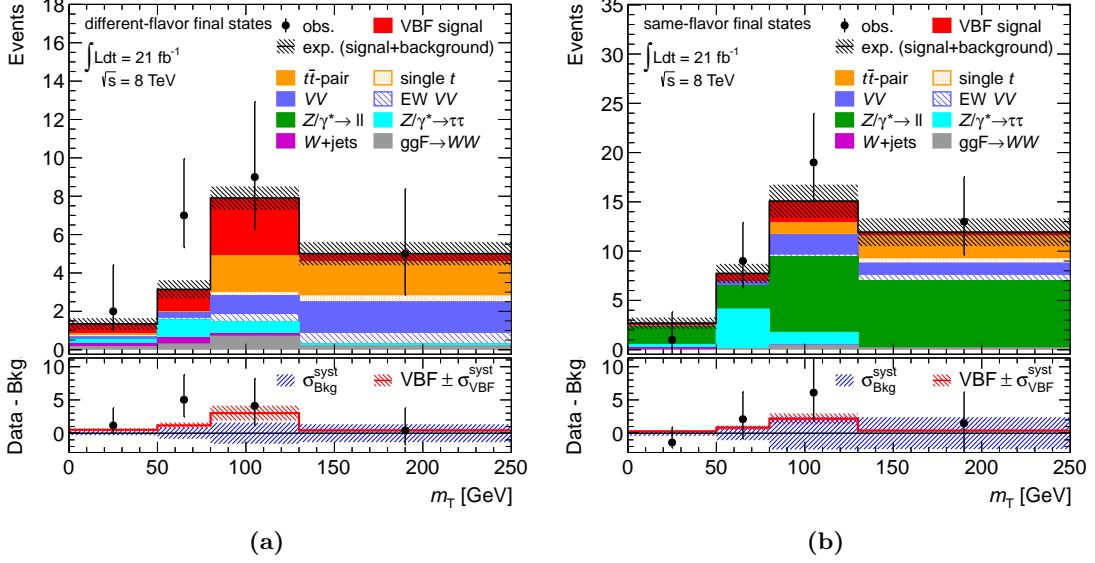
Figure 5.33: Expected and observed numbers of events in different m_T-ranges as employed by the likelihood function for (a) the different-flavor and (b) the same-flavor channel. The distributions are shown after the $\Delta\phi(\ell\ell)$ criteria. The predicted VBF Higgs signal is stacked on top of the total expected background. The black hatched area represents the statistical uncertainty in the signal-plus-background prediction. The vertical error bars indicate the statistical uncertainty of the data. The bottom panel compares the residuals of the data with respect to the expected backgrounds to the m_T-distribution expected from a Standard Model VBF Higgs boson (red line). The red and blue hatched areas indicate the systematic uncertainties $\sigma_{\text{VBF}}^{\text{syst}}$ and $\sigma_{\text{Bkg}}^{\text{syst}}$ on signal and background, respectively.

applying the normalization factors α_i, which are treated as free parameters. The small contribution s^{CR} of the expected signal to the control region is scaled with the signal strength parameter μ. Backgrounds $b_j^{i\text{-CR}}$ that contaminate the control region for the background i are scaled with factors β_j to extrapolate from control regions for backgrounds j as described in Section 5.4. In this analysis only the top quark and the QCD Z/γ^* background have free α- and β-parameters. For the diboson and electroweak Z/γ^* which are not determined by auxiliary measurements, the α- and β-parameters are set to unity. Two treatments of the gluon fusion process are tested in Section 5.6.3, one where the ggF contribution is fixed to the Standard Model predictions and estimated from Monte-Carlo simulation and treated like the diboson and electroweak Z/γ^* processes and one where it is determined from an auxiliary measurement and treated as the top

quark and the QCD Z/γ^* background. The expected background from W+jets processes is taken directly from the measurement in the W+jets control region (see Section 5.4.1) applying the fake factor as an event-by-event weight and $\alpha^{W+\text{jets}} = \beta^{W+\text{jets}} = 1$.

The expected signal and background yields f_l $(= s, b_i)$ in the signal region are affected by N^{syst} different sources of systematic uncertainties

$$\sigma_{lk} = \frac{f_l^{\text{nom}} - f_l^{k\text{-var}}}{f_l^{\text{nom}}} \tag{5.34}$$

where f_l^{nom} is the yield of the l-th process after the nominal analysis is applied and $f_l^{k\text{-var}}$ is the yield found if the k-th source of systematic uncertainty is varied by one standard deviation. For each systematic uncertainty σ_{lk}, a free parameter ζ_k is added to the Likelihood function. The signal and background yields f_l are parameterized as a function of σ_{lk} and ζ_k:

$$f_l((\sigma_{lk}), (\zeta_k)) = f_l^{\text{nom}} \times \prod_k \exp[\zeta_k \cdot \sqrt{\log{(1 + \sigma_{lk}^2)}}] \tag{5.35}$$

i.e. the nominal value f_l^{nom} is multiplied by the function $\exp[\zeta_k \cdot \sqrt{\log{(1 + \sigma_{lk}^2)}}]$ of ζ_k shown in Fig. 5.34a for different assumptions on σ_{lk}. The last term in the likelihood function (Eq. (5.33)) defines the distribution of ζ_k and constrains the range in which ζ_k and hence the yields are allowed to vary in the fit taking the size of the systematic uncertainty into account. For a distribution of ζ_k according to a standard Gaussian,

$$G(\zeta_k|0, 1) = \frac{1}{\sqrt{2\pi}} \exp[-\frac{\zeta_k^2}{2}] \quad , \tag{5.36}$$

the yields f_l are log-normally distributed as illustrated in Fig. 5.34b for different systematic uncertainties. The larger the relative uncertainty is, the less constraint is the yield to its nominal value in the fit.

Because in some cases the source of a systematic uncertainty k on a process determined in a control region affects the control region yield $b_i^{i\text{-CR}}(\zeta_k)$ in a similar way as the signal region yield $b_i^{\text{SR}}(\zeta_k)$, the effect of this uncertainty is absorbed by the α_i factor and largely cancels. In other words, the total yield $\alpha_i \cdot b_i^{\text{SR}}(\zeta_k)$ is stable against modifications in ζ_k, while the expected background yield $b_i^{\text{SR}}(\zeta_k)$ and the parameter α_i themselves are susceptible to the uncertainty.
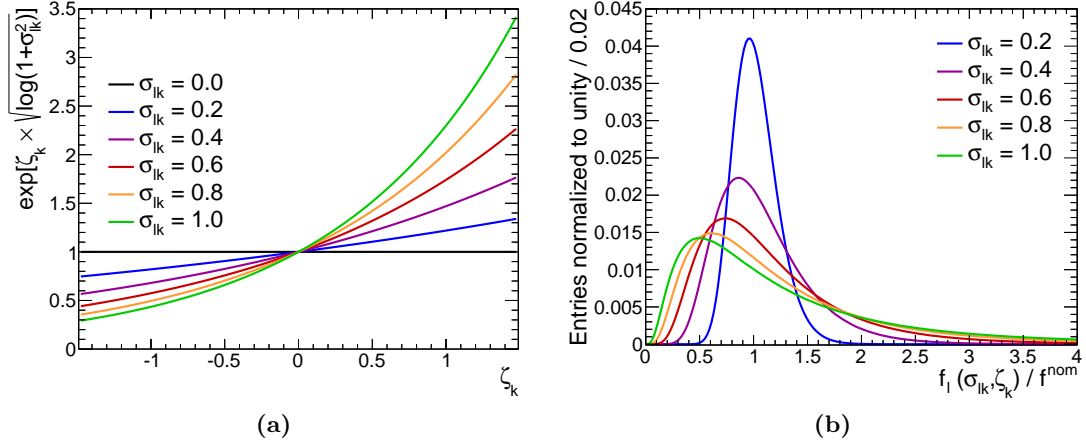
Figure 5.34: Impact of a relative systematic uncertainties σ_{lk} on (a) the functional dependence of the yields on the constraint parameter ζ_k and (b) the log-normal distribution of the yield $f_l(\sigma_{lk}, \zeta_k)$ for Gaussian distributed ζ_k normalized to its nominal value f_l^{nom}. The relative uncertainty is varied between 0% and 100% in steps of 20%.

Since control region selections have to be kinematically different from the signal region, to enhance the targeted background and reduce the signal contamination (see Section 5.4) some systematic uncertainties will affect signal and control region yields in different ways. For example the uncertainty in the b-tagging efficiency will impact the yields in the signal and the top quark control region differently, since the latter is defined by inverting the b-jet veto. The control measurement does not reduce the impact of the source of uncertainty in this case. The uncertainty in the b-tagging efficiency therefore has a large impact on the top quark yields (see Tables 5.15 and 5.16). In such a case the signal and background yields are treated as anti-correlated with respect to the uncertainty k.

The signal strength μ, the $\boldsymbol{\alpha} = (\alpha_i)$ and $\boldsymbol{\beta} = (\beta_i)$ factors as well as the constraint parameters $\boldsymbol{\zeta} = (\zeta_k)$ for the systematic uncertainties are free parameters in the fit of the models to the data maximizing the likelihood function. While the signal strength μ is the parameter of interest, $\boldsymbol{\theta} = (\boldsymbol{\alpha}, \boldsymbol{\beta}, \boldsymbol{\zeta})$ are nuisance parameters.

In order to test the compatibility of the signal-plus-background model with the data

for a given signal strength parameter μ, the profile likelihood ratio $\tilde{\lambda}(\mu)$ is introduced:

$$\tilde{\lambda}(\mu) = \begin{cases} \frac{\mathcal{L}(\mu, \hat{\hat{\boldsymbol{\theta}}}(\mu))}{\mathcal{L}(0, \hat{\hat{\boldsymbol{\theta}}}(0))} & \hat{\mu} < 0 \\ \frac{\mathcal{L}(\mu, \hat{\hat{\boldsymbol{\theta}}}(\mu))}{\mathcal{L}(\hat{\mu}, \hat{\boldsymbol{\theta}}(\hat{\mu}))} & \hat{\mu} \geq 0 \end{cases} \quad . \tag{5.37}$$

The numerator $\mathcal{L}(\mu, \hat{\hat{\boldsymbol{\theta}}}(\mu))$ is maximized over all nuisance parameters $\boldsymbol{\theta}$ for a given value of μ, referred to as *profiling* of the nuisance parameters $\boldsymbol{\theta}$. $\hat{\hat{\boldsymbol{\theta}}}(\mu)$ are the conditional maximum likelihood estimators of the nuisance parameters for a given value of μ. The denominator $\mathcal{L}(\hat{\mu}, \hat{\boldsymbol{\theta}}(\hat{\mu}))$ is maximized over all parameters including μ, such that $\hat{\mu}$ and $\hat{\boldsymbol{\theta}}(\hat{\mu})$ are the likelihood estimators of μ and $\boldsymbol{\theta}$ which maximize the likelihood function unconditionally. Only hypotheses with $\hat{\mu} \geq 0$ are physical, while the case $\hat{\mu} < 0$ is considered a downward fluctuation of the background.

The validity of the signal-plus-background hypothesis for a given signal strength μ is calculated using the test statistic

$$\tilde{q}_\mu = -2 \ln \tilde{\lambda}(\mu) \quad . \tag{5.38}$$

The hypothesis is less likely to be compatible with the data the higher the observed value of $\tilde{q}_\mu$ is. Hence, the absolute minimum of the test statistic is found for $\mu = \hat{\mu}$ with $\tilde{q}_{\hat{\mu}} = 0$.

The probability p_μ that the hypothesis with signal strength μ results in the observed or higher values of $\tilde{q}_\mu$ is

$$p_\mu = \int_{\tilde{q}_\mu^{\mathrm{obs}}}^{\infty} f(\tilde{q}_\mu | \mu, \hat{\hat{\boldsymbol{\theta}}}(\mu)) \, d\tilde{q}_\mu \quad , \tag{5.39}$$

where $f(\tilde{q}_\mu | \mu, \hat{\hat{\boldsymbol{\theta}}}(\mu))$ is the probability density function of the test statistic $\tilde{q}_\mu$. This function is determined using asymptotic formulae as described in [158] avoiding computation time consuming Monte-Carlo simulation.

The test statistic is used to define exclusion limits and signal significances as described below.

Exclusion Limits If no signal is evident in the data, an upper limit can be set on the signal strength parameter μ using the definition

$$
\tilde{q}_\mu = \begin{cases} -2\ln\tilde{\lambda}(\mu) & \hat{\mu} \leq \mu \\ 0 & \hat{\mu} > \mu \end{cases} \quad = \begin{cases} -2\ln\frac{\mathcal{L}(\mu,\hat{\hat{\boldsymbol{\theta}}}(\mu))}{\mathcal{L}(0,\hat{\hat{\boldsymbol{\theta}}}(0))} & \hat{\mu} < 0 \\ -2\ln\frac{\mathcal{L}(\mu,\hat{\hat{\boldsymbol{\theta}}}(\mu))}{\mathcal{L}(\hat{\mu},\hat{\boldsymbol{\theta}})} & 0 \leq \hat{\mu} \leq \mu \\ 0 & \hat{\mu} > \mu \end{cases} \quad . \tag{5.40}
$$

The restriction to $\hat{\mu} \leq \mu$ prevents an upward fluctuation of the data from being considered incompatible with the tested signal-plus-background hypothesis. In order to protect against excluding the signal-plus-background hypothesis when the sensitivity of the hypothesis test is small, a modified frequentist method, the so called $\mathrm{CL_s}$ method [151], with the conditional probability

$$
\mathrm{CL_s} := \frac{p_\mu}{1 - p_b} \quad , \tag{5.41}
$$

instead of $\mathrm{CL_{s+b}} = p_\mu$ is used to calculate the confidence interval with

$$
p_b = \int_{-\infty}^{\tilde{q}_\mu^{\mathrm{obs}}} f(\tilde{q}_\mu | 0, \hat{\hat{\boldsymbol{\theta}}}(0)) \, d\tilde{q}_\mu \quad . \tag{5.42}
$$

The denominator $1 - p_b$ in Eq. (5.41) can be interpreted as the probability that the background alone describes the data. The 95% $\mathrm{CL_s}$ exclusion limit on the signal strength is then found as the largest value μ_{up} for which $\mathrm{CL_s}$ is greater than 5%. For $\mu_{\mathrm{up}} \leq 1$ a signal as predicted by the Standard Model is excluded.

The $\mathrm{CL_s}$ approach is more conservative than the approach using confidence intervals based on $\mathrm{CL_{s+b}} = p_\mu$, since the latter only requires incompatibility of the signal-plus-background hypothesis with the data whereas $\mathrm{CL_s}$ requires in addition compatibility of the background-only hypothesis with the data.

To quantify the sensitivity of the analysis, the observed value $\mu_{\mathrm{up}}^{\mathrm{obs}}$ is compared to the expected value $\mu_{\mathrm{up}}^{\mathrm{exp}}$ determined from a fit to the expected background-only event sample from simulation and auxiliary measurements in the control region. An uncertainty σ due to uncertainties in the background model, is associated to $\tilde{q}_\mu^{\mathrm{exp}}$ replacing $\tilde{q}_\mu^{\mathrm{obs}}$. Confidence regions corresponding to n standard deviations for $\mu_{\mathrm{up}}^{\mathrm{exp}}$ are then calculated using $\tilde{q}_\mu^{\mathrm{exp}} \pm n \cdot \sigma$ instead of $\tilde{q}_\mu^{\mathrm{exp}}$ as an integration bound in Eqs. (5.39) and (5.42).

Signal Significance   The significance of a possible signal is evaluated based on the incompatibility of the data with the background-only hypothesis ($\mu = 0$ in Eqs. (5.31) and (5.32)). The probability that a background fluctuation leads to the observed or higher values of $\tilde{q}_0$ (Eq. (5.38) for $\mu = 0$) is given by

$$p_0^{\text{obs}} = \int_{\tilde{q}_0^{\text{obs}}}^{\infty} f(\tilde{q}_0 | 0, \hat{\hat{\boldsymbol{\theta}}}(0)) \, d\tilde{q}_0 \quad . \tag{5.43}$$

The expected p_0-value p_0^{exp} is calculated assuming the presence of a signal, i.e calculating the test statistics $\tilde{q}_0^{\text{exp}}$ from Eq. (5.38) for $\mu = 0$ but with a fit to a signal-plus-background event sample with $\mu = 1$. Replacing the lower integration bound in Eq. (5.43) by $\tilde{q}_0^{\text{exp}}$ leads to p_0^{exp}, the probability that a background fluctuation leads to values expected from the signal-plus-background model or greater. Again, as in the case of the expected exclusion limits, uncertainties in the model, signal-plus-background in the case of the p_0^{exp}-value, are propagate to the expected p_0-value.

The signal significance in units of standard deviations is given by

$$Z = \Phi^{-1}(1 - p_0) \tag{5.44}$$

where $\Phi(x)$ is the cumulative probability distribution of a standard Gaussian function $f(x)$ as shown in Fig. 5.35.
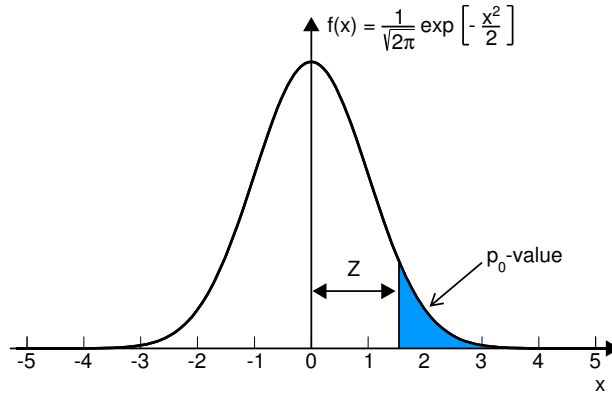
Figure 5.35: Illustration of the relation between the signal significance Z and the p_0-value using a standard Gaussian distribution $f(x)$ [159]

A significance of at least $Z = 3$, corresponding to a p_0-value of $1.5 \cdot 10^{-3}$, is usually required for evidence for a signal, while a significance of at least $Z = 5$, corresponding to a p_0-value of $2.9 \cdot 10^{-7}$, is required to claim a discovery.

5.6.3 The Final Results

Motivated by the discovery of the Higgs boson candidate [5,6] with a mass of 125.5 GeV [7] the signal significances and exclusion limits are quoted for a Higgs boson mass hypothesis of 125 GeV as a final result. However, mass hypothesis $110\,\text{GeV} < m_H < 200\,\text{GeV}$ are tested as well. Searches for a Higgs boson signal at masses above 200 GeV require a different event selection to separate the signal from the backgrounds due to different signal topology* [85].

The main aim of the analysis here is not the discovery of the Higgs boson in $H \rightarrow WW^{(*)} \rightarrow \ell\nu\ell\nu$ final states, which was done with higher sensitivity in an VBF and ggF inclusive search [91] but rather to independently probe for the production of the Higgs boson via VBF. According to the Standard Model prediction, VBF production is the dominant Higgs boson contribution after all selection criteria described in Section 5.3. However, about 15% contribution from gluon fusion production to Higgs boson processes is expected in the Standard Model. This fraction is considered part of the background for the VBF production rate measurement.

The Standard Model prediction for the gluon fusion cross section is not yet fully confirmed experimentally. Therefore two scenarios are investigated where the contribution from the ggF process is treated in different ways:

Scenario 1 The ggF cross section is taken from the Standard Model prediction.

Scenario 2 The ggF cross section is measured in a dedicated analysis (see [91]) in the same $H \rightarrow WW^{(*)} \rightarrow \ell\nu\ell\nu$ decay mode.

Scenario 1 Assuming Standard Model ggF cross section for the Higgs boson, the expected event yield is estimated from Monte-Carlo simulation. Only the mass hypothesis $m_H = 125\,\text{GeV}$ is tested, since the Standard Model predictions for ggF poduction of the Higgs boson for other mass hypotheses is excluded by ATLAS and CMS [5, 85–88].

---

*For example, the spin correlation described in Section 5.2.1 is only applicable for $m_H \leq 2 \times m_W$.

The fitted signal strengths, exclusion limits and signal significances for $m_H = 125\,\text{GeV}$ seperatly for different-flavor and same-flavor final states and for their combination are summarized in Table 5.19.

Combining different-flavor and same-flavor final states, a fitted signal strength of

$$\hat{\mu}_{\text{VBF}}^{\text{obs}}(m_H = 125\,\text{GeV}) = 2.2^{+1.0}_{-0.8} \quad . \tag{5.45}$$

is observed in $H \to WW^{(*)} \to \ell\nu\ell\nu$ decays. The observed signal strength is about twice the prediction of the Standard Model ($\mu_{\text{VBF}} = 1$), but compatible with it within 1.5 standard deviations. The different contributions to the uncertainty in the signal strength will be discussed at the end of this section. A CL_{s} upper limit of $\mu_{\text{up}}^{\text{obs}} = 3.39$ at 95% confidence level is set on the VBF signal strength in the $H \to WW^{(*)} \to \ell\nu\ell\nu$ decay channel at $m_H = 125\,\text{GeV}$, while a lower upper limit of $\mu_{\text{up}}^{\text{exp}} = 1.57$ is expected. The observed upper limit is higher than the expectation due to an excess of data events with respect to the background-only model. This excess is quantified as an observed signal significance of 2.9 standard deviations while a significance of 1.5 standard deviations is expected for a Standard Model Higgs boson with $m_H = 125\,\text{GeV}$. Same-flavor final states contributes only with 7% to the observed and expected signal significance (see Table 5.19).

Scenario 2 In order to account for a possible deviation of the gluon fusion Higgs boson production cross section from the Standard Model prediction an additional scenario is investigated. A separate signal strength parameter μ_{ggF}, scaling the ggF yield in the signal region, is introduced as a free parameter in the likelihood fit. The number or expected events in the signal region in Eq. (5.31) in the likelihood function is modified accordingly:

$$\mu \cdot s^{\text{SR}}(\boldsymbol{\zeta}) + \sum_i \alpha_i b_i^{\text{SR}}(\boldsymbol{\zeta}) \tag{5.46}$$

$$\longrightarrow \quad \mu \cdot s_{\text{VBF}}^{\text{SR}}(\boldsymbol{\zeta}) + \mu_{\text{ggF}} \cdot s_{\text{ggF}}^{\text{SR}}(\boldsymbol{\zeta}) + \sum_i \alpha_i b_i^{\text{SR}}(\boldsymbol{\zeta}) \quad . \tag{5.47}$$

This parameter μ_{ggF} is constrained by a dedicated measurement using a data sample enriched in gluon fusion production with Higgs boson decays $H \to WW^{(*)} \to \ell\nu\ell\nu$ as in the VBF analysis. The likelihood of the VBF analysis (Eq. (5.30)) is multiplied with the

Table 5.19: Summary of results for the VBF Higgs boson production rate measurement in the $qq\ell\nu\ell\nu$ final state for $m_H = 125\,\text{GeV}$. The fitted signal strength $\hat{\mu}_{\text{VBF}}$, the 95% upper CL_s limit μ_{up} and the signal significance in standard deviations (s.d.) are given separately for different-flavor (DF) and same-flavor (SF) final states and for their combination (DF+SF). Two different treatments of the gluon fusion production are compared, either taken from the Standard Model prediction (scenario 1) or from a dedicated ggF measurement [91] (scenario 2).

| | | Signal strength | | 95% upper CL_s Limit | | Signal significance [s.d.] | |
		$\hat{\mu}_{\text{VBF}}^{\text{obs}}$	$\hat{\mu}_{\text{VBF}}^{\text{exp}}$	$\mu_{\text{up}}^{\text{obs}}$	$\mu_{\text{up}}^{\text{exp}}$	Observed	Expected
Scenario 1	DF+SF	$2.2^{+1.0}_{-0.8}$	$1.0^{+0.8}_{-0.7}$	3.93	1.57	2.9	1.5
	DF	$2.1^{+1.1}_{-0.9}$	$1.0^{+0.9}_{-0.8}$	4.02	1.70	2.7	1.4
	SF	$2.3^{+2.5}_{-1.8}$	$1.0^{+2.1}_{-1.6}$	6.77	4.43	1.3	0.6
Scenario 2	DF+SF	$2.1^{+1.0}_{-0.8}$	$1.0^{+0.8}_{-0.7}$	3.80	1.59	2.8	1.5
	DF	$2.1^{+1.0}_{-0.9}$	$1.0^{+0.9}_{-0.8}$	3.90	1.69	2.6	1.4
	SF	$2.2^{+2.5}_{-1.8}$	$1.0^{+2.1}_{-1.7}$	6.64	4.45	1.2	0.6

likelihood $\mathcal{L}_{\text{ggF}}$ of the ggF dedicated analysis and a combined fit is performed. When measuring μ_{VBF} the gluon fusion signal strength parameter is like any other α-parameter a profiled nuisance parameter constrained by the ggF dedicated measurement.

The selection of the ggF data sample is described in [91]. The main differences of the ggF event selection compared to the VBF event selection is the requirement of less than two jets ($n_{\text{jet}} \leq 1$) in the final state making it orthogonal to the VBF selection. In addition, there are no requirements on the dijet system. The likelihood function $\mathcal{L}_{\text{ggF}}$ contains six signal region categories accounting for different jet multiplicity, dilepton final state and dilepton invariant mass range (see Section 6.1) which are used to measure the ggF contribution. Poisson terms for control measurements of background contributions in the ggF categories are added as well. The constraints on the systematic uncertainties are treated as correlated between the ggF and VBF analysis, if appropriate, i.e. if the two analysis are affected in the same way by the source of systematic.

The ggF and VBF signal strength parameter μ_{ggF} and μ_{VBF} can be measured simultaneously by profiling either the ggF contribution and constraining it based on the data sample with $n_{\text{jet}} < 2$ when measuring the μ_{VBF}, or, vice versa, profiling μ_{VBF} using the data with $n_{\text{jet}} \geq 2$ to constrain the VBF contribution when measuring μ_{ggF} in final states

with $n_{\text{jet}} < 2$. The VBF contribution in the latter case is, however, negligibly small. In this chapter only the measurement of μ_{VBF} is discussed. Results on the measurements of μ_{ggF} will be given in the next chapter.

Since the ggF cross section is now constrained from data, also Higgs boson mass hypotheses for which the ggF production has already been experimentally excluded are physically meaningful. For such mass values the fitted value of μ_{ggF} will simply be close to zero. However, due to the poor mass resolution in the final states with two leptons and two neutrinos, different mass hypothesis are not easily distinguishable by means of their corresponding transverse mass distributions. A Higgs boson of 125 GeV mass produced through gluon fusion will contaminate the search for a Higgs boson produced via VBF at a hypothesized mass of e.g. 115 GeV. The expected normalization of the ggF background corresponding to $m_H = 125$ GeV is fitted to data and hence correctly treated in the VBF search for a mass of $m_H = 115$ GeV. However, the shape of the gluon fusion m_{T}-distribution is taken from simulation for $m_H = 115$ GeV. Therefore, the treatment of the ggF production is not fully correct for mass hypotheses different from 125 GeV. Nevertheless it is the most model independent method to perform a VBF search for mass hypothesis different from 125 GeV.

Figure 5.36 shows the observed and expected CL_{s} upper limits on the signal strength μ at 95% confidence level as a function of the Higgs boson mass. Standard Model Higgs bosons produced through VBF are excluded in a mass range of $152\,\text{GeV} < m_H < 185\,\text{GeV}$, corresponding to an expected larger range of $130\,\text{GeV} < m_H \leq 200\,\text{GeV}$. The maximum sensitivity is reached for $m_H \approx 2 \cdot m_W \approx 160\,\text{GeV}$ where the branching fraction of the Higgs boson decaying into two W bosons is largest (see Fig. 2.7b). At smaller Higgs boson masses the branching ratio of the $H \to WW^{(*)}$ decay decreases rapidly. For larger Higgs boson masses the sensitivity degrades since the Higgs boson production cross section drops rapidly (see Fig. 2.7a) and the m_{T}-distribution of the signal shifts to larger values, making it more difficult to separate the signal from the WW and top quark backgrounds (see Fig. 5.13c). The one (two) standard deviation confidence regions on the expected upper limit are shown as yellow (green) bands. The observation agrees with the expectation within two standard deviations over a large range. However, a broad excess greater than two standard deviations is observed for $m_H < 140\,\text{GeV}$ indicating the presence of the Higgs boson signal in the data.

The excess of observed events above the expected background is quantified in terms
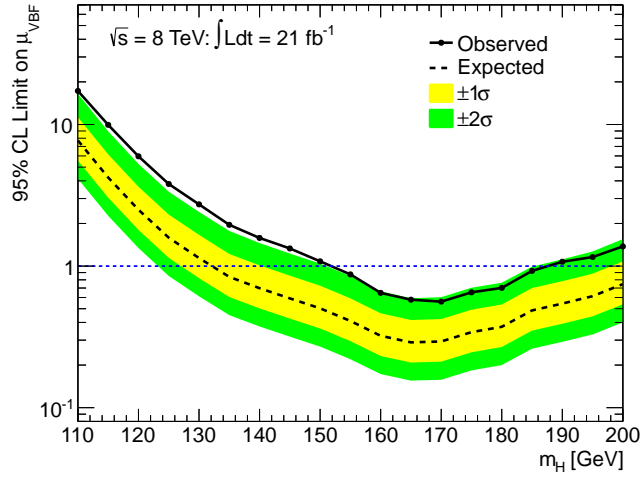
Figure 5.36: Expected and observed 95% CL upper limits on the signal strength for different-flavor and same-flavor final states combined as a function of the Higgs boson mass hypothesis m_H. The ggF background is determined from a dedicated ggF measurement [91] (scenario 2).

of the probability p_0 shown as a function of m_H in Fig. 5.37. A very broad dip around 125 GeV is observed. The expected p_0-values for the $\mu = 1$ hypothesis, i.e. for the Standard Model prediction are shown for comparison. Two cases are distinguished: the black dashed line shows p_0-values evaluated assuming a Higgs boson signal with the same mass hypothesis searched for. The red dashed line corresponds to the assumption of a signal with $m_H = 125$ GeV, independent of the mass hypothesis, accompanied by the 1σ and 2σ uncertainty bands. The observed distribution is compatible within two standard deviations with the distribution expected for a Standard Model Higgs boson with 125 GeV mass.

The fitted observed and expected ($m_H = 125$ GeV) signal strength parameters $\hat{\mu}_{\mathrm{VBF}}$ are shown as a function of the Higgs boson mass hypothesis in Fig. 5.38 with its uncertainty band, defined by $-2\ln\lambda(\mu) < 1$, corresponding to one standard deviation. The observed signal strength rapidly increases for decreasing Higgs boson mass. This is not an indication of a low mass Higgs boson signal amounting for example to five times the Standard Model predictions at $m_H = 115$ GeV. The behavior is rather an artefact of the poor mass resolution in the final state with two leptons and two neutrinos in combination with the rapidly falling $H \to WW^{(*)}$ branching fraction for decreasing Higgs boson mass (see Fig. 2.7b). Due to the poor mass resolution, the m_{T}-spectrum
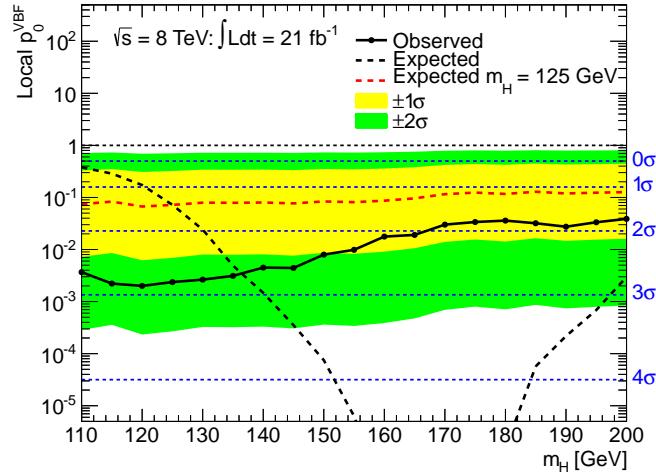
Figure 5.37: Expected and observed p_0^{VBF}-values for different-flavor and same-flavor final states combined. The right-hand side y-axis shows the corresponding signal significance in units of standard deviations as a function of the Higgs boson mass hypothesis m_H. The ggF background is determined from a dedicated ggF measurement [91] (scenario 2).

of the decay of a Higgs boson with $m_H = 115\,\mathrm{GeV}$ is not distinguishable from the one for $m_H = 125\,\mathrm{GeV}$. Consequently, due to the much smaller predicted event rate of $m_H = 115\,\mathrm{GeV}$, the presence of a Higgs boson with $m_H = 125\,\mathrm{GeV}$ can mimic a Higgs boson with $m_H = 115\,\mathrm{GeV}$ with apparently larger signal strength. To demonstrate the validity of this argument, the expected distribution of the signal strength $\hat{\mu}_{\mathrm{VBF}}$ is shown for comparison for a signal-plus-background hypothesis with $m_H = 125\,\mathrm{GeV}$. The increase of the signal strength with decreasing Higgs boson mass is seen as in the observed data.

The results from scenario 2 for a Higgs boson mass of $m_H = 125\,\mathrm{GeV}$ are summarized in Table 5.19. Very similar results as in the first scenario, where the used ggF production cross section is predicted by the Standard Model, are found. The observed signal significance for VBF production of the Higgs boson with $m_H = 125\,\mathrm{GeV}$ in $H \to WW^{(*)} \to \ell\nu\ell\nu$ decays amounts to 2.8 standard deviations while 1.5 standard deviations are expected. The corresponding VBF signal strength parameter $\hat{\mu}_{\mathrm{VBF}}^{\mathrm{obs}}$ is:

$$\hat{\mu}_{\mathrm{VBF}}^{\mathrm{obs}}(m_H = 125\,\mathrm{GeV}) = 2.1^{+1.0}_{-0.8} \quad . \tag{5.48}$$

The result is compatible with the Standard Model prediction for VBF Higgs boson
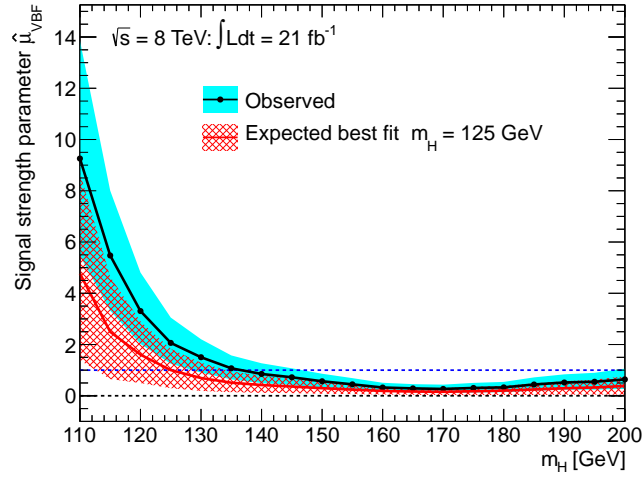
Figure 5.38: Observed and expected (for $m_H = 125\,\mathrm{GeV}$) signal strengths $\hat{\mu}_\mathrm{VBF}$ for different-flavor and same-flavor final states combined as a function of the Higgs boson mass hypothesis m_H shown as the black and red line, respectively. The ggF background is determined from a dedicated ggF measurement [91] (scenario 2).

production in this channel within 1.5 standard deviations.

The uncertainty on $\hat{\mu}_\mathrm{VBF}^\mathrm{obs}$ in Eq. (5.48) can be broken down in its statistical and systematic components, as shown in Table 5.20. The total uncertainty is dominated by statistical sources. The different-flavor final state, for which top quark processes are under the dominant background contributions is more affected by statistical sources, since the top quark control region has limited number of events (compare Tables 5.15 and 5.16). The same-flavor final state, dominated by Z/γ^* processes is less affected by statistical sources.

Table 5.20: Statistical and systematic components of the uncertainty on the observed signal strength $\hat{\mu}_\mathrm{VBF}^\mathrm{obs}$ for different-flavor and same-flavor final states separately and for their combination. Results are shown for scenario 2 where the ggF cross section is determined from a dedicated ggF measurement [91].

	$\hat{\mu}_\mathrm{VBF}^\mathrm{obs}$	σ^stat	σ^syst
Different-flavor	2.1	$^{+0.93}_{-0.84}$ (86%)	$^{+0.37}_{-0.34}$ (14%)
Same-flavor	2.2	$^{+1.98}_{-1.34}$ (63%)	$^{+1.52}_{-1.03}$ (37%)
Combined	2.1	$^{+0.87}_{-0.70}$ (76%)	$^{+0.49}_{-0.39}$ (24%)

In Table 5.21 the systematic uncertainty in $\hat{\mu}_{\mathrm{VBF}}^{\mathrm{obs}}$ is further broken down into the different experimental and theoretical contributions. For combined different-flavor and same-flavor final states experimental errors contribute with 62%, theoretical ones with 31% and the luminosity error with 6%. The by far dominant experimental uncertainty is in the jet energy scale and resolution. The dominant source of theoretical uncertainty is in QCD scales followed by the prediction of the WW background normalization and the $H \to WW^{(*)}$ branching fraction. Other theoretical errors come from the description of the $W\gamma^{(*)}$ background contribution which only affects the data sample used for determining the ggF contribution. The uncertainties in different-flavor and same-flavor event yields are estimated separately. The contribution to the uncertainty in the combined measurement from the dilepton final states scales with the contribution of the individual final state to the final result, i.e. if the same-flavor measurements contributes to the signal significance with 7%, the uncertainty in the same-flavor measurement contributes accordingly to the uncertainty in the combined measurement.

The categorization of the gluon fusion process as part of the total background to the analysis is motivated by the aim of the analysis to measure the VBF production rate. It it also possible to include events from gluon fusion production as an additional contribution to the signal*. Results of such an analysis are shown in Appendix D. Here, also individual different-flavor and same-flavor results for the full range of tested mass hypothesis are given.

The analysis described in this chapter only includes the dataset from 2012. The results are combined with results from the 2011 dataset and published in [91]. The selection requirements for the analysis of the 2011 dataset are identical to the ones used for the analysis of the 2012 dataset, with the exception of the jet vertex fraction and missing transverse energy requirements which are adapted for the lower pile-up rate. Additionally, slightly different trigger definitions were used in the 2011 data taking period. The 7 TeV and 8 TeV data are treated as separate event categories and are combined only for the final statistical interpretation.

The fitted signal strength and signal significances for the 7 TeV and 8 TeV data combined are shown in Fig. 5.39. For a Higgs boson mass of 125 GeV the observed excess is significant with 2.5 standard deviations while 1.6 standard deviations are

---

*The selection criteria presented in Section 5.3 are not optimal for this case since they are optimized assuming that the ggF production is a part of the background. The difference with respect to the results with optimum selection criteria are, however, expected to be very small.

Table 5.21: Breakdown of the systematic uncertainty in $\hat{\mu}_{\mathrm{VBF}}^{\mathrm{obs}}$ in its experimental and theoretical components for different-flavor, same-flavor and the combined final states. The ggF process is determined using a dedicated ggF measurement [91] (scenario 2).

	$\sigma_{\mathbf{experimental}}$		$\sigma_{\mathbf{theoretical}}$		$\sigma_{\mathbf{lumi}}$
Different-flavor			OCD scale	11%	
	JES/JER	24%	$\mathcal{B}(H \to WW^{(*)})$	8%	
	b-tagging efficiency	12%	WW normalization	8%	
	Lepton reconstruction	4%	PDF modelling	7%	
	Pile-up modelling	4%	UE and PS	7%	
	$E_{\mathrm{T}}^{\mathrm{miss}}$ reconstruction	0.5%	Top quark normalization	3%	
	Trigger efficiency	0.4%	Fake factor	2%	
			Other	<0.1%	
		45%		**47%**	**9%**
Same-flavor			WW normalization	1%	
	JES/JER	90%	OCD scale	0.9%	
	Pile-up modelling	3%	PDF modelling	0.8%	
	$E_{\mathrm{T}}^{\mathrm{miss}}$ reconstruction	0.6%	$\mathcal{B}(H \to WW^{(*)})$	0.8%	
	Lepton reconstruction	0.6%	Top quark normalization	0.6%	
	Trigger efficiency	0.1%	UE and PS	0.6%	
	b-tagging efficiency	0.1%	Other	<0.1%	
			Fake factor	<0.1%	
		94%		**5%**	**1%**
Combined			OCD scale	7%	
	JES/JER	50%	WW normalization	6%	
	b-tagging efficiency	5%	$\mathcal{B}(H \to WW^{(*)})$	6%	
	Pile-up modelling	4%	PDF modelling	5%	
	Lepton reconstruction	2%	UE and PS	4%	
	Trigger efficiency	0.4%	Top quark normalization	3%	
	$E_{\mathrm{T}}^{\mathrm{miss}}$ reconstruction	0.3%	Fake factor	0.9%	
			Other	<0.1%	
		62%		**31%**	**6%**
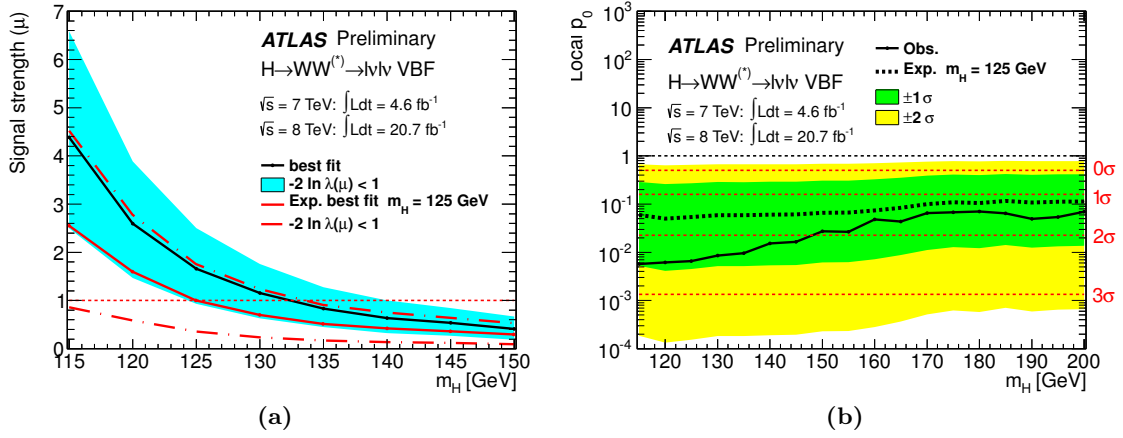
Figure 5.39: Results of the VBF Higgs boson production measurement in $H \rightarrow WW^{(*)} \rightarrow \ell\nu\ell\nu$ decays as a function of the Higgs boson mass m_H for different-flavor and same-flavor final states and for 7 TeV and 8 TeV data combined showing (a) the fitted signal strength and (b) the p_0-value and signal significance (from [91]).

expected. Comparing these results to the results obtained from the 2012 dataset only (scenario 2, Table 5.19) one finds that the 2011 dataset adds 7% in signal significance to the expected 2012 results. The observed signal significance is smaller compared to the combined result since no excess of events was observed in 2011 in $H \rightarrow WW^{(*)} \rightarrow \ell\nu\ell\nu$ decays. A fitted signal strength of

$$\hat{\mu}_{\text{VBF}}^{\text{obs}}(m_H = 125 \, \text{GeV}) = 1.66 \pm 0.79 \tag{5.49}$$

is measured, which is lower compared to the signal strength observed in 2012 data alone. Since the datasets of the two results are highly correlated, compatibility between the measurements are tested for the individual results of the 7 TeV and 8 TeV dataset. For an $H \rightarrow WW^{(*)} \rightarrow \ell\nu\ell\nu$ inclusive search the measurements with the two datasets are compatible within 1.8 standard deviations [91].

The results presented here are further combined with ATLAS measurements of other Higgs boson decay and production modes which will be described in the Chapter 6.

5.7   Analysis Improvements

Two possible future improvements of the analysis are considered in this section, a categorization of the signal event candidates into two samples with different signal-to-background ratio is investigated in Section 5.7.1 and new discriminating variables for further suppression of the large $Z/\gamma^* \to \ell\ell$ background in same-flavor final states are studied in Section 5.7.2.

The full implementation of these modifications into the analysis is beyond the scope of this thesis, because redefinition of the control regions and reevaluation of the systematic uncertainties is required. In the study here, no corrections from auxiliary measurements are applied to any of the background processes and only simulated background contributions are used. The systematic uncertainties are assumed to be the same as for the standard analysis given in Table 5.17. The analyses below are performed for a Higgs boson mass hypothesis of $m_H = 125\,\mathrm{GeV}$.

Rather than using the fit procedure and statistical analysis described in Section 5.6.2, the sensitivity of the improved analysis is estimated after the criteria $m_\mathrm{T} < 1.2 \times m_H$ defining the signal significance by $s/\sqrt{b + \sigma_b^2}$, where s an b are the expected signal and background yields and σ_b is the absolute systematic uncertainty in b.

5.7.1   Event Categorization in the Signal Region

The analysis gains sensitivity by dividing the signal region in categories with different signal-to-background ratios. By performing a categorization the analysis exploits the probability of an event to be signal-like depending on the category it is found in. When combining the two categories this information is lost and the analysis sensitivity degrades. In the simplest case, assuming no systematic uncertainty and sufficient number of background events, such that the statistical uncertainty in the background b can be estimated by $\sqrt{b}$, the sensitivity of an analysis is given by the signal significance $s/\sqrt{b}$ where s is the number of signal events. It can be shown that,

$$\frac{s_m + s_n}{\sqrt{b_m + b_n}} \le \sqrt{\left(\frac{s_n}{\sqrt{b_n}}\right)^2 + \left(\frac{s_m}{\sqrt{b_m}}\right)^2} \quad , \tag{5.50}$$

which means that the significances of two categories with $s_{n(m)}$ signal and $b_{n(m)}$ background events in the category $n(m)$ added in quadrature are always grater or equal to the

139
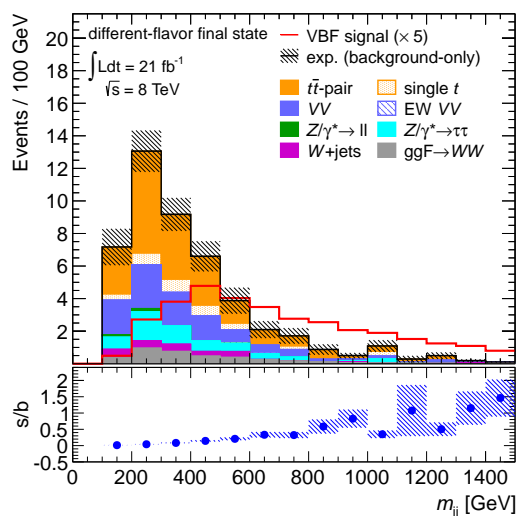
Figure 5.40: Simulated m_{jj}-distribution for VBF signal ($m_H = 125\,\text{GeV}$) and backgrounds in different-flavor final states after all selection criteria except for the requirement on m_{jj}. The black hatched area represents the statistical uncertainty in the total background prediction. The lower panel shows the signal-to-background ratio s/b with error margins.

sensitivity of a single category with $s_n + s_m$ signal and $b_n + b_m$ background events. The above relation is an exact equation for $s_m/b_m = s_n/b_n$, i.e. if the signal-to-background ratios are identical in the two categories no improvement is expected by the categorization. The standard analysis already performs a categorization in different-flavor and same-flavor events and in four m_T-bins, to exploit the different signal-to-background ratios in the dilepton categories and the distinct shape of the signal and background m_T-distributions (see Fig. 5.33).

The shape of the dijet invariant mass (m_{jj}) distribution is, like the shape of the m_T-distribution, distinct between signal and backgrounds containing QCD jets (see Fig. 5.40). The background m_{jj}-distribution falls much more rapidly than the signal distribution does, such that the signal-to-background ratio increases with increasing dijet invariant mass. The m_{jj} variable is, hence, a good candidate to investigate a categorization defined by a split in m_{jj}. Only different-flavor final states are used for this study.

Table 5.22 compares the sensitivities of the standard analysis, with m_{jj}-threshold of $m_{jj} > 500\,\text{GeV}$ with the sensitivity of the analysis with a split into a low-m_{jj} ($500\,\text{GeV} < m_{jj} < 800\,\text{GeV}$) and a high-$m_{jj}$ ($m_{jj} > 800\,\text{GeV}$) region. The threshold choice of $800\,\text{GeV}$ maximizes the combined signal significance of the high- and low-m_{jj} regions, calculated

Table 5.22: Signal significance $s/\sqrt{b + \sigma_b^2}$ for different-flavor final states with the standard requirement $m_{\text{jj}} > 500\,\text{GeV}$ and with splitting the signal sample at $m_{\text{jj}} = 800\,\text{GeV}$. The errors are due to the limited Monte-Carlo statistics, in particular due to the $t\bar{t}$ background Monte-Carlo sample.

	Signal significance
$m_{\text{jj}} > 500\,\text{GeV}$	1.24 ± 0.19
$500\,\text{GeV} < m_{\text{jj}} < 800\,\text{GeV}$	0.67 ± 0.12
$m_{\text{jj}} > 800\,\text{GeV}$	1.36 ± 0.20

$\left.\begin{array}{c} \\ \\ \end{array}\right\}$ combined: 1.52 ± 0.19

by adding the individual signal significances in quadrature. The signal significance in different-flavor final states is improved by 23% using the described categorization. It is assumed that the systematic uncertainties on the different backgrounds as well as the correction factors from auxiliary measurements are independent of the m_{jj} region. However, the second assumption is not valid for the Z/γ^* and the top quark background where observed and predicted m_{jj}-distributions disagree in the corresponding control regions (see Figs. 5.20a and 5.24b). Also, systematic uncertainties are expected to increase when adding more cuts to the analysis. The influence on the estimated signal significance has not been studied.

Figures 5.41a and 5.41b show the m_{T}-distribution after the event selection in the low and high m_{jj} regions, respectively. While a large fraction of the background accumulates in the low sensitivity region, the high sensitivity ($m_{\text{jj}} > 800\,\text{GeV}$) region now has a signal-to-background ratio close to one in the lower m_{T}-range. The thresholds defining the four m_{T}-bins used for the standard analysis shown in Fig. 5.41 may not be optimal when applying the m_{jj}-split and need to be reevaluated ideally individually for the high- and the low-m_{jj} category.

The analysis can be further improved by optimizing the cuts in discriminating variables that are correlated with the dijet invariant mass separately for the low-m_{jj} and high-m_{jj} regions. Figure 5.42a shows, as an example, the two-dimensional m_{jj}-ΔY_{jj}-distribution for VBF Higgs boson signal events, where a significant correlation exists. Figure 5.42b shows the ΔY_{jj}-distributions for signal and background which are shifted to larger values in the high- compared to the low-m_{jj} region. While the standard requirement of $\Delta Y_{\text{jj}} > 2.8$ remains a good choice in the low-m_{jj} region, the selection can be improved by a stricter requirement in the high-m_{jj} regime.

(a) $500\,\mathrm{GeV} < m_{\mathrm{jj}} < 800\,\mathrm{GeV}$

(b) $m_{\mathrm{jj}} > 800\,\mathrm{GeV}$
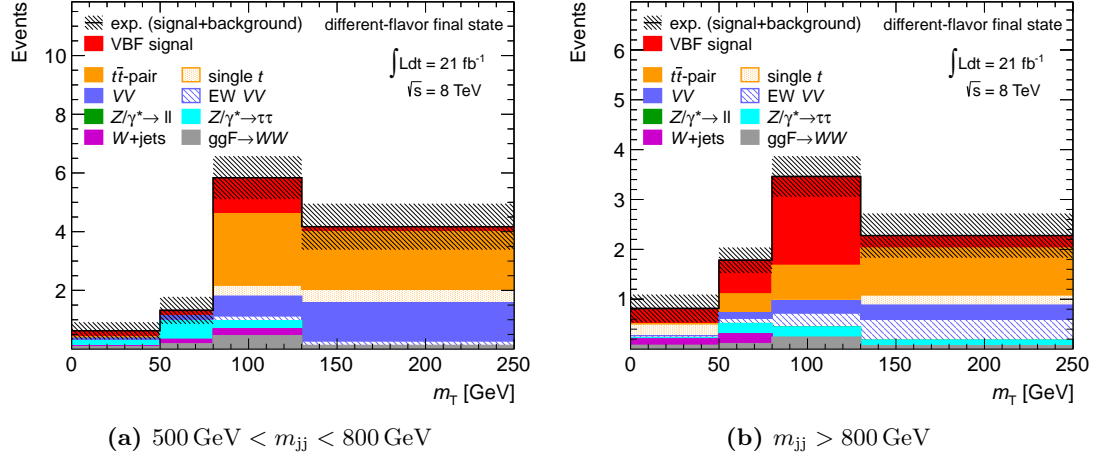
Figure 5.41: Expected m_{T}-distribution of different-flavor events after all signal selection criteria excluding the requirement on m_{T} for (a) the low and (b) the high sensitivity m_{jj} region. The signal is stacked on top of the backgrounds. The black hatched area represents the statistical uncertainty in the signal-plus-background prediction.

(a)

(b)
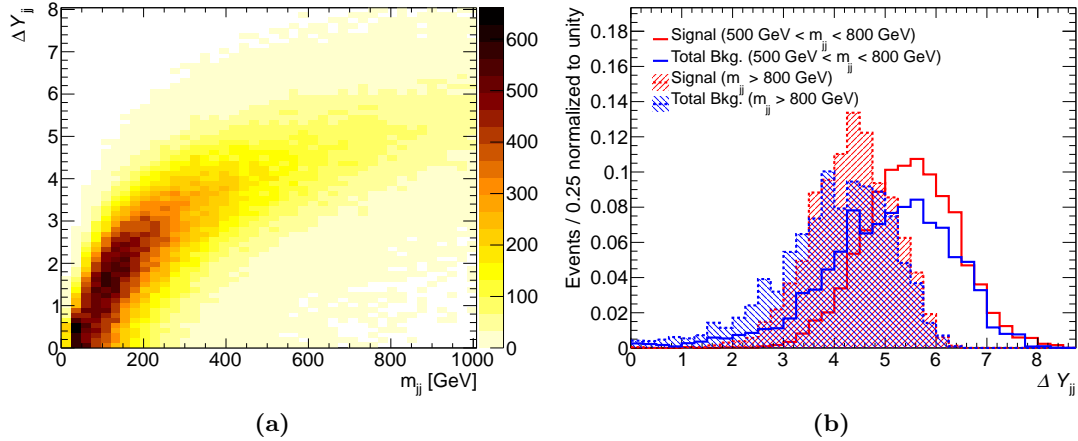
Figure 5.42: Illustration of the correlation between the dijet invariant mass m_{jj} and rapidity gap ΔY_{jj} in (a) the expected two-dimensional distribution for VBF Higgs boson signal events ($m_H = 125\,\mathrm{GeV}$) and in (b) the comparison of the expected ΔY_{jj}-distributions for signal and background in the high and low sensitivity m_{jj} regions. The distributions are shown after the preselection and Z rejection criteria.
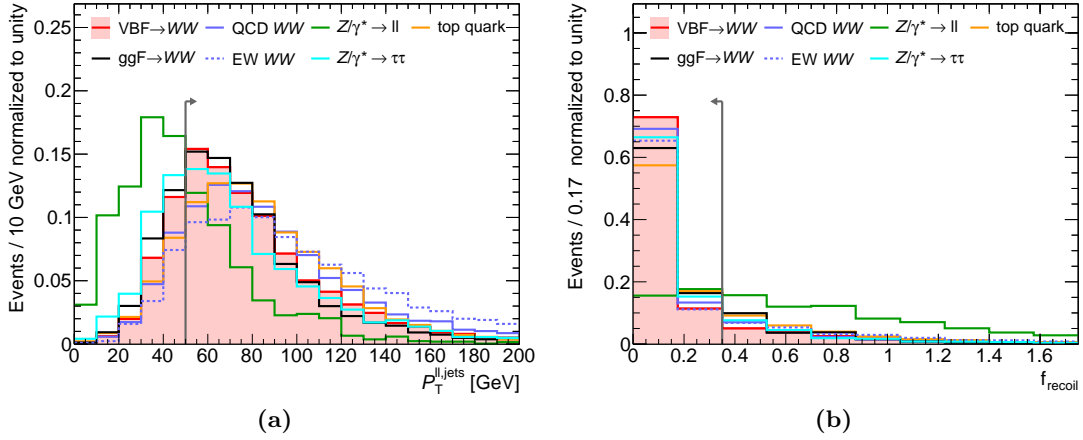
Figure 5.43: Expected distributions of (a) the transverse momentum $p_\mathrm{T}^{\ell\ell\mathrm{jets}}$ of the dilepton-plus-jets system and (b) the f_recoil variable after the requirement $p_\mathrm{T}^{\ell\ell\mathrm{jets}} > 50\,\mathrm{GeV}$ for the VBF signal ($m_H = 125\,\mathrm{GeV}$) and the different backgrounds. The distributions are normalized to unity.

Correlations are expected not only in dijet kinematic properties but also in the properties of the dijet-dilepton system. To fully exploit those correlations, a multi-variate approach may be used which accounts for correlations in an optimal way.

5.7.2 Background Rejection in Same-Flavor Final States

Due to the large additional $Z/\gamma^* \to \ell\ell$ background, same-flavor final states contribute only 5–10% to the total signal significance (see Table 5.19). Additional discriminating variables exploiting the $Z/\gamma^* \to \ell\ell$ topology, can be used to significantly reduce the $Z/\gamma^* \to \ell\ell$ background.

A characteristic property of $Z/\gamma^* \to \ell\ell$ events is the visible momentum balance due to the absence of neutrinos in the final state. Jets, predominantly from initial state radiation, recoil against the dilepton system. The total transverse momentum $p_\mathrm{T}^{\ell\ell\mathrm{jets}}$ of the dilepton-plus-jets system hence is expected to be small. Figure 5.43a shows the $p_\mathrm{T}^{\ell\ell\mathrm{jets}}$-distribution for the VBF $H \to WW^{(*)}$ signal, the $Z/\gamma^* \to \ell\ell$ and non-$Z/\gamma^* \to \ell\ell$ backgrounds. The variable shows a good separation between the signal and $Z/\gamma^* \to \ell\ell$ background. However, a significant fraction of reconstructed $Z/\gamma^* \to \ell\ell$ events has rather large values of $p_\mathrm{T}^{\ell\ell\mathrm{jets}}$. This is due to reconstructed objects, such as low-p_T jets, which

Table 5.23: Expected signal and background yields and signal significance $s/\sqrt{b+\sigma_b^2}$, with signal and background yields s and b, respectively and σ_b the systematic uncertainty in b. The errors are due to Monte-Carlo statistics.

	$N_{\mathrm{VBF}}^{\mathrm{exp}}$	$N_{Z/\gamma^* \rightarrow \ell\ell}^{\mathrm{exp}}$	$N_{\mathrm{non}\text{-}Z/\gamma^* \rightarrow \ell\ell}^{\mathrm{exp}}$	$s/\sqrt{b+\sigma_b^2}$
Standard selection	3.62 ± 0.09	16 ± 2	13 ± 2	0.38 ± 0.05
$p_{\mathrm{T}}^{\ell\ell\mathrm{jets}} > 50\,\mathrm{GeV}$	2.97 ± 0.08	6 ± 1	12 ± 2	0.50 ± 0.08
$f_{\mathrm{recoil}} < 0.35$	2.64 ± 0.08	2.7 ± 0.6	9 ± 1	0.63 ± 0.09

fail the object selection criteria and therefore do not enter in the $p_{\mathrm{T}}^{\ell\ell\mathrm{jets}}$ calculation. Such objects can recoil against the lepton-plus-jets system and lead to large values of $p_{\mathrm{T}}^{\ell\ell\mathrm{jets}}$ in $Z/\gamma^* \rightarrow \ell\ell$ events. The f_{recoil} variable,

$$f_{\mathrm{recoil}} = \frac{\sum |\mathrm{JVF}| \times p_{\mathrm{T}}^{\mathrm{jet}}}{p_{\mathrm{T}}^{\ell\ell\mathrm{jets}}} \quad , \tag{5.51}$$

measures the momentum recoil against the leptons-plus-jets system. The sum in the numerator is over all jets with $p_{\mathrm{T}}^{\mathrm{jet}} > 10\,\mathrm{GeV}$ in the ϕ-quadrant opposite to the direction of the $\boldsymbol{p}_{\mathrm{T}}^{\ell\ell\mathrm{jets}}$ vector. The jet vertex fraction JVF (Eq. (4.3)) is applied as a weight for each jet, to reduce the impact of jets originating from pile-up interactions. The distribution of the f_{recoil} variable after the requirement $p_{\mathrm{T}}^{\ell\ell\mathrm{jets}} > 50\,\mathrm{GeV}$ is shown in Fig. 5.43b. While the signal and non-$Z/\gamma^* \rightarrow \ell\ell$ backgrounds accumulate at small values of f_{recoil}, $Z/\gamma^* \rightarrow \ell\ell$ events have larger recoiling momenta.

An optimization using $s/\sqrt{b+\sigma_b^2}$ as figure of merit, as in the previous section, results in the highest signal significance for the requirements $p_{\mathrm{T}}^{\ell\ell\mathrm{jets}} > 50\,\mathrm{GeV}$ and $f_{\mathrm{recoil}} < 0.35$ indicated in Fig. 5.43. The numbers of expected signal and background events and the signal significance $s/\sqrt{b+\sigma_b^2}$ after applying these above requirements in addition to the standard selection are shown in Table 5.23. The $Z/\gamma^* \rightarrow \ell\ell$ background is reduced by almost a factor of six while more than 70% of the signal remains. The signal significance increases by 60% with respect to the standard analysis of same-flavor final states.

The new variables allow for a strong rejection of $Z/\gamma^* \rightarrow \ell\ell$ events, but rely on complex kinematic correlations between jets and leptons as well as on soft jet reconstruction, for which the predictions by Monte-Carlo simulation are less reliable. A detailed investigation of the modelling of these variables using data and a detailed study of

systematic uncertainties are still needed.

Additional discriminating variables improve the sensitivity in same-flavor final states by 60%, which increases the contribution of same-flavor final states to the total analysis sensitivity from 5% to 11%. Combining the improvement of the new variables in same-flavor final states with the m_{jj}-categorization for different-flavor final states the combined signal significance is expected to improve by 23%. In a further step the m_{jj}-categorization can also be applied to same-flavor final states leading to 32% expected improvement in signal significance compared to the standard analysis. A summary of the different analysis modifications comparing the corresponding expected signal significances is shown in Table 5.24.

All of the suggested improvements require a detailed understanding of the background predictions and of the systematic uncertainties. This may change the estimates given here. Nevertheless, it is worthwhile to further investigate these analysis modifications.

Table 5.24: Summary of the expected signal significance $Z = s/\sqrt{b + \sigma_b^2}$ for different-flavor (DF) and same-flavor (SF) final states as well as for their combination (DF+SF) for different analysis modifications. The contribution of same-flavor final states $(Z^{\mathrm{DF+SF}} - Z^{\mathrm{DF}})/Z^{\mathrm{DF+SF}}$ and the expected improvement in signal significance $(Z^{\mathrm{DF+SF}} - Z^{\mathrm{DF+SF}}_{\mathrm{standard}})/Z^{\mathrm{DF+SF}}_{\mathrm{standard}}$ of the combined final state with respect to the standard event selection are also shown.

$Z = s/\sqrt{b + \sigma_b^2}$	Z^{DF}	Z^{SF}	$Z^{\mathrm{DF+SF}}$	$\dfrac{Z^{\mathrm{DF+SF}} - Z^{\mathrm{DF}}}{Z^{\mathrm{DF+SF}}}$	$\dfrac{Z^{\mathrm{DF+SF}} - Z^{\mathrm{DF+SF}}_{\mathrm{standard}}}{Z^{\mathrm{DF+SF}}_{\mathrm{standard}}}$
Standard	1.24	0.38	1.30	5%	-
$f_{\mathrm{recoil}}/p_{\mathrm{T}}^{\ell\ell\mathrm{jets}}$ (SF)	1.24	0.63	1.39	11%	7%
m_{jj}-split (DF)	1.52	0.63	1.65	8%	23%
m_{jj}-split (SF)	1.52	0.78	1.71	11%	32%

Chapter 6

Combined Analysis of Higgs Production and Decay Channels

The results of the analysis of VBF Higgs boson production in $H \rightarrow WW^{(*)} \rightarrow \ell\nu\ell\nu$ decays presented in Chapter 5 are combined with the results for Higgs boson production and decays in other final state analyses. The Higgs boson properties obtained from the combined measurement are compared to the Standard Model predictions in order to probe for possible deviations. Two properties are discussed in particular in Sections 6.3 and 6.4: the signal strengths for different Higgs boson production channels and the Higgs boson couplings to vector bosons.

The results presented in this chapter are based on the combination of results for the three electroweak diboson final states $H \rightarrow \gamma\gamma$, $H \rightarrow WW^*$ with $W^{(*)} \rightarrow \ell\nu$ and $H \rightarrow ZZ^*$ with $Z^{(*)} \rightarrow \ell^+\ell^-$ [7]. The fermionic final states, such as the decay to b quarks or τ leptons are not included in the combination presented here. Results including the fermion final states can be found in [160].

In each of the weak diboson decay modes, the events are categorized such that the different Higgs boson production mechanisms are separated as much as possible. The analysis of the event category for VBF production in the $\ell\nu\ell\nu$ final state is the one presented in Chapter 5. A short description of the remaining analyses is given in Sections 6.1 and 6.2 for the $\ell\nu\ell\nu$ and for the diphoton and four-lepton final states, respectively. Details on the different analyses can be found in [86, 89, 91].

The analyses described below are based on the full dataset collected in the years 2011 and 2012, at $\sqrt{s} = 7\,\text{TeV}$ and $8\,\text{TeV}$. The 7 TeV and 8 TeV data are treated as separate event categories in the final combination.

6.1 The $\ell\nu\ell\nu$ Final State

For the analysis of the $\ell\nu\ell\nu$ final state, six event categories are built, distinguishing into same-flavor and different-flavor events as well as the jet multiplicity $n_{\mathrm{jet}} = 0, = 1$ and ≥ 2. The categories based on the jet multiplicity are in the following called *zero-jet*, *one-jet* and *inclusive two-jet*. The inclusive two-jet event categories are dedicated to the measurement of the VBF Higgs boson production rate, while the zero-jet and one-jet event categories are sensitive to ggF Higgs boson production. Analyses dedicated to the measurement of the VH Higgs boson production are described elsewhere [161].

The background composition differs between the different event categories as can be seen in Fig. 6.1. While the zero-jet category is dominated by Z/γ^* and WW background processes, the top quark background dominates the higher jet multiplicity event samples. The Z/γ^* background contributes more to same-flavor final states due to the contribution from $Z/\gamma^* \to \ell\ell$ decays. Because of the n_{jet}-dependent background composition, the selection criteria differ between the event categories (see Table 6.1). The definition of reconstructed objects and the preselection criteria are identical to those described in Chapter 4 and Section 5.3.

The main difference in the analysis of the VBF event categories compared to one of the ggF categories are the VBF topological criteria which are only applied for inclusive two-jet final states. The analyses of the ggF categories apply instead additional requirements to reduce the larger contribution of the Z/γ^* and diboson backgrounds. Kinematic properties of the Higgs boson decay are exploited using the missing transverse energy, the dilepton transverse momentum $p_{\mathrm{T}}^{\ell\ell}$ and the azimuthal angle $\Delta\phi_{\ell,\mathrm{MET}}$ between the dilepton system and the missing transverse energy. Additional suppression of the $Z/\gamma^* \to \ell\ell$ background in same-flavor final states can be achieved by exploiting the soft hadronic recoil against the dilepton-plus-jet system. The variable f_{recoil} defined in Eq. (5.51) is used for this purpose. Also, a modified definition of the missing transverse energy is employed,

$$
E_{\mathrm{T,rel}}^{\mathrm{miss}} = \begin{cases} E_{\mathrm{T}}^{\mathrm{miss}} \cdot \sin(\Delta\phi_{\mathrm{closest}}) & \Delta\phi_{\mathrm{closest}} \leq \pi/2 \\ E_{\mathrm{T}}^{\mathrm{miss}} & \Delta\phi_{\mathrm{closest}} > \pi/2 \end{cases}, \tag{6.1}
$$

where $\Delta\phi_{\mathrm{closest}}$ is the azimuthal angle between the $E_{\mathrm{T}}^{\mathrm{miss}}$ vector and the closest high-energy jet or lepton in the event. In same-flavor final states, additional suppression of
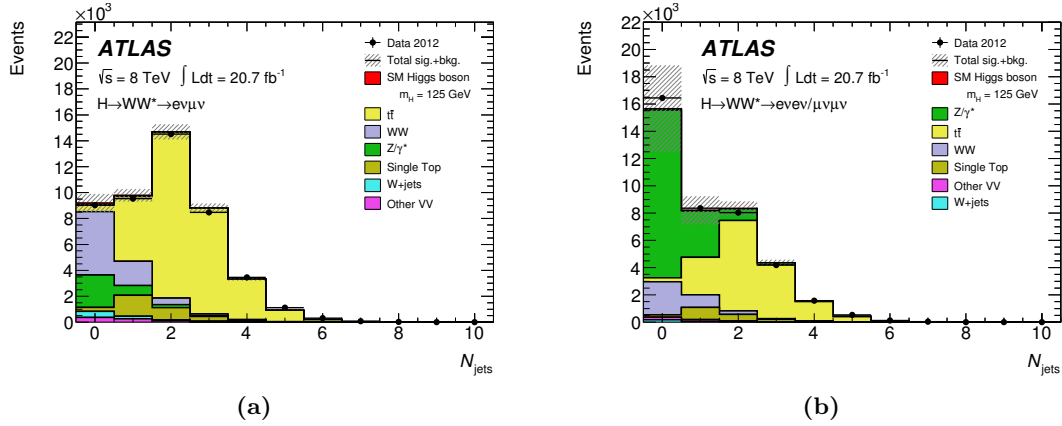
Figure 6.1: Expected and observed distributions of the jet multiplicity in events with two leptons and large missing transverse energy for (a) different-flavor and (b) same-flavor final states [7]. The hatched area corresponds to the statistical and systematic uncertainty.

the Z/γ^* background is achieved by a requirement on the track-based missing transverse momentum $p_{\mathrm{T,rel}}^{\mathrm{miss}}$ which is given by the total transverse momentum of charged tracks in the event replacing the $E_{\mathrm{T,STVF}}^{\mathrm{miss}}$ variable in the inclusive two-jet selection.

In the case of the different-flavor ggF categories, the events are split into a high- and low-sensitivity $m_{\ell\ell}$ region, corresponding to $10\,\mathrm{GeV} < m_{\ell\ell} < 30\,\mathrm{GeV}$ and $30\,\mathrm{GeV} < m_{\ell\ell} < 50\,\mathrm{GeV}$, respectively. The high-sensitivity region is more pure in signal, since the $m_{\ell\ell}$-distribution of backgrounds like diboson and top quark productions fall more rapidly with decreasing dilepton invariant mass than the signal distribution. Due to the stricter requirements for $Z/\gamma^* \to \ell\ell$ background reduction in same-flavor final states, fewer events pass the event selection compared to different-flavor final states. A weaker requirement on the dijet invariant mass of $m_{\ell\ell} < 50\,\mathrm{GeV}$ is, hence, applied to retain a sufficient number of same-flavor events. Considering the split in $m_{\ell\ell}$ for different-flavor zero and one-jet final states, in total six gluon fusion categories, three (one same-flavor and two different-flavor categories) for each jet multiplicity, are present.

While the WW background estimation in the VBF categories is solely based on simulation, it is determined by an auxiliary measurement in a dedicated control region in the ggF categories. The events in this control region are selected by removing the requirements on $\Delta\phi(\ell\ell)$ from the signal selection and requiring $50\,\mathrm{GeV} < m_{\ell\ell} < 100\,\mathrm{GeV}$ for the zero-jet and $m_{\ell\ell} > 80\,\mathrm{GeV}$ for the one-jet event category, respectively. The

Table 6.1: Summary of the $\ell\nu\ell\nu$ event selection criteria for the analysis of the dataset recorded in 2012. The criteria are applied equally to both lepton final states, unless indicated otherwise ("DF" for different-flavor, "SF" for same-flavor).

	ggF categories		VBF category
	$n_{\text{jet}} = 0$	$n_{\text{jet}} = 1$	$n_{\text{jet}} \geq 2$
Missing transverse momentum	DF: $E_{\text{T,rel}}^{\text{miss}} > 25\,\text{GeV}$ SF: $E_{\text{T,rel}}^{\text{miss}} > 45\,\text{GeV}$ SF: $p_{\text{T,rel}}^{\text{miss}} > 45\,\text{GeV}$		DF: $E_{\text{T}}^{\text{miss}} > 20\,\text{GeV}$ SF: $E_{\text{T}}^{\text{miss}} > 45\,\text{GeV}$ SF: $E_{\text{T,STVF}}^{\text{miss}} > 35\,\text{GeV}$
SF: f_{recoil}	< 0.05	< 0.2	-
General selection	$p_{\text{T}}^{\ell\ell} > 30\,\text{GeV}$ SF: $\|\Delta\phi_{\ell\ell,\text{MET}}\| > \pi/2$ - -	- - b-jet veto DF: $Z/\gamma^* \to \tau\tau$ veto	
	-		$p_{\text{T}}^{\text{tot}} > 45\,\text{GeV}$
VBF topology	- - - -		$m_{\text{jj}} > 500\,\text{GeV}$ $\Delta Y_{\text{jj}} > 2.8$ CJV OLV
Higgs boson decay topology	$m_{\ell\ell} < 50\,\text{GeV}$ DF: split in $m_{\ell\ell}$		$m_{\ell\ell} < 60\,\text{GeV}$ -
	$\Delta\phi(\ell\ell) < 1.8$ m_{T} fit		

W+jets and $Z/\gamma^* \to \tau\tau$ background contributions as well as the top quark background contribution in one-jet final states are estimated using the same methods as presented in Section 5.4 with selection criteria adapted for the zero- and one-jet analysis. The top quark background contribution in the zero-jet event categories is estimated using a control data sample with large missing transverse energy and without requirement on the jet multiplicity and a further constraint from a similar control region with b-jets [91].

The m_{T}-distribution of the combined zero- and one-jet events is shown in Fig. 6.2a, for the two dilepton final states and the 2011 and 2012 datasets combined. Fig. 6.2b shows the m_{T}-distribution of inclusive two-jet different-flavor events for the 2011 and 2012 datasets combined. An excess of events is observed, well compatible with the
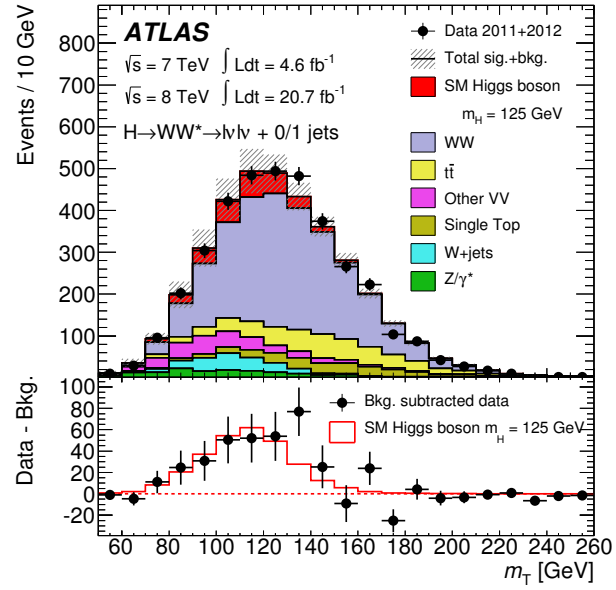
(a)
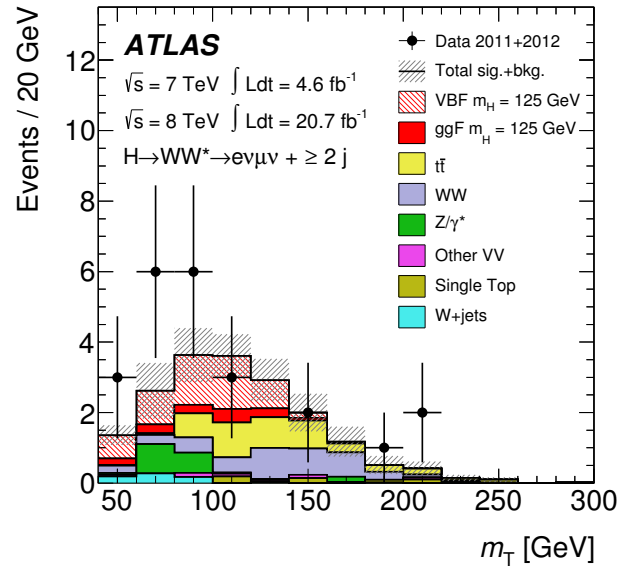
(b)

Figure 6.2: Expected and observed distributions of the transverse mass m_T for (a) the two dilepton final states and the zero-jet and one-jet categories combined and (b) for different-flavor final states in the inclusive two-jet category. Datasets of the years 2011 and 2012 are combined [7]. The hatched areas corresponds to the total systematic and statistical uncertainty in signal and background. The lower panel in (a) compares the data after background subtraction to the expected Standard Model Higgs boson signal.

151

prediction for a Standard Model Higgs boson with mass $m_H = 125\,\mathrm{GeV}$. As for the VBF analysis described in the previous chapter, a fit to the m_T-distribution of the data is performed for the zero- and one-jet categories. However, a different binning is chosen compared to the inclusive two-jet final states. The m_T-distribution is subdivided into five and three bins for the zero-jet and the one-jet channel, respectively. The bins are chosen such that they contain about the same amount of background. Combining the VBF and ggF event categories, the observed excess has a significance of 3.8 standard deviations for $m_H = 125.5\,\mathrm{GeV}$ corresponding to the combined mass measurement in the diphoton and the four-lepton Higgs boson decay channel (see next section).

6.2   The Diphoton and Four-Lepton Final State

Diphoton decays of the Higgs boson are selected requiring two well reconstructed isolated photons. The background is dominated by continuum $\gamma\gamma$ production with smaller contributions from γ+jet and dijet events. The expected background yield and shape is determined directly from data by fitting an analytic function to the diphoton invariant mass spectrum in a $m_{\gamma\gamma}$-range of $100-160\,\mathrm{GeV}$. The analysis is performed in mutually exclusive final states separating the VBF, VH and ggF production modes. The selection criteria defining the categories are summarized in Table 6.2. The categorization is performed in sequence, such that only events that failed the selection of previously listed categories are considered for the preceding categories.

VH **Categories** Three categories are defined depending on the decay products of the vector boson, either charged leptons, missing transverse energy for neutrinos or jets for hadronic decays. The latter is defined at low dijet invariant masses to be mutually exclusive with the VBF categories.

VBF Categories A multi-variate method called *Boosted Decision Tree* [162] (BDT) is used to combine several variables into one output BDT discriminator, exploiting the VBF topology. A tight (high signal-to-background ratio) and a loose (lower signal-to-background ratio) VBF category is defined by ranges in the BDT-discriminator.

ggF Categories From all events not passing the VH or VBF selections, categories with different signal-to-background ratio and different Higgs boson mass resolutions are built. The selection depends on weather or not one of the photons converted into an

Table 6.2: Categorization of diphoton final states in mutually exclusive categories dedicated to measure the VH, VBF and ggF production channels. The categorization is performed in sequence, i.e. events have to fail all selection requirements of previous categories.

	Category	Selection	Targeted process
VH	One-lepton	At least one electron or muon	$VH \to \ell\ell(\nu)\gamma\gamma$
	High-$E_{\mathrm{T}}^{\mathrm{miss}}$	$E_{\mathrm{T}}^{\mathrm{miss}}/\sigma_{E_{\mathrm{T}}^{\mathrm{miss}}} > 5$ with $\sigma_{E_{\mathrm{T}}^{\mathrm{miss}}} = 0.67[\sqrt{\mathrm{GeV}}]\sqrt{\Sigma E_{\mathrm{T}}}$	$VH \to \nu\nu(\ell)\gamma\gamma$
	Low-mass two-jet	$n_{\mathrm{jet}} \geq 2$ $60\,\mathrm{GeV} < m_{\mathrm{jj}} < 100\,\mathrm{GeV}$ $\Delta\eta_{\mathrm{jj}} < 3.5$ $p_{\mathrm{T}t} > 70\,\mathrm{GeV}$	$VH \to qq\gamma\gamma$
VBF	Loose	$n_{\mathrm{jet}} \geq 2$ $0.44 < \mathrm{BDT} < 0.74$	$qqH \to qq\gamma\gamma$
	Tight	$n_{\mathrm{jet}} \geq 2$ $\mathrm{BDT} > 0.74$	
ggF	Unconverted	Two unconverted photons	$H \to \gamma\gamma$
	Converted	At least one converted photon	
	Central	$|\eta| < 0.75$ for both photons	
	Rest	At least one non-central photon	
	High-$p_{\mathrm{T}t}$	$p_{\mathrm{T}t} > 60\,\mathrm{GeV}$	
	Low-$p_{\mathrm{T}t}$	$p_{\mathrm{T}t} < 60\,\mathrm{GeV}$	
	Converted transition	One converted photon One photon with $1.3 < |\eta| < 1.75$	

electron-positron pair, the photon pseudorapidities and the diphoton transverse momentum p_{Tt} orthogonal to the diphoton thrust axis in the transverse plain [163, 164]. The categories are combined, such that all 2^3 combinations exist. An additional category, *converted transition*, is added, where the mass resolution is particularly poor, due to the poor electron resolution in the transition region, leading to a total of nine ggF categories.

The analytical fit function is composed of a signal contribution described by the sum of a Chrystal Ball [165] and Gaussian function and a background contribution described by either a forth-order Bernstein polynomial [166], an exponential of a second-order polynomial or a single exponential function, depending on the event category.

The inclusive $m_{\gamma\gamma}$-distribution for both data taking years is shown in Fig. 6.3a together with the result of the fit. The maximum deviation from the background expectation is reached at $m_H = 126.8\,\mathrm{GeV}$. The significance of the observed excess is 7.4 standard deviations compared to 4.3 standard deviations expected for a Standard Model Higgs boson with $m_H = 126.8\,\mathrm{GeV}$. Figure 6.3b shows the $m_{\gamma\gamma}$ distribution of the VH and VBF categories. The significance of the excess observed here will be discussed in Section 6.3.

The search for Higgs boson decays into two Z bosons, each subsequently decaying to a pair of oppositely charged leptons, suffers from a small branching ratio. But the final state provides an excellent signal-to-background ratio, because of the large number of leptons. The dominant background is continuum $(Z^{(*)}/\gamma^*)(Z^{(*)}/\gamma^*)$ production with smaller contributions from Z boson production with additional jets and from $t\bar{t}$ productions.

Events are selected by requiring four well reconstructed energetic and isolated leptons with small impact parameters. The four-lepton invariant mass $m_{4\ell}$ is the final discriminating variable used for the statistical interpretation of the observed data. The observed and expected $m_{4\ell}$-distributions are shown in Fig. 6.4. The fitted signal corresponds to the Higgs boson mass of $m_H = 124.3\,\mathrm{GeV}$. The signal significance of the observed excess is 6.6 standard deviations while 4.4 standard deviations are expected for a Standard Model Higgs boson with $m_H = 124.3\,\mathrm{GeV}$.

As in the case of the $\ell\nu\ell\nu$ and diphoton channels, a categorization of final states is performed to separate out the different production mechanisms. VH and VBF production is separated from the dominant ggF production by requiring additional jets or leptons with kinematic properties expected for VH and VBF processes. Those are
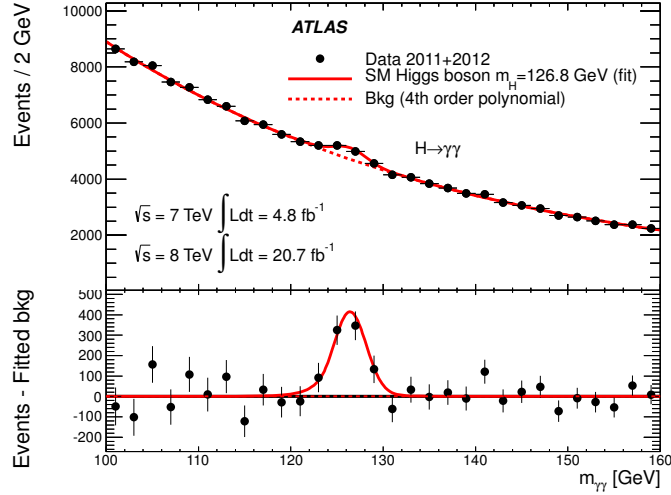
(a)
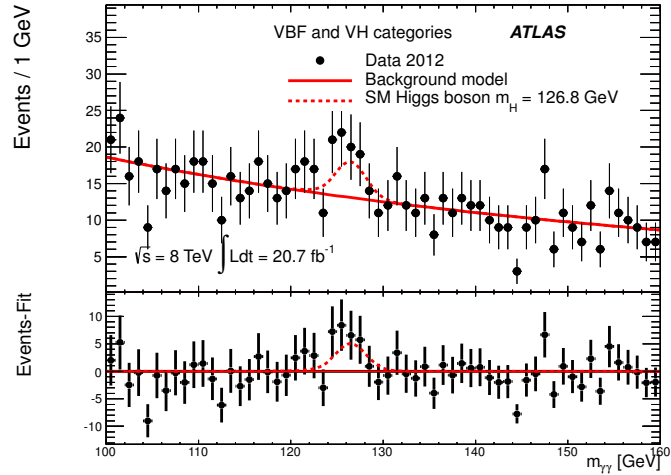
(b)

Figure 6.3: Invariant diphoton mass ($m_{\gamma\gamma}$) distribution for $H \to \gamma\gamma$ events (a) for all categories combined and (b) for the VH and VBF categories combining 7 TeV and 8 TeV data [7]. The fitted signal and background contributions for $m_H = 126.8$ GeV are also shown. The bottom figure shows the signal after background subtraction.

summarized in Table 6.3. The signal-to-background ratio, in particular for the VBF category, is very high. However, the number of expected events in the VBF category is very small due to the small production cross section and the small branching fraction, giving rise to large statistical uncertainties in the measurement of the VBF production rate in the four-lepton final state.
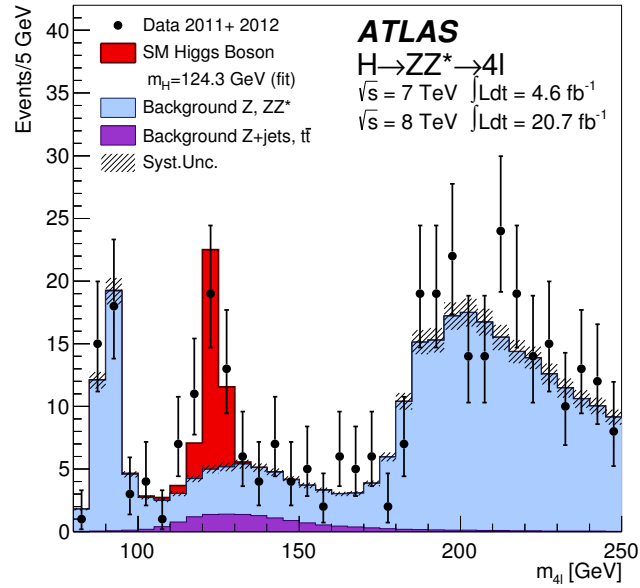
Figure 6.4: Observed four-lepton invariant mass distribution of selected $H \to ZZ^*$ events, combining the 7 TeV and 8 TeV data [7]. The fitted signal ($m_H = 124.3$ GeV) and the expected background contributions of the Standard Model Higgs boson are also shown.

The Higgs boson mass measurement in the four-lepton and diphoton final states are combined giving a value of

$$m_H = (125.5 \pm 0.6)\,\text{GeV} \qquad , \tag{6.2}$$

which is used for the signal strength and coupling measurements shown in the next section. The $\ell\nu\ell\nu$ final state does not contribute to the measurement of the Higgs boson mass, because of the poor mass determination in this final state.

Table 6.3: Categorization of four-lepton final states in mutually exclusive categories dedicated to measure the VBF, VH and ggF production channels.

Category	Selection
VBF	$n_{\mathrm{jet}} \geq 2$ $\Delta\eta_{\mathrm{jj}} > 3$ $m_{\mathrm{jj}} > 350\,\mathrm{GeV}$
VH	At least one additional lepton $p_{\mathrm{T}} > 8\,\mathrm{GeV}$
ggF	Not in VH or VBF category

6.3   Measurement of the Signal Production Strengths

A combined fit as described in Section 5.6.2 is performed comprising all final states described above. A signal strength

$$\mu = 1.33 \pm 0.20 \tag{6.3}$$

of all Higgs boson production and diboson decay modes is determined for a fixed mass of $m_H = 125.5\,\mathrm{GeV}$ assuming relative rates of the different production modes as in the Standard Model. The result is in good agreement with the Standard Model expectation. Statistical and systematic uncertainties contribute on similar level to the total uncertainty as shown in Fig. 6.5a which summarizes the result of the combined fit and of the measurements for individual production and decay event categories. The signal strength $\mu = 1.4^{+0.7}_{-0.6}$ obtained for VBF production in inclusive two-jet $\ell\nu\ell\nu$ final states can be compared to the result Eq. (5.49) in Section 5.6.3 of 1.66 ± 0.79, which treats the ggF production as a background while the former treats the ggF contribution as a signal. The results are well compatible.

The assumption that the relative contributions of the different production mechanisms follow the Standard Model predictions can be relaxed by measuring separately the signal strengths for vector boson mediated production ($\mu_{\mathrm{VBF}+VH} \times B/B_{\mathrm{SM}}$) and fermion mediated production ($\mu_{\mathrm{ggF}+ttH} \times B/B_{\mathrm{SM}}$) relative to the Standard Model for each decay channel. For this purpose, a simultaneous fit of these parameters is performed. The results for the three diboson final states are shown in Fig. 6.6. The sensitivity of
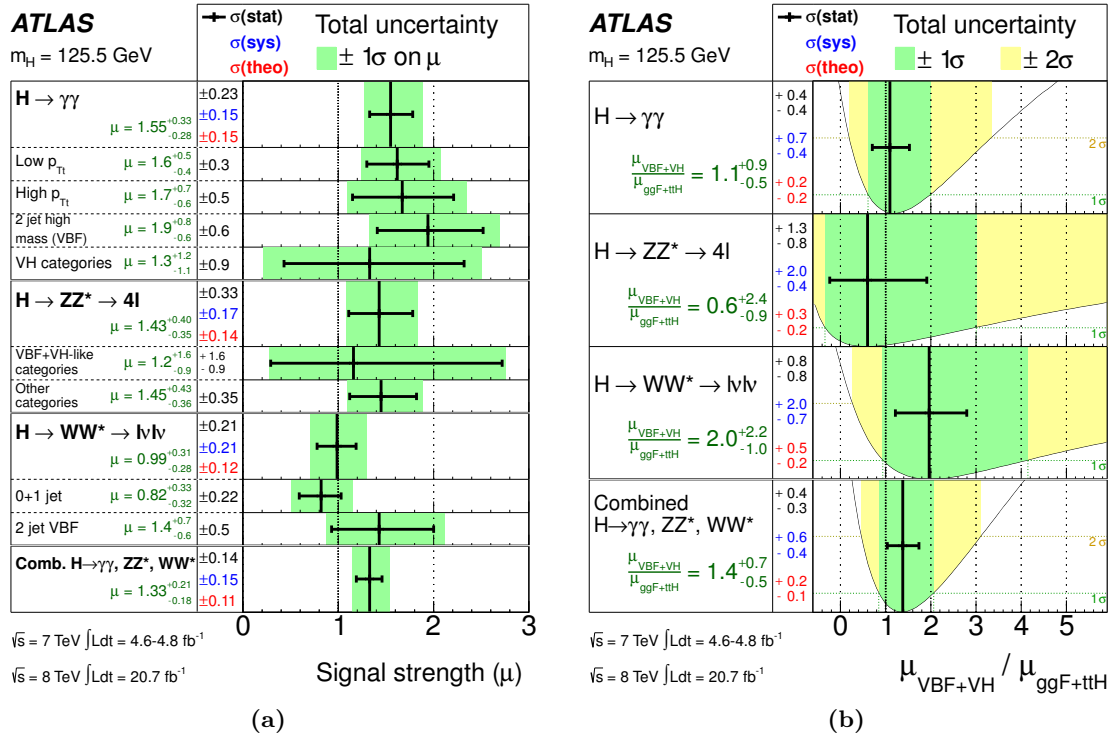
Figure 6.5: (a) Measured Higgs boson production strengths μ relative to the Standard Model expectation and (b) measurement of the ratio $\mu_{VBF+VH}/\mu_{ggF+ttH}$. Results are shown for a Higgs boson mass of 125.5 GeV, for each diboson final state separately and for their combination [7].

the VBF+VH measurement in the $\ell\nu\ell\nu$ channel presented in this thesis is comparable to the one in the diphoton final state. The four-lepton final state is less sensitive due to the small number of events in the VBF and VH event category*. The highest sensitivity ggF+ttH production strength measurement is achieved in the diphoton and four-lepton channels. Even though the absolute uncertainty in the $\ell\nu\ell\nu$ channel ggF+ttH measurement is of similar size as the one in the diphoton and four-lepton measurement (see Fig. 6.6) the $\ell\nu\ell\nu$ channel contributes less since the measured value is lower and hence, the relative uncertainty is larger.

The above results cannot be combined without making assumptions on the size of the different dibosonic branching fractions. A combination of the different final state

---

*The sharp lower edge of the four-lepton final state contour is due to the requirement of the total number of signal-plus-background events $\mu s + b$ to be positive, hence $\mu > -b/s$, and the small amount of expected background. There is no requirement on the sign of the signal strength itself.
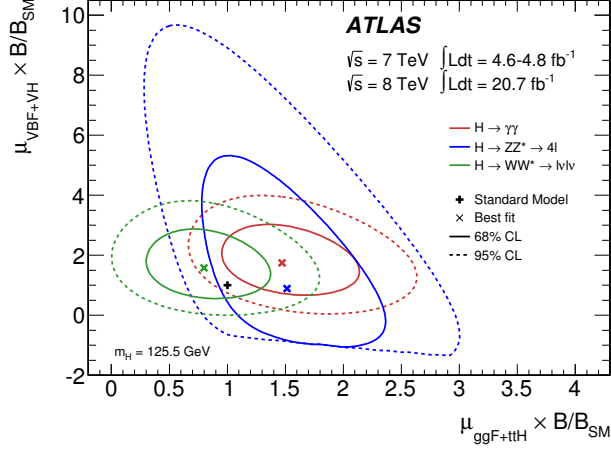
Figure 6.6: Profile likelihood ratio contours as a function of the production strength measurements in the diphoton, four-lepton and $\ell\nu\ell\nu$ channels [7].

results is therefore not possible in a model-independent way. This can be resolved by measuring the ratios,

$$\frac{\mu_{\mathrm{VBF}+VH} \times B/B_{\mathrm{SM}}}{\mu_{\mathrm{ggF}+ttH} \times B/B_{\mathrm{SM}}} \quad , \tag{6.4}$$

where the impact of the branching ratios B cancel. The results of fits of $\mu_{\mathrm{VBF}+VH}/\mu_{\mathrm{ggF}+ttH}$ as a free parameter are shown in Fig. 6.5b for the individual diboson channels and for their combination. Good agreement with the Standard Model expectation is found. The combined result is:

$$\frac{\mu_{\mathrm{VBF}+VH}}{\mu_{\mathrm{ggF}+ttH}} = 1.4^{+0.7}_{-0.5} \quad . \tag{6.5}$$

A similar test for VBF production alone, without the small VH contribution results in the same value

$$\frac{\mu_{\mathrm{VBF}}}{\mu_{\mathrm{ggF}+ttH}} = 1.4^{+0.7}_{-0.5} \quad . \tag{6.6}$$

The profiled likelihood ratio of this measurement as a function of $\mu_{\mathrm{VBF}}/\mu_{\mathrm{ggF}+ttH}$ is shown in Fig. 6.7. The probability of a vanishing VBF contribution is 0.04% corresponding to an 3.3 standard deviation evidence for VBF Higgs boson production. The sensitivity of the measurement is dominated by the diphoton channel since both ggF and VBF production measurements contribute to the ratio. The $\ell\nu\ell\nu$ channel contributes to this
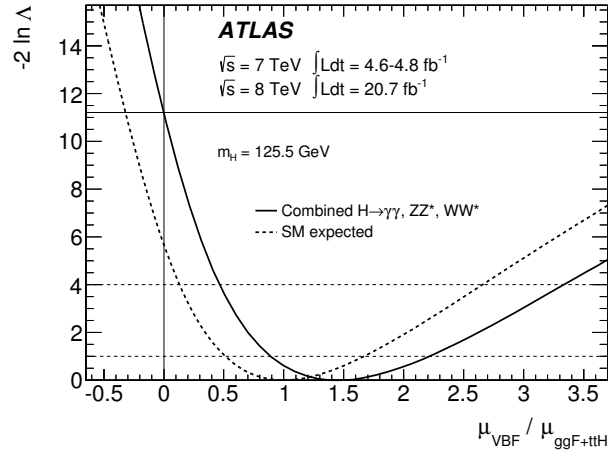
Figure 6.7: Observed and expected profiled log-likelihood ratio for the combined diphoton, four-lepton and $\ell\nu\ell\nu$ channels as a function of $\mu_{\mathrm{VBF}}/\mu_{\mathrm{ggF}+ttH}$ [7].

result with about 20%.

6.4 Measurement of Coupling Strengths

The measurement of the production strengths described above requires assumptions on the relative contributions of different Higgs boson production and decay processes. New physics processes beyond the Standard Model possibly modify both the production cross sections and the decay branching ratios. Such effects may not be visible by measuring only production and decay rates. In order to test for deviations from the Standard Model predictions in a model-independent way, the couplings of the Higgs boson to each Standard Model particle have to be measured. In this way correlations between production and decay strength are taken into account in different combinations of couplings. Two examples of coupling strength measurements to which the analysis presented in Chapter 5 contributes significantly are given below: The universal Higgs boson couplings to fermions and vector bosons, respectively, and the ratio between the Higgs boson coupling to W and Z bosons.

For the coupling measurements the production cross section times the branching ratio for the signal in the different event categories is expressed in terms of individual coupling strength parameters. A leading-order framework described in [167] is employed

which makes the following assumptions:

- The observed signal results from a single resonance with a mass of $m_H = 125.5\,\text{GeV}$, neglecting the uncertainty in the mass measurement.

- The width of the Higgs boson resonance is assumed to be negligible such that the production and decay process are independent and factorize. Hence, the product of the cross section and the branching ratio for a given channel $i \to H \to f$ can be decomposed as

$$\sigma \cdot B(i \to H \to f) = \frac{\sigma_i \cdot \Gamma_f}{\Gamma_H} \tag{6.7}$$

where σ_i is the production cross section through the initial state i, Γ_f the partial decay width into the final state f and Γ_H the total decay width of the Higgs boson.

- The boson under investigation is a CP-even scalar as predicted by the Standard Model (see Section 2.3) allowing only for modifications of the signal strengths, but not of the tensor structure of the Higgs boson coupling compared to the Standard Model.

A Higgs boson coupling scale factor κ_j is introduced for each process type $j = g,\ W,\ Z,\ \gamma,\ (\gamma Z)^*$ and fermions with respect to the Standard Model coupling strength. The partial decay widths Γ_{jj} and the production cross sections σ_{jj} are proportional to κ_j^2

$$\kappa_j^2 = \frac{\sigma_{jj}}{\sigma_{jj}^{\text{SM}}} = \frac{\Gamma_{jj}}{\Gamma_{jj}^{\text{SM}}} \quad . \tag{6.8}$$

where $\Gamma_{\gamma\gamma}$, $\Gamma_{\gamma Z}$ and σ_{gg} (also denoted as σ_{ggF}) are effective coupling strength for the decay to photons, to $Z\gamma$ and the gluon fusion production that can be parameterized as a function of κ_W and κ_{fermions} when assuming no beyond Standard Model contributions to the loops. Deviations of κ_j from unity would indicate new physics beyond the Standard Model.

As an example, the signal strength for the process $qq \to qqH \to qqWW$ (see Fig. 6.8a) studied in this thesis scales in the following way:

$$\mu_{\text{VBF}}^{H \to WW^{(*)}} = \frac{\sigma \times B(qq \to qqH \to qqWW)}{\sigma_{\text{SM}}(qq \to qqH) \times B_{\text{SM}}(H \to WW)} = \frac{\kappa_{\text{VBF}}^2 \cdot \kappa_W^2}{\kappa_H^2} \quad , \tag{6.9}$$

---

*The notation, adapted from [167], is slightly misleading for the decay to γZ due to two different particles in the final state. The corresponding scale factor is denoted with $\kappa_{(\gamma Z)}$.

where κ_H^2 is the scale factor for the total Higgs boson decay width and κ_{VBF} is the scale factor for VBF production given by

$$\kappa_{\mathrm{VBF}}^2(\kappa_W, \kappa_Z, m_H) = \frac{\kappa_W^2 \cdot \sigma_{W\mathrm{F}}(m_H) + \kappa_Z^2 \cdot \sigma_{Z\mathrm{F}}(m_H)}{\sigma_{W\mathrm{F}}(m_H) + \sigma_{Z\mathrm{F}}(m_H)} \quad , \tag{6.10}$$

where $\sigma_{W\mathrm{F}}$ and $\sigma_{Z\mathrm{F}}$ are the cross sections for the Higgs boson production via W and Z boson fusion, respectively, taken from [48]*.

The scale factor κ_H can be written as a function of the coupling scale factors κ_j,

$$\kappa_H^2(\kappa_j) = \sum_j \frac{\Gamma_{jj}(\kappa_j)}{\Gamma_H^{\mathrm{SM}}} = \sum_j \frac{\kappa_j^2 \Gamma_{jj}^{\mathrm{SM}}}{\Gamma_H^{\mathrm{SM}}} \quad , \tag{6.11}$$

with $j = W$, Z, γ, g and all Standard Model fermions dominated by bottom quarks. Parameterizing the total width as a function of couplings to Standard Model particles assumes no additional decays into particles beyond the Standard Model. For the ggF production as well as for the Higgs boson decay to photon pairs effective coupling scale factors κ_{ggF} and κ_γ are introduced which, similarly as in the case of κ_{VBF}, can be written as a function of the scale factors κ_W, κ_b, κ_t and κ_τ (see Fig. 6.8b and [167]), assuming that only the heaviest fermions contribute to the loops. For κ_γ the interference term between the top quark and W boson loop cannot be neglected such that κ_γ depends on a term $\kappa_t \cdot \kappa_W$, mixing fermion and vector boson coupling strengths.

The measured signal strength for the different production and decay channels can now be described in terms of the scale factors κ_j. Due to the limited data statistics, it is not possible to perform a fit of all coupling scale factors. Instead, assumptions are made such that the couplings to all fermions (F) have equal scale factors $\kappa_F := \kappa_t = \kappa_b = \kappa_\tau$ and similarly all couplings to vector bosons (V) $\kappa_V := \kappa_W = \kappa_Z$. The relative contribution of vector bosons and fermions to the $H \to \gamma\gamma$ loop are expected to follow the Standard Model predictions. The result of a fit to the observed data with κ_F and κ_V as free parameters is shown in Fig. 6.9 for the individual final states and their combination. Only the diphoton channel is sensitive to the relative sign of κ_F and κ_V due to the interference between W boson and top quark loops in $H \to \gamma\gamma$ decays (see Fig. 6.8b). The measurement is not sensitive to the absolute sign of either the vector boson or

---

*VBF Higgs boson production is predicted by the Standard Model to occur with about 75 (25)% probability through W (Z) boson fusion. Interference, between W and Z boson fusion is found to be smaller than 0.1% and can be ignored [47].

(a)

(b)
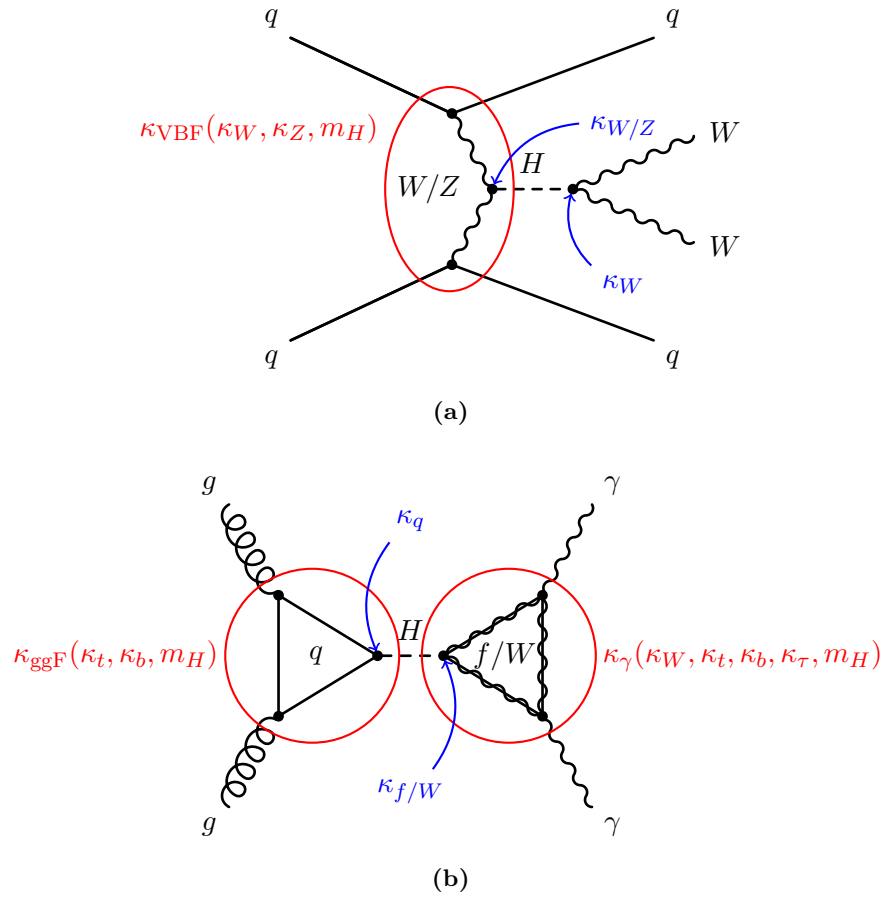
Figure 6.8: Dependence of the processes (a) $qq \to qqH \to qqWW$ and (b) $gg \to H \to \gamma\gamma$ on the coupling scale factors κ_j illustrated on their lowest-order Feynman diagrams.
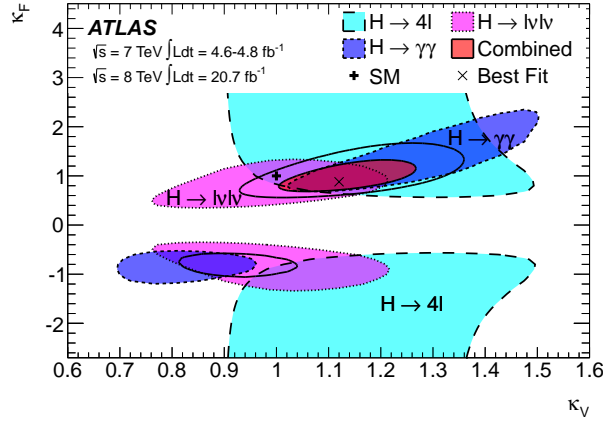
Figure 6.9: Profile likelihood ratio contours (68% CL) as a function of the fermion and weak vector boson coupling scale factors κ_F and κ_V, respectively, for the different final states considered and for their combination [7]. For the combined measurement also the 95% CL contour is shown.

fermion coupling scale factor. Hence, the measurement is only shown for $\kappa_V > 0$. The measurement favors the $\kappa_F > 0$ as in the Standard Model. However, also negative κ_F-values are compatible with the data at the two standard deviation level. The 68% CL intervals

$$0.76 \quad \leq \kappa_F \leq \quad 1.18 \tag{6.12}$$

$$1.05 \quad \leq \kappa_V \leq \quad 1.22 \tag{6.13}$$

are obtained when profiling over κ_V and κ_F, respectively. The presented measurement has access to the fermion coupling only via the ggF- and $H \to \gamma\gamma$-loops. The sensitivity of the κ_F measurement significantly increase when the decays to b quarks and τ leptons are added to the combination [160].

The custodial symmetry in the Standard Model requires that the couplings of the W and Z boson to the Higgs boson are identical as described in Section 2.1. This can be tested by measuring the ratio $\lambda_{WZ} = \kappa_W/\kappa_Z$. The ratio is measured in decays into WW^* and ZZ^* normalized to the Standard Model expectation,

$$\lambda_{WZ}^2 = \frac{B(H \to WW^*)/B(H \to ZZ^*)}{B_{\mathrm{SM}}(H \to ZZ^*)/B_{\mathrm{SM}}(H \to WW^*)} \quad . \tag{6.14}$$

where no assumptions on the different production mechanisms are needed. The fit to
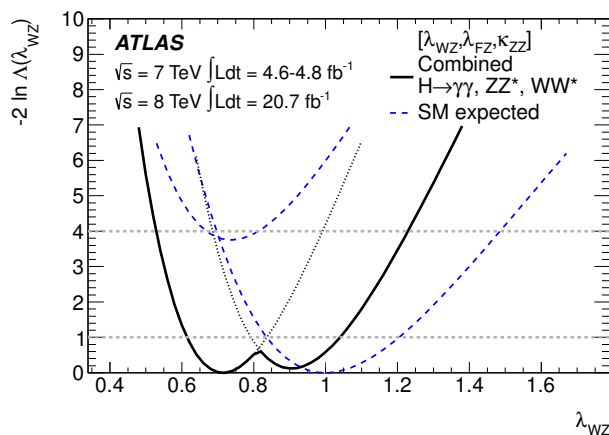
Figure 6.10: Observed and expected profile log-likelihood ratio as a function of the coupling scale factor probing the custodial symmetry [7]. The dotted line indicates the continuation of the observed likelihood ratio for the second solution.

the data profiling $\mu_{\mathrm{ggF}+ttH} \times B(H \to ZZ^*)/B_{\mathrm{SM}}(H \to ZZ^*)$ gives $\lambda_{WZ} = 0.81^{+0.16}_{-0.15}$ in agreement with Standard Model prediction $\lambda_{WZ} = 1$.

A more sensitive measurement can be achieved if information from the VH and VBF production modes and from the $H \to \gamma\gamma$ decay mode are included. The likelihood function can then be parameterized in terms of three free parameters: λ_{WZ}, $\lambda_{FZ} = \kappa_F \kappa_Z / \kappa_H$ and $\kappa_{ZZ} = \kappa_Z \kappa_Z / \kappa_H$* assuming absence of new physics contributing to the loops. A fit to the data with profiled λ_{FZ} and κ_{ZZ} parameters gives the log-likelihood ratio as a function of λ_{WZ} shown in Fig. 6.10. The 68% CL interval is found to be:

$$0.61 \leq \lambda_{WZ} \leq 1.04 \tag{6.15}$$

in agreement with the expectation from the Standard Model.

New physics can lead to loop contributions to the $H \to \gamma\gamma$ decay, causing deviations of λ_{WZ} from unity without violating the custodial symmetry. Therefore, a test is performed with the additional profiled parameter $\lambda_{\gamma Z} = \kappa_\gamma / \kappa_Z$ introduced to absorb effects of hypothetical particles beyond the Standard Model. This measurement gives

$$\lambda_{WZ} = 0.82 \pm 0.15 \quad . \tag{6.16}$$

---

*Using λ_{FZ} and κ_{ZZ} as profiled parameters rather than κ_Z and κ_F has the advantage that no assumptions on the total Higgs boson width are needed.

All measurements discussed in this chapter show no significant deviation from the Standard Model predictions for a Higgs boson with $m_H \approx 125\,\mathrm{GeV}$. The precision of the measurements increases when the fermion final states are added to the combination (see [160]) and when more data at higher energies becomes available. Assuming that the theoretical uncertainties will halve, the precision of the measurements presented above are expected to decrease by roughly a factor of three and an other factor of two for $300\,\mathrm{fb}^{-1}$ and $3000\,\mathrm{fb}^{-1}$ of proton-proton collisions at $\sqrt{s} = 14\,\mathrm{TeV}$, respectively [168]. An integrated luminosity of $300\,\mathrm{fb}^{-1}$ is expected to be delivered by the LHC by 2022 and $3000\,\mathrm{fb}^{-1}$ is the goal of the High-Luminosity-LHC [169].

Chapter 7

Summary

The Standard Model successfully describes the interactions between elementary particles based on the principle of local gauge symmetry. The predictions of the Standard Model have been experimentally verified with high precision. The discovery of a new boson with mass of $(125.5 \pm 0.6)\,\mathrm{GeV}$ and $(125.7 \pm 0.4)\,\mathrm{GeV}$ compatible with the Standard Model Higgs boson by the LHC experiments ATLAS and CMS, respectively, completes the experimental verification of the Standard Model particle content. The properties of the Higgs boson candidate have been compared to the Standard Model predictions, e.g. by measurements of the different production and decay rates. A measurement of the Vector Boson Fusion (VBF) production rate in decays into two W bosons each decaying into a muon or electron and a neutrino, $H \to WW^{(*)} \to \ell\nu\ell\nu$, has been performed in this thesis.

The VBF production has a characteristic signature with two jets with large dijet invariant mass and rapidity gap accompanying the Higgs boson. At low Higgs boson masses, the $H \to WW^{(*)} \to \ell\nu\ell\nu$ decay is characterized by small dilepton opening angles and invariant masses. The event selection achieves signal-to-background ratios of 0.4 and 0.1 with different-flavor ($e\nu\mu\nu$) and same-flavor ($e\nu e\nu/\mu\nu\mu\nu$) final states, respectively. Diboson, top quark, Drell-Yan and single W boson production dominate the background. The yields of top quark, W boson and Drell-Yan background are determined from auxiliary measurements using signal depleted control data. The diboson background is determined from Monte-Carlo simulation. Gluon fusion (ggF) production contributes to the background as well and is determined from $H \to WW^{(*)} \to \ell\nu\ell\nu$ events enriched in ggF production.

Due to the two invisible neutrinos in the final state, the Higgs boson mass cannot be directly reconstructed. Instead, the transverse mass m_{T}, determined from the lepton

four-momenta and the missing transverse energy, is used as final discriminating variable. Since the transverse mass gives a rather poor Higgs boson mass determination the analysis relies on mass measurements in diphoton and four-lepton Higgs boson decays with a combined result of $m_H = 125.5\,\text{GeV}$ by the ATLAS experiment.

Proton-proton collision data recorded by the ATLAS detector at a center-of-mass energy of $8\,\text{TeV}$ and corresponding to an integrated luminosity of $21\,\text{fb}^{-1}$ has been analyzed. After the event selection, 23 (42) events are observed in the different-flavor (same-flavor) channel, where 5 ± 1 (4 ± 1) signal and 12 ± 5 (34 ± 8) background events are expected. The observed m_T-distribution is interpreted in terms of a background-only and a signal-plus-background hypothesis. With the latter Standard Model Higgs boson production via vector boson fusion is excluded in a mass range of $152\,\text{GeV} \leq m_H \leq 185\,\text{GeV}$.

For $m_H = 125\,\text{GeV}$, an excess of events compared to the background-only expectation is observed with a significance of 2.8 standard deviations. The same-flavor channel contributes only 7% to the total significance due to the larger Drell-Yan background in this final state. The measured signal strength, the observed event rate relative to the vector boson fusion production rate in the Standard Model for $m_H = 125\,\text{GeV}$ is $2.1^{+1.0}_{-0.8}$. The uncertainty is dominated by statistics, systematic uncertainties contribute only about 25% to the total uncertainty. The dominant systematic uncertainties are from the jet energy scale and resolution as well as from cross section predictions for signal and background processes.

The measurement presented has been combined with ATLAS measurements of other diboson decays of the Higgs boson resulting in an evidence of VBF Higgs boson production with a significance of 3.3 standard deviations. The analysis furthermore contributes to the combined measurement of Higgs boson couplings to vector bosons and to the test of the custodial symmetry of the Standard Model predicting equal couplings of the Higgs boson to W and Z bosons. The results show no significant deviation from the Standard Model predictions. More precise tests will be performed at upcoming runs of the LHC at center-of-mass energies of 13–14 TeV and integrated luminosities of about $300\,\text{fb}^{-1}$ expected by the end of the decade.

Appendices

Appendix A

Monte-Carlo Samples

In this chapter details, such as the number of generated events N_{events}, the cross section times branching fraction $\sigma \times \mathcal{B}$ used to normalize the simulated events to the measured luminosity, the generator filter efficiency ϵ_{filter} and the integrated luminosity $\int L \text{dt}$, to which the amount of simulated events corresponds are given for the different Monte-Carlo samples used in the analysis. The event generators are listed in Table 5.1.

Table A.1: Number of simulated events N_{events} and the expected rate $(\sigma \times \mathcal{B})$ of the VBF Higgs boson process for different Higgs boson masses m_H including the corresponding integrated luminosity calculated taking into account the generator filter efficiency ϵ_{filter}.

$m_H[\text{GeV}]$	N_{events}	$\sigma \times \mathcal{B}[\text{pb}]$	ϵ_{filter}	$\int L \, \text{dt}[\text{fb}^{-1}]$
110	300000	0.0091	0.46	71509.2
115	299899	0.016	0.48	40115.3
120	299900	0.024	0.49	24872.5
125	300000	0.036	0.51	16610.9
130	299899	0.048	0.52	12056.4
135	299999	0.061	0.53	9384.4
140	299998	0.073	0.53	7697.4
145	299899	0.084	0.54	6606.0
150	299999	0.094	0.55	5872.4
155	99998	0.10	0.55	1764.5
160	99999	0.11	0.56	1582.9
165	99898	0.11	0.56	1539.3
170	100000	0.11	0.56	1592.9
175	100000	0.11	0.57	1668.0
180	100000	0.099	0.57	1774.3
185	99900	0.086	0.57	2028.0
190	99900	0.077	0.57	2272.5
195	99998	0.072	0.57	2461.0
200	99900	0.068	0.57	2584.2

Table A.2: Number of simulated events N_{events} and the expected rate ($\sigma \times \mathcal{B}$) of the WH Higgs boson process for different Higgs boson masses m_H including the corresponding integrated luminosity calculated taking into account the generator filter efficiency $\epsilon_{\mathrm{filter}}$.

$m_H[\mathrm{GeV}]$	N_{events}	$\sigma \times \mathcal{B}[\mathrm{pb}]$	$\epsilon_{\mathrm{filter}}$	$\int L\,\mathrm{dt}[\mathrm{fb}^{-1}]$
110	20000	0.0052	1.0	3822.1
115	15000	0.0083	1.0	1812.9
120	20000	0.012	1.0	1696.2
125	20000	0.016	1.0	1272.1
130	20000	0.019	1.0	1031.6
135	20000	0.022	1.0	890.1
140	19999	0.025	1.0	806.8
145	20000	0.026	1.0	762.6
150	20000	0.027	1.0	743.6
155	20000	0.027	1.0	737.9
160	20000	0.027	1.0	744.8
165	20000	0.026	1.0	765.7
170	20000	0.024	1.0	848.6
175	20000	0.021	1.0	952.0
180	20000	0.018	1.0	1085.6
185	20000	0.015	1.0	1316.2
190	20000	0.013	1.0	1557.8
195	20000	0.011	1.0	1777.4
200	20000	0.010	1.0	1999.3

Table A.3: Number of simulated events N_{events} and the expected rate $(\sigma \times \mathcal{B})$ of the ZH Higgs boson process for different Higgs boson masses m_H including the corresponding integrated luminosity calculated taking into account the generator filter efficiency ϵ_{filter}.

$m_H[\text{GeV}]$	N_{events}	$\sigma \times \mathcal{B}[\text{pb}]$	ϵ_{filter}	$\int L \, \text{dt}[\text{fb}^{-1}]$
110	20000	0.0028	1.0	6805.5
115	20000	0.0046	1.0	4329.4
120	20000	0.0066	1.0	3014.1
125	20000	0.0089	1.0	2247.4
130	20000	0.011	1.0	1810.5
135	20000	0.013	1.0	1549.5
140	20000	0.014	1.0	1394.0
145	20000	0.015	1.0	1310.0
150	20000	0.016	1.0	1267.9
155	20000	0.016	1.0	1247.8
160	20000	0.016	1.0	1243.8
165	20000	0.016	1.0	1271.4
170	20000	0.014	1.0	1403.7
175	20000	0.013	1.0	1570.9
180	20000	0.011	1.0	1797.9
185	20000	0.0092	1.0	2174.7
190	20000	0.0078	1.0	2571.0
195	20000	0.0068	1.0	2931.9
200	20000	0.0061	1.0	3284.9

Table A.4: Number of simulated events N_{events} and the expected rate ($\sigma \times \mathcal{B}$) of the ggF Higgs boson process for different Higgs boson masses m_H including the corresponding integrated luminosity calculated taking into account the generator filter efficiency ϵ_{filter}.

$m_H[\text{GeV}]$	N_{events}	$\sigma \times \mathcal{B}[\text{pb}]$	ϵ_{filter}	$\int L\,\text{dt}[\text{fb}^{-1}\,]$
110	499998	0.13	0.44	9090.9
115	500000	0.21	0.46	5251.4
120	497397	0.31	0.48	3337.0
125	500000	0.44	0.49	2311.2
130	499900	0.56	0.5	1728.7
135	499299	0.71	0.51	1379.8
140	499998	0.82	0.52	1165.2
145	499999	0.92	0.53	1028.7
150	499798	1.99	0.54	933.7
155	200000	1.10	0.54	346.3
160	200000	1.10	0.55	319.8
165	199997	1.10	0.55	329.0
170	200000	1.9	0.56	350.9
175	200000	0.95	0.56	376.0
180	199999	0.87	0.56	413.3
185	199900	0.74	0.56	484.2
190	200000	0.65	0.56	546.6
195	199499	0.59	0.56	600.7
200	199999	0.55	0.56	639.9

Table A.5: Number of simulated events N_{events} and the expected rate ($\sigma \times \mathcal{B}$) of top quark processes including the corresponding integrated luminosity calculated taking into account the generator filter efficiency ϵ_{filter}. The simulation of the $t\bar{t}$ process uses a generator dilepton filter indicated with (2ℓ).

Process	N_{events}	$\sigma \times \mathcal{B}[\text{pb}]$	ϵ_{filter}	$\int L\,\text{dt}[\text{fb}^{-1}\,]$
$t\bar{t}$ (2ℓ)	9977340	238.2143	0.11	399.2
t-channel $\to e$	2000000	9.86	1.0	211.0
t-channel $\to \mu$	1991000	9.86	1.0	210.0
t-channel $\to \tau$	1999000	9.86	1.0	210.9
s-channel $\to e$	999000	0.61	1.0	1648.5
s-channel $\to \mu$	998000	0.61	1.0	1646.9
s-channel $\to \tau$	999000	0.61	1.0	1648.5
Wt	4967000	22.202	1.0	222.0

Table A.6: Number of simulated events N_{events} and the expected rate ($\sigma \times \mathcal{B}$) of WW QCD processes including the corresponding integrated luminosity calculated taking into account the generator filter efficiency ϵ_{filter}.

Process	N_{events}	$\sigma \times \mathcal{B}[\text{pb}]$	ϵ_{filter}	$\int L\,\text{dt}[\text{fb}^{-1}]$
$gg \to WW \to ee\nu\nu$	30000	0.024	1.0	1271.2
$gg \to WW \to e\mu\nu\nu$	30000	0.021	1.0	1442.3
$gg \to WW \to e\tau\nu\nu$	30000	0.021	1.0	1442.3
$gg \to WW \to \mu\mu\nu\nu$	30000	0.024	1.0	1271.2
$gg \to WW \to \mu e\nu\nu$	30000	0.021	1.0	1442.3
$gg \to WW \to \mu\tau\nu\nu$	30000	0.021	1.0	1442.3
$gg \to WW \to \tau\tau\nu\nu$	30000	0.024	1.0	1271.2
$gg \to WW \to \tau e\nu\nu$	30000	0.021	1.0	1442.3
$gg \to WW \to \tau\mu\nu\nu$	30000	0.021	1.0	1442.3
$q\bar{q}, qg \to WW \to ee\nu\nu$	300000	0.63	1.0	475.4
$q\bar{q}, qg \to WW \to \mu e\nu\nu$	300000	0.63	1.0	475.4
$q\bar{q}, qg \to WW \to \tau e\nu\nu$	300000	0.63	1.0	475.4
$q\bar{q}, qg \to WW \to e\mu\nu\nu$	300000	0.63	1.0	475.4
$q\bar{q}, qg \to WW \to \mu\mu\nu\nu$	300000	0.63	1.0	475.4
$q\bar{q}, qg \to WW \to \tau\mu\nu\nu$	300000	0.63	1.0	475.4
$q\bar{q}, qg \to WW \to e\tau\nu\nu$	300000	0.63	1.0	475.4
$q\bar{q}, qg \to WW \to \mu\tau\nu\nu$	300000	0.63	1.0	475.4
$q\bar{q}, qg \to WW \to \tau\tau\nu\nu$	299999	0.63	1.0	475.4

Table A.7: Number of simulated events N_{events} and the expected rate ($\sigma \times \mathcal{B}$) of QCD ZZ processes including the corresponding integrated luminosity calculated taking into account the generator filter efficiency ϵ_{filter}.

Process	N_{events}	$\sigma \times \mathcal{B}[\text{pb}]$	ϵ_{filter}	$\int L\, \text{dt}[\text{fb}^{-1}\,]$
$q\bar{q}, qg \to ZZ \to 4e$	599998	0.074	0.91	8993.8
$q\bar{q}, qg \to ZZ \to 2e2\mu$	599799	0.17	0.83	4245.1
$q\bar{q}, qg \to ZZ \to 2e2\tau$	599899	0.17	0.58	6026.8
$q\bar{q}, qg \to ZZ \to 4\mu$	600000	0.074	0.91	8946.9
$q\bar{q}, qg \to ZZ \to 2\mu2\tau$	600000	0.17	0.59	5981.9
$q\bar{q}, qg \to ZZ \to 4\tau$	300000	0.074	0.11	38491.4
$q\bar{q}, qg \to ZZ \to ee\nu\nu$	299400	0.17	1.0	1782.1
$q\bar{q}, qg \to ZZ \to \mu\mu\nu\nu$	300000	0.17	1.0	1785.7
$q\bar{q}, qg \to ZZ \to \tau\tau\nu\nu$	299999	0.17	1.0	1785.7
$gg \to ZZ \to 4e$	90000	0.00067	1.0	134328.4
$gg \to ZZ \to 4\mu$	89699	0.00067	1.0	133879.1
$gg \to ZZ \to 2e2\mu$	89899	0.0014	1.0	66591.9

Table A.8: Number of simulated events N_{events} and the expected rate ($\sigma \times \mathcal{B}$) of WZ, $W\gamma$ and $W\gamma^*$ QCD diboson processes including the corresponding integrated luminosity calculated taking into account the generator filter efficiency ϵ_{filter}. For the WZ sample a generator filter requiring two charged leptons with $m_{\ell\ell} > 7\,\text{GeV}$ is applied. The $W\gamma^*$ samples are simulated for a γ^* decay with $m_{\ell\ell} < 7\,\text{GeV}$. For part of the $W\gamma$ samples a lepton-plus-photon filter, indicated with $(1\ell + 1\gamma)$, is employed.

Process	N_{events}	$\sigma \times \mathcal{B}[\text{pb}]$	ϵ_{filter}	$\int L\,dt[\text{fb}^{-1}]$
$W^+Z \to e\nu ee$	190000	1.13	0.29	458.4
$W^+Z \to e\nu\mu\mu$	190000	0.94	0.35	575.1
$W^+Z \to e\nu\tau\tau$	76000	0.17	0.17	2609.3
$W^+Z \to \mu\nu ee$	189999	1.13	0.29	462.7
$W^+Z \to \mu\nu\mu\mu$	190000	0.95	0.35	567.1
$W^+Z \to \mu\nu\tau\tau$	76000	0.17	0.17	2581.3
$W^+Z \to \tau\nu ee$	75400	1.13	0.14	377.2
$W^+Z \to \tau\nu\mu\mu$	76000	0.94	0.18	443.7
$W^+Z \to \tau\nu\tau\tau$	19000	0.17	0.06	1888.8
$W^-Z \to e\nu ee$	189899	0.98	0.3	652.9
$W^-Z \to e\nu\mu\mu$	190000	0.64	0.35	842.3
$W^-Z \to e\nu\tau\tau$	76000	0.11	0.16	4230.4
$W^-Z \to \mu\nu ee$	190000	0.94	0.3	682.0
$W^-Z \to \mu\nu\mu\mu$	190000	0.65	0.35	826.9
$W^-Z \to \mu\nu\tau\tau$	76000	0.11	0.16	4216.2
$W^-Z \to \tau\nu ee$	76000	0.94	0.15	548.6
$W^-Z \to \tau\nu\mu\mu$	76000	0.64	0.19	637.5
$W^-Z \to \tau\nu\tau\tau$	19000	0.11	0.06	3029.7
$W\gamma^* \to l\nu ee$	399699	5.51	1.0	71.4
$W\gamma^* \to l\nu\mu\mu$	299800	1.13	1.0	217.6
$W\gamma^* \to l\nu\tau\tau$	30000	0.15	1.0	203.8
$W\gamma + 0\,\text{partons}\,(1\ell + 1\gamma)$	14296300	229.2070	0.31	198.2
$W\gamma + 1\,\text{parton}\,(1\ell + 1\gamma)$	5393980	59.536	0.45	202.0
$W\gamma + 2\,\text{partons}\,(1\ell + 1\gamma)$	2899390	21.193	0.54	248.9
$W\gamma + 3\,\text{partons}\,(1\ell + 1\gamma)$	859697	7.64	0.63	191.7
$W\gamma + 4\,\text{partons}$	364999	2.19	1.0	172.0
$W\gamma + 5\,\text{or more partons}$	60000	0.47	1.0	128.7

Table A.9: Number of simulated events N_{events} and the expected rate ($\sigma \times \mathcal{B}$) of electroweak diboson and Drell-Yan processes including the corresponding integrated luminosity calculated taking into account the generator filter efficiency ϵ_{filter}.

Process	N_{events}	$\sigma \times \mathcal{B}[\text{pb}]$	ϵ_{filter}	$\int L \, dt[\text{fb}^{-1}]$
$WW \to \ell\nu\ell\nu + 2$ jets from EW	199898	0.039	1.0	5125.6
$WZ \to \ell\ell\ell\nu + 2$ jets from EW	20000	0.013	1.0	1592.5
$ZZ \to \ell\ell\nu\nu + 2$ jets from EW	100000	0.0011	1.0	81208.4
$ZZ \to \ell\ell\ell\ell + 2$ jets from EW	499994	0.00074	1.0	679635.2
$Z \to ee + 2$ jets from EW	499996	0.36	1.0	1392.8
$Z \to \mu\mu + 2$ jets from EW	499898	0.36	1.0	1394.7
$Z \to \tau\tau + 2$ jets from EW	499896	0.46	1.0	1084.7

Table A.10: Number of simulated events N_{events} and the expected rate ($\sigma \times \mathcal{B}$) of Drell-Yan QCD processes with $10\,\text{GeV} < m_{\ell\ell} < 60\,\text{GeV}$ including the corresponding integrated luminosity calculated taking into account the generator filter efficiency ϵ_{filter}. The processes for which a dilepton filter was employed are indicated with (2ℓ).

Process	N_{events}	$\sigma \times \mathcal{B}[\text{pb}]$	ϵ_{filter}	$\int L \, dt[\text{fb}^{-1}]$
$Z \to ee + 0$ partons (2ℓ)	6994180	3477.31302	0.01	192.3
$Z \to ee + 1$ parton (2ℓ)	4497280	108.979	0.2	202.9
$Z \to ee + 2$ partons (2ℓ)	1468390	52.476	0.14	200.8
$Z \to ee + 3$ partons (2ℓ)	438397	11.102	0.21	186.6
$Z \to ee + 4$ partons (2ℓ)	108930	2.24	0.25	166.8
$Z \to ee + 5$ or more partons	112180	0.69	1.0	162.0
$Z \to \mu\mu + 0$ partons (2ℓ)	6984690	3477.31300	0.01	184.9
$Z \to \mu\mu + 1$ parton (2ℓ)	4491590	108.979	0.21	195.8
$Z \to \mu\mu + 2$ partons (2ℓ)	1503400	52.476	0.14	199.7
$Z \to \mu\mu + 3$ partons (2ℓ)	153599	11.102	0.21	63.6
$Z \to \mu\mu + 4$ partons (2ℓ)	108890	2.24	0.26	163.2
$Z \to \mu\mu + 5$ or more partons	115000	0.69	1.0	165.8
$Z \to \tau\tau + 0$ partons (2ℓ)	27969	3477.31302	0.0	330.3
$Z \to \tau\tau + 1$ parton (2ℓ)	30000	108.979	0.0	202.8
$Z \to \tau\tau + 2$ partons (2ℓ)	27610	52.476	0.0	300.3
$Z \to \tau\tau + 3$ partons (2ℓ)	29600	11.102	0.0	675.7
$Z \to \tau\tau + 4$ partons	365497	2.24	1.0	141.0
$Z \to \tau\tau + 5$ or more partons	114420	0.69	1.0	165.1

Table A.11: Number of simulated events N_{events} and the expected rate ($\sigma \times \mathcal{B}$) of Drell-Yan QCD processes with $60\,\text{GeV} < m_{\ell\ell} < 2\,\text{TeV}$ including the corresponding integrated luminosity calculated taking into account the generator filter efficiency ϵ_{filter}. The processes for which a dilepton filter was employed are indicated with (2ℓ). Samples employing a VBF filter, requiring two jets with large dijet invariant mass and rapidity gap, are indicated with (VBF) and are used in the analysis if the selection criteria m_{jj} and ΔY_{jj} are already applied.

Process	N_{events}	$\sigma \times \mathcal{B}[\text{pb}]$	ϵ_{filter}	$\int L\,\text{dt}[\text{fb}^{-1}\,]$
$Z \to ee + 0\,\text{partons}$	6604280	711.6407	1.0	9.3
$Z \to ee + 1\,\text{parton}$	1329990	155.1397	1.0	8.6
$Z \to ee + 2\,\text{partons}$	404798	48.439	1.0	8.3
$Z \to ee + 3\,\text{partons}$	109998	14.128	1.0	7.7
$Z \to ee + 4\,\text{partons}$	30000	3.35	1.0	8.0
$Z \to ee + 5\,$ or more partons	295000	1.10	1.0	260.3
$Z \to \mu\mu + 0\,\text{partons}$	6389980	712.6409	1.0	9.0
$Z \to \mu\mu + 1\,\text{parton}$	1334900	154.1394	1.0	8.6
$Z \to \mu\mu + 2\,\text{partons}$	404897	48.441	1.0	8.3
$Z \to \mu\mu + 3\,\text{partons}$	110000	14.128	1.0	7.7
$Z \to \mu\mu + 4\,\text{partons}$	29999	3.35	1.0	7.9
$Z \to \mu\mu + 5\,$ or more partons	303498	1.10	1.0	267.6
$Z \to \tau\tau + 0\,\text{partons}\,(2\ell)$	5468790	712.6409	0.04	193.8
$Z \to \tau\tau + 1\,\text{parton}\,(2\ell)$	2459600	155.1395	0.05	335.8
$Z \to \tau\tau + 2\,\text{partons}\,(2\ell)$	513399	48.440	0.05	198.9
$Z \to \tau\tau + 3\,\text{partons}\,(2\ell)$	176599	14.128	0.06	211.1
$Z \to \tau\tau + 4\,\text{partons}\,(2\ell)$	29600	3.35	0.07	114.8
$Z \to \tau\tau + 5\,$ or more partons	308896	1.10	1.0	271.8
$Z \to ee + 0\,\text{partons}\,(\text{VBF})$	6419080	712.6409	0.03	268.9
$Z \to ee + 1\,\text{parton}\,(\text{VBF})$	3394290	155.1395	0.08	270.7
$Z \to ee + 2\,\text{partons}\,(\text{VBF})$	3134990	48.440	0.25	260.7
$Z \to ee + 3\,\text{partons}\,(\text{VBF})$	1636800	14.128	0.47	246.0
$Z \to ee + 4\,\text{partons}\,(\text{VBF})$	653597	3.35	0.68	253.8
$Z \to \mu\mu + 0\,\text{partons}\,(\text{VBF})$	1261800	712.6409	0.01	272.3
$Z \to \mu\mu + 1\,\text{parton}\,(\text{VBF})$	1584690	155.1395	0.04	266.9
$Z \to \mu\mu + 2\,\text{partons}\,(\text{VBF})$	1734590	48.441	0.14	251.3
$Z \to \mu\mu + 3\,\text{partons}\,(\text{VBF})$	1345590	14.128	0.35	268.2
$Z \to \mu\mu + 4\,\text{partons}\,(\text{VBF})$	534799	3.35	0.59	238.0

Appendix B

Background Composition

In this chapter tables showing the event yields after the different stages of the signal selection are presented where the different considered backgrounds are further broken down into their components.

The event yields of different diboson processes are shown in Tables B.1 and B.2 for different-flavor and same-flavor events, respectively. W boson and Z boson pair processes with higher-order electroweak (EW) and QCD jet production are given separately. Diboson event yields with higher-order QCD jet production from WZ and $W\gamma^{(*)}$ processes are given as well. Since the contribution of $W\gamma^{(*)}$ processes with higher-order electroweak jet production is expected to be small and no simulated sample exist for this process only the WZ electroweak process is included in the analysis and shown in the table.

The top quark background broken down into the contribution from top-quark-pair production ($t\bar{t}$), single top quark production in association with a W boson (Wt), the single top t- and the s-channel production (see also Fig. 5.5) is shown in Table B.3. A breakdown of Z/γ^* processes in their decays to muons or electrons as well as to τ leptons is shown in Table B.4. The yields are shown separately for processes with higher-order electroweak and QCD jet production (see also Fig. 5.6).

Table B.1: Expected event yields of the different considered diboson processes throughout the different stages of the signal selection in different-flavor events. The errors are due to Monte-Carlo statistics.

	$N_{\text{QCD }WW}$	$N_{\text{EW }WW}$	$N_{WZ/W\gamma^*/W\gamma}$	$N_{\text{EW }WZ}$	$N_{\text{QCD }ZZ}$	$N_{\text{EW }ZZ}$
Preselection	946±8	62.0±0.6	312±15	6.3±0.3	28.3±0.4	0.363±0.005
$m_{\ell\ell} > 10\,\text{GeV}$	946±8	62.0±0.6	310±15	6.3±0.3	28.2±0.4	0.363±0.005
$E_T^{\text{miss}} > 20\,\text{GeV}$	881±7	58.7±0.6	274±15	5.7±0.3	18.9±0.3	0.277±0.004
b-jet veto	648±6	37.1±0.5	186±7	3.0±0.2	13.6±0.3	0.155±0.003
$p_T^{\text{tot}} < 45\,\text{GeV}$	559±6	31.9±0.4	143±7	2.2±0.2	9.4±0.2	0.087±0.003
$Z \to \tau\tau$ veto	514±6	29.8±0.4	131±7	2.0±0.2	7.9±0.2	0.077±0.003
$\Delta Y_{jj} > 2.8$	85±2	15.3±0.3	23±3	0.9±0.1	1.27±0.09	0.032±0.002
$m_{jj} > 500\,\text{GeV}$	22±1	12.1±0.3	4.6±0.6	0.7±0.1	0.23±0.04	0.025±0.002
Central jet veto	15.6±1.0	9.8±0.2	2.3±0.4	0.32±0.07	0.14±0.03	0.011±0.001
Outside lepton veto	10.3±0.8	8.4±0.2	1.6±0.3	0.3±0.07	0.11±0.03	0.008±0.001
$m_{\ell\ell} < 60\,\text{GeV}$	2.5±0.4	1.38±0.09	0.5±0.2	0.09±0.04	0.03±0.02	0.0025±0.0007
$\Delta\phi(\ell\ell) < 1.8$	2.3±0.4	1.2±0.08	0.5±0.2	0.09±0.04	0.012±0.008	0.0018±0.0006
$m_T \leq 1.2 \cdot m_H$	1.6±0.3	0.77±0.07	0.4±0.2	0.09±0.04	0.009±0.007	0.0011±0.0004

Table B.2: Expected event yields of the different considered diboson processes throughout the different stages of the signal selection in same-flavor events. The errors are due to Monte-Carlo statistics.

	$N_{\text{QCD } WW}$	$N_{\text{EW } WW}$	$N_{WZ/W\gamma^*/W\gamma}$	$N_{\text{EW } WZ}$	$N_{\text{QCD } ZZ}$	$N_{\text{EW } ZZ}$
Preselection	945±8	62.3±0.6	903±15	30.2±0.7	396±2	8.82±0.05
$m_{\ell\ell} > 12\,\text{GeV}$	942±8	62.2±0.6	896±15	30.1±0.7	394±2	8.8±0.05
$Z \to \ell\ell$ veto	745±7	51.7±0.5	301±13	9.1±0.4	91.9±0.8	1.31±0.02
$E_{\text{T}}^{\text{miss}} > 45\,\text{GeV}$	522±6	40.3±0.5	173±10	6.4±0.3	23.8±0.5	0.81±0.01
$E_{\text{T,STVF}}^{\text{miss}} > 35\,\text{GeV}$	498±6	39.0±0.5	156±9	6.0±0.3	20.2±0.5	0.77±0.01
b-jet veto	369±5	24.3±0.4	109±7	3.3±0.2	14.5±0.4	0.47±0.01
$p_{\text{T}}^{\text{tot}} < 45\,\text{GeV}$	315±4	20.8±0.3	78±5	2.2±0.2	11.2±0.4	0.38±0.01
$\Delta Y_{\text{jj}} > 2.8$	50±2	10.9±0.2	9±1	0.8±0.1	1.6±0.1	0.211±0.008
$m_{\text{jj}} > 500\,\text{GeV}$	14.9±0.9	8.6±0.2	3±1	0.7±0.1	0.32±0.06	0.17±0.007
Central jet veto	9.8±0.8	6.8±0.2	2±1	0.39±0.09	0.22±0.05	0.13±0.007
Outside lepton veto	6.5±0.6	5.9±0.2	2±1	0.31±0.08	0.09±0.03	0.115±0.006
$m_{\ell\ell} < 60\,\text{GeV}$	2.0±0.3	1.19±0.08	1±1	0.14±0.05	0.02±0.02	0.025±0.003
$\Delta\phi(\ell\ell) < 1.8$	1.8±0.3	1.0±0.07	1±1	0.12±0.05	0.02±0.02	0.022±0.003
$m_{\text{T}} \leq 1.2 \cdot m_H$	1.2±0.3	0.6±0.06	1±1	0.07±0.03	0.02±0.02	0.01±0.002

Table B.3: Expected event yields of the different considered top quark processes throughout the different stages of the signal selection. The expected yields are corrected with the auxiliary measurement in the top quark control region. The errors are due to Monte-Carlo statistics.

	$N_{t\bar{t}}$	N_{Wt}	$N_{\text{t-channel}}$	$N_{\text{s-channel}}$
Preselection	43236±73	2437±21	16±2	0.5±0.1
$m_{\ell\ell} > 10\,\text{GeV}$	43203±73	2436±21	16±2	0.5±0.1
$E_\text{T}^\text{miss} > 20\,\text{GeV}$	40604±71	2282±20	14±2	0.5±0.1
b-jet veto	2930±21	345±8	5±1	0.02±0.02
$p_\text{T}^\text{tot} < 45\,\text{GeV}$	2318±18	282±8	4.0±0.9	0.02±0.02
$Z \to \tau\tau$ veto	2147±18	260±7	3.9±0.9	0.02±0.02
$\Delta Y_\text{jj} > 2.8$	376±7	54±3	1.0±0.4	0.0±0.0
$m_\text{jj} > 500\,\text{GeV}$	93±3	11±1	0.2±0.2	0.0±0.0
Central jet veto	30±1	5.1±0.8	0.1±0.1	0.0±0.0
Outside lepton veto	22±1	4.2±0.7	0.1±0.1	0.0±0.0
$m_{\ell\ell} < 60\,\text{GeV}$	4.5±0.7	0.7±0.3	0.0±0.0	0.0±0.0
$\Delta\phi(\ell\ell) < 1.8$	3.7±0.6	0.7±0.3	0.0±0.0	0.0±0.0
$m_\text{T} \leq 1.2 \cdot m_H$	2.8±0.6	0.5±0.3	0.0±0.0	0.0±0.0

(a) different-flavor final states

	$N_{t\bar{t}}$	N_{Wt}	$N_{\text{t-channel}}$	$N_{\text{s-channel}}$
Preselection	43421±74	2413±21	15±2	0.5±0.1
$m_{\ell\ell} > 12\,\text{GeV}$	43296±73	2404±21	15±2	0.5±0.1
$Z \to \ell\ell$ veto	33924±65	1904±19	9±1	0.4±0.1
$E_\text{T}^\text{miss} > 45\,\text{GeV}$	24756±56	1390±16	6±1	0.26±0.09
$E_\text{T,STVF}^\text{miss} > 35\,\text{GeV}$	23824±55	1340±16	5±1	0.25±0.09
b-jet veto	1745±16	200±6	2.6±0.7	0.05±0.04
$p_\text{T}^\text{tot} < 45\,\text{GeV}$	1373±14	168±6	2.4±0.7	0.05±0.04
$\Delta Y_\text{jj} > 2.8$	253±5	35±2	0.5±0.3	0.0±0.0
$m_\text{jj} > 500\,\text{GeV}$	62±2	9±1	0.2±0.2	0.0±0.0
Central jet veto	19±1	4.1±0.7	0.0±0.0	0.0±0.0
Outside lepton veto	14±1	3.1±0.6	0.0±0.0	0.0±0.0
$m_{\ell\ell} < 60\,\text{GeV}$	3.7±0.6	0.8±0.3	0.0±0.0	0.0±0.0
$\Delta\phi(\ell\ell) < 1.8$	3.3±0.5	0.7±0.3	0.0±0.0	0.0±0.0
$m_\text{T} \leq 1.2 \cdot m_H$	1.8±0.4	0.4±0.2	0.0±0.0	0.0±0.0

(b) same-flavor final states

Table B.4: Expected event yields of the different considered Z/γ^* processes throughout the different stages of the signal selection. The expected yields are corrected with the auxiliary measurement in the Z boson enriched control regions. The errors are due to Monte-Carlo statistics.

	$N_{\text{QCD } Z/\gamma^* \to \ell\ell}$	$N_{\text{EW } Z/\gamma^* \to \ell\ell}$	$N_{\text{QCD } Z/\gamma^* \to \tau\tau}$	$N_{\text{EW } Z/\gamma^* \to \tau\tau}$
Preselection	142±24	0.9±0.1	2113±20	17.5±0.7
$m_{\ell\ell} > 10\,\text{GeV}$	141±24	0.9±0.1	2108±20	17.5±0.7
$E_{\text{T}}^{\text{miss}} > 20\,\text{GeV}$	112±22	0.6±0.1	1671±18	15.5±0.6
b-jet veto	63±16	0.38±0.08	1223±15	10.2±0.5
$p_{\text{T}}^{\text{tot}} < 45\,\text{GeV}$	46±14	0.24±0.07	1045±14	8.8±0.5
$Z \to \tau\tau$ veto	30±11	0.08±0.03	567±10	4.6±0.3
$\Delta Y_{\text{jj}} > 2.8$	5±4	0.04±0.03	88±4	2.7±0.3
$m_{\text{jj}} > 500\,\text{GeV}$	0.8±0.3	0.04±0.03	16±2	1.8±0.2
Central jet veto	0.1±0.1	0.04±0.03	8±1	1.6±0.2
Outside lepton veto	0.1±0.1	0.04±0.03	5.5±1.0	1.6±0.2
$m_{\ell\ell} < 60\,\text{GeV}$	0.0±0.0	0.0±0.0	3.7±0.8	0.7±0.1
$\Delta\phi(\ell\ell) < 1.8$	0.0±0.0	0.0±0.0	1.4±0.5	0.4±0.1
$m_{\text{T}} \leq 1.2 \cdot m_H$	0.0±0.0	0.0±0.0	1.3±0.5	0.4±0.1

(a) different-flavor final states

	$N_{\text{QCD } Z/\gamma^* \to \ell\ell}$	$N_{\text{EW } Z/\gamma^* \to \ell\ell}$	$N_{\text{QCD } Z/\gamma^* \to \tau\tau}$	$N_{\text{EW } Z/\gamma^* \to \tau\tau}$
Preselection	899339±1967	4213±9	2148±20	18.3±0.7
$m_{\ell\ell} > 12\,\text{GeV}$	895581±1967	4213±9	2136±20	18.3±0.7
$Z \to \ell\ell$ veto	112052±537	445±3	2029±19	16.6±0.7
$E_{\text{T}}^{\text{miss}} > 45\,\text{GeV}$	10739±159	43.5±0.9	772±12	10.4±0.5
$E_{\text{T,STVF}}^{\text{miss}} > 35\,\text{GeV}$	4711±93	23.2±0.7	673±11	9.7±0.5
b-jet veto	3290±76	13.5±0.5	499±9	6.7±0.4
$p_{\text{T}}^{\text{tot}} < 45\,\text{GeV}$	2354±65	9.1±0.4	424±9	6.0±0.4
$\Delta Y_{\text{jj}} > 2.8$	500±33	4.1±0.3	53±3	3.2±0.3
$m_{\text{jj}} > 500\,\text{GeV}$	119±4	2.8±0.2	18±2	2.4±0.3
Central jet veto	61±3	2.0±0.2	10±1	2.1±0.2
Outside lepton veto	41±3	1.6±0.2	7±1	1.8±0.2
$m_{\ell\ell} < 60\,\text{GeV}$	22±2	0.27±0.07	6.1±1.0	1.3±0.2
$\Delta\phi(\ell\ell) < 1.8$	19±2	0.2±0.06	4.5±0.9	1.2±0.2
$m_{\text{T}} \leq 1.2 \cdot m_H$	15±2	0.08±0.04	4.5±0.9	1.2±0.2

(b) same-flavor final states

Appendix C

Top Quark Background Uncertainty

The default Monte-Carlo generator for $t\bar{t}$ processes MC@NLO+HERWIG fails to describe the dijet distributions correctly, which leads to a correction factor $\alpha_{\text{top quark}} = 0.6$ when requirements on the dijet kinematics are applied (see Section 5.4.3). The background determination procedure corrects for those mis-descriptions, however, whether the description in the signal region shows the same behavior is not certain. To estimate this uncertainty the default $t\bar{t}$ generator MC@NLO+HERWIG is compared to available alternative generators: ALPGEN+HERWIG and POWHEG+PYTHIA8. No comparison on single top processes is performed due to lack of alternative generators available for this process.

The analysis is sensitive to NLO and NNLO corrections (see Section 5.4.3). A comparison with ALPGEN+HERWIG, which uses the MLM matching scheme allows for investigations on the extra jet production in higher-order processes. The additional comparison to POWHEG+PYTHIA8 gives the possibility to investigate differences between the different parton shower algorithms HERWIG and PYTHIA.

A shape comparison of the dijet invariant mass and rapidity gap of the default and alternative generators in the signal and top quark control region is shown in Fig. C.1. A shift is observed for both alternative generators compared to the default one. The comparison in the signal region shows a similar behavior, however, this is less significant due to the smaller statistics available.

The yields of the different generators are compared for the different selection criteria in the top quark control region and signal region selection (see Table C.1). Large deviations of up to 50% are found in the top quark control region. The yields in the

(a) Signal-like selection after $Z/\gamma^* \to \tau\tau$ veto.

(b) Signal-like selection after ΔY_{jj} requirement.

(c) Top quark CR after $Z/\gamma^* \to \tau\tau$ veto.

(d) Top quark CR after ΔY_{jj} requirement.
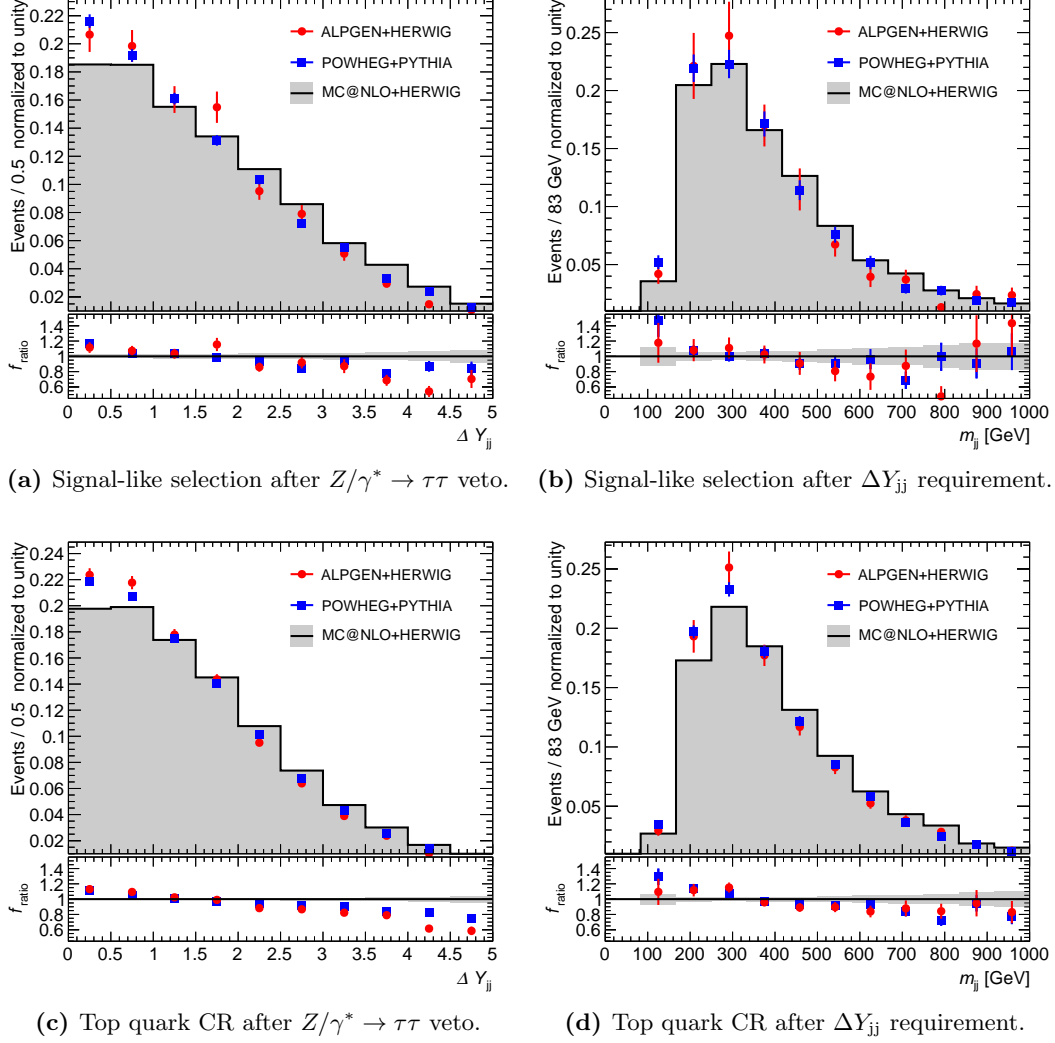
Figure C.1: Generator comparison of the dijet rapidity gap (ΔY_{jj}) and invariant mass (m_{jj}) distributions of the $t\bar{t}$ process. The distributions are normalized to unity. The lower panel shows the ratio (f_{ratio}) of the distributions of the two alternative generators ALPGEN+HERWIG and POWHEG+PYTHIA8 to the default generator MC@NLO+HERWIG. The uncertainties shown are from statistical sources.

signal regions are corrected to the data in the control region as described in Section 5.4.3, for each generator individually before they are compared. The differences between the generators are smaller in the signal region after the correction compared to the ones in the control region. The background determination, hence, reduces the differences between the generators. A maximal difference, with a significance level of at least three standard deviations, in the signal region is found to be 15% for the comparison of the default generator with the ALPGEN+HERWIG generator after the criteria, $\Delta Y_{jj} > 2.8$, is applied. The 15% difference is taken as a theoretical systematic uncertainty in the top quark background determination.

	f_{POWHEG} [%]	f_{ALPGEN} [%]
b-jet veto	10±1	6±2
$p_{\mathrm{T,tot}} <45$ GeV	10±1	6±2
$Z \to \tau\tau$ veto	10±1	7±2
$\Delta Y_{jj} > 2.8$	7±3	**15±5**
$m_{jj} > 500$ GeV	7±6	20±7
central jet veto	12±11	16±14
outside lepton veto	9±12	26±15

(a) Signal-like selection

	f_{POWHEG} [%]	f_{ALPGEN} [%]
exactly one b-jet	1±0	2±1
$p_{\mathrm{T,tot}} <45$ GeV	1±1	3±1
$Z \to \tau\tau$ veto	1±1	97±1
$\Delta Y_{jj} > 2.8$	13±1	25±2
$m_{jj} > 500$ GeV	24±2	34±3
central jet veto	46±3	49±4
outside lepton veto	45±4	49±5

(b) Top quark control region selection

Table C.1: Difference f_{POWHEG} and f_{ALPGEN} between the expected $t\bar{t}$ yields of the default generator MC@NLO+HERWIG and the alternative generators POWHEG+PYTHIA8 and ALPGEN+HERWIG, respectively. The differences are given in percent with respect to the yield of the default generator: $f_{\mathrm{alternative}} = |N_{\mathrm{alternative}} - N_{\mathrm{default}}|/N_{\mathrm{default}}$. The yields in the signal-like selection are corrected to the data in the top quark control region for each generator individually before $f_{\mathrm{alternative}}$ is calculated. The errors are due to Monte-Carlo statistics.

Appendix D

Individual Dilepton Flavor Results

This chapter contains additional material in order to compare the results of the different-flavor and same-flavor analysis (compare Fig. D.1b to Fig. D.2b). In addition, results of an analysis where the ggF Higgs boson process is considered as part of the signal (inclusive search) are compared with results, where the ggF contribution is considered as background (exclusive search) and profiled (see Table D.1 and compare the right and left-hand-side figures in Figs. D.1–3).

Table D.1: Comparison of the results for Higgs boson searches at $m_H = 125\,\text{GeV}$ in the $qq\ell\nu\ell\nu$ final state between a Higgs boson inclusive search where the ggF process is considered part of the signal and a VBF exclusive search where the ggF process is considered part of the background and profiled using a dedicated ggF measurement [91].

| | | 95% upper CL$_\text{s}$ Limit | | Signal significance [s.d.] | | Signal strength | |
		μ_up^obs	μ_up^exp	Observed	Expected	$\hat{\mu}^\text{obs}$	$\hat{\mu}^\text{exp}$
Exclusive search	DF+SF	3.80	1.59	2.8	1.5	$2.1^{+1.0}_{-0.8}$	$1.0^{+0.8}_{-0.7}$
	DF	3.90	1.69	2.6	1.4	$2.1^{+1.0}_{-0.9}$	$1.0^{+0.9}_{-0.8}$
	SF	6.64	4.45	1.2	0.6	$2.2^{+2.5}_{-1.8}$	$1.0^{+2.1}_{-1.7}$
Inclusive search	DF+SF	3.43	1.26	3.3	1.9	$2.0^{+0.8}_{-0.7}$	$1.0^{+0.7}_{-0.6}$
	DF	3.45	1.34	3.1	1.8	$1.9^{+0.9}_{-0.7}$	$1.0^{+0.7}_{-0.6}$
	SF	6.02	3.77	1.5	0.7	$2.2^{+2.2}_{-1.6}$	$1.0^{+1.8}_{-1.3}$

(a) Higgs boson inclusive search

(b) VBF exclusive search (scenario 2)

Figure D.1: Expected and observed 95% CL upper limits on the signal strength (top row), local p_0-value and signal significance (middle row) and the best-fit signal strength $\hat{\mu}$ (bottom row) for different-flavor final states as a function of the Higgs boson mass m_H. In (a) the results for the Higgs boson inclusive search are shown, where the ggF process is considered part of the signal. In (b) the results of the VBF exclusive search are shown, where the ggF process is considered part of the background and profiled using a dedicated ggF measurement [91].

(a) Higgs boson inclusive search   **(b)** VBF exclusive search (scenario 2)
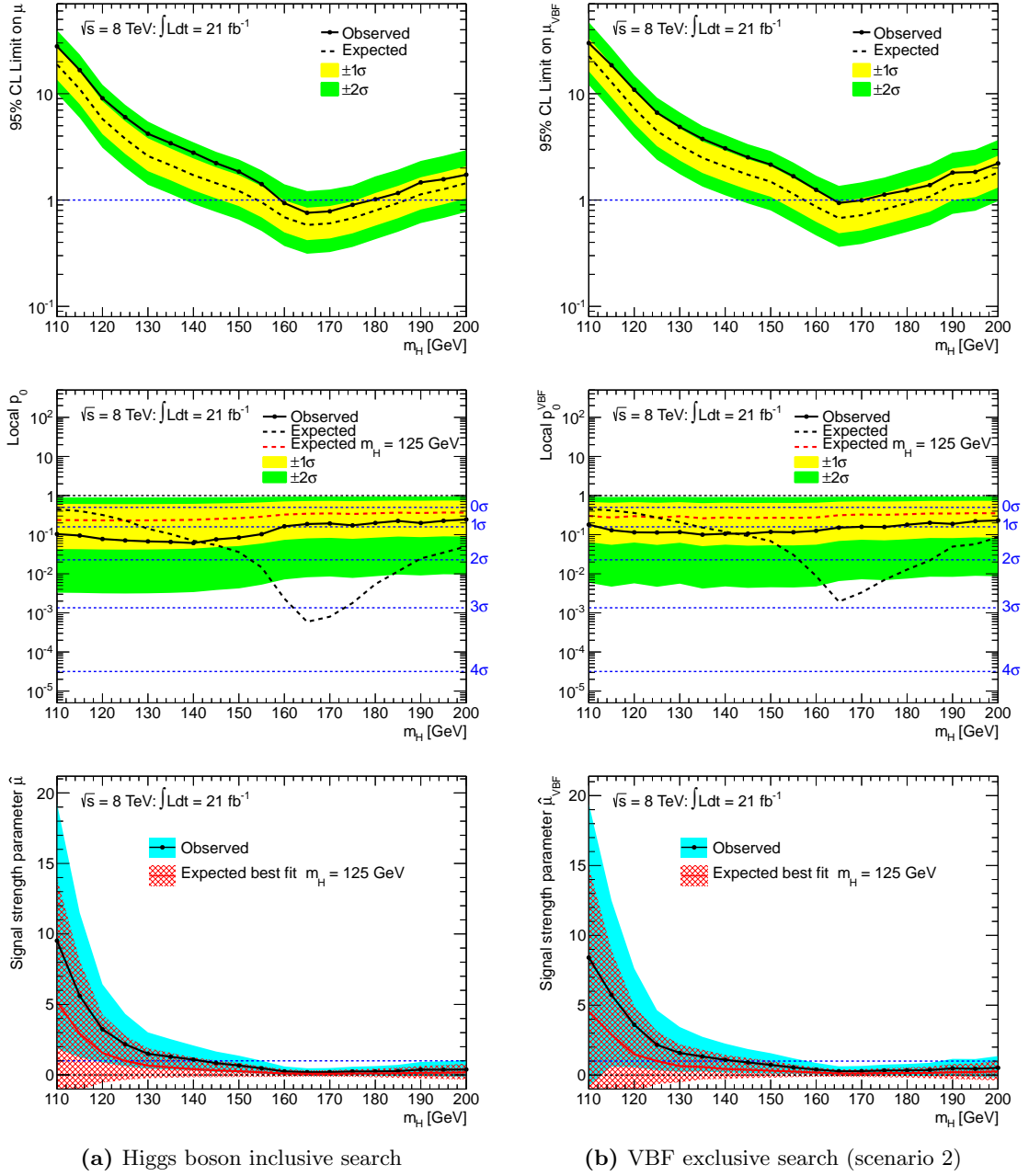
Figure D.2: Expected and observed 95% CL upper limits on the signal strength (top row), local p_0-value and signal significance (middle row) and the best-fit signal strength $\hat{\mu}$ (bottom row) for same-flavor final states as a function of the Higgs boson mass m_H. In (a) the results for the Higgs boson inclusive search are shown, where the ggF process is considered part of the signal. In (b) the results of the VBF exclusive search are shown, where the ggF process is considered part of the background and profiled using a dedicated ggF measurement [91].

(a) Higgs boson inclusive search

(b) VBF exclusive search (scenario 2)

Figure D.3: Expected and observed 95% CL upper limits on the signal strength (top row), local p_0-value and signal significance (middle row) and the best-fit signal strength $\hat{\mu}$ (bottom row) for combined different-flavor and same-flavor final states as a function of the Higgs boson mass m_H. In (a) the results for the Higgs boson inclusive search are shown, where the ggF process is considered part of the signal. In (b) the results of the VBF exclusive search are shown, where the ggF process is considered part of the background and profiled using a dedicated ggF measurement [91].

Bibliography

[1] F. Englert and R. Brout, *Broken symmetry and the mass of gauge vector mesons*, Phys.Rev.Lett. **13** (1964) 321.

[2] P. W. Higgs, *Broken symmetries and the masses of gauge bosons*, Phys.Rev.Lett. **13** (1964) 508.

[3] P. W. Higgs, *Spontaneous symmetry breakdown without massless bosons*, Phys.Rev. **145** (1966) 1156.

[4] G. Guralnik, C. Hagen, and T. Kibble, *Global conservation laws and massless particles*, Phys.Rev.Lett. **13** (1964) 585.

[5] ATLAS Collaboration, G. Aad et al., *Observation of a new particle in the search for the Standard Model Higgs boson with the ATLAS detector at the LHC*, Phys.Lett. **B716** (2012) 1.

[6] CMS Collaboration, S. Chatrchyan et al., *Observation of a new boson at a mass of 125 GeV with the CMS experiment at the LHC*, Phys.Lett. **B716** (2012) 30.

[7] ATLAS Collaboration, G. Aad et al., *Measurements of Higgs boson production and couplings in diboson final states with the ATLAS detector at the LHC*, Phys.Lett. **B726** (2013) 88, `arXiv:hep-ex/1307.1427`.

[8] CMS Collaboration, S. Chatrchyan et al., *Combination of standard model Higgs boson searches and measurements of the properties of the new boson with a mass near 125 GeV*, CMS-PAS-HIG-13-005, CERN, 2013, `http://cds.cern.ch/record/1494149`.

[9] W. Hollik, *Quantum field theory and the Standard Model*, `arXiv:hep-ph/1012.3883`.

[10] J. Beringer et al., *(Particle Data Group)*, Phys. Rev. **D86,** (2012) 010001.

[11] ATLAS Collaboration, G. Aad et al., *Combination of ATLAS and CMS results on the mass of the top-quark using up to 4.9 fb^{-1} of $\sqrt{s} = 7$ TeV LHC data*, ATLAS-CONF-2013-102, CERN, 2013, `https://cds.cern.ch/record/1601811`.

[12] S. Tomonaga, *On a relativistically invariant formulation of the quantum theory of wave fields*, Prog.Theor.Phys. **1** (1946) 27.

[13] J. S. Schwinger, *Quantum electrodynamics. I. A covariant formulation*, Phys.Rev. **74** (1948) 1439.

[14] J. S. Schwinger, *On quantum electrodynamics and the magnetic moment of the electron*, Phys.Rev. **73** (1948) 416.

[15] R. Feynman, *Mathematical formulation of the quantum theory of electromagnetic interaction*, Phys.Rev. **80** (1950) 440.

[16] R. Feynman, *The theory of positrons*, Phys.Rev. **76** (1949) 749.

[17] R. Feynman, *Space - time approach to quantum electrodynamics*, Phys.Rev. **76** (1949) 769.

[18] S. Glashow, *Partial symmetries of weak interactions*, Nucl.Phys. **22** (1961) 579.

[19] S. Weinberg, *A Model of Leptons*, Phys.Rev.Lett. **19** (1967) 1264.

[20] A. Salam, *Weak and Electromagnetic Interactions*, Conf.Proc. **C680519** (1968) 367.

[21] A. Salam and J. C. Ward, *Electromagnetic and weak interactions*, Phys.Lett. **13** (1964) 168.

[22] H. Fritzsch, M. Gell-Mann, and H. Leutwyler, *Advantages of the color octet gluon picture*, Phys.Lett. **B47** (1973) 365.

[23] J. Goldstone, *Field theories with superconductor solutions*, Il Nuovo Cimento **19** no. 1, (1961) 154.

[24] J. Goldstone, A. Salam, and S. Weinberg, *Broken symmetries*, Phys. Rev. **127** (1962) 965.

[25] S. Dawson et al., *The Higgs hunter's guide*, Front.Phys. **80** (2000) 1.

[26] J. M. Campbell, J. Huston, and W. Stirling, *Hard interactions of quarks and gluons: A primer for LHC physics*, Rept.Prog.Phys. **70** (2007) 89.

[27] J. C. Collins and D. E. Soper, *The theorems of perturbative QCD*, Ann.Rev.Nucl.Part.Sci. **37** (1987) 383.

[28] R. K. Ellis, W. J. Stirling, and B. Webber, *QCD and collider physics.* Press syndicate of the University of Cambringe, 1996.

[29] H.-L. Lai et al., *New parton distributions for collider physics*, Phys.Rev. **D82** (2010) 074024, `arXiv:hep-ph/1007.2241`.

[30] P. M. Nadolsky et al., *Implications of CTEQ global analysis for collider observables*, Phys.Rev. **D78** (2008) 013004.

[31] M. Botje et al., *The PDF4LHC working group interim recommendations*, `arXiv:hep-ph/1101.0538`.

[32] LHC Higgs Cross Section Working Group Collaboration, S. Dittmaier et al., *Handbook of LHC Higgs cross sections: 1. Inclusive observables*, `arXiv:hep-ph/1101.0593`.

[33] `https://twiki.cern.ch/twiki/bin/view/LHCPhysics/` `CERNYellowReportPageAt8TeV2012update`.

[34] A. Djouadi, M. Spira, and P. Zerwas, *Production of Higgs bosons in proton colliders: QCD corrections*, Phys.Lett. **B264** (1991) 440.

[35] S. Dawson, *Radiative corrections to Higgs boson production*, Nucl.Phys. **B359** (1991) 283.

[36] M. Spira et al., *Higgs boson production at the LHC*, Nucl.Phys. **B453** (1995) 17.

[37] R. V. Harlander and W. B. Kilgore, *Next-to-next-to-leading order Higgs production at hadron colliders*, Phys.Rev.Lett. **88** (2002) 201801.

[38] C. Anastasiou and K. Melnikov, *Higgs boson production at hadron colliders in NNLO QCD*, Nucl.Phys. **B646** (2002) 220.

[39] V. Ravindran, J. Smith, and W. L. van Neerven, *NNLO corrections to the total cross-section for Higgs boson production in hadron hadron collisions*, Nucl.Phys. **B665** (2003) 325.

[40] U. Aglietti et al., *Two loop light fermion contribution to Higgs production and decays*, Phys.Lett. **B595** (2004) 432.

[41] S. Actis et al., *NLO electroweak corrections to Higgs boson production at hadron colliders*, Phys.Lett. **B670** (2008) 12.

[42] S. Catani et al., *Soft gluon resummation for Higgs boson production at hadron colliders*, JHEP **0307** (2003) 28.

[43] C. Anastasiou et al., *Inclusive Higgs boson cross-section for the LHC at 8 TeV*, JHEP **1204** (2012) 4.

[44] D. de Florian and M. Grazzini, *Higgs production at the LHC: updated cross sections at $\sqrt{s} = 8$ TeV*, Phys.Lett. **B718** (2012) 117.

[45] J. Baglio and A. Djouadi, *Higgs production at the LHC*, JHEP **1103** (2011) 55.

[46] M. Ciccolini, A. Denner, and S. Dittmaier, *Strong and electroweak corrections to the production of Higgs + 2jets via weak interactions at the LHC*, Phys.Rev.Lett. **99** (2007) 161803.

[47] M. Ciccolini, A. Denner, and S. Dittmaier, *Electroweak and QCD corrections to Higgs production via vector-boson fusion at the LHC*, Phys.Rev. **D77** (2008) 013002.

[48] K. Arnold et al., *VBFNLO: A Parton level Monte Carlo for processes with electroweak bosons*, Comp.Phys.Comm. **180** (2009) 1661.

[49] P. Bolzoni et al., *Higgs production via vector-boson fusion at NNLO in QCD*, Phys.Rev.Lett. **105** (2010) 011801.

[50] T. Han and S. Willenbrock, *QCD correction to the $pp \rightarrow WH$ and ZH total cross-sections*, Phys.Lett. **B273** (1991) 167.

[51] D. A. Restrepo, *From hierarchical radiative quark mass matrices and mixing to FCNC in $SU(2)_L \times U(1)_Y \times U(1)_H$*, UDEA-PE-96-52, 1996, http://cds.cern.ch/record/307206, arXiv:hep-ph/9607356.

[52] M. Ciccolini, S. Dittmaier, and M. Kramer, *Electroweak radiative corrections to associated WH and ZH production at hadron colliders*, Phys.Rev. **D68** (2003) 073003.

[53] LHC Higgs Cross Section Working Group Collaboration, S. Dittmaier et al., *Handbook of LHC Higgs cross sections: 2. Differential distributions*, arXiv:hep-ph/1201.3084.

[54] V. Del Duca et al., *Monte Carlo studies of the jet activity in Higgs + 2 jet events*, JHEP **0610** (2006) 16.

[55] J. Bjorken, *Rapidity gaps and jets as a new physics signature in very high-energy hadron hadron collisions*, Phys.Rev. **D47** (1993) 101.

[56] J. Bjorken, *A full acceptance detector for SSC physics at low and intermediate mass scales: An expression of interest to the SSC*, Int.J.Mod.Phys. **A7** (1992) 4189.

[57] Y. L. Dokshitzer, V. A. Khoze, and T. Sjostrand, *Rapidity gaps in Higgs production*, Phys.Lett. **B274** (1992) 116.

[58] https://twiki.cern.ch/twiki/bin/view/LHCPhysics/CERNYellowReportPageBR2.

[59] D. L. Rainwater and D. Zeppenfeld, *Observing $H \to W^*W^* \to e^\pm \mu^\mp + \not{p}_T$ in weak boson fusion with dual forward jet tagging at the CERN LHC*, Phys.Rev. **D60** (1999) 113004.

[60] A. Djouadi, J. Kalinowski, and M. Spira, *HDECAY: A program for Higgs boson decays in the standard model and its supersymmetric extension*, Comput.Phys.Commun. **108** (1998) 56.

[61] A. Bredenstein et al., *Precise predictions for the Higgs-boson decay $H \to WW/ZZ \to 4\,leptons$*, Phys.Rev. **D74** (2006) 013004.

[62] A. Bredenstein et al., *Radiative corrections to the semileptonic and hadronic Higgs-boson decays $H \to WW/ZZ \to 4\,fermions$*, JHEP **0702** (2007) 80.

[63] M. Dobbs et al., *Les Houches guidebook to Monte Carlo generators for hadron collider physics*, arXiv:hep-ph/0403045.

[64] B. Andersson et al., *Parton fragmentation and string dynamics*, Phys.Rept. **97** (1983) 31.

[65] J. Alwall et al., *Comparative study of various algorithms for the merging of parton showers and matrix elements in hadronic collisions*, Eur.Phys.J. **C53** (2008) 473.

[66] P. Nason and C. Oleari, *NLO Higgs boson production via vector-boson fusion matched with shower in POWHEG*, JHEP **1002** (2010) 037.

[67] S. Frixione and B. R. Webber, *Matching NLO QCD computations and parton shower simulations*, JHEP **0206** (2002) 29.

[68] M. L. Mangano et al., *ALPGEN, a generator for hard multiparton processes in hadronic collisions*, JHEP **0307** (2003) 1.

[69] B. P. Kersevan and E. Richter-Was, *The Monte Carlo event generator AcerMC version 2.0 with interfaces to PYTHIA 6.2 and HERWIG 6.5*, arXiv:hep-ph/0405247.

[70] J. Alwall et al., *MadGraph/MadEvent v4: The new web generation*, JHEP **0709** (2007) 28.

[71] J. Alwall et al., *MadGraph 5 : Going beyond*, JHEP **1106** (2011) 128.

[72] R. C. Gray et al., *Backgrounds to Higgs boson searches from $W\gamma^* \to \ell\nu\ell(\ell)$ asymmetric internal conversion*, arXiv:hep-ph/1110.1368.

[73] N. Kauer and G. Passarino, *Inadequacy of zero-width approximation for a light Higgs boson signal*, JHEP **1208** (2012) 116.

[74] T. Binoth et al., *Gluon-induced W-boson pair production at the LHC*, JHEP **0612** (2006) 46.

[75] T. Gleisberg et al., *Event generation with SHERPA 1.1*, JHEP **0902** (2009) 7.

[76] T. Sjostrand, S. Mrenna, and P. Z. Skands, *PYTHIA 6.4 physics and manual*, JHEP **0605** (2006) 26.

[77] T. Sjostrand, S. Mrenna, and P. Z. Skands, *A brief introduction to PYTHIA 8.1*, Comp.Phys.Comm. **178** (2008) 852.

[78] G. Corcella et al., *HERWIG 6: An event generator for hadron emission reactions with interfering gluons*, JHEP **0101** (2001) 10.

[79] J. Butterworth, J. R. Forshaw, and M. Seymour, *Multiparton interactions in photoproduction at HERA*, Z.Phys. **C72** (1996) 637.

[80] A. Djouadi, *The anatomy of electro-weak symmetry breaking. I: The Higgs boson in the standard model*, Phys.Rept. **457** (2008) 1.

[81] K. Riesselmann, *Limitations of a standard model Higgs boson*, arXiv:hep-ph/9711456.

[82] J. Ellis et al., *The probable fate of the Standard Model*, Phys.Lett. **B679** (2009) 369.

[83] G. Degrassi et al., *Higgs mass and vacuum stability in the Standard Model at NNLO*, JHEP **1208** (2012) 98.

[84] ALEPH, DELPHI, L3 and OPAL Collaboration, LEP Electroweak Working Group, *Electroweak measurements in electron-positron collisions at W-boson-pair energies at LEP*, Phys.Rep. **532** (2013) 119.

[85] ATLAS Collaboration, G. Aad et al., *Search for a high-mass Higgs boson in the $H \rightarrow WW \rightarrow l\nu l\nu$ decay channel with the ATLAS detector using 21 fb^{-1} of proton-proton collision data*, ATLAS-CONF-2013-067, CERN, 2013, http://cds.cern.ch/record/1562879.

[86] ATLAS Collaboration, G. Aad et al., *Measurements of the properties of the Higgs-like boson in the four lepton decay channel with the ATLAS detector using 25 fb1 of proton-proton collision data*, ATLAS-CONF-2013-013, CERN, 2013, http://cds.cern.ch/record/1523699.

[87] CMS Collaboration, S. Chatrchyan et al., *Updated measurements of the Higgs boson at 125 GeV in the two photon decay channel*, CMS-PAS-HIG-13-001, CERN, 2013, `https://cds.cern.ch/record/1530524`.

[88] CMS Collaboration, S. Chatrchyan et al., *Search for a standard-model-like Higgs boson with a mass in the range 145 to 1000 GeV at the LHC*, Eur.Phys.J. **C73** (2013) 2469.

[89] ATLAS Collaboration, G. Aad et al., *Measurements of the properties of the Higgs-like boson in the two photon decay channel with the ATLAS detector using 25 fb^{-1} of proton-proton collision data*, ATLAS-CONF-2013-012, CERN, 2013, `http://cds.cern.ch/record/1523698`.

[90] CMS Collaboration, S. Chatrchyan et al., *Measurement of the properties of a Higgs boson in the four-lepton final state*, CMS-HIG-13-002, CERN-PH-EP-2013-220, CERN, 2013, `arXiv:hep-ex/1312.5353`.

[91] ATLAS Collaboration, G. Aad et al., *Measurements of the properties of the Higgs-like boson in the $WW^{(*)} \to \ell\nu\ell\nu$ decay channel with the ATLAS detector using 25 fb^{-1} of proton-proton collision data*, ATLAS-CONF-2013-030, CERN, 2013, `http://cds.cern.ch/record/1527126`.

[92] CMS Collaboration, S. Chatrchyan et al., *Measurement of Higgs boson production and properties in the WW decay channel with leptonic final states*, JHEP **1401** (2014) 96.

[93] ATLAS Collaboration, G. Aad et al., *Evidence for Higgs boson decays to the $\tau^+\tau^-$ final state with the ATLAS detector*, ATLAS-CONF-2013-108, CERN, 2013, `http://cds.cern.ch/record/1632191`.

[94] CMS Collaboration, S. Chatrchyan et al., *Evidence for the 125 GeV Higgs boson decaying to a pair of τ leptons*, CMS-HIG-13-004, CERN-PH-EP-2014-001, CERN, 2014, `arXiv:hep-ex/1401.5041`.

[95] ATLAS Collaboration, G. Aad et al., *Search for the bb decay of the Standard Model Higgs boson in associated W/ZH production with the ATLAS detector*, ATLAS-CONF-2013-079, CERN, 2013, `http://cds.cern.ch/record/1563235`.

[96] CMS Collaboration, S. Chatrchyan et al., *Search for the standard model Higgs boson produced in association with a W or a Z boson and decaying to bottom quarks*, Phys.Rev. **D89** (2014) 012003.

[97] ATLAS Collaboration, G. Aad et al., *Search for a Standard Model Higgs boson in $H \to \mu\mu$ decays with the ATLAS detector.*, ATLAS-CONF-2013-010, CERN, 2013, `http://cds.cern.ch/record/1523695`.

[98] CMS Collaboration, S. Chatrchyan et al., *Search for the standard model Higgs boson in the dimuon decay channel in pp collisions at sqrt(s)= 7 and 8 TeV*, CMS-PAS-HIG-13-007, CERN, 2013, `http://cds.cern.ch/record/1606831`.

[99] L. Landau, *On the angular momentum of a two-photon system*, Dokl.Akad.Nauk Ser.Fiz. **60** (1948) 207.

[100] C.-N. Yang, *Selection Rules for the Dematerialization of a Particle Into Two Photons*, Phys.Rev. **77** (1950) 242.

[101] Y. Gao, A. V. Gritsan, Z. Guo, et al., *Spin determination of single-produced resonances at hadron colliders*, Phys.Rev. **D81** (2010) 075022.

[102] ATLAS Collaboration, G. Aad et al., *Evidence for the spin-0 nature of the Higgs boson using ATLAS data*, Phys.Lett. **B726** (2013) 120.

[103] L. Evans and P. Bryant, *LHC machine*, JINST **3** (2008) S08001.

[104] O. S. Brüning et al., *LHC design report. 1. The LHC main ring*, CERN-2004-003-V-1, CERN, 2004, `http://dx.doi.org/10.5170/CERN-2004-003-V-1`.

[105] O. S. Brüning et al., *LHC design report. 2. The LHC infrastructure and general services*, CERN-2004-003-V-2, CERN, 2004, `http://dx.doi.org/10.5170/CERN-2004-003-V-2`.

[106] M. Benedikt et al., *LHC design report. 3. The LHC injector chain*, CERN-2004-003-V-3, CERN-2004-003, CERN, 2004, `http://dx.doi.org/10.5170/CERN-2004-003-V-3`.

[107] ATLAS Collaboration, G. Aad et al., *The ATLAS Experiment at the CERN Large Hadron Collider*, JINST **3** (2008) S08003.

[108] CMS Collaboration, *CMS technical proposal*, CERN-LHCC-94-38, 1994, `http://cds.cern.ch/record/290969`.

[109] LHCb Collaboration, *LHCb technical proposal*, CERN-LHCC-98-004, CERN, 1998, `http://cds.cern.ch/record/622031`.

[110] ALICE Collaboration, *ALICE: Technical proposal for a large ion collider experiment at the CERN LHC*, CERN-LHCC-95-71, CERN, 1995, `http://cds.cern.ch/record/293391`.

[111] *LEP design report. The LEP Injector chain*, CERN-LEP/TH/83-29, CERN, 1983, `https://cds.cern.ch/record/98881`.

[112] *LEP design report. The LEP main ring*, CERN-LEP-84-01, CERN, 1984,
`http://cds.cern.ch/record/102083`.

[113] J. Haffner, *The CERN accelerator complex. Complexe des acclrateurs du CERN*,
2013. `http://cds.cern.ch/record/1621894`.

[114] `https://twiki.cern.ch/twiki/bin/view/AtlasPublic/LuminosityPublicResults`.

[115] ATLAS Collaboration, G. Aad et al., *Improved luminosity determination in pp
collisions at $\sqrt{s} = 7$ TeV using the ATLAS detector at the LHC*, Eur.Phys.J.
C73 (2013) 2518.

[116] S. van der Meer, *Calibration of the effective beam height in the ISR*,
CERN-ISR-PO-68-31, CERN, 1968, `http://cds.cern.ch/record/296752`.

[117] C. Rubbia, *Measurement of the luminosity of $p\bar{p}$ collider with a (generalized) Van
der Meer method*, CERN-$p\bar{p}$-Note-38, CERN, 1977,
`https://cds.cern.ch/record/1025746`.

[118] GEANT4 Collaboration, S. Agostinelli et al., *GEANT4: A simulation toolkit*,
Nucl.Instr.Meth. **A506** (2003) 250.

[119] ATLAS Collaboration, G. Aad et al., *The ATLAS simulation infrastructure*, Eur.
Phys. J. C **70** (2010) 823.

[120] ATLAS Collaboration, G. Aad et al., *The simulation principle and performance
of the ATLAS fast calorimeter simulation FastCaloSim*,
ATL-PHYS-PUB-2010-013, CERN, 2010,
`http://cds.cern.ch/record/1300517`.

[121] ATLAS Collaboration, G. Aad et al., *Atlas computing: technical design report*,
CERN-LHCC-2005-022, CERN, 2005, `http://cds.cern.ch/record/837738`.

[122] T. Cornelissen et al., *Concepts, design and implementation of the ATLAS New
Tracking (NEWT)*, ATL-SOFT-PUB-2007-007, CERN, 2007,
`http://cds.cern.ch/record/1020106`.

[123] T. Cornelissen et al., *Single track performance of the Inner Detector New Track
reconstruction (NEWT)*, ATL-INDET-PUB-2008-002, CERN, 2008,
`http://cds.cern.ch/record/1092934`.

[124] R. Fruhwirth, *Application of Kalman filtering to track and vertex fitting*,
Nucl.Instr.Meth. **A262** (1987) 444.

[125] ATLAS Collaboration, G. Aad et al., *Performance of the ATLAS silicon pattern recognition algorithm in data and simulation at $\sqrt{s} = 7$ TeV*, ATLAS-CONF-2010-072, CERN, 2010, `http://cds.cern.ch/record/1281363`.

[126] ATLAS Collaboration, G. Aad et al., *Performance of primary vertex reconstruction in proton-proton collisions at $\sqrt{s} = 7$ TeV in the ATLAS experiment*, ATLAS-CONF-2010-069, CERN, 2010, `http://cds.cern.ch/record/1281344`.

[127] ATLAS Collaboration, G. Aad et al., *Reconstruction of primary vertices in pp collisions at energies of 900 GeV and 7 TeV with the ATLAS detector*, `arXiv:hep-ex/1010.1483`.

[128] R. Fruhwirth, W. Waltenberger, and P. Vanlaer, *Adaptive vertex fitting*, J.Phys. **G34** (2007) N343.

[129] ATLAS Collaboration, G. Aad et al., *Expected performance of the ATLAS experiment - Detector, trigger and physics*, `arXiv:hep-ex/0901.0512`.

[130] M. Cacciari, G. P. Salam, and G. Soyez, *The anti-k_t jet clustering algorithm*, JHEP **04** (2008) 63.

[131] ATLAS Collaboration, G. Aad et al., *Jet energy scale and its systematic uncertainty in proton-proton collisions at $\sqrt{(s)}=7$ TeV with ATLAS 2011 data*, ATLAS-CONF-2013-004, CERN, 2013, `http://cds.cern.ch/record/1337782`.

[132] M. Cacciari, G. P. Salam, and G. Soyez, *FastJet user manual*, Eur.Phys.J. **C72** (2012) 1896.

[133] M. Cacciari and G. P. Salam, *Dispelling the N^3 myth for the k_t jet-finder*, Phys.Lett. **B641** (2006) 57.

[134] E. Abat, J. Abdallah, T. Addy, P. Adragna, et al., *Combined performance studies for electrons at the 2004 ATLAS combined test-beam*, JINST **5** (2010) P11006.

[135] M. Cacciari and G. P. Salam, *Pileup subtraction using jet areas*, Phys.Lett. **B659** (2008) 119.

[136] ATLAS Collaboration, G. Aad et al., *Jet energy resolution in proton-proton collisions at $\sqrt{s} = 7$ TeV recorded in 2010 with the ATLAS detector*, Eur.Phys.J. **C73** (2013) 2306.

[137] ATLAS Collaboration, G. Aad et al., *Commissioning of the ATLAS high-performance b-tagging algorithms in the 7 TeV collision data*, ATLAS-CONF-2011-102, CERN, 2011, `http://cds.cern.ch/record/1369219`.

[138] ATLAS Collaboration, G. Aad et al., *Measuring the b-tag efficiency in a top-pair sample with 4.7 fb^{-1} of data from the ATLAS detector*, ATLAS-CONF-2012-097, CERN, 2012, `http://cds.cern.ch/record/1460443`.

[139] ATLAS Collaboration, G. Aad et al., *Measurement of the b-tag efficiency in a sample of jets containing muons with 5 fb^1 of data from the ATLAS detector*, ATLAS-CONF-2012-043, CERN, 2012, `http://cds.cern.ch/record/1435197`.

[140] ATLAS Collaboration, G. Aad et al., *Measurement of the mistag rate with 5 fb^1 of data collected by the ATLAS detector*, ATLAS-CONF-2012-040, CERN, 2012, `http://cds.cern.ch/record/1435194`.

[141] ATLAS Collaboration, G. Aad et al., *Expected electron performance in the ATLAS experiment*, ATL-PHYS-PUB-2011-006, CERN, 2011, `http://cds.cern.ch/record/1345327`.

[142] ATLAS Collaboration, G. Aad et al., *Improved electron reconstruction in ATLAS using the gaussian sum filter-based model for bremsstrahlung*, ATLAS-CONF-2012-047, CERN, 2012, `http://cds.cern.ch/record/1449796`.

[143] ATLAS Collaboration, G. Aad et al., *Electron performance measurements with the ATLAS detector using the 2010 LHC proton-proton collision data*, Eur.Phys.J. **C72** (2012) 1909.

[144] ATLAS Collaboration, L. Chevalier et al., *A muon identification and combined reconstruction procedure for the ATLAS detector at the LHC using the MUONBOY, STACO, MuTag reconstruction packages*, Nucl.Instr.Meth. **572** no. 1, (2007) 77.

[145] ATLAS Collaboration, G. Aad et al., *Preliminary results on the muon reconstruction efficiency, momentum resolution, and momentum scale in ATLAS 2012 pp collision data*, ATLAS-CONF-2013-088, CERN, 2013, `http://cds.cern.ch/record/1580207`.

[146] ATLAS Collaboration, G. Aad et al., *Performance of missing transverse momentum reconstruction in proton-proton collisions at 7 TeV with ATLAS*, Eur.Phys.J. **C72** (2012) 1844.

[147] ATLAS Collaboration, G. Aad et al., *Performance of missing transverse momentum reconstruction in ATLAS with 2011 proton-proton collisions at $\sqrt{s} = 7$ TeV*, ATLAS-CONF-2012-101, CERN, 2012, `http://cds.cern.ch/record/1463915`.

[148] ATLAS Collaboration, G. Aad et al., *Performance of the ATLAS trigger system in 2010*, Eur.Phys.J. **C72** (2012) 1849.

[149] ATLAS Collaboration, G. Aad et al., *Performance of the ATLAS muon trigger in 2011*, ATLAS-CONF-2012-099, CERN, 2012, `http://cds.cern.ch/record/1462601`.

[150] ATLAS Collaboration, G. Aad et al., *Performance of the ATLAS electron and photon trigger in p-p collisions at $\sqrt{s} = 7$ TeV in 2011*, ATLAS-CONF-2012-048, CERN, 2012, `http://cds.cern.ch/record/1450089`.

[151] A. L. Read, *Presentation of search results: The CL(s) technique*, J.Phys. **G28** (2002) 2693.

[152] J. M. Campbell, R. K. Ellis, and C. Williams, *Vector boson pair production at the LHC*, JHEP **1107** (2011) 18.

[153] S. Moch and P. Uwer, *Heavy-quark pair production at two loops in QCD*, Nucl.Phys.Proc.Suppl. **183** (2008) 75.

[154] S. Dittmaier and M. Huber, *Radiative corrections to the neutral-current Drell-Yan process in the Standard Model and its minimal supersymmetric extension*, JHEP **1001** (2010) 60.

[155] J. M. Campbell and R. K. Ellis, *An update on vector boson pair production at hadron colliders*, Phys.Rev. **D60** (1999) 113006.

[156] A. Martin et al., *Parton distributions for the LHC*, Eur.Phys.J. **C63** (2009) 189.

[157] R. D. Ball et al., *Impact of heavy quark masses on parton distributions and LHC phenomenology*, Nucl.Phys. **B849** (2011) 296.

[158] G. Cowan et al., *Asymptotic formulae for likelihood-based tests of new physics*, Eur.Phys.J. **C71** (2011) 1554.

[159] S. Stern, *Searches for Higgs boson decays to muon pairs in the Standard Model and in its minimal supersymmetric extension with the ATLAS detector*, PhD thesis, Technische Universität München, July, 2013, MPI report, MPP-2013-243, CERN-TESIS-2013-108, `http://cds.cern.ch/record/1594973`.

[160] ATLAS Collaboration, G. Aad et al., *Updated coupling measurements of the Higgs boson with the ATLAS detector using up to 25 fb^{-1} of proton-proton collision data*, ATLAS-CONF-2014-013, CERN, 2014, `https://cds.cern.ch/record/1666896`.

[161] ATLAS Collaboration, G. Aad et al., *Search for associated production of the Higgs boson in the $WH \rightarrow WWW^{(*)} \rightarrow \ell\nu\ell\nu\ell\nu$ and $ZH \rightarrow ZWW^{(*)} \rightarrow \ell\ell\ell\nu\ell\nu$ channels with the ATLAS detector at the LHC*, ATLAS-CONF-2013-075, CERN, 2013, `http://cds.cern.ch/record/1562933`.

[162] A. Hoecker, P. Speckmayer, J. Stelzer, et al., *TMVA 4 (Toolkit for multivariate data analysis with ROOT) User Guide*, CERN-OPEN-2007-007, 2009, `arXiv:physics/0703039`.

[163] OPAL Collaboration, K. Ackerstaff et al., *Search for anomalous production of dilepton events with missing transverse momentum in e^+e^- collisions at $\sqrt{s} = 161\ GeV\ and\ 172\ GeV$*, Eur.Phys.J. **C4** (1998) 47.

[164] M. Vesterinen and T. Wyatt, *A Novel Technique for Studying the Z Boson Transverse Momentum Distribution at Hadron Colliders*, Nucl.Instr.Meth. **A602** (2009) 432.

[165] M. Oreglia, *A Study of the Reactions $\psi' \to \gamma\gamma\psi$*, PhD thesis, Stanford University, 1980, SLAC-0236, `http://cds.cern.ch/record/128793`.

[166] M. S. Bernstein, *Démonstartion du théorème de Weierstrass fondée sur le calcul des probabilités*, Comm.Soc.Math. Kharkov 13 (1912).

[167] LHC Higgs Cross Section Working Group Collaboration, A. David et al., *LHC HXSWG interim recommendations to explore the coupling structure of a Higgs-like particle*, `arXiv:hep-ph/1209.0040`.

[168] ATLAS Collaboration, G. Aad et al., *Projections for measurements of Higgs boson cross sections, branching ratios and coupling parameters with the ATLAS detector at a HL-LHC*, ATL-PHYS-PUB-2013-014, CERN, 2013, `http://cds.cern.ch/record/1611186`.

[169] L. Rossi and O. Brüning, *High Luminosity Large Hadron Collider. A description for the European Strategy Preparatory Group*, CERN-ATS-2012-236, CERN, 2012, `https://cds.cern.ch/record/1471000`.

List of Figures

210

211

List of Tables

213

214